

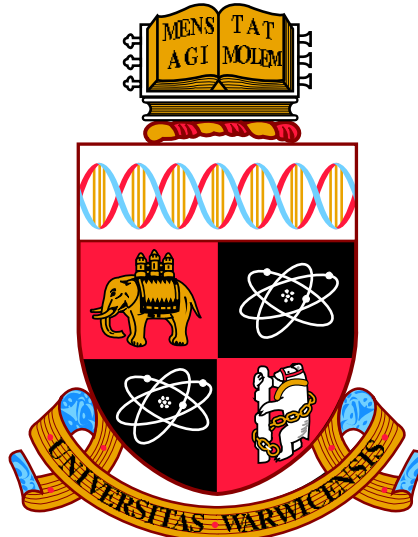
Studies of excited D mesons in B meson decays

by

Charlotte Louise Mary Wallace

Thesis

Submitted to the University of Warwick
for the degree of
Doctor of Philosophy



Department of Physics
University of Warwick, U.K.

March 2016

Contents

Acknowledgements	viii
Declaration of authorship	x
Abstract	xii
1 Introduction	1
2 Theory	3
2.1 The Standard Model	3
2.1.1 Fundamental particles and forces	3
2.1.2 Hadrons	5
2.2 <i>CP</i> violation and the CKM matrix	5
2.2.1 Symmetries in the Standard Model	5
2.2.1.1 Charge conjugation and parity	6
2.2.2 <i>CP</i> violation in the SM	7
2.2.2.1 Types of <i>CP</i> violation	7
2.2.3 Quark mixing and CKM matrix	9
2.2.3.1 Wolfenstein parametrisation	10
2.2.4 Unitarity triangles	11
2.2.5 The CKM angle γ	12
2.2.5.1 Measurement techniques	13
2.3 Charm spectroscopy	18
2.3.1 Excited states	18
2.3.2 Predicted states	19

2.3.3	Experimental status	20
2.4	Dalitz plot analysis formalism	23
2.4.1	Kinematics of three-body decays	23
2.4.2	The isobar model	25
2.4.2.1	Angular distribution	26
2.4.2.2	Blatt–Weisskopf barrier factors	26
2.4.2.3	Resonance lineshapes	27
2.4.3	Experimental details	28
2.4.3.1	The square Dalitz plot	28
2.4.3.2	Fitting	29
3	The Large Hadron Collider and LHCb detector	31
3.1	The Large Hadron Collider	31
3.2	LHCb detector	33
3.3	Tracking	35
3.3.1	VELO	35
3.3.2	Dipole magnet	37
3.3.3	Tracking stations	38
3.3.3.1	Silicon Tracker	38
3.3.3.2	Outer Tracker	40
3.4	Particle Identification	40
3.4.1	RICH detectors	40
3.4.1.1	RICH1	42
3.4.1.2	RICH2	42
3.4.1.3	HPDs	43
3.4.2	Calorimeters	43
3.4.2.1	SPD, PS and ECAL	44
3.4.2.2	HCAL	45
3.4.3	Muon chambers	45
3.5	Trigger and stripping	48
3.6	Online system	50

3.7	Software	50
3.7.1	Core software	50
3.7.2	Software analysis tools	51
3.8	Running conditions and datasets	52
3.9	Detector performance	53
4	$B \rightarrow Dhh'$ common tools and techniques	57
4.1	Analysis outline	58
4.2	Selection	58
4.2.1	Trigger	58
4.2.2	Stripping	58
4.2.3	Offline selection requirements	59
4.2.4	Neural networks	61
4.2.5	Particle identification requirements	65
4.2.6	Veto	66
4.3	Backgrounds	67
4.3.1	Combinatorial background	67
4.3.2	Peaking background	68
4.3.3	Charmless background	68
4.3.4	Partially reconstructed background	69
4.4	Efficiency	71
4.4.1	Geometrical efficiency	72
4.4.2	Selection efficiency	72
4.4.2.1	Tracking and L0 hadron trigger corrections	72
4.4.3	PID efficiency	73
4.4.4	Spline interpolation	74
4.4.5	Total efficiency	74

5 Branching fraction measurement of the $B^+ \rightarrow D^- K^+ \pi^+$ decay	77
5.1 Motivation	77
5.2 Fits to B^+ invariant mass distributions	78
5.2.1 Fit components	79
5.2.1.1 Signal	79
5.2.1.2 Combinatorial background	80
5.2.1.3 Peaking background	80
5.2.1.4 Partially reconstructed background	81
5.2.2 Fit validation	82
5.2.3 Fit results	83
5.3 Systematic uncertainties	84
5.3.1 Cross checks	86
5.4 Results	86
6 Dalitz plot analysis of $B^+ \rightarrow D^- K^+ \pi^+$ decays	88
6.1 Fit strategy	88
6.2 Background Dalitz plot distributions	89
6.3 Partial wave analysis using angular moments	91
6.4 Dalitz plot fit	93
6.4.1 Fit model	93
6.4.2 Fit results	94
6.4.2.1 Secondary minima	96
6.4.3 Testing the baseline model	98
6.5 Systematic uncertainties	99
6.5.1 Experimental uncertainties	100
6.5.2 Model uncertainties	102
6.5.3 Cross checks	104
6.6 Results	105

7 Search for $B^+ \rightarrow D^+ K^+ \pi^-$ decays	107
7.1 Motivation	107
7.2 Event selection and analysis strategy	108
7.2.1 Selection differences	109
7.2.2 Fit strategy	110
7.3 Fits to B^+ invariant mass distributions	111
7.3.1 Fit components	112
7.3.1.1 Signal	112
7.3.1.2 Combinatorial background	113
7.3.1.3 Peaking background	113
7.3.1.4 Partially reconstructed background	114
7.3.2 Fit validation	115
7.3.3 Fit results	115
7.3.4 Efficiency	116
7.4 Systematic uncertainties	119
7.4.1 Fit model	119
7.4.2 Efficiency ratio	120
7.4.3 Cross checks	121
7.5 Results	121
7.6 Quasi-two-body decays	122
7.6.1 Fit strategy	123
7.6.2 Fit model	125
7.6.3 Fit results	125
7.6.4 Systematics	126
7.6.5 Results	126
8 Dalitz plot analysis of $B^+ \rightarrow D^- \pi^+ \pi^+$ decays	130
8.1 Fit strategy	130
8.2 Background Dalitz plot distributions	131
8.3 Partial wave analysis using angular moments	132
8.4 Dalitz plot fit	135

8.4.1	Fit model	136
8.4.2	Fit results	138
8.4.2.1	Secondary minima	144
8.4.3	Testing the baseline model	144
8.4.3.1	Adding fixed resonances	144
8.4.3.2	Alternative models	147
8.5	Systematic uncertainties	147
8.5.1	Experimental uncertainties	147
8.5.2	Model uncertainties	148
8.5.3	Cross checks	151
8.6	Results	151
9	Summary	154
A	VELO material description	158
A.1	Method	158
A.2	Results	159
Bibliography		163

Acknowledgements

The past few years have been a challenging and incredibly rewarding experience. A few people have made a particularly memorable contribution during my postgraduate studies and I'm grateful for their support. Without them I don't think this work would have been possible.

I am indebted to Tim Gershon, an excellent supervisor who is incredibly knowledgable and always full of new ideas. Thank you for the opportunity to work in this interesting area of research and allowing me to travel to some fantastic places in the process!

Thanks to my second supervisor, Michal Kreps, for his guidance in the first few months of my PhD. I would also like to thank Tom Latham and Daniel Craik for demystifying some of the inner workings of LAURA++ and ROOT – many of the results in this thesis were made possible by your contributions. A special thank you is reserved for Mark Whitehead, who was never too busy to help me. The last few years would not have been the same without your words of support and encouragement. Thank you for your endless patience.

Thank you to all the other members of the Warwick LHCb group, past and present, for our numerous trips to The Old Bakery and Sunam Balti. Thanks also to the Bristol particle physics group for welcoming me over the last few months – especially Daniel, Andrew and Claire for sharing your office with me.

I'm tremendously grateful to Sam, whose support and patience has made me a better physicist and programmer. You always know when I need a break from physics and a cup of tea or a pint of ale (and of course you're more than happy to join me for the latter!). Thank you for reading the first drafts of this thesis, and for believing in me even when I didn't believe in myself.

I would not have completed my PhD without the support of my friends and family, in particular my parents. I can't begin to thank you for your words of wisdom and the enduring love and support which you've shown me for as long as I can remember. This thesis is dedicated to you both and to Grandma and Grampy, without whom I would not be where I am today.

Declaration of authorship

I declare that the work in this thesis is all my own, unless it is explicitly referenced in the text. No part of this research has been submitted for another qualification from this or any other university.

Charlotte Wallace

Signed:

Date:

Abstract

This thesis documents the studies of several three-body B^+ meson decays, each with a charged charmed meson in the final state. All analyses presented use a data sample recorded by the LHCb detector in 2011 and 2012, corresponding to an integrated luminosity of 3.0 fb^{-1} of pp collision data.

The $B^+ \rightarrow D^- K^+ \pi^+$ and $B^+ \rightarrow D^+ K^+ \pi^-$ decay modes are observed for the first time. The branching fraction of the favoured $B^+ \rightarrow D^- K^+ \pi^+$ decay mode is measured relative to the topologically similar $B^+ \rightarrow D^- \pi^+ \pi^+$ decay and the $B^+ \rightarrow D^- K^+ \pi^+$ final state is used as a normalisation channel for the suppressed $B^+ \rightarrow D^+ K^+ \pi^-$ decay branching fraction measurement.

Searches are performed for the quasi-two-body decays $B^+ \rightarrow D^+ K^*(892)^0$ and $B^+ \rightarrow D_2^*(2460)^0 K^+$, using the sample of $B^+ \rightarrow D^+ K^+ \pi^-$ candidate decays. No significant signals are observed for either decay mode and upper limits are set on their branching fractions.

Excited charmed mesons decaying to $D^- \pi^+$ are studied by performing fits to the Dalitz plots of $B^+ \rightarrow D^- K^+ \pi^+$ and $B^+ \rightarrow D^- \pi^+ \pi^+$ candidates. A structure at $m(D^- \pi^+) \sim 2.78 \text{ GeV}/c^2$ in the $D^- K^+ \pi^+$ data sample is determined to have spin-1 for the first time. Evidence from the $B^+ \rightarrow D^- \pi^+ \pi^+$ Dalitz plot suggests that the states at $m(D^- \pi^+) \sim 2.76 \text{ GeV}/c^2$ and $3.00 \text{ GeV}/c^2$, have spin-3 and spin-2, respectively. The mass and width parameters of these states are measured precisely, as are those of the well known $\bar{D}_2^*(2460)^0$ resonance. Fit fractions and product branching fractions are calculated for all contributions in the $B^+ \rightarrow D^- K^+ \pi^+$ and $B^+ \rightarrow D^- \pi^+ \pi^+$ amplitude models.

Chapter 1

Introduction

The Standard Model of particle physics is a well established theory, developed over the second half of the 20th century to explain the properties of fundamental particles and their interactions. The theory has been extensively tested by a series of innovative experiments which have driven advances in detector technology and computational techniques. Definitive predictions made by the Standard Model have led to the discovery of several particles – most recently the famous ‘Higgs boson’ which was hypothesised more than forty years before its discovery at the Large Hadron Collider in 2012. Despite these undeniable successes, the theory is known to be incomplete. Several observed phenomena are not described by the Standard Model: gravity, neutrino mixing, dark matter and the dominance of matter over antimatter in the universe. The research presented in this thesis is related to the latter.

Equal amounts of matter and antimatter should have been created in the Big Bang, so our existence – in a universe dominated by matter – implies that particles and their antiparticles are affected differently by the laws of physics. This asymmetry between matter and antimatter is accommodated in the Standard Model by ‘*CP* violation’, though the predicted amount is only enough to explain about a billionth of the matter in the present day universe. In order to understand the observed deficit of antimatter, additional sources of *CP* violation must be found. Therefore a major goal in high energy physics is to test the Standard Model by making precise measurements of *CP*-violating processes.

Studies of rare decays and *CP* violation at the LHCb experiment offer a method to search for new physics, beyond the predictions of the Standard Model. Research at LHCb is focussed on particles containing a beauty or charm quark. The amount of *CP* violation in the quark sector is quantified by one parameter in the Standard Model, but studying a wide range of processes and making precise measurements of many related quantities allows the theory to be overconstrained. The *CP*-violating phase in the weak interaction,

γ , can be determined by studying various decays of B mesons. It is important to study such decays in order to measure this parameter more precisely.

This thesis presents the studies of several B^+ meson decays¹ performed using LHCb data and published in Refs. [1] and [2]. The branching fractions of the $B^+ \rightarrow D^- K^+ \pi^+$ and $B^+ \rightarrow D^+ K^+ \pi^-$ decays are reported. Neither mode has been observed before. Resonant and nonresonant amplitudes contributing to the $B^+ \rightarrow D^- K^+ \pi^+$ and $B^+ \rightarrow D^- \pi^+ \pi^+$ decay modes are investigated by performing Dalitz plot analyses. The dominant resonances in both final states are excited charmed mesons which decay as $\bar{D}^{**0} \rightarrow D^- \pi^+$. Studying the amplitudes contributing to $B^+ \rightarrow D^- K^+ \pi^+$ and $B^+ \rightarrow D^- \pi^+ \pi^+$ decays offers an opportunity to measure the spectrum of D^{**} states and test the theoretical predictions for their parameters. Improved knowledge of the D^{**} resonances in $B^+ \rightarrow D^- K^+ \pi^+$ and $B^+ \rightarrow D^- \pi^+ \pi^+$ decays would be useful for potential measurements of γ using related decay channels in the future.

The remainder of this document is organised as follows. A general introduction to the Standard Model, CP violation and charmed meson spectroscopy is presented in Chap. 2. An overview of Dalitz plot analysis techniques is also given, before Chap. 3 introduces the Large Hadron Collider and the LHCb experiment. Chapter 4 details some analysis techniques which are common to the work presented in later chapters. The results of the branching fraction measurement and Dalitz plot analysis of the $B^+ \rightarrow D^- K^+ \pi^+$ decay are presented in Chaps. 5 and 6, respectively. Chapter 7 describes the search for the suppressed $B^+ \rightarrow D^+ K^+ \pi^-$ decay and contributions from the quasi-two-body modes $B^+ \rightarrow D^{**0} K^+$, $D^{**0} \rightarrow D^+ \pi^-$ and $B^+ \rightarrow K^{*0} D^+$, $K^{*0} \rightarrow K^+ \pi^-$. A Dalitz plot analysis of the $B^+ \rightarrow D^- \pi^+ \pi^+$ decay is detailed in Chap. 8, and Chap. 9 gives a summary and conclusion of the work. Appendix A details a study of the material distribution within the LHCb VELO sub-detector.

¹Note that the inclusion of charge conjugate processes is implied throughout this work, unless stated otherwise.

Chapter 2

Theory

2.1 The Standard Model

Our current understanding of the structure and dynamics of the universe is contained in the Standard Model (SM) of particle physics. The model describes the fundamental particles, their properties, and their interactions via the weak, electromagnetic (EM) and strong forces. This quantum field theory (QFT) has had great success in predicting experimental measurements, yet several observed phenomena are not described by the SM, including the gravitational force, neutrino masses, dark matter and the matter-antimatter asymmetry in the universe. Many studies at the LHCb experiment are related to trying to improve our understanding of the latter.

2.1.1 Fundamental particles and forces

According to the SM, all matter is composed of a small number of fundamental particles, each with definite properties determined by their quantum numbers. The quantum numbers which are related to a gauge symmetry, such as electric charge, are conserved by all types of interactions, whilst others may not be conserved in certain processes.

Particles are defined as either fermions or bosons, depending whether the value of their intrinsic ‘spin angular momentum’ quantum number, s , is a half-integer or integer value. In the SM there are three types of fundamental particle: spin- $\frac{1}{2}$ fermions, spin-1 gauge bosons and a scalar, spin-0, boson.

The fundamental fermions, shown in Tab. 2.1, are the constituents of all visible matter. These particles can be organised into three generations, each with two quarks, a charged lepton and a neutral neutrino.

The three fundamental forces are mediated by spin-1 gauge bosons: the EM force is carried by the massless photon which couples to electric charge; the weak interaction is

Table 2.1: Properties of the fundamental fermions of the SM, arranged in three generations. Masses are taken from Ref. [3].

Fermion	Symbol	Charge (e)	Mass (MeV/ c^2)	Possible interactions			Generation
				EM	Weak	Strong	
up-quark	u	+2/3	$2.3^{+0.7}_{-0.5}$	✓	✓	✓	I
down-quark	d	-1/3	$4.8^{+0.5}_{-0.3}$	✓	✓	✓	
electron	e^-	-1	$0.510998928 \pm 0.000000011$	✓	✓		
electron neutrino	ν_e	0	< 0.000002	✓			
charm-quark	c	+2/3	1275 ± 25	✓	✓	✓	II
strange-quark	s	-1/3	95 ± 5	✓	✓	✓	
muon	μ^-	-1	$105.6583715 \pm 0.0000035$	✓	✓		
muon neutrino	ν_μ	0	< 0.000002	✓			
top-quark	t	+2/3	173210 ± 874	✓	✓	✓	III
bottom-quark	b	-1/3	4180 ± 30	✓	✓	✓	
tau	τ^-	-1	1776.86 ± 0.12	✓	✓		
tau neutrino	ν_τ	0	< 0.000002	✓			

carried by the massive Z^0 and W^\pm bosons, both of which couple to ‘weak isospin’ and ‘weak hypercharge’; the strong force mediators are 8 massless gluons which couple to the ‘colour charge’. Quarks are the only fundamental fermions which possess a nonzero colour charge (quarks can have a colour of red, green or blue), allowing them to interact via the strong force, as shown in Tab. 2.1.

The final fundamental particle in the SM is the Higgs boson, which has only recently been discovered [4, 5]. The existence of this particle was predicted by theoretical models explaining the spontaneous symmetry breaking of the electroweak interaction [6, 7, 8]. All massive particles have mass as a result of their interaction with the Higgs field.

Every type of particle has an antiparticle – a particle with identical mass but opposite values for all internal quantum numbers, including electric charge and lepton number.² Antiparticles are denoted by a sign change (*e.g.* the electron, e^- , and positron, e^+) or a bar (*e.g.* the anti-electron neutrino, $\bar{\nu}_e$, or the anti-down quark, \bar{d}).

The SM has been brought together in a rather ad-hoc manner as the combination of several QFTs, each describing a different physical process. The interactions of charged particles are described by Quantum Electrodynamics (QED). At low energies the three fundamental forces are quite distinct, but a major success of the SM was the unification of electromagnetism and the weak force by the Electroweak (EW) theory. Finally, Quantum Chromodynamics (QCD) describes the strong interaction.

²If all the internal quantum numbers of a particle are zero, as is the case for the photon, the particle and antiparticle are indistinguishable.

2.1.2 Hadrons

The masses of charged leptons are measured more precisely than those of the quarks, as shown by the measurements presented in Tab. 2.1. This is because isolated leptons can easily be observed in nature, but quarks cannot exist as free particles due to colour confinement; quarks have only been observed as constituents of colour-neutral bound states called hadrons.³ There are two well established types of hadrons: mesons (a quark and an anti-quark) and baryons (three quarks or three anti-quarks). Recently the existence of exotic multi-quark states has been confirmed with studies of the tetraquark, $Z(4430)^+$ [9, 10, 11], and the $P_c(4380)^+$ and $P_c(4450)^+$ pentaquark candidates [12].

Some mesons relevant to this thesis are listed in Tab. 2.2 with their quark content and measured mass. Flavoured mesons are given a symbol based on the flavour of their heaviest quark and the identity of the lighter quark is given by a subscripted letter (unless it is u or d). The flavour quantum numbers are defined such that they have the same sign as charge, so the s -quark has negative strangeness and the c -quark has positive charm.

Table 2.2: Properties of mesons relevant to this thesis. These particles are the pseudoscalar (spin-0) ground state for the quark content shown. Masses are taken from Ref. [3].

Meson	Symbol	Quark content	Mass (MeV/ c^2)
Pion	π^\pm	$u\bar{d}, d\bar{u}$	139.57018 ± 0.00035
	π^0	$(u\bar{u} - d\bar{d})/\sqrt{2}$	134.9766 ± 0.0006
Kaon	K^\pm	$s\bar{u}, u\bar{s}$	493.677 ± 0.016
	$(\overline{K})^0$	$s\bar{d}, d\bar{s}$	497.611 ± 0.013
D meson	D^\pm	$c\bar{d}, d\bar{c}$	1869.61 ± 0.09
	$(\overline{D})^0$	$c\bar{u}, u\bar{c}$	1864.84 ± 0.05
Strange D meson	D_s^\pm	$c\bar{s}, s\bar{c}$	1968.30 ± 0.10
B meson	B^\pm	$b\bar{u}, u\bar{b}$	5279.29 ± 0.15
	$(\overline{B})^0$	$b\bar{d}, d\bar{b}$	5279.61 ± 0.16
Strange B meson	$(\overline{B}_s)^0$	$b\bar{s}, s\bar{b}$	5366.79 ± 0.23

2.2 CP violation and the CKM matrix

2.2.1 Symmetries in the Standard Model

Symmetries play an important role in physics. Noether's theorem [13] describes that every continuous symmetry is associated to the conservation of a quantity, and vice

³This is true for five of the six quarks; the short lifetime of the top quark means that it decays too quickly to hadronise and form a colour-neutral state. In addition, the short t -quark lifetime presents a challenge for mass measurements.

versa. For example, the conservation of momentum can be attributed to the invariance of a system under spatial translations, $\vec{r} \rightarrow \vec{r} + \Delta\vec{r}$.

2.2.1.1 Charge conjugation and parity

Parity is a discrete symmetry which, for normal vectors, inverts all components: $\hat{P}(\vec{r}) \equiv \hat{P}(x, y, z) = (-x, -y, -z) = -\vec{r}$. Scalar quantities are unaffected by parity inversion, as are pseudovectors *e.g.* angular momentum ($\hat{P}(\vec{L}) = \hat{P}(\vec{r} \times \vec{p}) = -\vec{r} \times -\vec{p} = \vec{r} \times \vec{p} = \vec{L}$). On the other hand, a pseudoscalar (*e.g.* a quantity given by the dot product of an ordinary vector and a pseudovector) will change sign with a parity transformation. Thus the two possible parity eigenvalues are $P = -1$ (for vectors and pseudoscalars) and $P = +1$ (for scalars and pseudovectors). All hadrons are eigenvalues of the parity operator.

Another discrete symmetry is charge conjugation. The \hat{C} operator changes the sign of all internal quantum numbers – most noticeably electric charge – turning particles into their antiparticle. The intrinsic spin of a particle is unaffected by this transformation, as are all kinematic variables such as mass, energy and momentum. Again the only two possible eigenvalues of charge conjugation are $+1$ and -1 . Only neutral states such as the photon and π^0 are eigenstates of \hat{C} .

Regardless of the particle, applying either the \hat{C} or \hat{P} operator twice returns the original state ($\hat{C}^2 = \hat{P}^2 = \hat{I}$). The electromagnetic and strong interactions are invariant under both the parity and charge conjugation transformations. However, charge conjugation changes a left-handed neutrino into a left-handed anti-neutrino, whilst under the parity transformation a left-handed neutrino becomes a right-handed neutrino. Both of these symmetries are therefore maximally violated by the weak force, which couples only to left-handed neutrinos and right-handed anti-neutrinos. A combination of the two transformations, CP , converts a left-handed neutrino into a right-handed anti-neutrino (and vice versa), so this symmetry was once thought to be conserved by the weak force [14, 15]. The violation of CP symmetry has been observed in several different particle systems. An additional symmetry can be defined by including the time reversal symmetry (T) which transforms $t \rightarrow -t$. No experimental evidence for the violation of CPT symmetry has been found. This is consistent with the CPT theorem which states that the combination of C , P and T symmetries (in any order) must be an exact symmetry of any interaction in a Lorentz invariant local gauge theory.

Although CP violation has only been observed in weak interactions, the mathematical description of QCD does not forbid CP violation in strong decays. Since there is no known reason for CP symmetry to be conserved in QCD, this is a fine tuning problem known as the ‘strong CP problem’. The best known solution to this problem is the Peccei–Quinn model [16], which predicts scalar particles called axions.

2.2.2 CP violation in the SM

The study of CP violation is of great interest due to its role in the observed asymmetry of matter and antimatter in our universe. Sakharov proposed three conditions necessary to produce the observed excess of baryons over anti-baryons [17]:

- at least one interaction must violate the conservation of baryon number, a quantum number which is zero for all fundamental particles except quarks,
- both C and CP symmetries must be violated by some processes in order for baryons to become more plentiful than anti-baryons,
- at some point in the history of the universe interactions must have occurred out of thermal equilibrium, while processes violating baryon number, C and CP symmetries were occurring.

The currently known CP -violating processes are insufficient to produce the matter-antimatter asymmetry observed [18].

2.2.2.1 Types of CP violation

CP violation can manifest itself via three mechanisms:

- CP violation in decay – occurs when the decay amplitude of a state differs from that of its CP conjugate, this can affect both charged and neutral decays;
- CP violation in neutral meson mixing – occurs in cases where the mass eigenstates of the neutral meson are not CP eigenstates;
- CP violation in the interference between mixing and decay – occurs when a neutral meson and its antiparticle decay to the same final state, either before or after mixing, and the two interfere with a non-trivial phase difference.

More information about each of these processes is now given.

CP violation in decay

The decay amplitude, A_f , for the decay $B \rightarrow f$ can be written as a sum over all contributing amplitudes,

$$A_f = \sum_j |A_j| e^{i(\delta_j - \phi_j)}, \quad (2.1)$$

where each real valued amplitude A_j has a strong phase, δ_j , and a weak phase, ϕ_j . Strong phases do not change sign under the CP transformation, but weak phases do. Thus the equivalent expression for the CP conjugate decay $\bar{B} \rightarrow \bar{f}$ is given by

$$\bar{A}_{\bar{f}} = \sum_j |A_j| e^{i(\delta_j + \phi_j)}. \quad (2.2)$$

CP violation in decay occurs if the ratio of these total amplitudes differs from unity:

$$\left| \frac{\bar{A}_{\bar{f}}}{A_f} \right| = \left| \frac{\sum_j |A_j| e^{i(\delta_j + \phi_j)}}{\sum_j |A_j| e^{i(\delta_j - \phi_j)}} \right| \neq 1, \quad (2.3)$$

which will occur in cases where two or more contributing amplitudes have different strong and weak phases.

This type of CP violation was first observed in the decays of neutral kaons [19]; observations have since been made in several other decay modes including those of charged mesons [20], for which this is the only CP violation mechanism available.

CP violation in mixing

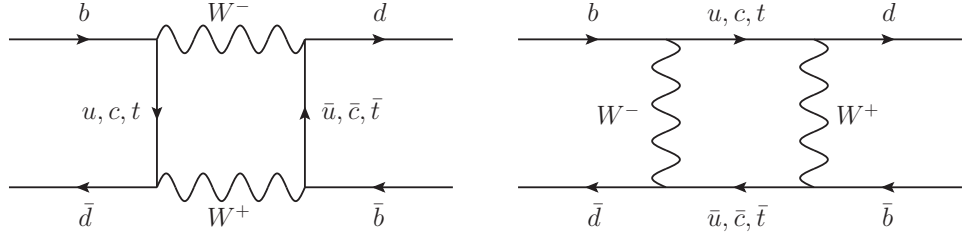


Figure 2.1: Feynman diagrams for $B^0 - \bar{B}^0$ mixing. The emission or absorption of a charged W boson allows quarks to change flavour. Such diagrams are called ‘box’ Feynman diagrams.

The mass eigenstates of neutral mesons are mixtures of flavour eigenstates. This allows neutral mesons to mix, or oscillate, between the flavour eigenstates, *e.g.* B^0 and \bar{B}^0 . As described in Sec. 2.2.3, the weak interaction allows quarks to change flavour. This flavour changing occurs in neutral meson mixing, as shown by the Feynman diagrams for the oscillations of neutral B mesons in Fig. 2.1.

Considering the neutral B meson system (the formalism below applies to other neutral meson systems in the same way), each mass eigenstate can be expressed as a linear combination of the flavour eigenstates,

$$|B_L\rangle = p|B^0\rangle + q|\bar{B}^0\rangle \quad \text{and} \quad |B_H\rangle = p|B^0\rangle - q|\bar{B}^0\rangle, \quad (2.4)$$

where the labels L and H refer to the light and heavy eigenstates, respectively, and p and q are constant complex parameters satisfying the relation $|p|^2 + |q|^2 = 1$. The

flavour eigenstates are swapped by the CP transformation using a convention in which $(\hat{C}\hat{P}|B^0\rangle = |\bar{B}^0\rangle$ and $\hat{C}\hat{P}|\bar{B}^0\rangle = |B^0\rangle)$ so the CP even and CP odd eigenstates can be defined as

$$|B_{CP+}\rangle = \frac{|B^0\rangle + |\bar{B}^0\rangle}{\sqrt{2}} \quad \text{and} \quad |B_{CP-}\rangle = \frac{|B^0\rangle - |\bar{B}^0\rangle}{\sqrt{2}}. \quad (2.5)$$

The mass eigenstates can then be rewritten as

$$|B_L\rangle = \frac{p+q}{\sqrt{2}}|B_{CP+}\rangle + \frac{p-q}{\sqrt{2}}|B_{CP-}\rangle \quad \text{and} \quad |B_H\rangle = \frac{p+q}{\sqrt{2}}|B_{CP-}\rangle - \frac{p-q}{\sqrt{2}}|B_{CP+}\rangle. \quad (2.6)$$

CP violation occurs in the mixing of neutral mesons if the mass eigenstates are not CP eigenstates, *i.e.* $|q/p| \neq 1$. This causes a difference in the rates of $B^0 \rightarrow \bar{B}^0$ and $\bar{B}^0 \rightarrow B^0$ oscillations. This type of CP violation has been measured in the K^0 system [19].

CP violation in interference between mixing and decay

If a particle and its antiparticle are able to decay to the same final state then CP violation can also occur as a result of interference between the decays with and without mixing, *e.g.* $B^0 \rightarrow f$ and $B^0 \rightarrow \bar{B}^0 \rightarrow f$. The complex parameter λ_f can be defined to be

$$\lambda_f = \frac{q}{p} \frac{\bar{A}_f}{A_f}, \quad (2.7)$$

where A_f and \bar{A}_f are the amplitudes for the processes $B^0 \rightarrow f$ and $B^0 \rightarrow \bar{B}^0 \rightarrow f$, respectively. The condition for CP violation in the interference of decay and mixing is $\text{Im}(\lambda_f) \neq 0$. This type of CP violation has been measured in the B^0 system [21].

2.2.3 Quark mixing and CKM matrix

The weak interaction allows quarks to change from one flavour to another via the emission or absorption of a charged W boson. Such a transition occurs most commonly between quarks of the same generation, *e.g.* $d \rightarrow u$, but changes between different generations are also allowed. The gauge bosons mediating the weak interaction couple to weak eigenstates of the quarks (u', d', c', s', t', b') rather than the mass eigenstates (u, d, c, s, t, b) . The convention is to define the weak eigenstates and mass eigenstates to be the same for up-type quarks,

$$\begin{pmatrix} u' \\ c' \\ t' \end{pmatrix} = \begin{pmatrix} u \\ c \\ t \end{pmatrix}, \quad (2.8)$$

whilst for down-type quarks the weakly interacting states are related to the physical quarks by the Cabibbo–Kobayashi–Maskawa (CKM) matrix [22, 23], V_{CKM} :

$$\begin{pmatrix} d' \\ s' \\ b' \end{pmatrix} = V_{\text{CKM}} \begin{pmatrix} d \\ s \\ b \end{pmatrix} = \begin{pmatrix} V_{ud} & V_{us} & V_{ub} \\ V_{cd} & V_{cs} & V_{cb} \\ V_{td} & V_{ts} & V_{tb} \end{pmatrix} \begin{pmatrix} d \\ s \\ b \end{pmatrix}. \quad (2.9)$$

Each matrix element, V_{ij} , is a complex number specifying the coupling for the quark transition $j \rightarrow i$. All information about quark mixing is contained in these elements.

Probability conservation requires the CKM matrix to be unitary, *i.e.* $V_{\text{CKM}}^\dagger V_{\text{CKM}} = I$, which halves the number of free parameters to nine real numbers. Five of the nine free parameters can be absorbed into the quark fields, so the matrix can be written in terms of just three magnitudes and one phase,

$$V_{\text{CKM}} = \begin{pmatrix} 1 & 0 & 0 \\ 0 & c_{23} & s_{23} \\ 0 & -s_{23} & c_{23} \end{pmatrix} \begin{pmatrix} c_{13} & 0 & s_{13}e^{-\delta} \\ 0 & 1 & 0 \\ -s_{13}e^{\delta} & 0 & c_{13} \end{pmatrix} \begin{pmatrix} c_{12} & s_{12} & 0 \\ -s_{12} & c_{12} & 0 \\ 0 & 0 & 1 \end{pmatrix}, \quad (2.10)$$

where s_{ij} and c_{ij} are the sine and cosine of the Euler angles θ_{ij} and δ is the CP -violating phase.

2.2.3.1 Wolfenstein parametrisation

Another common way to parametrise the CKM matrix uses the Wolfenstein parameters [24] λ , A , ρ and η , defined by

$$\lambda = s_{12}, \quad A = \frac{s_{23}}{s_{12}^2}, \quad \rho = \frac{s_{13}}{s_{12}s_{23}} \cos \delta \quad \text{and} \quad \eta = \frac{s_{13}}{s_{12}s_{23}} \sin \delta. \quad (2.11)$$

Then the CKM matrix (with terms up to $\mathcal{O}(\lambda^3)$) is

$$V_{\text{CKM}} = \begin{pmatrix} 1 - \frac{\lambda^2}{2} & \lambda & A\lambda^3(\rho - i\eta) \\ -\lambda & 1 - \frac{\lambda^2}{2} & A\lambda^2 \\ A\lambda^3(1 - \rho - i\eta) & -A\lambda^2 & 1 \end{pmatrix} + \mathcal{O}(\lambda^4). \quad (2.12)$$

This parametrisation highlights the relative sizes of the matrix elements. As expected, the diagonal elements corresponding to quark transitions within the same generation (V_{ud} , V_{cs} and V_{tb}) have the largest magnitudes. In this parametrisation the phase δ is contained only in the ρ and η terms, which appear, at $\mathcal{O}(\lambda^3)$, only in the V_{ub} and V_{td} matrix elements. With this convention, since only relative phases are observable, it is clear that CP violation measurements are only possible by studying the phase difference between $b \rightarrow u$ or $t \rightarrow d$ transitions and other amplitudes.

Table 2.3: Best fit values for the Wolfenstein parameters [25].

Parameter	Value
A	$0.8227^{+0.0066}_{-0.0136}$
λ	$0.22543^{+0.00042}_{-0.00031}$
$\bar{\rho}$	$0.1504^{+0.0121}_{-0.0062}$
$\bar{\eta}$	$0.3540^{+0.0069}_{-0.0076}$

Current best fit values for the Wolfenstein parameters are given in Tab. 2.3⁴ and the experimentally measured magnitudes of the CKM matrix elements [25] are

$$|V_{\text{CKM}}| = \begin{pmatrix} 0.974254^{+0.000071}_{-0.000097} & 0.22542^{+0.00042}_{-0.00031} & 0.003714^{+0.000072}_{-0.000060} \\ 0.22529^{+0.00041}_{-0.00032} & 0.973394^{+0.000074}_{-0.000096} & 0.04180^{+0.00033}_{-0.00068} \\ 0.008676^{+0.000087}_{-0.000150} & 0.04107^{+0.00031}_{-0.00067} & 0.999118^{+0.000024}_{-0.000014} \end{pmatrix}. \quad (2.13)$$

2.2.4 Unitarity triangles

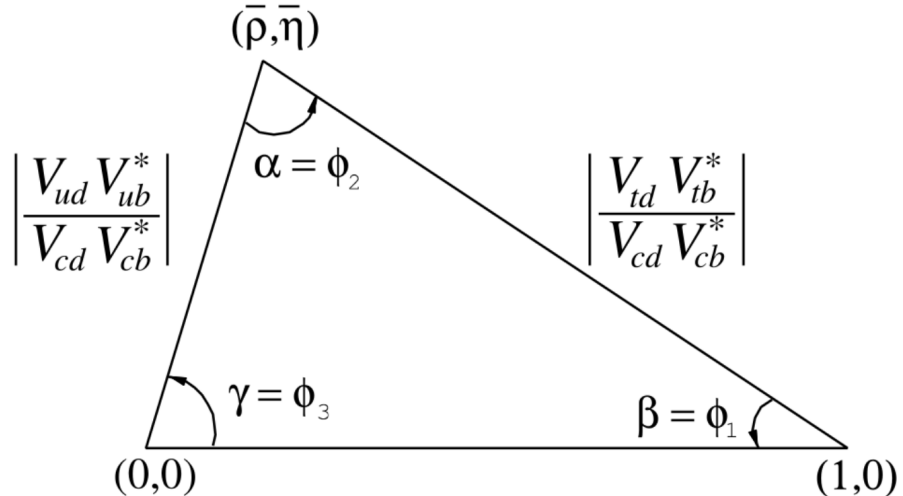


Figure 2.2: The most commonly used unitarity triangle, formed by applying the unitarity constraint to the first and third columns of the CKM matrix, drawn in the $\bar{\rho} - \bar{\eta}$ plane. Figure taken from Ref. [3].

Imposing unitarity on the CKM matrix elements by requiring

$$\sum_i V_{ij} V_{ik}^* = 0 \quad (j \neq k), \quad (2.14)$$

⁴The parameters $\bar{\rho}$ and $\bar{\eta}$ are defined by $\bar{\rho} = \rho \left(1 - \frac{\lambda^2}{2}\right)$ and $\bar{\eta} = \eta \left(1 - \frac{\lambda^2}{2}\right)$.

produces six equations:

$$\begin{aligned} V_{ub}V_{ud}^* + V_{cb}V_{cd}^* + V_{tb}V_{td}^* &= 0, & \underline{V_{ud}V_{ub}^* + V_{cd}V_{cb}^* + V_{td}V_{tb}^*} &= 0, \\ V_{ud}V_{us}^* + V_{cd}V_{cs}^* + V_{td}V_{ts}^* &= 0, & \underline{V_{us}V_{ud}^* + V_{cs}V_{cd}^* + V_{ts}V_{td}^*} &= 0, \\ V_{us}V_{ub}^* + V_{cs}V_{cb}^* + V_{ts}V_{tb}^* &= 0, & \underline{V_{ub}V_{us}^* + V_{cb}V_{cs}^* + V_{tb}V_{ts}^*} &= 0. \end{aligned} \quad (2.15)$$

Each relation is the vanishing sum of three complex numbers, so can be represented as a closed triangle in the complex plane. All six triangles have the same area, equal to $J/2$ where J is the Jarlskog invariant [26] – a convention-independent measure of the amount of CP violation in the SM. The most commonly used triangle is shown in Fig. 2.2, which is derived from the underlined relation in Eq. 2.15 but rescaled to have one side along the horizontal axis with unit length. The vertices of this triangle in the $\bar{\rho} - \bar{\eta}$ plane are at $(0,0)$, $(1,0)$ and $(\bar{\rho}, \bar{\eta})$, and the internal angles are given by

$$\alpha \equiv \arg \left(-\frac{V_{td}V_{tb}^*}{V_{ud}V_{ub}^*} \right), \quad \beta \equiv \arg \left(-\frac{V_{cd}V_{cb}^*}{V_{td}V_{tb}^*} \right), \quad \gamma \equiv \arg \left(-\frac{V_{ud}V_{ub}^*}{V_{cd}V_{cb}^*} \right), \quad (2.16)$$

which are alternatively called ϕ_2 , ϕ_1 and ϕ_3 , respectively. A major goal of modern flavour physics is to overconstrain the CKM matrix by measuring as many parameters as possible using a variety of independent experiments and methods. Precise measurement of the CKM parameters is a test for physics beyond the SM; if the sum of the CKM angles $(\alpha + \beta + \gamma) \neq 180^\circ$, then at least one of the processes used for the measurements is affected by contributions from physics which is not correctly described by the current theory. Figure 2.3 shows the current constraints on the unitarity triangle, obtained from a global fit to all available measurements, and the measured values of the CKM angles are shown in Tab. 2.4.

Table 2.4: Current experimental values for the angles of the unitarity triangle [25].

Angle	Value (°)
α	$87.6^{+3.5}_{-3.3}$
β	$21.85^{+0.68}_{-0.67}$
γ	$73.2^{+6.3}_{-7.0}$

2.2.5 The CKM angle γ

One focus of the LHCb experiment is to improve the measurement of the unitarity triangle angle γ , which is currently the least precisely measured angle of the triangle, with uncertainties of about 7° [25, 27, 28]. From Eq. 2.16, sensitivity to the CKM angle γ comes from interference between decay amplitudes featuring the V_{ub} and V_{cb} CKM matrix elements, *i.e.* $b \rightarrow u\bar{c}s$ and $b \rightarrow c\bar{u}s$ transitions such as $B^\pm \rightarrow Dh^\pm$ decays, where h is either a kaon or a pion. These decays are dominated by tree level Feynman diagrams, *i.e.* there are no loops with virtual contributions from heavier particles so

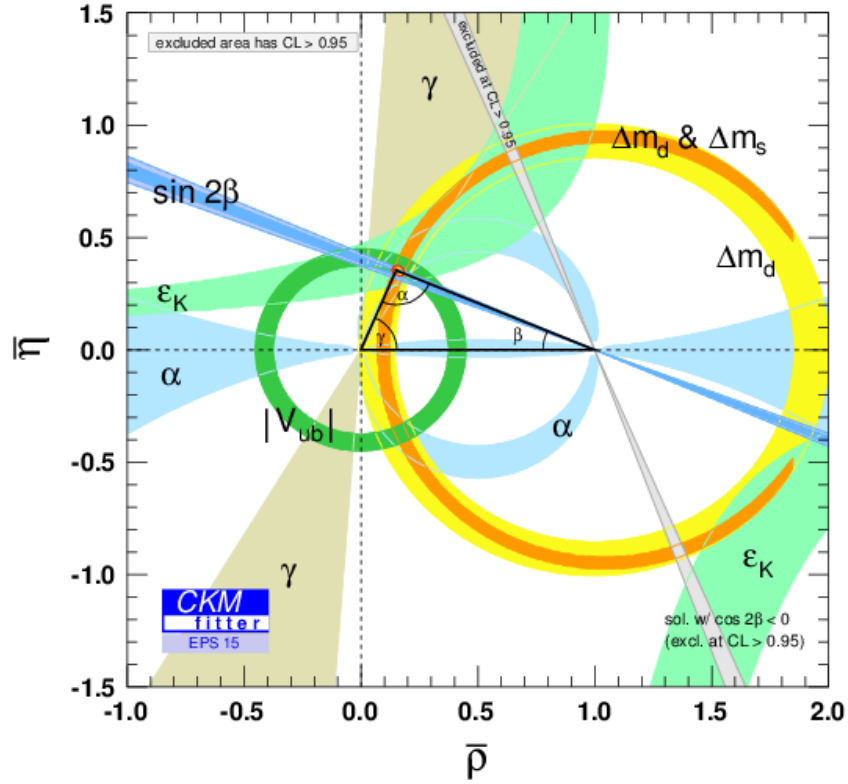


Figure 2.3: The current experimental constraints on the unitarity triangle, shown in the $\bar{\rho} - \bar{\eta}$ plane. Inputs include ϵ_K , a measurement of CP violation in the kaon sector, and Δm_d (Δm_s), the oscillation frequencies between the mass eigenstates in the B^0 (B_s^0) systems. Figure taken from Ref. [25].

there is unlikely to be any enhancement from physics beyond the SM. However, the angle can also be measured using processes containing loops, and any difference in the results obtained using these two methods would indicate new physics.

2.2.5.1 Measurement techniques

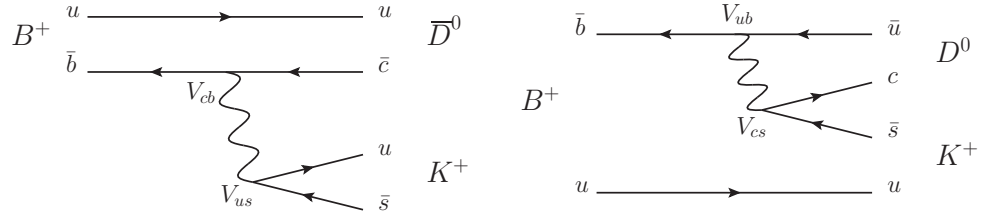


Figure 2.4: Feynman diagrams for (left) $B^+ \rightarrow \bar{D}^0 K^+$ and (right) $B^+ \rightarrow D^0 K^+$ decays.

Several methods have been used to make time-independent measurements of the CKM angle γ . The amplitudes of the decays $B^+ \rightarrow D^0 K^+$ and $B^+ \rightarrow \bar{D}^0 K^+$ (for which decay diagrams are shown in Fig. 2.4) interfere when the neutral D meson is reconstructed in a

final state accessible to both D^0 and \bar{D}^0 decays. Any asymmetry in the observed yields for a decay and its conjugate process, *e.g.* $B^+ \rightarrow DK^+$ and $B^- \rightarrow DK^-$, is sensitive to γ . Three common methods, which use different D final states, are summarised below: the Gronou, London and Wyler (GLW) method; the Atwood, Dunietz and Soni (ADS) method; and the Giri, Grossman, Soffer and Zupan (GGSZ) method.

GLW method

For the GLW method [29, 30] the D meson is reconstructed in a CP eigenstate, f_{CP} , *e.g.* one of the CP even final states $D \rightarrow K^+K^-$ or $D \rightarrow \pi^+\pi^-$, or the CP odd $D \rightarrow K_s^0\pi^0$ decay channel.⁵ The decay $B^+ \rightarrow D_{CP}K^+$ has two contributions: one with the amplitudes $B^+ \rightarrow D^0K^+$ and $D^0 \rightarrow f_{CP}$ and one with the amplitudes $B^+ \rightarrow \bar{D}^0K^+$ and $\bar{D}^0 \rightarrow f_{CP}$. The relative weak phase between the $B^+ \rightarrow D^0K^+$ and $B^+ \rightarrow \bar{D}^0K^+$ amplitudes is given by γ and the relative strong phase is denoted δ_B . The amplitudes can therefore be written as

$$A_B = A(B^\pm \rightarrow D^0K^\pm) \quad \text{and} \quad A_B r_B e^{i(\delta_B \pm \gamma)} = A(B^\pm \rightarrow \bar{D}^0K^\pm), \quad (2.17)$$

for B^\pm decays, where r_B is the ratio of the magnitudes of the two amplitudes.⁶ In the case of a CP eigenstate final state, the amplitudes of the D^0 and \bar{D}^0 decays have the same magnitude – to a good approximation, there is no CP violation in D decays so the phase difference between $D^0 \rightarrow f_{CP}$ and $\bar{D}^0 \rightarrow f_{CP}$ is zero. Thus $A_D = A(D^0 \rightarrow f_{CP}) = A(\bar{D}^0 \rightarrow f_{CP}) = \bar{A}_D$.

The decay width of a process is the square of the sum of all contributing amplitudes, *e.g.* for the decay $B^\pm \rightarrow D_{CP+}K^\pm$,

$$\Gamma(B^\pm \rightarrow D_{CP+}K^\pm) = |A_B|^2 |A_D|^2 \left| 1 + r_B e^{i(\delta_B \pm \gamma)} \right|^2. \quad (2.18)$$

The relevant decay widths for the GLW method can be related to observable CP asymmetries,

$$A_{CP\pm} = \frac{\Gamma(B^- \rightarrow D_{CP\pm}K^-) - \Gamma(B^+ \rightarrow D_{CP\pm}K^+)}{\Gamma(B^- \rightarrow D_{CP\pm}K^-) + \Gamma(B^+ \rightarrow D_{CP\pm}K^+)} \quad (2.19)$$

$$= \frac{\pm 2r_B \sin \delta_B \sin \gamma}{1 + r_B^2 \pm 2r_B \cos \delta_B \cos \gamma}, \quad (2.20)$$

which can be measured to determine γ , r_B and δ_B if sufficient independent constraints are available.

⁵Note that CP odd eigenstates are more challenging to reconstruct in the LHCb detector due to the neutral particles in the final state.

⁶Elsewhere in this document r_B is used to refer to the ratio of magnitudes of alternative B^\pm decay modes.

The decay $B^+ \rightarrow \bar{D}^0 K^+$ is both colour and CKM suppressed with respect to $B^+ \rightarrow D^0 K^+$. This leads to a small value of r_B for these decays, so interference effects between the two contributing amplitudes are $\mathcal{O}(10\%)$. The relative suppression is illustrated in Fig. 2.5 (left) which shows the two interfering decay paths of $B^+ \rightarrow D^0 K^+$ and $B^+ \rightarrow \bar{D}^0 K^+$ used in the GLW method.

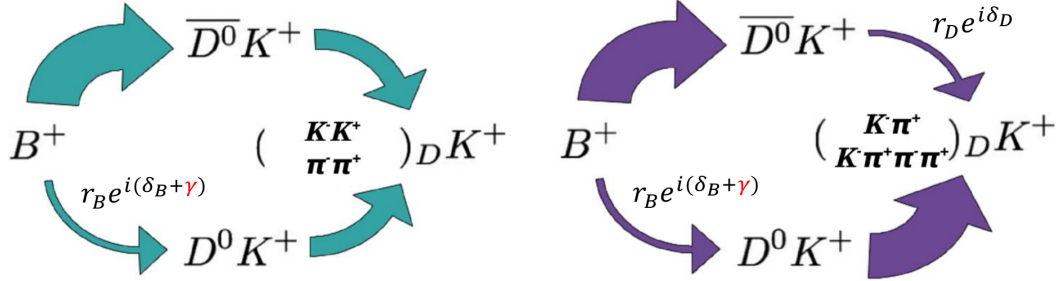


Figure 2.5: Diagram of the two interfering decay paths for $B^+ \rightarrow D^0 K^+$ and $B^+ \rightarrow \bar{D}^0 K^+$ when both neutral D mesons decay to a common final state. The D meson is reconstructed in a (left) CP eigenstate final state for the GLW method and (right) non CP eigenstate final state for the ADS method.

It is not possible to make an independent measurement of r_B for $B^+ \rightarrow DK^+$ decays when the D meson is reconstructed in a CP even final state. An alternative approach is to study the decays of $B^+ \rightarrow D^{**} K^+$ decays, where D^{**} is an excited D or \bar{D} meson which can decay as either $D^{**} \rightarrow D^+ \pi^-$ or $D^{**} \rightarrow D \pi^0$ [31]. The $B^+ \rightarrow D^{**} K^+ \rightarrow D \pi^0 K^+$ process is potentially useful for a measurement of γ and the alternative D^{**} decay can be used to make an independent measurement of r_B by considering the ratio of branching fractions for the $B^+ \rightarrow D^{**0} K^+ \rightarrow D^+ \pi^- K^+$ and $B^+ \rightarrow \bar{D}^{**0} K^+ \rightarrow D^- \pi^+ K^+$ decay modes. A measurement of r_B using these decays is described in Chap. 7.

ADS method

For the ADS method [32] the neutral D meson is reconstructed in non CP eigenstate final states *e.g.* $D \rightarrow K^\pm \pi^\mp$. This choice boosts the interference effects between contributing decay amplitudes and hence offers enhanced sensitivity to γ . The $K^- \pi^+$ final state is accessible from either the Cabibbo favoured (CF) decay of $D^0 \rightarrow K^- \pi^+$ ($\bar{D}^0 \rightarrow K^+ \pi^-$) or the doubly Cabibbo suppressed (DCS) $\bar{D}^0 \rightarrow K^- \pi^+$ ($D^0 \rightarrow K^+ \pi^-$) decay. The amplitudes of the DCS and CF D decays are not the same; the ratio of the D^0 and \bar{D}^0 decay magnitudes is denoted r_D and their relative strong phase difference is δ_D . The ratio r_D is small ($\sim 6\%$) for final states used in the ADS method, making these decay modes quasi-flavour-specific.

As shown in Fig. 2.5 (right), the two interfering amplitudes for $B^+ \rightarrow DK^+$ then each proceed via one favoured and one suppressed decay, so are of a comparable size. The

four possible decay rates are given by

$$\Gamma(B^\pm \rightarrow (K^\mp\pi^\pm)_D K^\pm) \propto 1 + (r_B r_D)^2 + 2r_B r_D \cos(\delta_B - \delta_D \pm \gamma), \quad (2.21)$$

$$\Gamma(B^\pm \rightarrow (K^\pm\pi^\mp)_D K^\pm) \propto r_B^2 + r_D^2 + 2r_B r_D \cos(\delta_B + \delta_D \pm \gamma), \quad (2.22)$$

where the constant of proportionality is the same in both expressions.

Observable quantities can be constructed in a similar way to those defined for the GLW method. The asymmetry of suppressed rates is given by

$$A_{\text{ADS}} = \frac{\Gamma(B^- \rightarrow (K^+\pi^-)_D K^-) - \Gamma(B^+ \rightarrow (K^-\pi^+)_D K^+)}{\Gamma(B^- \rightarrow (K^+\pi^-)_D K^-) + \Gamma(B^+ \rightarrow (K^-\pi^+)_D K^+)} \quad (2.23)$$

$$= \frac{2r_B r_D \sin(\delta_B + \delta_D) \sin \gamma}{r_D^2 + r_B^2 + 2r_B r_D \cos(\delta_B + \delta_D) \cos \gamma}, \quad (2.24)$$

and the ratio of suppressed to favoured,

$$R_{\text{ADS}} = \frac{\Gamma(B^- \rightarrow (K^+\pi^-)_D K^-) + \Gamma(B^+ \rightarrow (K^-\pi^+)_D K^+)}{\Gamma(B^- \rightarrow (K^-\pi^+)_D K^-) + \Gamma(B^+ \rightarrow (K^+\pi^-)_D K^+)} \quad (2.25)$$

$$= \frac{r_D^2 + r_B^2 + 2r_B r_D \cos(\delta_B + \delta_D) \cos \gamma}{1 + (r_B r_D)^2 + 2r_B r_D \cos(\delta_B - \delta_D) \cos \gamma}. \quad (2.26)$$

In order to overconstrain measurements of γ using the ADS method alone, additional final states must be considered for the neutral D meson decays. One possible choice is the four-body $D \rightarrow K\pi\pi\pi$ decay. The number of unknowns can also be reduced by using values of r_D and δ_D measured at other experiments or from charm mixing.

GGSZ method

Another method to measure γ involves studying the Dalitz plot distribution⁷ of candidates reconstructed in a self-conjugate final state of the D meson, *e.g.* $D \rightarrow K_S^0\pi^+\pi^-$. In the case of a three-body D decay mode, the amplitude of the decay $B^- \rightarrow DK^-$, A_{B^-} , at each point in phase space is a superposition of contributions from $B^- \rightarrow D^0 K^-$ and $B^- \rightarrow \bar{D}^0 K^-$ (where D , D^0 and \bar{D}^0 all decay to the same final state),

$$A_{B^-}(m_-^2, m_+^2) \propto A_{D^0}(m_-^2, m_+^2) + r_B e^{i(\delta_B - \gamma)} A_{\bar{D}^0}(m_-^2, m_+^2), \quad (2.27)$$

where m_\pm^2 are the squared invariant masses of the $K_S^0\pi^\pm$ combinations, used to define the position in the Dalitz plot and A_{D^0} ($A_{\bar{D}^0}$) is the amplitude of the decay $D^0 \rightarrow K_S^0\pi^+\pi^-$ ($\bar{D}^0 \rightarrow K_S^0\pi^+\pi^-$). Assuming no CP violation in the decay of the neutral D meson, the

⁷Information about the Dalitz plot analysis formalism is given in Sec. 2.4.

amplitudes are related by

$$A_{D^0}(m_+^2, m_-^2) = A_{\bar{D}^0}(m_+^2, m_-^2). \quad (2.28)$$

The square of the B decay amplitude given in Eq. 2.27 depends on the strong phase difference between the D^0 and \bar{D}^0 decays, $\delta_D(m_+^2, m_-^2)$, which varies over phase space and for a self-conjugate final state, $\delta_D(m_+^2, m_-^2) = -\delta_D(m_-^2, m_+^2)$. A model-dependent approach to measure γ can be followed, where $\delta_D(m_+^2, m_-^2)$ is taken from an amplitude analysis of flavour-tagged $D^0 \rightarrow K_s^0 \pi^+ \pi^-$ decays [33] and used as input to a simultaneous fit of the $B^+ \rightarrow (K_s^0 \pi^+ \pi^-)_D K^+$ and $B^- \rightarrow (K_s^0 \pi^+ \pi^-)_D K^-$ Dalitz plots [34]. A disadvantage of this type of analysis is that deficiencies in the assumed Dalitz plot model can introduce large systematic uncertainties, the magnitudes of which are often difficult to estimate. Therefore it is desirable to avoid any model uncertainty by using a model-independent method to measure γ .

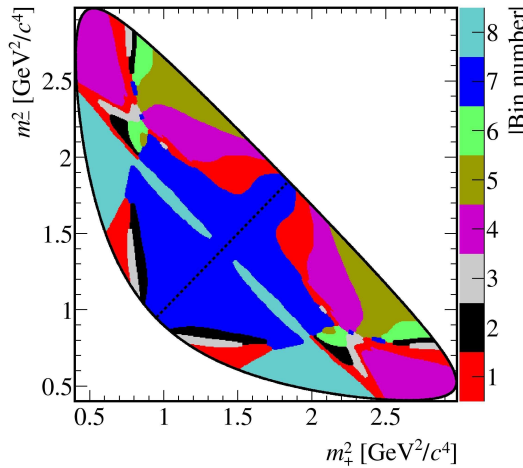


Figure 2.6: The Dalitz plot binning scheme used by LHCb for the model-independent measurement of γ from $B^\pm \rightarrow (K_s^0 \pi^+ \pi^-)_D K^\pm$ decays. Figure taken from Ref. [35].

The GGSZ [36] method is a model-independent approach to measuring CP violation; the sensitivity to γ can be increased by dividing the available phase space into bins representing areas with similar values of $\delta_D(m_+^2, m_-^2)$. The value of $\cos \delta_D$ and $\sin \delta_D$ for each bin can be obtained without an amplitude model – one method exploits the quantum coherence of D^0 – \bar{D}^0 pairs produced at the $\psi(3770)$ resonance to measure $\cos \delta_D$ and $\sin \delta_D$ (averaged over regions of phase space) directly [37]. The binning scheme used for the most recent analysis of this kind at LHCb is shown in Fig. 2.6.

2.3 Charm spectroscopy

2.3.1 Excited states

The analyses presented in this thesis involve the study of orbitally excited charmed ($c\bar{u}$) mesons, denoted D^{**} states. The $q\bar{q}'$ mesons described above are the ground states which have quantum numbers corresponding to the lowest energy configuration. Excited states have the same quark content but different quantum numbers. These quantum numbers determine the properties of excited states such as mass, lifetime and allowed decay channels. Excited states have higher masses and much shorter lifetimes than the ground state because they decay via the strong or electromagnetic interaction rather than the weak force.

A two quark system can have a total spin (S) of 0 or 1, corresponding to the quark spins being aligned antiparallel or parallel respectively. The orbital angular momentum of the system, L , can take any positive integer value; $L = 0, 1, 2, 3$ states are referred to using the letters S, P, D and F, respectively. An important conserved quantity in particle physics is the total angular momentum, J , calculated as the vector sum of L and S , where J can take integer values in the range $|L - S| \leq J \leq L + S$. Thus in the ground state ($L = 0$), the only allowed values of J are 0 and 1 – corresponding to S being 0 or 1, respectively. For orbital excitations the number of allowed states increases to four, *e.g.* in the case of P-wave ($L = 1$) states $J \in 0, 1, 2$ for $S = 1$ and there is an additional $J = 1$ state for $S = 0$.

Other quantum numbers include charge conjugation, C , and parity, P , corresponding to the symmetries described in Sec. 2.2.1. All fundamental particles have an intrinsic value of P , which can be combined for composite objects with additional contributions included to account for interactions between the constituents. In the case of $q\bar{q}'$ mesons, $P = (-1)^{L+1}$ with the result often simplified to ‘+’ (even) or ‘-’ (odd). The convention is to use a superscripted ‘*’ to label states with ‘natural’ spin parity ($P = (-1)^J$, so $J^P = 0^+, 1^-, 2^+, 3^-, \dots$), which can decay to two pseudoscalars. A numerical subscript after the meson symbol is used to denote the spin (J) of the state, and for a strongly decaying excited state the measured mass is often given in parentheses. Spectroscopic notation of the form ${}^{2S+1}L_J$ can also be used to refer to excited states.

In addition to orbitally excited states, mesons also have radial excitations. The quark and anti-quark are more separated in radially excited states, but the internal quantum numbers are unchanged. Radial excitations appear at higher masses because QCD confinement pushes these states to higher energies. This is shown in Fig. 2.7, which shows the S-wave radially excited $c\bar{u}$ states (marked ‘2S’) – these states have the same quantum numbers as the first orbital excitations (marked ‘1S’) but their predicted masses are $\sim 700 \text{ MeV}/c^2$ higher.

2.3.2 Predicted states

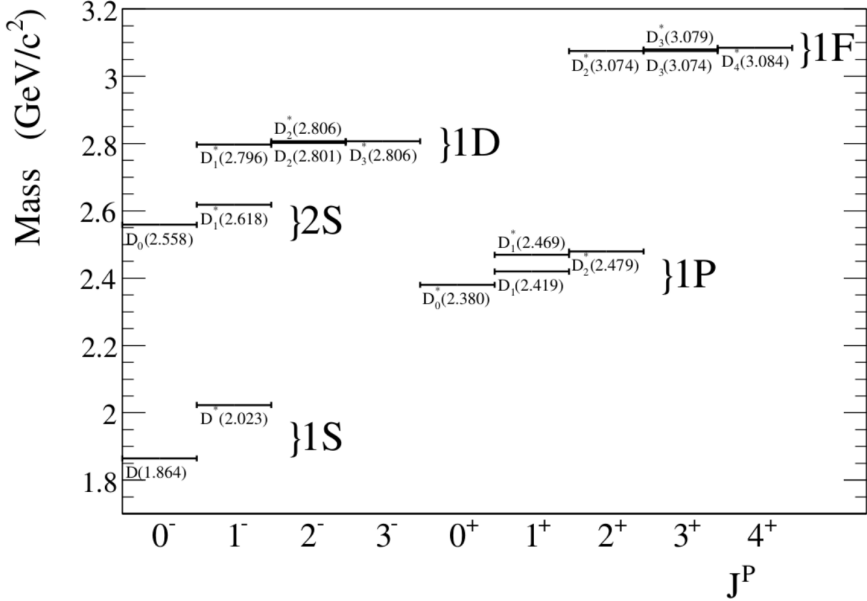


Figure 2.7: Expected mass spectrum for $c\bar{u}$ states. Braces indicate the states sharing the same orbital angular momentum, L . Excited states are shown up to ‘2S’ (radially excited S-wave states). States are grouped into columns by their spin parity, J^P . Figure taken from Ref. [38], created using information in Ref. [39].

The spectrum of excited charmed states can be predicted using various approaches, including lattice QCD and effective theories. Precise measurement of the properties of charmed mesons offers a method of testing the predictions of these theories. Figure 2.7 shows the predicted mass spectrum of excited D^{**} states.

Heavy Quark Effective Theory (HQET) makes approximations based on the large mass difference between the two quarks in a $q\bar{q}'$ state such as $c\bar{u}$ ($m_Q \gg m_q$). In the limit $m_Q \rightarrow \infty$ the heavy quark spin can be considered as decoupled from the other quantum numbers and only the properties of the light quark determine those of the meson. The total angular momentum of the light quark is then $j_q = s_q + L$, where s_q is the light quark spin and L is the orbital angular momentum. If s_Q is the spin of the heavy quark, the total angular momentum of the meson, J , is a combination of j_q and s_Q which are separately conserved quantum numbers. Since s_q and s_Q can each be $\pm \frac{1}{2}$, for any nonzero L there are two doublets of states characterised by j_q , *e.g.* for P-wave ($L = 1$) mesons there are two $j_q = \frac{1}{2}$ states (with $J^P = 0^+, 1^+$) and two $j_q = \frac{3}{2}$ states (with $J^P = 1^+, 2^+$) [40]. In the heavy quark limit all states with the same orbital angular momentum have the same mass, but this degeneracy is broken by applying corrections ($1/m_Q$) due to the finite mass of the heavy quark. This leads to the predictions illustrated in Fig. 2.7; states with the same orbital angular momentum are expected to have similar masses, with the different L multiplets separated by larger mass differences.

The conservation of angular momentum and parity impose constraints on the strong decays of the D^{**} states. Only D^{**} states with natural spin parity may decay to two pseudoscalars in processes such as $D^{**0} \rightarrow D^+ \pi^-$ or $D^{**+} \rightarrow D^0 \pi^+$. In contrast, unnatural spin parity D^{**} states can decay to a vector and pseudoscalar, *e.g.* $D^{**0} \rightarrow D^{*+} \pi^-$.

HQET can also be used to predict the decay widths of the excited charmed states. Using the assumption of an infinitely heavy c -quark, the two $j_q = \frac{1}{2}$ 1P states should decay through an S-wave, while the two 1P states with $j_q = \frac{3}{2}$ are expected to decay exclusively through a D-wave, as shown in Fig. 2.8. The states which decay via S-wave are expected to be broad whilst the states decaying through a D-wave are expected to be narrow due to the larger angular momentum barrier which must be overcome. The true, finite, c -quark mass means that the two $J^P = 1^+$ 1P states can be a mixture of the $j_q = \frac{1}{2}$ and $\frac{3}{2}$ states, but the $j_q = \frac{1}{2}$ and $\frac{3}{2}$ states still favour S-wave and D-wave transitions, respectively, as shown by the measured widths of the four 1P D^{**} states in Tab. 2.5. The $D_0^*(2400)^0$ and $D_1'(2430)^0$ appear to be the $j_q = \frac{1}{2}$ states which decay quickly through an S-wave to produce broad resonances, whilst $D_2^*(2460)^0$ and $D_1(2420)^0$ states decay through a D-wave and are narrower.

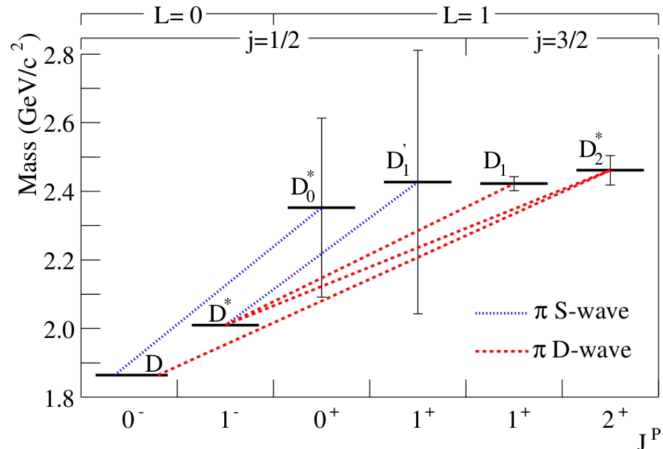


Figure 2.8: The mass spectrum of predicted 1P states of excited $c\bar{u}$ states with their expected pion transitions for strong decays to the ground state. The error bars show the predicted decay widths of the D_0^* and D_1' , which are expected to decay through an S-wave transition. Figure taken from Ref. [41].

2.3.3 Experimental status

In recent years significant progress has been made in measuring the properties of these excited charmed states. A summary of the experimental status of D^{**} states is given in Tab. 2.5. Results have come from both Dalitz plot analyses (see Sec. 2.4 for more detail) and prompt production studies. Measurements of the mass and width parameters of the $D_2^*(2460)^0$ state are summarised in Figs. 2.9 and 2.10, respectively. The two latest studies of this resonance were performed using LHCb data – the results from the

Table 2.5: Measured properties of neutral D^{**} states. Where more than one uncertainty is given, the first is statistical and the other(s) systematic.

Resonance	Mass (MeV/ c^2)	Width (MeV)	J^P	Ref.
$D_0^*(2400)^0$	2318 ± 29	267 ± 40	0^+	[3]
$D_1(2420)^0$	2421.4 ± 0.6	27.4 ± 2.5	1^+	[3]
$D'_1(2430)^0$	$2427 \pm 26 \pm 20 \pm 15$	$384^{+107}_{-75} \pm 24 \pm 70$	1^+	[42]
$D_2^*(2460)^0$	2462.6 ± 0.6	49.0 ± 1.3	2^+	[3]
$D^*(2600)$	$2608.7 \pm 2.4 \pm 2.5$	$93 \pm 6 \pm 13$	natural	[43]
$D^*(2650)$	$2649.2 \pm 3.5 \pm 3.5$	$140 \pm 17 \pm 19$	natural	[44]
$D^*(2760)$	$2763.3 \pm 2.3 \pm 2.3$	$60.9 \pm 5.1 \pm 3.6$	natural	[43]
$D^*(2760)$	$2760.1 \pm 1.1 \pm 3.7$	$74.4 \pm 3.4 \pm 19.1$	natural	[44]

$B^+ \rightarrow D^- K^+ \pi^+$ Dalitz plot analysis [1] (documented in Chap. 6) agree with the world average values, whilst the results obtained from inclusive studies [44] are seen to be in some tension with the PDG averages [45].

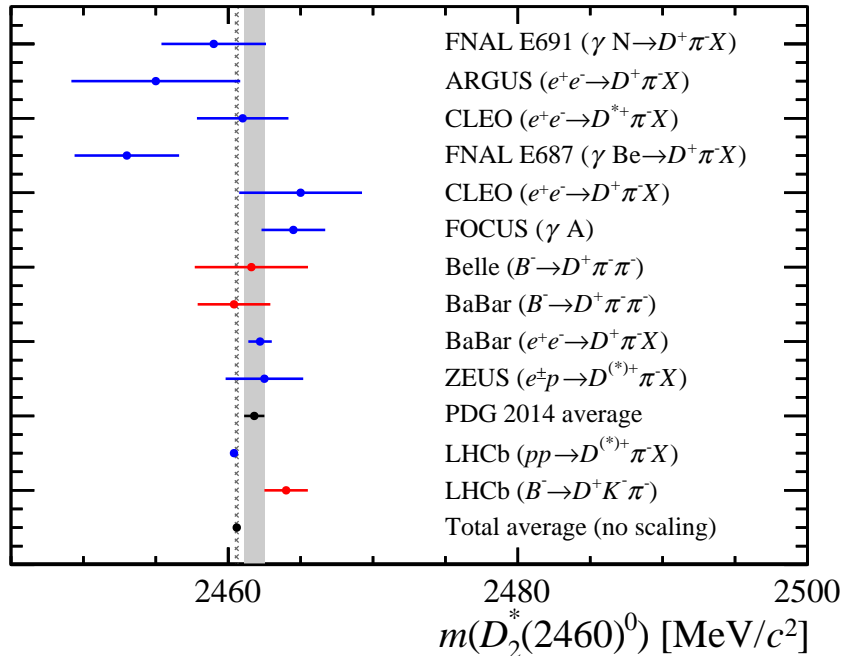


Figure 2.9: Compilation of results for $m(D_2^*(2460)^0)$ [45]. Measurements from inclusive (exclusive) studies are shown in blue (red). The uncertainty on the PDG average (light grey shaded area) is inflated due to a scale factor that accounts for disagreement between measurements. Including the latest results [1, 44] gives an average of $m(D_2^*(2460)^0) = 2460.59 \pm 0.13$ MeV/ c^2 , where no scale factor has been applied. The uncertainties on this average are shown by the hatched area.

Amplitude analysis techniques, such as Dalitz plot fits, use information from the kinematics of a decay mode and have the advantage of high purity data samples. These features make such analyses better suited to making precise measurements of resonances and understanding the nature of new states. This method considers interferences between the contributing amplitudes and allows the angular distributions to be studied;

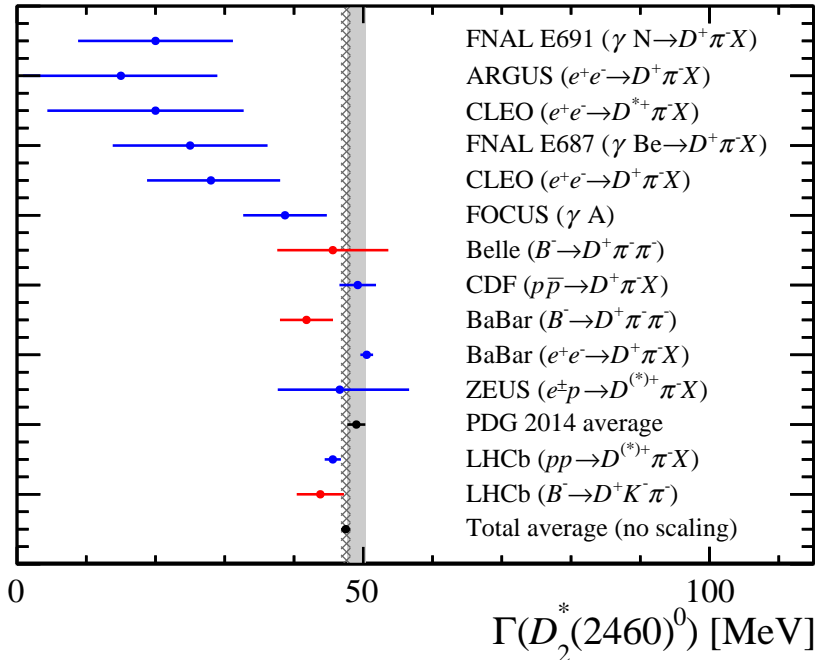


Figure 2.10: Compilation of results for $\Gamma(D_2^*(2460)^0)$ [45]. Measurements from inclusive (exclusive) studies are shown in blue (red). The uncertainty on the PDG average (light grey shaded area) is inflated due to a scale factor that accounts for disagreement between measurements. Including the latest results [1, 44] gives an average of $\Gamma(D_2^*(2460)) = 47.47 \pm 0.67$ MeV, where no scale factor has been applied. The uncertainties on this average are shown by the hatched area.

with enough statistics it is possible to determine the quantum numbers of individual states unambiguously. The results obtained from a Dalitz plot analysis depend on the amplitude model developed, which is only an approximation. Additionally, the scope of Dalitz plot analyses is limited by the allowed decay products of D^{**} states – the Dalitz plot corresponding to the decay of a pseudoscalar to three pseudoscalars can have contributions from only natural spin parity states. Unnatural spin parity states can be investigated separately via the amplitude analysis of three-body decays with a vector meson in the final state or with four-body decays, but the increased number of degrees of freedom make these methods more complicated. On the other hand, all final states of D^{**} mesons can be studied in inclusive production by reconstructing $D^{**} \rightarrow D^+ \pi^-, D^0 \pi^+, D^{*+} \pi^-$ final states in samples of $p p \rightarrow D^{(*)} \pi X$ decays at LHC experiments (or $e^+ e^- \rightarrow c \bar{c} \rightarrow D^{(*)} \pi X$ at the B factories), where X is any set of additional particles which do not have to be reconstructed. These inclusive studies are not sensitive to the quantum numbers of excited states but can be used to determine whether a state has natural or unnatural spin parity.

2.4 Dalitz plot analysis formalism

Dalitz plot [46] (DP) analysis is a powerful method to study the amplitudes of resonant and nonresonant contributions to multi-body particle decays and the interference between them. This thesis is concerned with the decays of charged B mesons to several three-body final states. The kinematics of such decays are described briefly below and an outline of the Dalitz plot analysis technique is given.

2.4.1 Kinematics of three-body decays

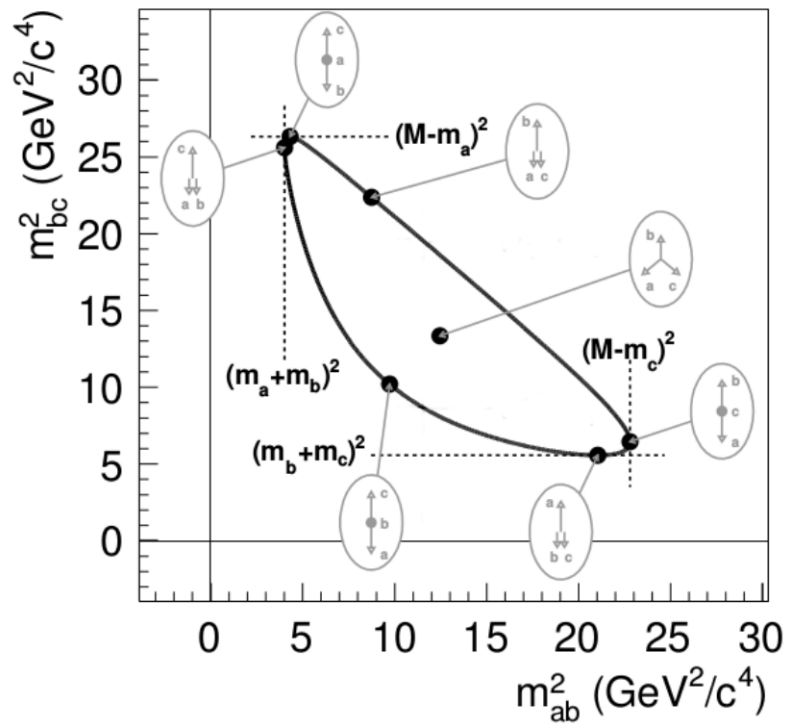


Figure 2.11: An illustrative Dalitz plot for the decay of a particle of mass M to three particles with masses m_a, m_b, m_c . The kinematically allowed region, restricted by the conservation of four-momentum, is the area within the dark line. Momentum vectors of the three daughters are drawn at various points in phase space, (in the rest frame of the decaying parent particle). Figure taken from Ref. [38], illustrating the decay $B^0 \rightarrow \pi^- \bar{D}^0 K^+$.

The kinematics of a pseudoscalar decaying to three spin-0 particles, *e.g.* $X \rightarrow abc$, can be uniquely defined with two variables. This fact can be exploited to create a two-dimensional scatter plot to represent the phase space. This scatter plot is known as a Dalitz plot. For a three-body decay any point in the phase space must satisfy

$$m_X^2 + m_a^2 + m_b^2 + m_c^2 = m_{ab}^2 + m_{ac}^2 + m_{bc}^2, \quad (2.29)$$

where $m_{X,a,b,c}$ are the masses of particles X, a, b, c ; $m_{ij}^2 = p_{ij}^2 = (p_i + p_j)^2$ is the square of the invariant mass of a pair of daughter particles i and j ; and p_i is the four-momentum of particle i . Any two of these three invariant mass squared combinations can be plotted against each other to construct a DP.⁸ An example is shown in Fig. 2.11, which shows the allowed ranges of the squared invariant mass variables, $(m_i + m_j)^2 \leq m_{ij}^2 \leq (m_X - m_k)^2$.

The partial decay rate of the $X \rightarrow abc$ decay is given by

$$d\Gamma = \frac{1}{(2\pi)^3} \frac{1}{32m_X^3} |\mathcal{A}|^2 dm_{ab}^2 dm_{bc}^2, \quad (2.30)$$

where \mathcal{A} is the Lorentz-invariant decay amplitude and $|\mathcal{A}|^2$ indicates the average decay amplitude of the decaying particle X . For constant $|\mathcal{A}|^2$, the kinematically allowed region of phase space will be uniformly populated in the DP coordinates m_{ab}^2 and m_{bc}^2 . Any variation from this uniformity suggests that the decay has some dynamical structure *e.g.* $X \rightarrow R c$ and $R \rightarrow ab$, where a short-lived intermediate resonance R is produced and decays quickly to daughters a and b via the strong interaction.

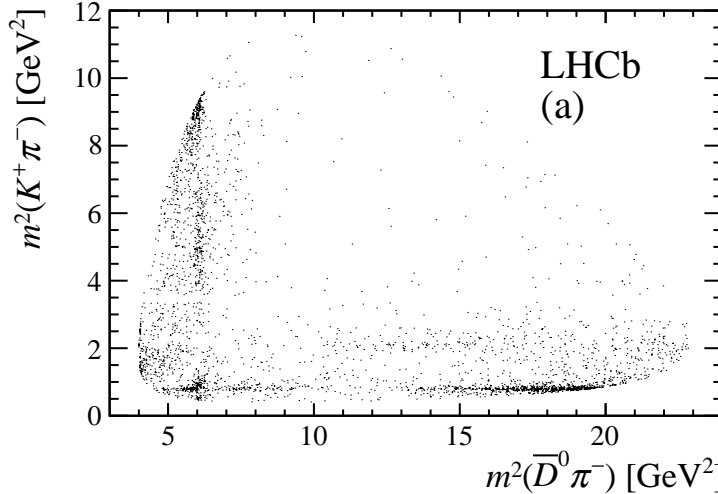


Figure 2.12: Dalitz plot of the $B^0 \rightarrow \bar{D}^0 K^+ \pi^-$ decay in LHCb data, showing resonant amplitudes decaying to $K^+ \pi^-$ (horizontal bands) and $\bar{D}^0 \pi^-$ (vertical bands). Figure taken from Ref. [47].

Structures within the DP can be studied to obtain information about the magnitudes and relative phases of amplitudes contributing to a decay. As shown in Fig. 2.12, resonant amplitudes appear as bands in the DP.⁹ In this example there are horizontal and vertical bands, corresponding to resonances decaying to $K^+ \pi^-$ and $\bar{D}^0 \pi^-$ respectively. Any

⁸In principle any two independent kinematic parameters can be chosen to describe the amplitude of a three-body decay, however, in order to allow clear visualisation of amplitude structures, it is convenient to choose variables for which the phase space term is constant within the kinematically allowed region. For this reason m_{ij}^2 vs m_{jk}^2 is the common choice of DP variables for relativistic decays. An alternative representation is introduced in Sec. 2.4.3.1.

⁹Note that Figs. 2.11 and 2.12 are two of the three different possible DP representations of the $B^0 \rightarrow \bar{D}^0 K^+ \pi^-$ decay.

resonance in the final pair of daughter particles would produce bands along the top-right diagonal, with higher mass resonances closer to the centre of the DP. Clearly the orientation of bands in a DP depends on the choice of invariant mass variables and their ordering on the axes.

The angular probability distribution of the resonance decay depends on the spin of the resonance, as described in Sec. 2.4.2.1, since angular momentum is always conserved. In strong decays, such as $R \rightarrow ab$, parity must be also be conserved, so the quantum numbers of a resonance can be determined by studying its angular distribution in the DP. Often one can learn about the spin of a contributing resonance simply from visual inspection of the DP; the number of ‘dips’ along the band gives the spin of the resonance that the band corresponds to. This spin-dependent structure arises because angular dependence is proportional to the Legendre polynomials, as described in Sec. 2.4.2.1. For example the prominent vertical band in Fig. 2.12 has three lobes (two dips), so must be due to a tensor resonance, whilst the strongest horizontal band has two lobes – the signature of a vector resonance.

The phase difference between two resonances decaying to different final states can also be visible from a DP if their amplitudes overlap in a region of phase space. Different contributions can be seen to interfere constructively or destructively depending on the relative phases of their amplitudes. The phase of each amplitude can be determined by fitting experimental data in a full DP analysis.

2.4.2 The isobar model

The isobar model [48, 49, 50] is commonly used to parametrise the complex amplitude of a decay. All contributing amplitudes, both resonant and nonresonant, are combined as a coherent sum

$$\mathcal{A}(m_{ab}^2, m_{bc}^2) = \sum_{j=1}^N c_j F_j(m_{ab}^2, m_{bc}^2), \quad (2.31)$$

where c_j are complex coefficients containing information about the relative magnitudes and phases of various components and the $F_j(m_{ab}^2, m_{bc}^2)$ terms are the dynamical amplitudes of each contribution. The $F_j(m_{ab}^2, m_{bc}^2)$ are each normalised such that, over the whole phase space, $\int \int_{DP} |F_j(m_{ab}^2, m_{bc}^2)|^2 dm_{ab}^2 dm_{bc}^2 = 1$. The amplitude of a resonance decaying to daughters a and b is given by

$$F(m_{ab}^2, m_{bc}^2) = R(m_{ab}) \times X(|\vec{p}| r_{BW}, L) \times X(|\vec{q}| r_{BW}, L) \times T(\vec{p}, \vec{q}, L), \quad (2.32)$$

where the functions R , X and T are the resonance mass lineshape (Sec. 2.4.2.3), the Blatt–Weisskopf barrier factor terms (Sec. 2.4.2.2) and the angular probability distribution (Sec. 2.4.2.1), respectively; r_{BW} is the radial parameter of the decaying particle; L is the orbital angular momentum between the resonance and the daughter produced

directly from the mother decay (the bachelor), for spin-0 daughters this is equivalent to the spin of the resonance; \vec{p} and \vec{q} are the momenta of the bachelor particle and one of the resonance daughters, both evaluated in the rest frame of the resonance.

2.4.2.1 Angular distribution

The angular probability distribution for the products from the decay of a spin- L resonance is described by the term $T(\vec{p}, \vec{q}, L)$ in Eq. 2.32. In the Zemach tensor formalism [51, 52], these are given by

$$\begin{aligned} L = 0 : T(\vec{p}, \vec{q}) &= 1, \\ L = 1 : T(\vec{p}, \vec{q}) &= -2\vec{p} \cdot \vec{q}, \\ L = 2 : T(\vec{p}, \vec{q}) &= \frac{4}{3} [3(\vec{p} \cdot \vec{q})^2 - (|\vec{p}| |\vec{q}|)^2], \\ L = 3 : T(\vec{p}, \vec{q}) &= -\frac{24}{15} [5(\vec{p} \cdot \vec{q})^3 - 3(\vec{p} \cdot \vec{q})(|\vec{p}| |\vec{q}|)^2], \end{aligned} \quad (2.33)$$

which are proportional to the Legendre polynomials, $P_L(\cos \theta)$, where θ is the helicity angle (the angle between \vec{p} and \vec{q}). The effect of the pq factors is to suppress the amplitude at low values of the break-up momentum in either the parent or resonance decay. The Blatt–Weisskopf barrier factors are required to correct for this behaviour above the angular momentum barrier.

2.4.2.2 Blatt–Weisskopf barrier factors

The maximum angular momentum L is limited by the linear momentum q in a two-body decay, due to the conservation of both angular momentum and energy. This means that low momentum decay products can have difficulty generating enough angular momentum to conserve the spin of the decaying resonance. Blatt–Weisskopf factors [53] are used to weight the amplitude to account for this spin-dependence of particle decays. The decay amplitude of a resonance has two such factors, as shown in Eq. 2.32, corresponding to the decays of the mother particle and the resonance itself. The form of $X(z)$, where $z = |\vec{q}| r_{\text{BW}}$ or $|\vec{p}| r_{\text{BW}}$,¹⁰ for a resonance with spin L , is

$$\begin{aligned} L = 0 : X(z) &= 1, \\ L = 1 : X(z) &= \sqrt{\frac{1+z_0^2}{1+z^2}}, \\ L = 2 : X(z) &= \sqrt{\frac{z_0^4+3z_0^2+9}{z^4+3z^2+9}}, \\ L = 3 : X(z) &= \sqrt{\frac{z_0^6+6z_0^4+45z_0^2+225}{z^6+6z^4+45z^2+225}}, \end{aligned} \quad (2.34)$$

where z_0 is the value of z when the invariant mass is equal to the ‘pole mass’, m_0 , of the resonance. In this notation X is normalised so that $X(z_0) = 1$.

¹⁰The barrier radii of all resonances are taken to be $r_{\text{BW}} = 4.0 \text{ GeV}^{-1} \approx 0.8 \text{ fm}$ [54, 55] in this thesis unless otherwise stated.

2.4.2.3 Resonance lineshapes

The dynamical function $R(m)$ of Eq. 2.32 is used to describe the mass lineshape. The most commonly used form is the relativistic Breit–Wigner (RBW) function

$$R(m) = \frac{1}{(m_0^2 - m^2) - i m_0 \Gamma(m)}, \quad (2.35)$$

where m is the invariant mass of the relevant two-daughter combination and the mass-dependent decay width is

$$\Gamma(m) = \Gamma_0 \left(\frac{q}{q_0} \right)^{2L+1} \left(\frac{m_0}{m} \right) X^2(q r_{\text{BW}}), \quad (2.36)$$

where q_0 is the value of $q = |\vec{q}|$ at $m = m_0$. The real and imaginary parts of the resonance amplitude, $R(m)$, are described by an anticlockwise circle in the Argand plane due to the phase motion of a resonance as a function of m .

Resonances whose pole mass lies outside the kinematically allowed phase space region can also contribute to a decay. For this kind of off-shell or ‘virtual’ contribution, m_0 in Eqs. 2.35 and 2.36 must be replaced with an ‘effective mass’ in the kinematically allowed region, calculated using the ad-hoc formula

$$m_0^{\text{eff}}(m_0) = m^{\text{min}} + (m^{\text{max}} - m^{\text{min}}) \left(1 + \tanh \left(\frac{m_0 - \frac{m^{\text{min}} + m^{\text{max}}}{2}}{m^{\text{max}} - m^{\text{min}}} \right) \right), \quad (2.37)$$

where m^{max} and m^{min} are the upper and lower limits of the kinematically allowed range, respectively. The q_0 value in Eq. 2.36 is then the value of q at $m = m_0^{\text{eff}}(m_0)$. This parametrisation ensures that only the tail of the RBW function enters the DP for virtual contributions. The result is an amplitude similar in form to a nonresonant contribution, with an angular distribution corresponding to the spin of the virtual state.

Nonresonant decays of the form $X \rightarrow abc$ may also contribute to the DP. In the past the nonresonant amplitude in D decays has often been modelled as a constant term with no variation in magnitude or phase across the DP. With the far larger available phase space for a B decay, it has become clear that nonresonant amplitudes can vary across the DP, so a more complicated parametrisation is required. Several parametrisations have been used experimentally, but a model that has been found to describe nonresonant contributions well for several B decay DP analyses is an exponential form factor (EFF) [56],

$$R(m) = e^{-\alpha m^2}, \quad (2.38)$$

where α is a shape parameter that can be determined from a fit to the data. This is an ad-hoc description, with no solid theoretical grounding. Blatt–Weisskopf barrier factors are not included in Eq. 2.32 for nonresonant amplitudes of this form.

2.4.3 Experimental details

2.4.3.1 The square Dalitz plot

It can be seen in Figs. 2.11 and 2.12 that the kinematic boundary is curved when drawn in regular DP coordinates. Another common representation uses square Dalitz plot (SDP) coordinates which maps the available phase space onto a unit square, as shown in Fig. 2.13 (right). This phase space depiction is easier to divide into bins and has the additional advantage of inflating the corners of the DP where interesting resonances usually lie.

The SDP coordinates of the decay $X \rightarrow abc$ are given by¹¹

$$\begin{aligned} m' &\equiv \frac{1}{\pi} \arccos \left(2 \frac{m_{ab} - m_{ab}^{\min}}{m_{ab}^{\max} - m_{ab}^{\min}} - 1 \right), \\ \theta' &\equiv \frac{1}{\pi} \theta_{ab}, \end{aligned} \quad (2.39)$$

where $m_{ab}^{\max} = m_X - m_c$ and $m_{ab}^{\min} = m_a + m_b$ are the kinematic limits of m_{ab} and θ_{ab} is the angle between the bachelor and one of the resonance daughters in the rest frame of the resonance. The new variables have validity ranges between 0 and 1. The SDP is described further in Ref. [57]

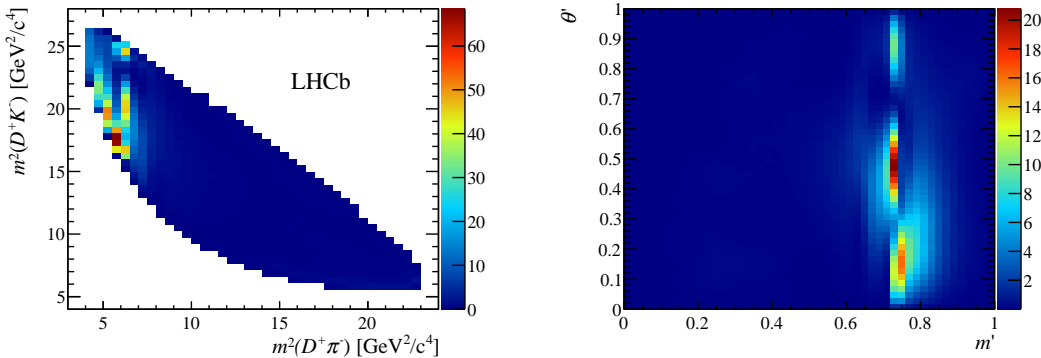


Figure 2.13: Conventional (left) and square (right) DPs obtained from simulated $B^+ \rightarrow D^- K^+ \pi^+$ decays. The generation model uses $D^*(2007)^0$, $D_0^*(2400)^0$, $D_2^*(2460)^0$ and B^* resonances and a spin-0 nonresonant term.

For a decay where the final state contains two identical bosons, *e.g.* $X \rightarrow aab$, the symmetry can be exploited to create a ‘folded’ DP. The two ab combinations are ordered by invariant mass to create a DP of the form shown in Fig. 2.14. This halves the number of integrals to be calculated for the DP fit, without any effect on physics since the amplitude must be symmetric under the interchange of two identical bosons. In addition, the folding effectively doubles the statistics of simulated events. The SDP coordinates

¹¹The choice of variables in Eq. 2.39 is not unique – there are six possible definitions due to the freedom to choose both the pair of daughters and the order in which they appear in the SDP definition.

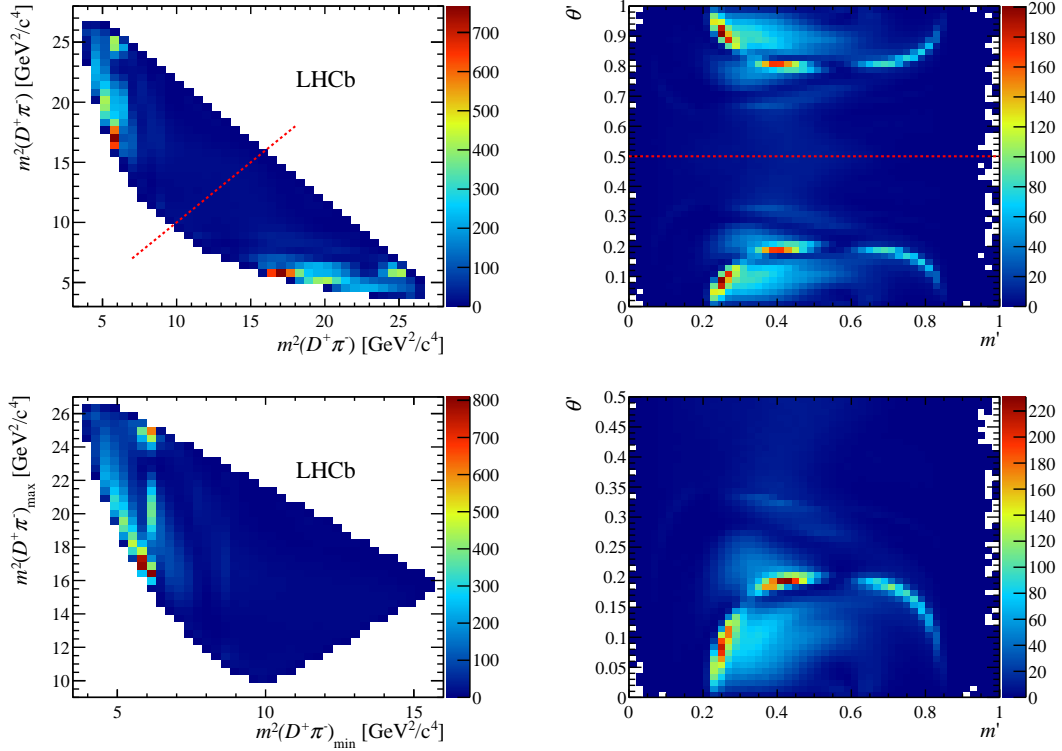


Figure 2.14: Conventional (left) and square (right) DPs obtained from simulated $B^+ \rightarrow D^-\pi^+\pi^+$ decays. The line of symmetry is drawn on these plots and the ‘folded’ versions are shown in the bottom row. The generation model uses $D^*(2007)^0$, $D_0^*(2400)^0$, $D_2^*(2460)^0$ and B^* resonances and a spin-0 nonresonant term.

are calculated using the expression in Eq. 2.39. For this folded SDP $0 \leq \theta' \leq 0.5$, but m' is still valid between 0 and 1.

2.4.3.2 Fitting

In the absence of any reconstruction effects, and neglecting the detector acceptance considerations, the DP probability density function for signal events is

$$\mathcal{P}_{\text{sig}}(m_{ab}^2, m_{bc}^2) \equiv \frac{|\mathcal{A}(m_{ab}^2, m_{bc}^2)|^2}{\iint_{\text{DP}} |\mathcal{A}(m_{ab}^2, m_{bc}^2)|^2 dm_{ab}^2 dm_{bc}^2}. \quad (2.40)$$

During the data collection process the theoretical amplitudes and distributions described in Sec. 2.4.2 can become distorted. In particular the efficiency of reconstructing events will not be constant over the phase space. The squared amplitude at any point in phase space is multiplied by the efficiency at that point so Eq. 2.40 becomes

$$\mathcal{P}_{\text{sig}}(m_{ab}^2, m_{bc}^2) = \frac{\epsilon(m_{ab}^2, m_{bc}^2) |\mathcal{A}(m_{ab}^2, m_{bc}^2)|^2}{\iint_{\text{DP}} \epsilon(m_{ab}^2, m_{bc}^2) |\mathcal{A}(m_{ab}^2, m_{bc}^2)|^2 dm_{ab}^2 dm_{bc}^2}, \quad (2.41)$$

where $\epsilon(m_{ab}^2, m_{bc}^2)$ parametrises the efficiency of reconstructing and selecting signal events as a function of DP position. This function can be obtained using simulated data and passed to the fitter as a histogram.

Although carefully chosen selection requirements can improve the purity of data samples significantly, background events will still remain. The likelihood function to be maximised in an unbinned fit to experimental data is then

$$\mathcal{L} = \prod_i^{N_c} \left[\sum_k N_k \mathcal{P}_k^i(m_{ab}^2, m_{bc}^2) \right], \quad (2.42)$$

where the index i runs over N_c candidate events; k distinguishes the signal and background components, with a yield of N_k for each component; and \mathcal{P}_k^i is the probability density function for each event category. For signal events \mathcal{P}_{sig} is given by Eq. 2.41, while the corresponding function for background categories, \mathcal{P}_{bkg} , can be determined from simulation.

The main results obtained from a DP fit are the coefficients, c_j , and (occasionally) parameters of the dynamical amplitudes, $F_j(m_{ab}^2, m_{bc}^2)$, such as the masses and widths of resonances. However, different parametrisations and choices of normalisation, phase convention and amplitude formalism mean that the c_j values are not always comparable between studies. Fit fractions provide a convention-independent way to compare results and can be used to calculate the branching fractions of contributing decay modes. The fit fraction of each amplitude is defined as

$$FF_j = \frac{\iint_{\text{DP}} |c_j F_j(m_{ab}^2, m_{bc}^2)|^2 dm_{ab}^2 dm_{bc}^2}{\iint_{\text{DP}} |\mathcal{A}(m_{ab}^2, m_{bc}^2)|^2 dm_{ab}^2 dm_{bc}^2}. \quad (2.43)$$

In the case of net constructive or destructive interference the sum of fit fractions will not be unity. Interference fit fractions can be defined for $i < j$ to quantify the net amount of interference between pairs of amplitudes in the DP:

$$FF_{ij} = \frac{\iint_{\text{DP}} 2 \mathcal{R}e \left[c_i c_j^* F_i(m_{ab}^2, m_{bc}^2) F_j(m_{ab}^2, m_{bc}^2)^* \right] dm_{ab}^2 dm_{bc}^2}{\iint_{\text{DP}} |\mathcal{A}(m_{ab}^2, m_{bc}^2)|^2 dm_{ab}^2 dm_{bc}^2}. \quad (2.44)$$

Chapter 3

The Large Hadron Collider and LHCb detector

The data presented in this thesis were collected at the Large Hadron Collider beauty (LHCb) [58] experiment at the Large Hadron Collider (LHC) [59]. This chapter gives a brief overview of the LHC and a description of the LHCb detector.

3.1 The Large Hadron Collider

The LHC is the world's largest and most energetic particle accelerator, located at the European Organisation for Nuclear Research (CERN) in Switzerland. The accelerator is designed to collide two beams of protons or lead ions¹² at a maximum centre-of-mass energy of 14 TeV. The LHC tunnel, originally constructed to contain the Large Electron Positron (LEP) collider, lies about 100 m underground and has a circumference of approximately 27 km.

To achieve the design collision energy, a series of particle accelerators are required to increase progressively the energy of the proton beams before they are injected into the LHC beam pipes. A schematic of the CERN accelerator complex is shown in Fig. 3.1. At the beginning of the process an electric field is used to ionise hydrogen atoms and create the protons which are then accelerated to 50 MeV in LINAC2. Next these protons are accelerated further by the Proton Synchrotron Booster, the Proton Synchrotron and the Super Proton Synchrotron, which take the beam to 1.4 GeV, 25 GeV and 450 GeV respectively. The particles are then injected into the two LHC beam pipes and begin circulating in opposite directions where they are accelerated towards the design energy of 7 TeV each. The LHC can be filled with protons several times a day. In normal running conditions each 'fill' can remain stable for over 8 hours.

¹²This thesis considers only data from proton-proton collisions.

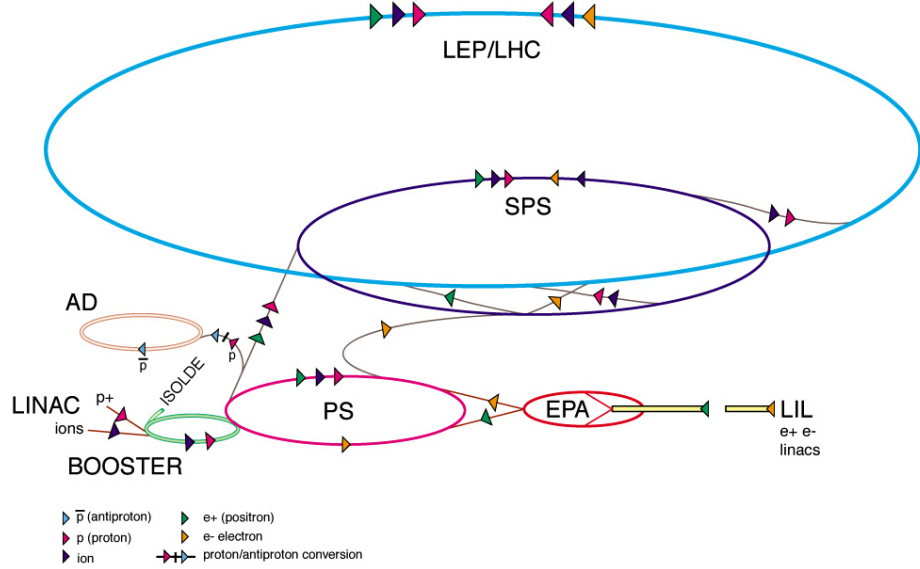


Figure 3.1: The accelerator complex at CERN. Figure taken from Ref. [60].

The LHC uses a combination of 1232 dipole magnets and 392 quadrupole magnets to accelerate and focus the proton beams. These superconducting magnets are made from niobium-titanium and cooled to 1.9 K using superfluid helium. The maximum magnetic flux density experienced by the beams is 8.33 T. The protons are grouped into bunches, of which there can be at most 2808 per beam. At the design luminosity of $10^{34} \text{ cm}^{-2}\text{s}^{-1}$ each bunch consists of 1.1×10^{11} protons. The collider is designed to produce a minimum bunch spacing of 25 ns though none of the data used in this thesis was taken at this collision rate.

There are 8 sections to the LHC, each with a straight segment, a bending arc and an interaction point. The two proton beams are directed such that particle collisions occur only at the interaction points of the four major experiments: ATLAS [61], CMS [62], ALICE [63] and LHCb. Of these large particle detectors only LHCb is specifically designed to study heavy flavour physics. ATLAS and CMS are both ‘general purpose’ detectors; they are primarily searching for physics beyond the SM in the on-shell production of new particles and discovered the Higgs boson in 2012 [4, 5]. ALICE specialises in studies of heavy ion collisions.

The LHC has been in operation since 2009, but for safety reasons the accelerator has not yet run with the design specifications. The data analysed in this thesis were collected in 2011 and 2012 with beam energies of 3.5 TeV and 4 TeV, respectively. Some smaller data samples were also taken in 2009, 2010 and 2015. Between February 2013 and April 2015 the LHC was shut down for planned upgrades. The data-taking period from 2010 to 2012 is known as ‘Run I’. ‘Run II’ began in 2015 with beam energies of 6.5 TeV. The period between these two runs, known as Long Shutdown 1 (LS1), was used for planned maintenance and minor upgrades.

3.2 LHCb detector

Each collision at the LHC is capable of creating a large number of beauty and charm hadrons and, in contrast to the e^+e^- collisions at BaBar [64] and Belle [65], the high centre-of-mass energy allows the production of all b -hadron species. The production cross sections for $b\bar{b}$ and $c\bar{c}$ pairs are both very high at the LHC; for a centre-of-mass energy of 7 TeV LHCb measured $\sigma(pp \rightarrow b\bar{b}X) = (284 \pm 20 \pm 49) \mu\text{b}$ [66] and the comparable number for charm production is about 20 times larger [67, 68]. In 2011 and 2012 LHCb recorded $\sim 10^{12}$ heavy flavour decays – the world’s largest sample of exclusively reconstructed charm and beauty baryon decays. Precision measurements of the production and decay of these heavy flavour particles offer an interesting way to search for physics beyond the SM. Many aspects of LHCb, from the design of individual sub-detectors to the detector geometry, were chosen specifically to exploit these data samples.

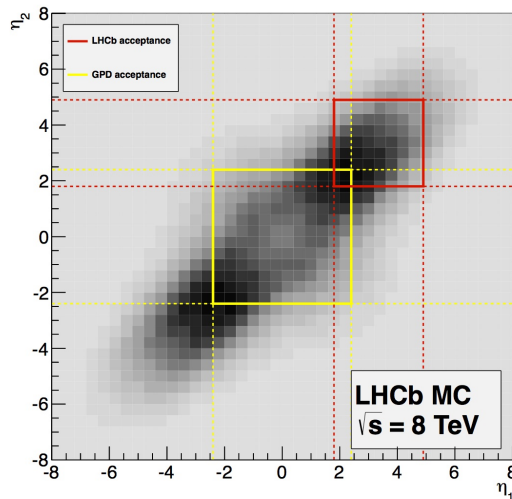


Figure 3.2: Pseudorapidity of $b\bar{b}$ quark pairs in proton-proton collisions at a centre-of-mass energy $\sqrt{s} = 8$ TeV generated using PYTHIA8 [69] (where $\eta_1(\eta_2)$ is the pseudorapidity of the $b(\bar{b})$ quark). Overlaid is a comparison of the acceptance of LHCb and the general purpose detectors. Figure taken from Ref. [70].

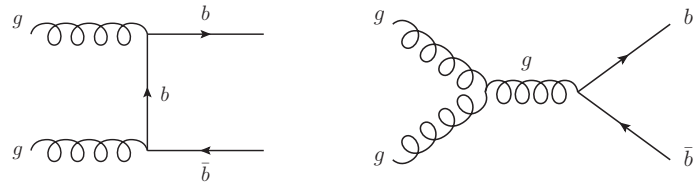


Figure 3.3: Examples of Feynman diagrams for $b\bar{b}$ production from gluon-gluon fusion.

Gluon-gluon fusion (as shown by the Feynman diagrams in Fig. 3.3) is the dominant $b\bar{b}$ production mechanism at the LHC. In collisions which create b -hadrons, the parton density functions for the high energy proton-proton interactions are such that the momenta

of the two colliding partons are very asymmetric in the detector frame. The created $b\bar{b}$ pair is therefore strongly boosted in the direction of the higher momentum parton and the resulting b -hadron and \bar{b} -hadron are produced in the same forward or backward cone. This event topology influenced the design of LHCb, which is a single-arm spectrometer with sufficient coverage to detect most of the pair-produced b -hadrons in the forward direction.¹³ The angular acceptance of the detector is 15 mrad to 300 mrad (250 mrad) in the vertical (horizontal) direction which corresponds to a pseudorapidity range of $1.6 < \eta < 4.9$. The pseudorapidity of a particle is defined as

$$\eta = -\ln \left(\tan \left(\frac{\theta}{2} \right) \right), \quad (3.1)$$

where θ is the angle between the particle's momentum and the beam axis. Figure 3.2 shows the distribution of $b\bar{b}$ pairs in pseudorapidity and illustrates the coverage of LHCb.

The boosted b -hadrons have high momentum in the forward direction, so they travel a measurable distance ($\mathcal{O}(10\text{ mm})$) in the LHCb detector before decaying. Due to the high multiplicity of tracks from the primary vertex (PV) near the interaction point, it is essential to correctly identify and reconstruct the displaced ‘secondary’ vertex (SV) in order to distinguish heavy flavour decays from backgrounds. Precise tracking systems provide excellent vertex resolution in LHCb which also allows decay-time to be measured accurately. Good particle identification (PID) systems are also necessary to distinguish particles, *e.g.* kaons and pions; many decays have kinematically similar event topologies but different final state particles, so some backgrounds can only be rejected using PID techniques. Finally the trigger and data acquisition systems must be efficient and versatile to cope with the high data rate and changing running conditions.

The location of objects within LHCb is described using a right handed Cartesian coordinate system. The z -axis is in the direction of the beam pipe from the VELO through the detector, the y -axis points vertically upwards and the x -axis is horizontal. The origin is taken as the nominal interaction point in LHCb. The $x - y$ plane is termed the ‘transverse’ plane, which is used to define quantities such as transverse energy, E_T , and transverse momentum, p_T . Some sub-detectors are instead described using cylindrical polar coordinates (r, ϕ, z) . The term ‘downstream’ is used to describe an object at a larger positive z -value, while an ‘upstream’ object has a smaller z -coordinate.

The LHCb detector is composed of several sub-detectors, each designed to perform specific tasks as part of the data-taking process. The layout of the detector is shown in Fig. 3.4. An overview of the sub-detectors is given in the remainder of this chapter.

¹³Over half of the b -hadrons are lost by not probing the central and backward regions as well as the forward region, but constraints of cost, space and time led to this solution.

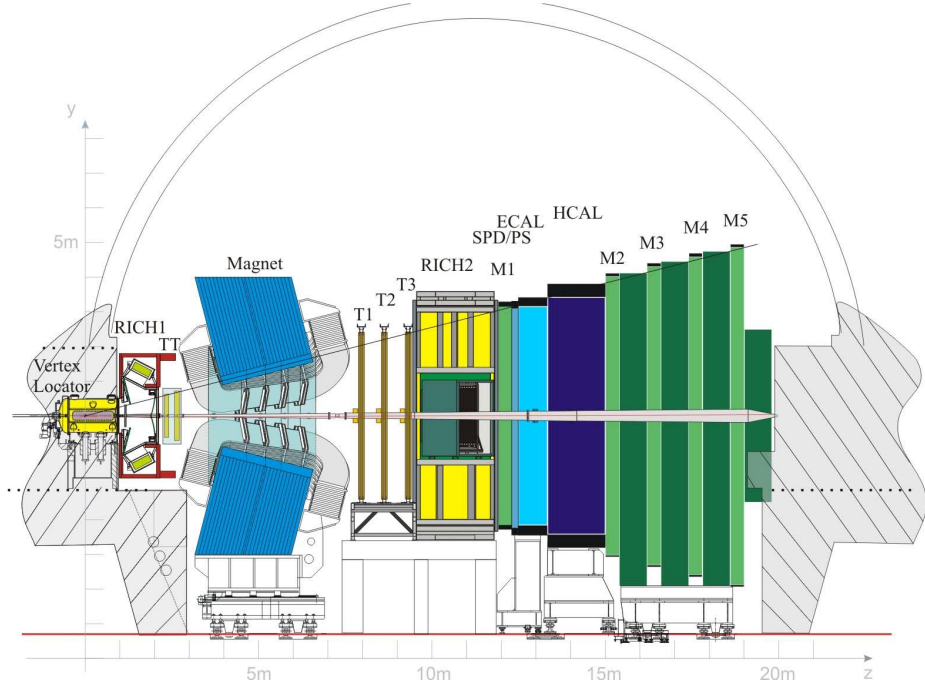


Figure 3.4: Cross-section of the LHCb detector with sub-detectors labelled. Figure taken from Ref. [71].

3.3 Tracking

Information from several sub-detectors is used for track reconstruction in LHCb: the VErtex LOcator, VELO; the Tracker Turicensis, TT; and the T1, T2 and T3 tracking stations. LHCb's dipole magnet also plays an important role in the tracking.

3.3.1 VELO

The VELO sub-detector [72, 73] is built in two halves around the beam line between $-0.2 < z < 0.8$ m. Each half contains 21 modules of silicon sensors aligned perpendicular to the beam. To reduce radiation damage the VELO halves are separated horizontally by about 6 cm during LHC beam injection. Once the beam is stable the VELO is closed to offer an angular acceptance of 15–300 mrad and an aperture of ~ 8 mm for the beam to pass through. When the VELO is fully closed the sensors in the two halves overlap slightly to ensure full coverage and to aid alignment of the modules. Figure 3.5 shows the layout of the sensor modules along the z -direction and the sensor positions when the VELO is open and closed. Modules are also placed upstream of the nominal interaction point to determine the PV position more accurately.

Each VELO module consists of a pair of microstrip silicon sensors, denoted the R- and ϕ -sensors, designed to measure the radial and azimuthal position of a track, respectively. Both types of sensor are approximately semi-circular, ~ 300 μ m thick and have a radius of 42 mm. The geometry of the strips differs between the two sensor types, as shown

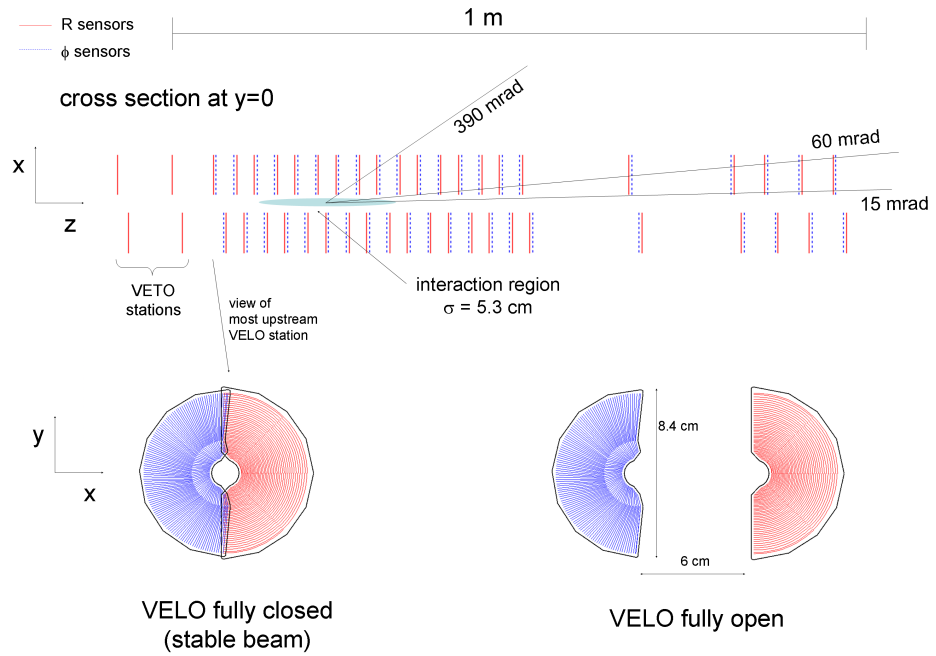


Figure 3.5: (top) Layout of the VELO modules along the beam line, shown in the $x - z$ plane. (bottom) View of sensors in the transverse plane showing the VELO sensors in both the open and closed positions. Figure taken from Ref. [58].

in Fig. 3.6. The R-sensors have strips arranged in concentric arcs around the beam line, with 512 in each 45° sector. The inter-strip distance, or strip pitch, increases from 38 μm near the beam to 102 μm at the edge of the sensor. On the ϕ -sensors there are 683 short strips near the centre with a pitch of 38–78 μm and covering the remaining area to the outside edge of the sensor are 1365 longer strips with a pitch of 39–97 μm .

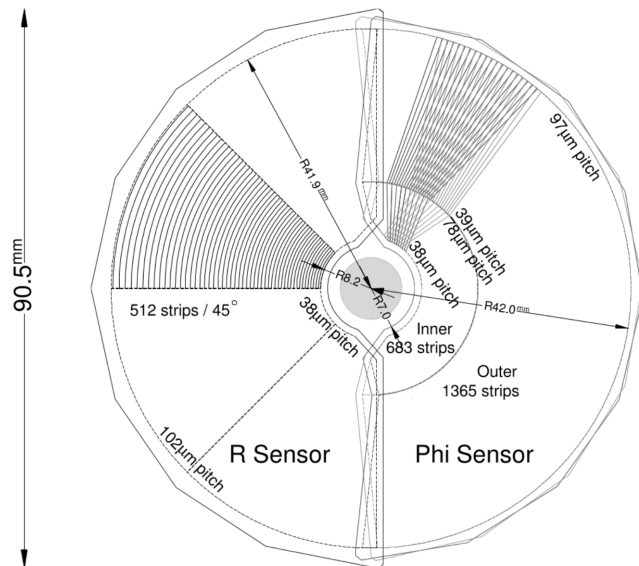


Figure 3.6: The strip geometry for R- and ϕ -sensors. Figure taken from Ref. [58].

The VELO has its own vacuum which is separated from the rest of the detector by a ~ 0.3 mm thick aluminium foil casing to prevent RF (radio frequency) pickup from the beam. The sub-detector is maintained at a temperature between -10°C and 0°C to improve performance and reduce the effects of radiation damage.

My studies of the material description of the VELO are documented in App. A.

3.3.2 Dipole magnet

A water-cooled dipole magnet [74] is used to deflect the trajectories of charged particles passing through LHCb. The magnet produces a field in the vertical direction; the amount of deflection experienced by a particle in the horizontal direction is used to calculate its momentum. The magnet covers the full detector acceptance between the TT and T1, as shown in Fig. 3.4, with dimensions of $11\text{ m} \times 8\text{ m} \times 5\text{ m}$ and a total mass of 1600 tons.

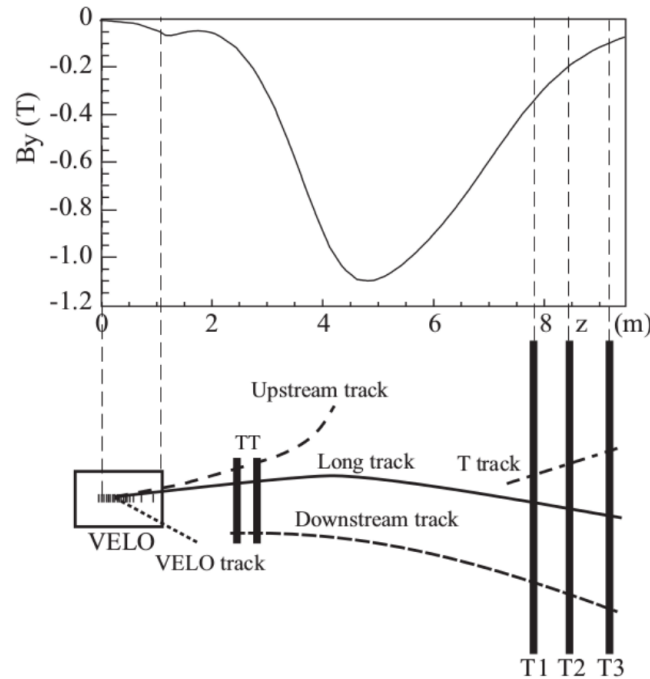


Figure 3.7: (top) Vertical component of the dipole magnetic flux density, B_y , in the z -direction. (bottom) A schematic of the five reconstructable tracks types at LHCb. Figure taken from Ref. [75].

The magnetic flux density provided by the LHCb magnet as a function of z -position is shown in Fig. 3.7. The field is at its maximum of 3.62 Tm in the region between the TT and T1. Upstream of the TT the integrated magnetic field is 0.12 Tm . The VELO sub-detector has magnetic shielding to ensure the field is reduced enough that tracks are not bent in this region. Shielding is also used around photodetectors in the RICH to prevent the deflection of photoelectrons.

3.3.3 Tracking stations

The measurement of particle momentum is based on information from four planar tracking stations in the $x - y$ plane: the TT is located between the first RICH detector, RICH1, and the dipole magnet. T1-T3 are downstream of the magnet and made up of the Inner Tracker (IT) [76] and Outer Tracker (OT) [77, 78]. The TT and IT use similar technology, so these detectors are together referred to as the Silicon Tracker (ST).

3.3.3.1 Silicon Tracker

Both the TT and IT are formed from silicon microstrip sensors with an average strip pitch of 200 μm . There are 143 360 read out strips in the TT, offering a total active area of approximately 8.4 m^2 . The IT has 129 024 strips and an active area of 4.0 m^2 . Both detectors are maintained at a temperature below 5° C .

The TT consists of 4 sensor layers positioned in 2 pairs approximately 30 cm apart along the beam line. Each layer is 150 cm wide and 130 cm high so the TT covers the full detector acceptance. The second and third layers are rotated with respect to the other two to give better resolution of the transverse position. The relative orientation of the layers, $(0^\circ, -5^\circ, +5^\circ, 0^\circ)$, is shown in Fig. 3.8.

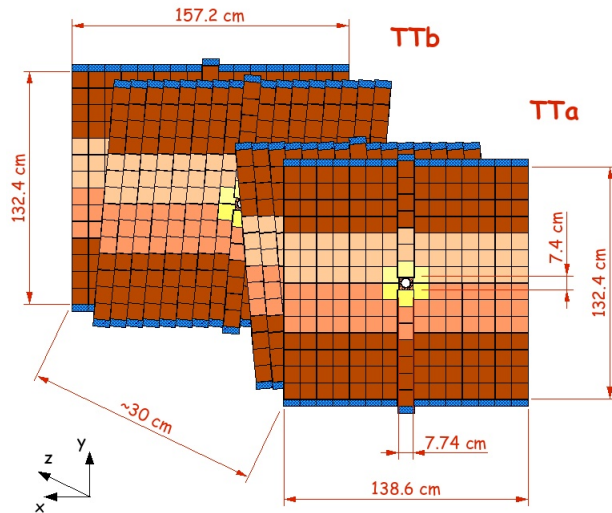


Figure 3.8: The four layers of silicon strip sensors in the TT. Different regions of read out strips are indicated by different shades of orange and yellow. The read out hybrids are shown in blue. Figure taken from Ref. [79].

The three tracking stations each have four IT modules arranged in a cross shape around the beam pipe to cover an area 120 cm wide and 40 cm high, as shown in Fig. 3.9 (left). Each module is made up of four silicon sensor layers in the same $(0^\circ, -5^\circ, +5^\circ, 0^\circ)$ orientation as the TT layers.

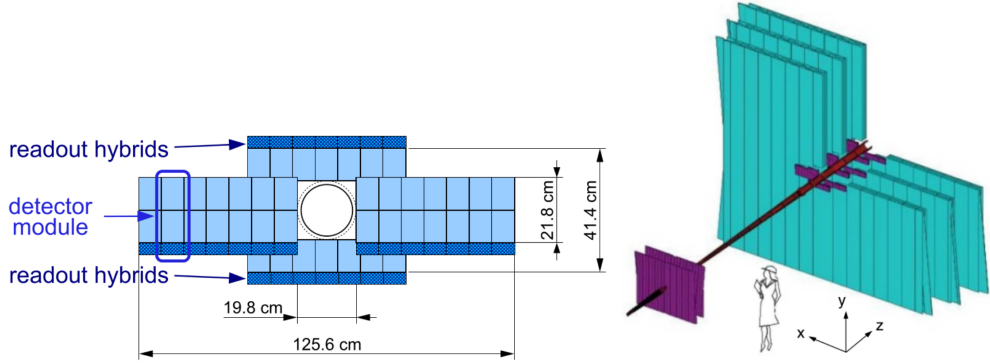


Figure 3.9: (left) Layout of silicon sensors in the IT. (right) Schematic of the full tracking system, excluding the VELO and magnet. The ST is shown in purple with the TT on the left and the IT around the beam pipe in T1-T3. The OT is shown in pale blue. Figures both taken from Ref. [58].

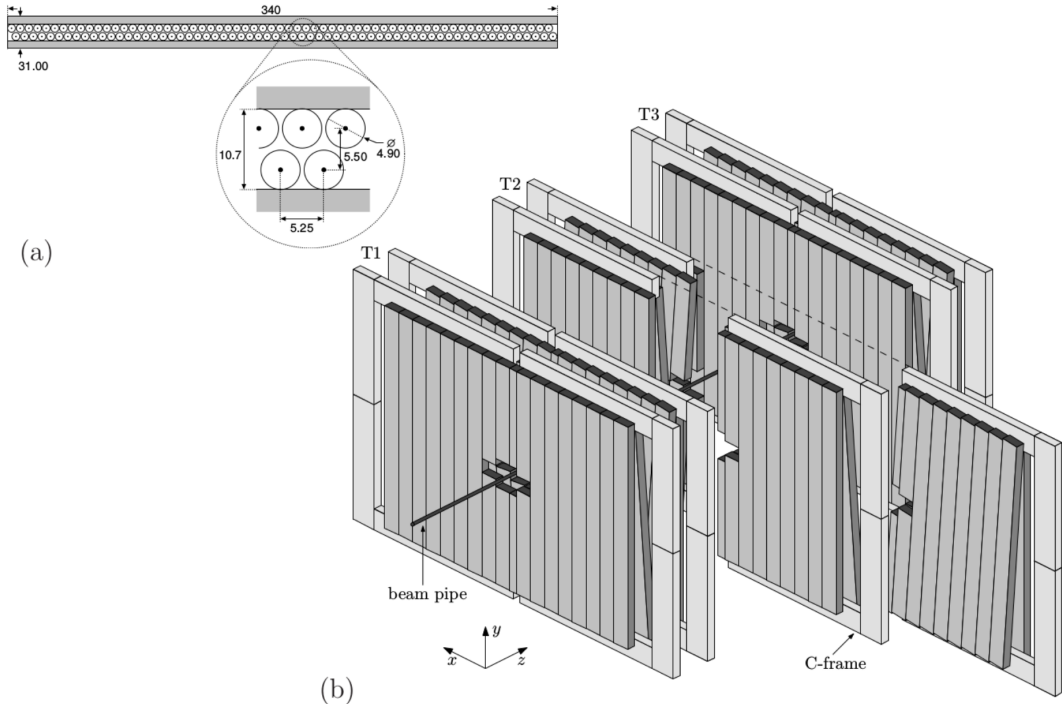


Figure 3.10: (a) Cross-section of an OT module. (b) Arrangement of the straw tube layers within the T1-T3 tracking stations. Figures taken from Ref. [78].

The IT only covers $\sim 2\%$ of the active area of each tracking station but, due to the Lorentz boost of the produced b -hadrons, $\sim 20\%$ of all charged particles originating from near the interaction point will pass through the silicon region of the T1-T3 stations. The high particle flux in this region close to the beam line necessitates the use of silicon detectors to withstand the higher radiation levels. This design also reduces detector occupancy close to the beam pipe so track positions can be reconstructed more accurately.

3.3.3.2 Outer Tracker

The overall layout of the tracking system is illustrated in Fig. 3.9 (right). Figure 3.10 (b) shows how the OT surrounds the IT in the T1-T3 tracking stations. An active area of $\sim 29 \text{ m}^2$ ensures that the full detector acceptance is covered.

T1-T3 each have four OT modules arranged in the same (0° , -5° , $+5^\circ$, 0°) rotated manner as the other tracking stations. Each OT module contains two staggered layers of 64 ‘straw’ drift tubes, as shown in Fig. 3.10 (a). The gas-tight tubes have an inner diameter of 4.9 mm and contain a mixture of argon and CO_2 in the ratio 7:3. The tube diameter and drift gas were both chosen to ensure a minimum drift time across the tubes of less than 50 ns.

3.4 Particle Identification

Accurate particle identification is vital for differentiating signal and background events which differ only by the species of particles in the final state. Two Ring-Imaging Cherenkov (RICH) detectors (described in Sec. 3.4.1) can distinguish the species of charged particles, in particular hadrons which cannot easily be identified by the calorimeters. The calorimeter system (Sec. 3.4.2) and muon chambers (Sec. 3.4.3) are used to identify electrons, photons and muons.

The likelihood of a particle being a particular species can be determined using information from all these sub-detectors. For example, the likelihood for a charged particle to be a kaon is given by $\mathcal{L}_K = \mathcal{L}_K^{\text{RICH}} \times \mathcal{L}_{\text{hadron}}^{\text{CALO}} \times \mathcal{L}_{\text{non } \mu}^{\text{MUON}}$. The difference between the logarithm of two such likelihood values can be computed to form a PID requirement for LHCb analysts. Kaons and pions could then be separated by placing a requirement on the value of $\Delta \log \mathcal{L}(K - \pi) \equiv \log \mathcal{L}_K - \log \mathcal{L}_\pi$.

The analyses presented in this thesis use ‘ProbNN’ variables as PID requirements. These variables take a value between 0 and 1 representing a Bayesian probability for a particular particle hypothesis. A dedicated neural network is used for each particle hypothesis – K , π , p , e^- , μ^- – combining information from the tracking stations and the sub-detectors involved in PID, in particular the RICH detectors. The likelihood ratio variables are important inputs to these neural networks.

3.4.1 RICH detectors

LHCb uses two RICH detectors [80, 81] to give information about the probable species of charged particles over a large momentum range. RICH1 offers PID for low momentum particles in the range 2–40 GeV/ c . This sub-detector is located between the VELO and

TT and covers the full angular acceptance of 25–300 mrad. RICH2 offers PID information for particles in the high momentum region 15–100 GeV/ c ; such high momentum tracks are more likely to be in the forward region so a smaller angular range of 15–120 mrad is covered. This sub-detector sits after the tracking stations. Both detectors are used to measure Cherenkov radiation which is emitted by particles passing through a medium with a velocity greater than the local speed of light. A cone of light is produced in the forward direction with an angle θ_C , which depends on the particle velocity, v , and the refractive index of the medium, n ,

$$\cos \theta_C = \frac{c}{nv}. \quad (3.2)$$

Thus the RICH detectors can calculate the velocity of a particle by measuring θ_C , and this combined with momentum information from the tracking system can be used to determine the particle's mass.

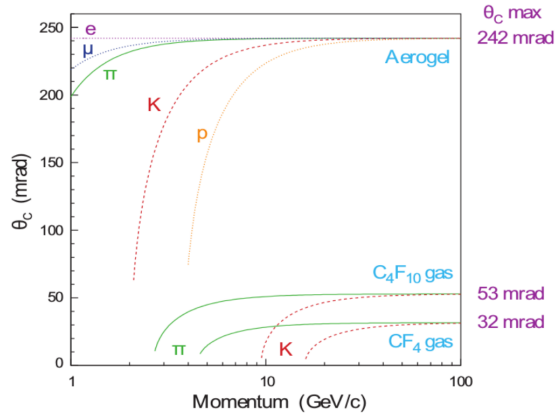


Figure 3.11: Cherenkov angle as a function of track momentum for the three radiators used in the RICH detectors. Figure taken from Ref. [58].

Cherenkov photons are collected and focussed onto planes of hybrid photodetectors (HPDs) outside the LHCb acceptance using a combination of spherical and flat mirrors. The sensitivity to particles of different momenta is made possible by using radiators with different refractive indices. For a particle with $\beta < 1/n$ no Cherenkov light will be emitted, but if the velocity is too high the discrimination power is lost as $\cos \theta_C \rightarrow 1/n$. RICH1 was constructed with both aerogel¹⁴ and C₄F₁₀ radiators, which have refractive indices of 1.03 and 1.0014 respectively for 400 nm light. RICH2 has a CF₄ radiator with $n = 1.0005$. Figure 3.11 shows the Cherenkov angle for particles of different momentum traversing the three radiators.

¹⁴The aerogel radiator in RICH1 was found to be ineffective during Run I data-taking so was removed for Run II.

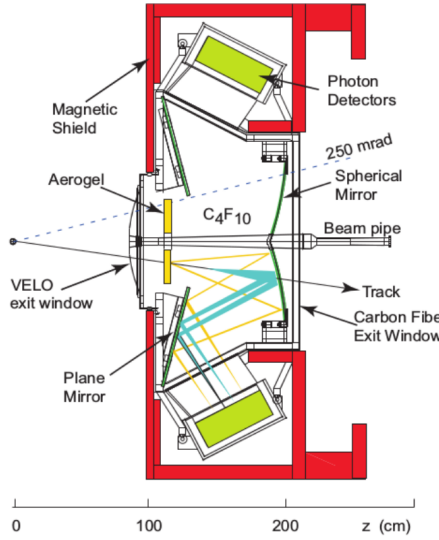


Figure 3.12: Cross-section of the RICH1 detector in the $y-z$ plane. Figure taken from Ref. [58].

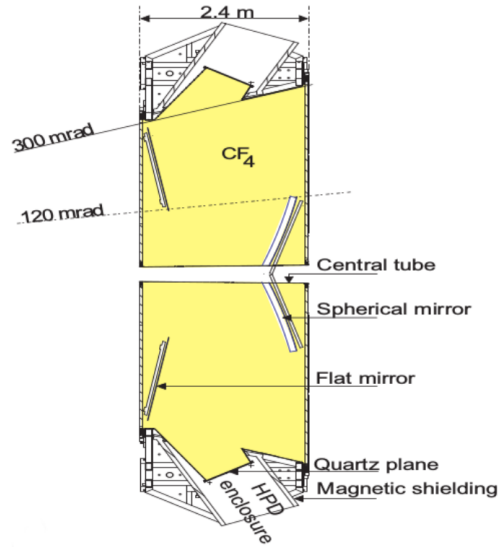


Figure 3.13: Cross-section of the RICH2 detector in the $x-z$ plane. Figure taken from Ref. [58].

3.4.1.1 RICH1

A cross-section of the RICH1 detector is shown in Fig. 3.12. A sealed aluminium box contains the C_4F_{10} gas, aerogel tiles and the mirror assembly. Iron shielding is used to protect the HPDs from the dipole's magnetic field and reduce the deflection of photo-electrons.

The detector contains 3.5 m^3 of C_4F_{10} gas, and the silica aerogel is included as a 50 mm thick wall on the upstream side of the aluminium box. The low refractive index of aerogel allows positive identification of lower momentum particles and provides improved discrimination between kaons and protons.

There are four spherical mirrors arranged symmetrically around the beam pipe. These mirrors are within the LHCb acceptance so are constructed from lightweight carbon-fibre. All other components of the optical system, including the two planes of flat mirrors, are located above and below the beam pipe, outside the particle acceptance. The total RICH1 material budget within the spectrometer acceptance is just 0.08 radiation lengths (X_0).

3.4.1.2 RICH2

RICH2 uses a 95 m^3 volume of CF_4 gas for its radiator. This is contained within a sealed box with the mirror array, as shown in Fig. 3.13. The detector is located downstream of T3 to reduce the amount of material before the tracking stations. High momentum

tracks are less affected by the larger magnetic field in this region of the detector but the HPDs must still be shielded to protect their photoelectron efficiency.

RICH2 has 52 spherical primary mirrors which focus Cherenkov light onto two planes of flat mirrors to the left and right of the beam pipe. As for RICH1, the planar mirrors and HPDs are outside the LHCb acceptance which leaves a RICH2 material budget of $\sim 0.15 X_0$ within the acceptance.

3.4.1.3 HPDs

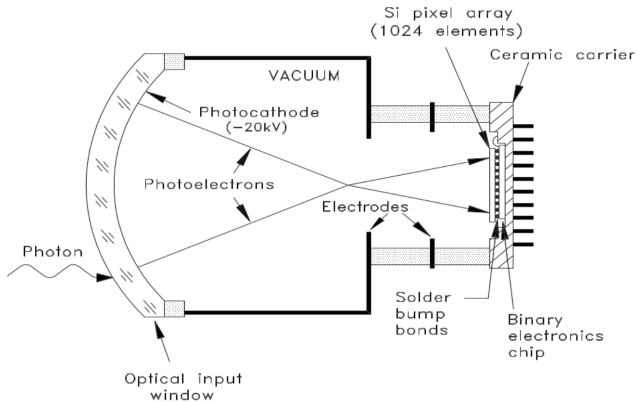


Figure 3.14: Diagram of an HPD used to detect Cherenkov photons produced in the radiators of both RICH1 and RICH2. Figure taken from Ref. [58].

The HPDs used to detect Cherenkov photons in both the RICH1 and RICH2 detectors are vacuum tubes with an active diameter of 75 mm. A diagram of an HPD is shown in Fig. 3.14. Incident photons pass through a 7 mm thick quartz window which sits across the front of each HPD. Photoelectrons are produced as the incident photons hit a multialkali photocathode inside the HPD. An accelerating voltage of -16 kV is used to accelerate the photoelectrons towards a silicon pixel array at the back of each HPD.

Individual HPDs are hexagonally close-packed and arranged in planes. Each detector has two planes of HPDs, giving a total of 484 HPDs in the two RICH detectors.

3.4.2 Calorimeters

The LHCb calorimeter system [82, 83] has four elements: A Scintillator Pad Detector (SPD), PreShower detector (PS), Electromagnetic calorimeter (ECAL) and Hadronic calorimeter (HCAL). These sub-detectors are shown in Fig. 3.4, located between the first and second muon stations. The four detectors together measure the energy and position of electrons, hadrons and photons. Information from the calorimeter system is also used for PID and is an important input for the first level of the trigger (discussed

in Sec. 3.5) where the decision to keep or throw away an event must be made just 4 μs after a proton-proton interaction.

Calorimeters use absorber material with a large radiation length to stop particles in the detector. Particles colliding with the calorimeter material lose energy and create a cascade shower of particles which can be detected to estimate the energy of the original particle. The particle shower shape is indicative of the species of incident particle – hadrons interacting by the strong force create a wider shower than electrons or photons interacting via the EM interaction. Figure 3.15 illustrates the location and structure of showers within the calorimeter system.

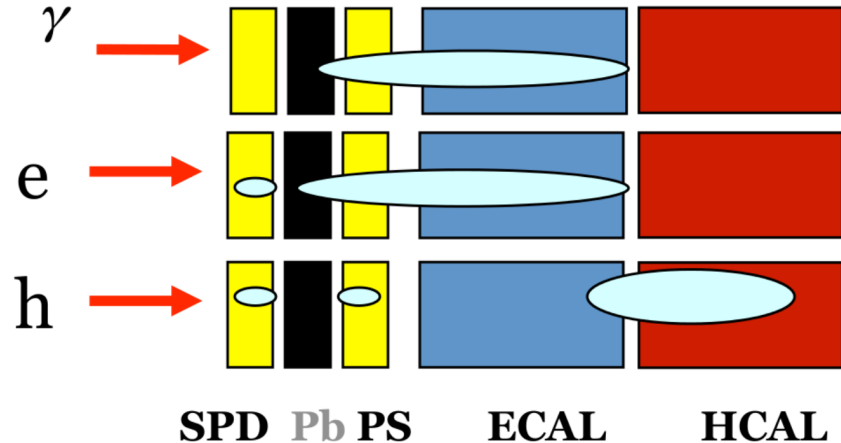


Figure 3.15: Schematic to show the location and structure of showers within the LHCb calorimeter for photons, electrons and charged hadrons. Figure taken from Ref. [84].

3.4.2.1 SPD, PS and ECAL

Accurate electron identification is an important input to the LHCb trigger, so good longitudinal separation of EM showers is required in order to reject the copious backgrounds from charged and neutral pions and high energy photons. The SPD and PS detectors are placed before the ECAL to identify such backgrounds.

The SPD and PS are two scintillator pad detectors sitting either side of a 15 mm thick lead converter which corresponds to 2.5 radiation lengths for electrons. Each of the two planes has a total active area of about $7.6 \text{ m} \times 6.2 \text{ m}$; the dimensions of the SPD are about 0.45 % smaller than those of the PS to maintain the same angular acceptance. Scintillation light from the SPD and PS detectors is transferred to multianode photomultiplier tubes (PMTs) using wavelength-shifting (WLS) fibres.

The SPD determines the electric charge of a particle before it showers, allowing electrons to be differentiated from γ and $\pi^0 \rightarrow \gamma\gamma$ backgrounds. The PS detector is used to distinguish electrons from charged hadrons as the former are more likely to shower in the lead absorber.

The four parts of the calorimeter system all have a finer granularity near the beam line where particle flux is higher, since the hit density varies by two orders of magnitude over the surface of the calorimeter. The layout of the scintillator pads in the PS and SPD follows the same structure as the ECAL which is pictured in Fig. 3.16 (left).

The ECAL is a sampling calorimeter with 66 alternating layers of lead absorber and polystyrene scintillator with a thickness of 2 mm and 4 mm, respectively. The layers are arranged perpendicular to the beam line with the total thickness of 42 cm which corresponds to $25 X_0$. This depth ensures showers from high energy electrons and photons are fully contained within the calorimeter. The granularity of the ECAL is somewhat coarser than that of the SPD and PS; WLS fibres, which carry the scintillation light, are bunched together and passed to individual PMTs.

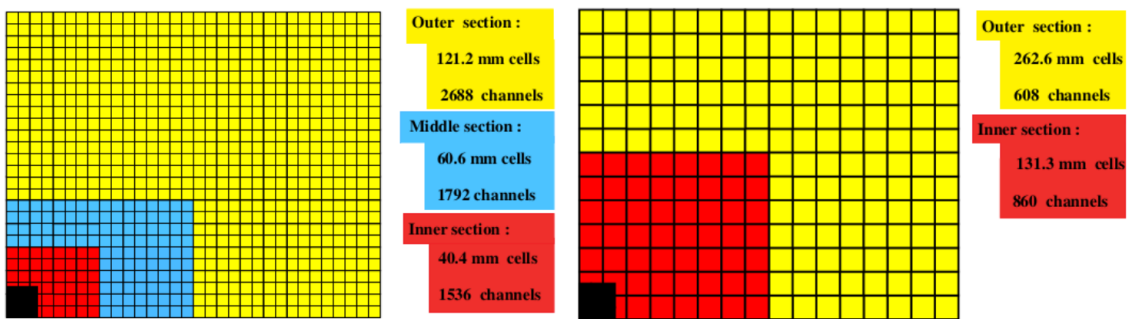


Figure 3.16: The segmentation of the calorimeter system elements shown for just one quadrant of the sub-detector with the beam pipe hole in black. (left) SPD, PS and ECAL and (right) HCAL. Figure taken from Ref. [58].

3.4.2.2 HCAL

The HCAL is also a sampling calorimeter, using iron and scintillating tiles as the absorber and active material, respectively. Due to space constraints in the LHCb cavern the depth of the HCAL is limited to about 1.6 m, which corresponds to 5.6 nuclear interaction lengths. As in the ECAL, WLS fibres are bunched together to pass the scintillator light to PMTs for read out. The read out cells are larger than in the ECAL, SPD and PS due to the differences in dimension and structure of hadronic and EM showers. Again the granularity is finer close to the beam pipe, where the particle flux is higher, as shown in Fig. 3.16 (right). The wider transverse spread of hadronic showers also influences the HCAL structure, shown in Fig. 3.17. Unlike in the ECAL, the HCAL scintillating tiles are oriented in the $x - y$ plane and therefore lie parallel to the beam axis.

3.4.3 Muon chambers

The correct identification of muons at LHCb is vital, especially since the final states of many CP -sensitive decays contain muons. The LHCb muon system [85, 86] has five

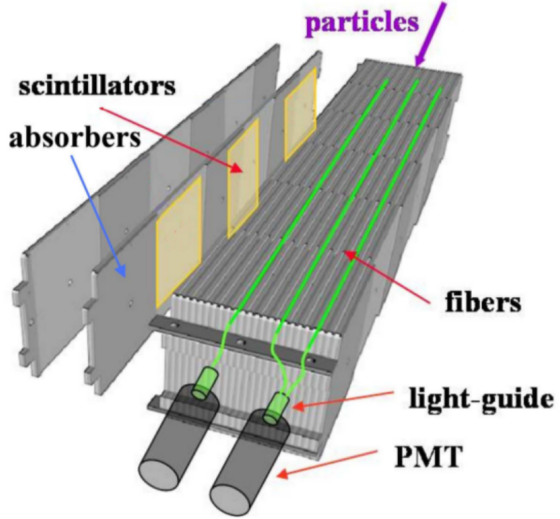


Figure 3.17: Exploded view of an HCAL module showing the orientation of scintillators and absorbers parallel to the beam axis. Figure taken from Ref. [58].

stations, named M1-M5, which are orientated perpendicular to the beam line between 12 and 18 m from the interaction point. Information from the muon stations is used to inform the trigger decision for events (described in Sec. 3.5) as well as identifying muon candidates.

The five muon stations all have an acceptance of 20–306 mrad in the horizontal direction and 16–258 mrad in the vertical direction. The $x - y$ dimensions of the stations scale with their distance along the beam line to achieve the same acceptance for all stations. The total active area of the stations is 435 m^2 .

Figure 3.18 shows the layout of the five stations. Their position within the LHCb detector is shown in Fig. 3.4. The first station, M1, is located upstream of the calorimeter system to give a better p_T estimate for the muon candidates before they pass through the more dense calorimeter material. The remaining four layers are all downstream of the calorimeters and are each separated by 80 cm thick iron blocks to absorb any hadronic backgrounds surviving past the HCAL. Only muons with momentum greater than $6 \text{ GeV}/c$ will penetrate all layers; including the calorimeters this corresponds to a distance of 20 interaction lengths. Stations M1-M3 offer a good p_T resolution of $\sim 20\%$ in the horizontal plane whilst the final two stations, M4 and M5, merely confirm that the candidate has penetrated all of the iron absorbers. A muon candidate must have hits in all five layers of the detector.

Each muon station is divided into chambers which contain rectangular ‘logical pads’ of different dimensions. The pad dimensions scale in the ratio 1:2:4:8 with distance from the beam pipe to give comparable particle flux across each pad. Smaller logical pads are placed closer to the beam line to offer greater transverse momentum resolution in this area. The layout of chambers and logical pads in M1 is shown in Fig. 3.19.

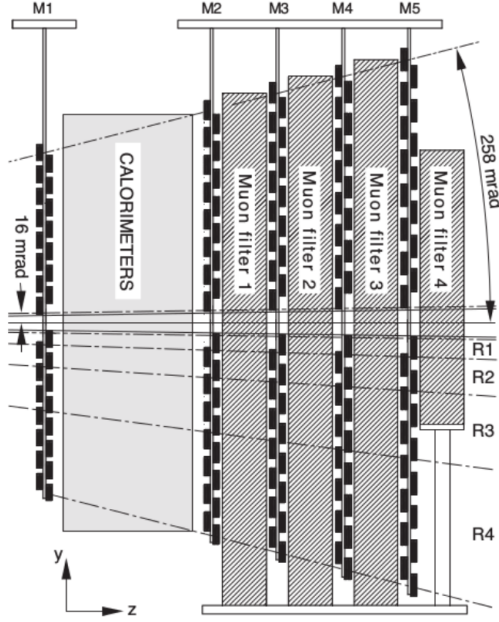


Figure 3.18: View of the LHCb muon detector. Figure taken from Ref. [87].

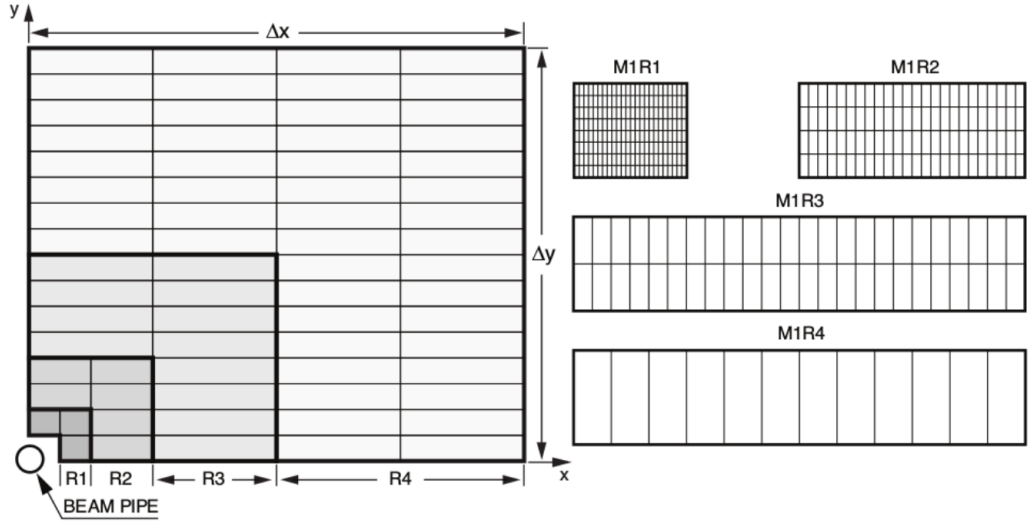


Figure 3.19: (left) One quarter of the M1 station divided into regions R1-R4, each of which is shown in different shades of grey. Individual chambers are depicted as rectangles. (right) The division of each chamber into logical pads in M1. The number of pad rows per chamber is the same for all muon stations. In stations M2 and M3 the number of pad columns per chamber doubles, while in M4 and M5 it halves with respect to M1. Figure taken from Ref. [58].

Multi-wire Proportional Chambers (MWPCs) are utilised for more than 99 % of the area of the muon stations; the only exception is a 3 m^2 area in the centre of M1 (R1), where the high particle flux necessitates the use of triple Gas Electron Multipliers (GEMs) which have a higher radiation tolerance.

The twelve chambers in the R1 region of M1 each have two triple-GEM detectors from which a logical OR result is returned. These chambers contain a ‘fast gas’ mixture of

argon, CO₂ and CF₄ in the ratio 45:15:40 to give fast time resolution.

The MWPCs have vertical anode wires in 5 mm gas gaps between cathode plates. The wires are 20–30 cm long with a spacing of 2 mm in the *x*-direction. The gas gaps are filled with a mixture of argon, CO₂ and CF₄ in the ratio 40:55:5. Stations M2–M5 have four gas gaps in the *z*-direction whilst M1 has only two to reduce the amount of material before the calorimeter. A logical OR is taken from the results of adjacent gap pairs. The MWPCs offer a time resolution of 5 ns – far less than the 25 ns design bunch spacing.

3.5 Trigger and stripping

The LHCb trigger [88, 89] is designed to reduce the event rate from the bunch crossing frequency, of up to 40 MHz, to a rate of ~ 3 kHz for storage and analysis. The majority of events recorded by the detector are not interesting for flavour physics measurements; typical branching fractions of *b*-hadron decays are $\mathcal{O}(10^{-3})$ or less, and only a small fraction of LHC collisions actually produce $b\bar{b}$ pairs. The trigger has three stages to remove many of these uninteresting events¹⁵: a hardware trigger (L0) and two high-level C++ software triggers (HLT1 and HLT2). Only events passing all stages are saved for further study. In general, the trigger selects events with high p_T daughter tracks and displaced secondary vertices, which are features of *b*-hadron decays due to their large invariant mass and relatively long lifetimes, respectively.

The L0 trigger uses information from the muon system, ECAL and HCAL to select events with muon, electron and photon candidates. Data from these sub-detectors is passed to the L0 decision unit (L0DU) which returns a decision for each event 4 μ s after the proton-proton collision. At this stage the rate is reduced to 1.1 MHz – the maximum rate at which the electronics are capable of reading out the whole detector.

Information from the SPD is used to reject complex events with large numbers of tracks. Such events have potentially large backgrounds and are time-consuming to reconstruct in the HLT trigger software. Events with high p_T muon candidates and $E_T > 2.5$ GeV in either the ECAL or HCAL are kept for further analysis by the HLT trigger. A lower limit is also imposed on the total energy in all HCAL cells to ensure that the saved events have visible collisions.

Events kept by the L0 trigger are passed to the HLT for further reduction in the rate before the final samples are written to disk. The HLT trigger software is flexible, so can be modified to cope with changing detector conditions and different physics requirements. The trigger software is run on the event filter farm, an array of multi-processor PCs, allowing more than 20 000 copies of the HLT to be run simultaneously.

¹⁵This description applies to the trigger used in Run I data-taking; the trigger was significantly changed for Run II.

In the first stage, HLT1, hits from the VELO and TT are passed to a simplified track reconstruction algorithm. Reconstructed tracks and calorimeter information can then be used to verify both charged and neutral particles selected by the L0 trigger. HLT1 requires a good quality reconstructed track with high p_T and a large impact parameter¹⁶ (IP). This reduces the event rate to about 30 kHz which is low enough for events to be more fully reconstructed in HLT2. No PID information is included, as this would be too time consuming, but the three-momentum of each track can be calculated and a mass hypothesis is assumed in order to form composite particles. HLT2 uses many different selections, known as trigger lines, which are targeted towards different physics goals. Of particular relevance for the analyses presented in this thesis are the topological trigger lines [90] which are designed to select events likely to contain b -hadron candidates decaying to two, three or four tracks. These lines offer good background rejection but keep kinematic distributions unbiased.

A deferred HLT trigger was introduced for 2012 data-taking. About 20 % of the L0 trigger output was written to disk and processed during downtime between fills rather than straight away. This strategy allowed a more efficient use of the computing resources and increased the output rate of the HLT to approximately 5 kHz.

Events passing each trigger line can, during offline analysis, be divided into two categories depending on which track (or, in the case of HLT2, tracks) caused the trigger to accept the event, or ‘fire’. For events categorised as ‘TOS’ (Triggered On Signal) with respect to a given trigger line, the signal candidate of a particular decay passed the trigger requirements. In the case of a ‘TIS’ (Triggered Independent of Signal) event the trigger fired on another track or energy deposit within the event. These two outcomes are not exclusive as the trigger can fire on both the signal candidate and another particle in the event. These TIS candidates are useful as they allow analysts to test for systematic bias that could result from selecting only TOS events.

Several times a year the LHCb dataset is prepared for analysis in a process called ‘stripping’. This makes analysis more efficient as it decreases the time taken to select signal candidates. Many different ‘stripping lines’ exist, which use different algorithms to select events with some desired set of characteristics. The user can select an appropriate stripping line, or write their own, in order to study a particular decay chain. For example the stripping lines used for analyses in this thesis select $B \rightarrow Dhh'$ decays where $h^{(\prime)}$ is a kaon or pion. The events selected by these lines must satisfy requirements on variables including particle masses, momenta and vertex quality, as discussed in Chap. 4.

¹⁶The impact parameter is defined as the shortest distance between a track and the PV.

3.6 Online system

The LHCb online system [91] is responsible for transferring data from the front-end electronics to be stored for offline analysis. Events selected by the trigger are transported for permanent storage by the Data Aquisition (DAQ) system. The data-taking conditions and environmental parameters such as temperature and pressure must also be stored and the online system ensures that all the sub-detector outputs are synchronised with the LHC clock.

3.7 Software

3.7.1 Core software

The LHCb core software [92] is mostly based on the C++ GAUDI framework [93]. Multiple projects are based on this framework and used to perform specific tasks such as Monte Carlo (MC) generation, event reconstruction and offline data analysis.

The GAUSS project is used to perform the generation of events for MC samples and model the interaction of particles with the detector material. Particles from the initial proton-proton collision are generated with PYTHIA [94] before EVTGEN [95, 96] is used to model the decay chain using measured branching fractions and decay properties. Interactions with the detector are modelled by GEANT4 [97] using information from the detector description database (DDDB) which describes the full detector layout. All interactions with the detector material are modelled, such as multiple scattering in the tracking stations and showering in the calorimeters. The output of GAUSS includes truth information about the generated particles, including the PID and true locations of hits within the detector.

Detector hits in the GAUSS output are digitised using BOOLE. The effects of sub-detector resolution and imperfections are taken into account and LHC backgrounds are incorporated. The MC output is in the same format as real data from the detector, but with truth information included.

LHCb events are reconstructed using the BRUNEL package. Input can be either direct from the LHCb DAQ system or the digitised output from BOOLE. In either case an output DST file is generated. Information from the sub-detectors is used to reconstruct events and calculate particle properties such as PID likelihoods and momentum. Relevant details about the calibration and alignment of the detector are supplied in a file called the conditions database (CondDB).

After event reconstruction by BRUNEL, offline data analysis of both real and simulated data samples is performed using the DAVINCI software package. The DST format is

converted to nTuples which can be analysed in the ROOT framework [98]. The user can select and reconstruct any decay chain of interest using the many tools available for common tasks such as fitting vertices and calculating kinematic variables.

MOORE is run online in the event filter farm to configure and operate the HLT. The package can also be run offline to add HLT information to simulated data.

3.7.2 Software analysis tools

The PIDCALIB software package offers a data-driven method to estimate the efficiencies of PID requirements applied to simulated samples. Calibration data samples are required for this task since the distributions of PID variables in MC do not perfectly match those in data. The efficiency of PID requirements depend on event kinematics, so data samples with known particle species are used to determine the efficiency of any given requirement as a function of various kinematic variables and detector occupancy. The efficiency can be calculated for each track individually and for final states with multiple particles the correlations between tracks are taken into account. For kaons and pions, as in the analyses presented in this thesis, the calibration data sample is $D^{*+} \rightarrow D^0(K^-\pi^+)\pi_s^+$. From the charge of the slow, low momentum, pion (π_s) the neutral D meson can be unambiguously identified as D^0 or \bar{D}^0 . Then, since the decay $D^0 \rightarrow K^-\pi^+$ is almost 300 times more likely than $D^0 \rightarrow K^+\pi^-$, the flavours of the D^0 daughters can be determined with near certainty based on their charges. Similar calibration samples exist for protons and muons.

The LAURA++ [99] Dalitz plot fitting software is used to perform the analyses presented in Chaps. 6 and 8. Members of the LHCb group at the University of Warwick have developed LAURA++ to perform maximum likelihood fits for Dalitz plot analysis of three-body decays. The signal model is implemented using the isobar formalism, as described in Sec. 2.4.2.

The **sPlot** technique [100] allows different categories of event to be separated based on the result of a fit with multiple components. Using the fitted yield of each component, and information from the fit PDFs and the correlation matrix, a set of weights, called ‘**sWeights**’, can be calculated for each event. The sum of **sWeights** for a given event is equal to one and for the full fit range the **sWeights** are normalised such that the sum of weights from all events is equal to the integrated yield.

Neural networks are important analysis tools in high energy particle physics research, as they are commonly used to separate different types of events in a dataset. Software can be trained to recognise the characteristics of different event categories (*e.g.* signal and background) and then apply this knowledge to similar data samples. Based on a simplified model of the neurons and connections in the human brain, a neural network has several layers of interconnected ‘nodes’. Passing data events through the network allows

the algorithms to recognise patterns and learn about the differences between categories. The analyses in this thesis use the NEUROBAYES neural network package [101]. The trained neural network can then be applied to any event and a discriminating variable between -1 and 1 is returned. In the case of separating signal and background events, a value of 1 would correspond to a very signal-like event while a value of -1 would suggest a very background-like event.

3.8 Running conditions and datasets

LHCb is designed to run at a lower instantaneous luminosity than the maximum available from the LHC: $\sim 2 \times 10^{32} \text{ cm}^{-2}\text{s}^{-1}$. This is done to reduce the average number of visible interactions per bunch crossing, known as ‘pile-up’. Lower pile-up decreases the detector occupancy thus making events easier to reconstruct as well as reducing the amount of radiation damage to the detector.

The LHCb detector was aligned and calibrated at the end of 2009 with collisions at a centre-of-mass energy $\sqrt{s} = 0.9 \text{ TeV}$. In 2010 38 pb^{-1} of data were recorded at $\sqrt{s} = 7 \text{ TeV}$ with a maximum instantaneous luminosity of $10^{32} \text{ cm}^{-2}\text{s}^{-1}$ – about 50 % of the design luminosity for LHCb. During this time the pile-up was, however, higher than the design value due to a low number of bunches in the LHC: LHCb operating conditions during LHC Run I are shown in Fig. 3.20.

In 2011 and 2012 the instantaneous luminosity was kept roughly stable for LHCb by adjusting the transverse overlap of the two colliding beams. The effect of this ‘luminosity levelling’ process is shown in Fig. 3.21. Over the course of each fill the luminosity is constant to within 5 %. This reduces systematic uncertainties related to detector occupancy varying throughout running time.

For 2011 data-taking the pile-up was steadily reduced as the number of bunches increased to ~ 3000 (the most possible with 50 ns bunch spacing). For most of the year the luminosity at LHCb was $3.5 \times 10^{32} \text{ cm}^{-2}\text{s}^{-1}$. In 2012 the beam energy was increased to 4 TeV and the luminosity increased slightly to $\sim 4 \times 10^{32} \text{ cm}^{-2}\text{s}^{-1}$. The total amount of data recorded in 2011 and 2012 was just over 3 fb^{-1} with 1.11 fb^{-1} at $\sqrt{s} = 7 \text{ TeV}$ and 2.08 fb^{-1} at $\sqrt{s} = 8 \text{ TeV}$.

The polarity of LHCb’s spectrometer magnet was flipped a couple of times per month to collect roughly equal data samples with each set up. Charged particles passing through the magnetic field are deflected in the $x - z$ plane, so combining datasets taken with the two magnet polarities cancels any left-right detector asymmetries. The datasets are termed ‘MagUp’ and ‘MagDown’.

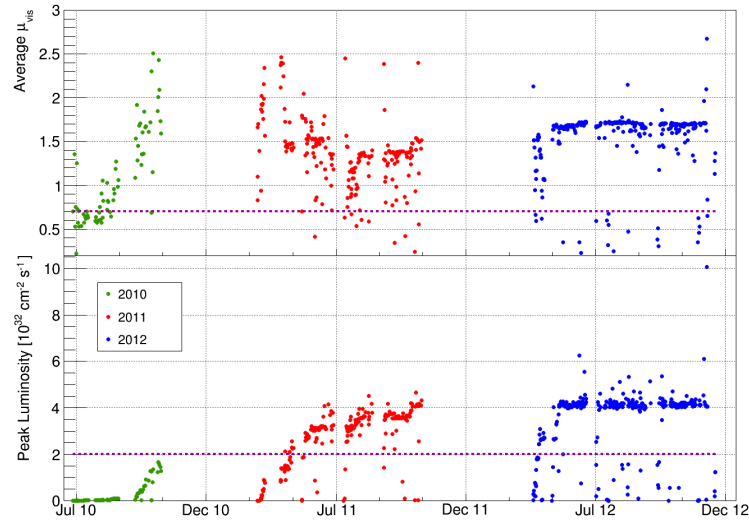


Figure 3.20: (top) Pile-up and (bottom) instantaneous luminosity at LHCb during Run I data-taking. Design values are shown by the dotted lines. Figure taken from Ref. [75].

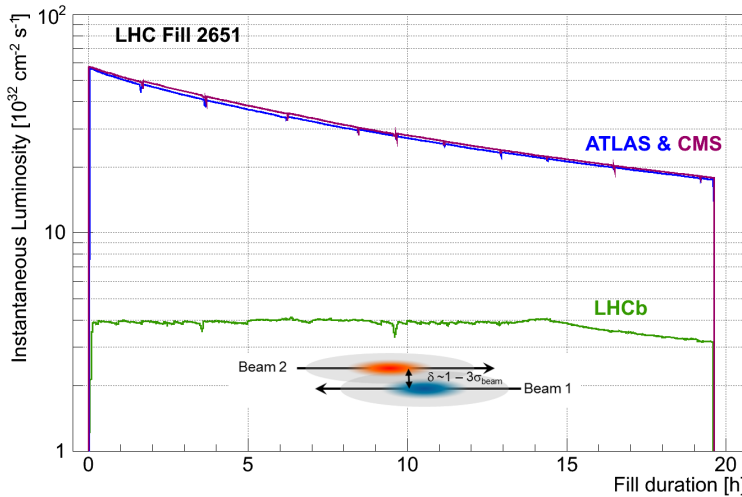


Figure 3.21: Instantaneous luminosity of ATLAS, CMS and LHCb during a fill in 2012. Luminosity levelling is utilised by LHCb to keep this value roughly constant. Figure taken from Ref. [75].

3.9 Detector performance

This section presents a brief review of the LHCb detector performance during the Run I data-taking period. Emphasis is placed on the tracking and PID systems since these are of most interest for the measurements discussed in this thesis. More detail is given in Refs. [73, 75, 81].

The VELO was designed to reconstruct primary and secondary vertices precisely to allow accurate determination of particle decay-time and track IP. Figure 3.22 shows

the PV and IP resolution for 2012 data. The PV position in the transverse plane can be measured with a typical resolution of 10–20 μm , depending on the number of tracks associated with the vertex. The z -position of a vertex can be resolved to 50–100 μm . The IP resolution is shown in Fig. 3.22 as a function of $1/p_{\text{T}}$. For tracks with $p_{\text{T}} > 1 \text{ GeV}$ an excellent IP resolution of $< 35 \mu\text{m}$ is obtained.

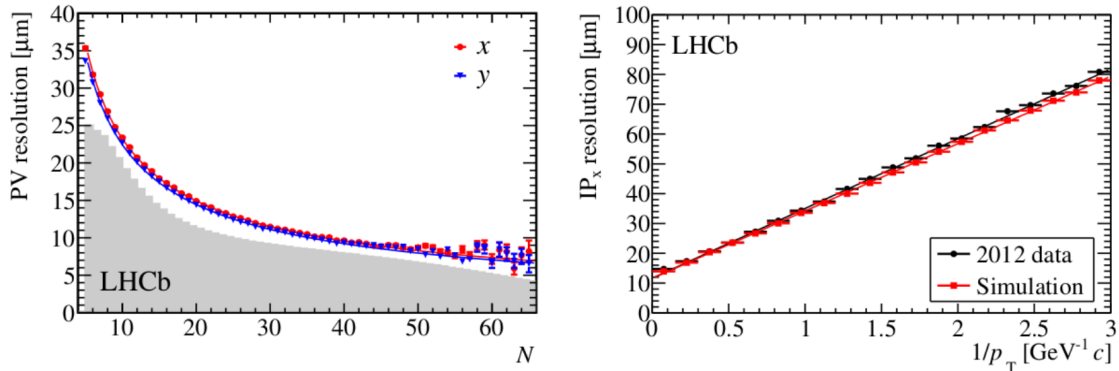


Figure 3.22: (left) Primary vertex resolution for events with only one PV. Resolution is shown as a function of track multiplicity for both the x - and y -directions. Overlaid is a shaded histogram indicating the number of tracks in each PV for events passing HLT2. (right) Resolution of the x -direction component of track IP, as a function of $1/p_{\text{T}}$. Both plots are made using data collected in 2012. Figures taken from Ref. [75].

The efficiency of track reconstruction is the probability of correctly reconstructing a charged track traversing the full detector – known as a ‘long’ track, as drawn in Fig. 3.7. For ‘reconstructable’ tracks, *i.e.* those fully within the LHCb detector acceptance, the efficiency of track reconstruction was found to be at least 98 % in 2011 data. This is shown in Fig. 3.23 as a function of several variables. The performance in 2012 data is seen to be slightly worse, which is partially due to the higher hit multiplicity at the increased centre-of-mass energy. As the number of tracks in the final state increases it becomes more important to reconstruct tracks efficiently, so this excellent performance is useful for many analyses including those presented in this thesis.

The differentiation of charged hadrons offered by the RICH detectors is particularly vital for analyses presented in this document where the final states contain both kaons and pions. Figure 3.24 shows the ability of RICH1 to determine the species of a particle from the measured Cherenkov angle. The efficiency of various PID requirements can be computed using calibration data samples, as described in Sec. 3.7. Figure 3.25 shows the efficiency of kaon identification and pion mis-identification for two different $\Delta \log \mathcal{L}(\text{K} - \pi)$ requirements, one chosen for high signal purity and one for high efficiency.

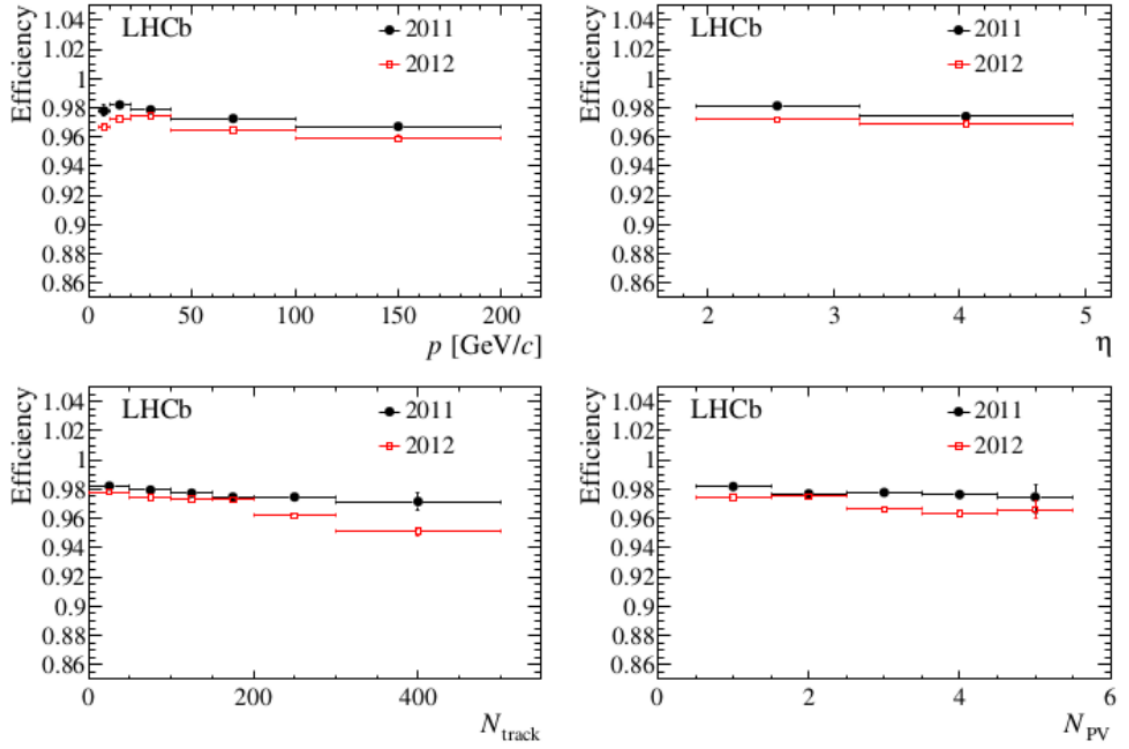


Figure 3.23: Track reconstruction efficiency shown for (black) 2011 and (red) 2012 data as a function of momentum, p , pseudorapidity, η , track multiplicity, N_{track} and number of primary vertices, N_{PV} . Figures taken from Ref. [75].

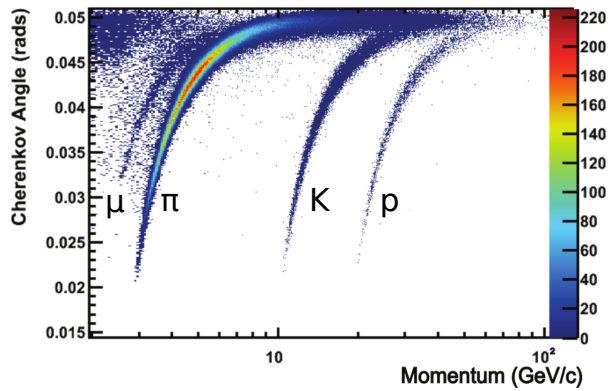


Figure 3.24: Cherenkov angle measured for the C_4F_{10} radiator in RICH1 as a function of track momentum. Figure taken from Ref. [81].

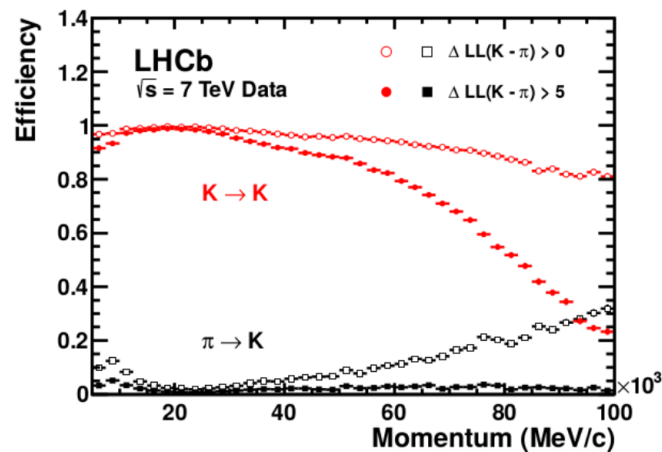


Figure 3.25: Plot showing the efficiency of (red) K identification and (black) $\pi \rightarrow K$ mis-identification in a calibration data sample of $D^{*+} \rightarrow D^0(K^-\pi^+)\pi_s^+$ decays. The distributions are shown as a function of track momentum for two different PID requirements: $\Delta \log \mathcal{L}(K - \pi) > 0$ (open shapes) and $\Delta \log \mathcal{L}(K - \pi) > 5$ (filled shapes). Figure taken from Ref. [81].

Chapter 4

$B \rightarrow Dhh'$ common tools and techniques

The following chapters present several studies of $B \rightarrow Dhh'$ decays – decays of a charged B meson to a charged D and two other light mesons, K^\pm or π^\pm . The data sample used for all of these analyses corresponds to an integrated luminosity of $\sim 3 \text{ fb}^{-1}$ of pp collision data collected by LHCb during Run I, as described in Sec. 3.8. For all final states studied, the charged D meson is reconstructed in the Cabibbo favoured three-body decay $D^- \rightarrow K^+ \pi^- \pi^-$.

The branching fraction measurement of the $B^+ \rightarrow D^- K^+ \pi^+$ decay mode [1], using the $B^+ \rightarrow D^- \pi^+ \pi^+$ decay as a normalisation channel, is detailed in Chap. 5. This is the first observation of the $B^+ \rightarrow D^- K^+ \pi^+$ decay, and sufficient signal is observed to perform a Dalitz plot analysis to study the resonant structure. The Dalitz plot analyses of the $B^+ \rightarrow D^- K^+ \pi^+$ and $B^+ \rightarrow D^- \pi^+ \pi^+$ decay channels are documented in Chaps. 6 and 8 respectively. These two studies both offer information about the spectrum of excited charmed mesons decaying to $D^- \pi^+$.

Chapter 7 describes the search for the rare $B^+ \rightarrow D^+ K^+ \pi^-$ decay [2], which was also previously unobserved. The branching fraction of $B^+ \rightarrow D^+ K^+ \pi^-$ is measured relative to that of the favoured $B^+ \rightarrow D^- K^+ \pi^+$ decay and searches are performed for the quasi-two-body decays $B^+ \rightarrow D_2^*(2460)^0 K^+$ and $B^+ \rightarrow D^+ K^*(892)^0$. The former is of interest for the potential measurement of the CKM angle γ using $B^+ \rightarrow D K^+ \pi^0$ decays [31].

The remainder of this chapter introduces some analysis details which are common to all the $B \rightarrow Dhh'$ studies described in this document. The strategy is very similar for all analyses presented, but the details presented here are specific to the study of the $B^+ \rightarrow D^- K^+ \pi^+$ decay mode [1]. Any differences for other analyses are discussed in the relevant chapters.

4.1 Analysis outline

Several steps are common to all the data analyses presented here:

- events passing an appropriate stripping line are stored and specific trigger requirements applied (described in Sec. 3.5.);
- a neural network (introduced in Sec. 3.7) is trained to separate signal-like candidates from background events;
- PID requirements are imposed on final state tracks to reduce the contribution from mis-identified background decays further. Specific background contributions are vetoed by rejecting candidates according to their invariant mass in some two- or three-body combination;
- a fit is performed to the B candidate invariant mass distribution using probability density functions (PDFs) to model signal and background shapes, and extract the yields of individual components;
- using simulated data, the efficiency of event reconstruction and selection is calculated as a function of Dalitz plot position;
- systematic biases introduced by analysis decisions are investigated, and the effects quantified in order to understand the uncertainty on the final result.

4.2 Selection

4.2.1 Trigger

Requirements are placed on the trigger decisions returned at both the hardware and software stages. The ‘L0 hadron TOS’ trigger fires on events in which a particle from the signal decay creates a large E_T deposit in the HCAL. An event is classified as a ‘L0 global TIS’ candidate either if it contains a high p_T muon or if one of the calorimeters registers a large E_T object which is inconsistent with being in the signal decay. Events classified as either global TIS or hadron TOS by the L0 hardware trigger are retained for further analysis. In addition, one of the topological trigger lines introduced in Sec. 3.5 must have fired in the HLT software stage, selecting events containing probable b -hadron candidates decaying to two, three or four tracks.

4.2.2 Stripping

Two stripping lines are used to select the events studied in this thesis: one to identify candidate $B^+ \rightarrow D^- K^+ \pi^+$ and $B^+ \rightarrow D^- \pi^+ \pi^+$ decays and the other to choose possible

$B^+ \rightarrow D^+ K^+ \pi^-$ decays. Both lines select charged B meson candidates decaying to a charged D meson with two other charged tracks (called ‘bachelor’ particles). The D decay must also be reconstructed from three charged hadrons, *i.e.* $D^- \rightarrow K^+ \pi^- \pi^-$. The requirements imposed by these two lines are identical (except for particle charges) and are summarised in Tab. 4.1.

To improve the quality and purity of selected B candidate decays, requirements are placed on: the reconstructed mass, m_B^{reco} ; the reconstructed decay time, τ_B^{reco} ; the quality of the fit performed to the B production vertex, $(\chi^2/\text{ndf})_{\text{vertex}}$; the minimum χ^2_{IP} between the reconstructed B candidate and any PV in the event, where χ^2_{IP} is the difference between the χ^2 of the PV reconstruction with and without the considered particle; the cosine of the angle between the B candidate’s reconstructed momentum and the vector pointing from the event PV to the B decay vertex, $\cos \theta_{\text{dir. own PV}}$; the total p_{T} of all final state tracks, $\Sigma_{\text{all}} p_{\text{T}}$; and the output variable of a BDT [90], used to identify the SV of a B decay.

Similar criteria are applied to variables relating to the D candidate and the two combined bachelor tracks, with additional requirements made on ‘ $\chi^2_{\text{flight w.r.t. best PV}}$ ’, the square of the distance between the reconstructed decay vertex and the most likely PV, divided by the uncertainty on this quantity; and the maximum DOCA (distance of closest approach) between any of the daughter tracks, $\text{max}_{\text{daughters}}(\text{DOCA})$. Further requirements are placed on the track p , p_{T} , and fit quality, $(\chi^2/\text{ndf})_{\text{track}}$, and the total number of long tracks in the event, $N_{\text{long tracks}}$.

4.2.3 Offline selection requirements

Additional selection requirements are made offline, aiming to reduce the contributions from background decays so that MVA techniques may be used to purify the data sample further and isolate true signal decays. A summary of the initial selection applied to $B^+ \rightarrow D^- K^+ \pi^+$ and $D^- \pi^+ \pi^+$ datasets for the analyses in Chaps. 5, 6 and 8 is given in Tab. 4.2 (the applied PID requirements are discussed in more detail in Sec. 4.2.5). Tighter requirements are placed on the reconstructed masses of the B and D candidates and the p of all final state tracks. Events are also rejected unless both B and D candidates have a significant flight distance from their associated production vertex. These criteria were updated during the later search for $B^+ \rightarrow D^+ K^+ \pi^-$ – the differences are outlined in Chap. 7.

Decay vertices are refitted with the D candidate mass constrained to the world average value, m_D^{PDG} [3], in order to improve the resolution of the reconstructed B meson mass. Wherever possible the offline selection places requirements on variables calculated with this constraint applied. All DP and SDP coordinates are calculated using parameters with an additional B mass constraint applied.

Table 4.1: Requirements of the $B \rightarrow Dhh'$ stripping lines.

Particle	Parameter	Requirement
B	m_B^{reco}	$> 4.75 \text{ and } < 7.0 \text{ GeV}/c^2$
	τ_B^{reco}	$> 0.2 \text{ ps}$
	$(\chi^2/\text{ndf})_{\text{vertex}}$	< 10
	$\text{minPVs } \chi^2_{\text{IP}}$	< 25
	$\cos \theta_{\text{dir. own PV}}$	> 0.999
	$\Sigma_{\text{all} p\text{T}}$	$> 5.0 \text{ GeV}/c$
	BBDT output	> 0.05
D	$ m_D^{\text{reco}} - m_D^{\text{PDG}} $	$< 100 \text{ MeV}/c^2$
	$(\chi^2/\text{ndf})_{\text{vertex}}$	< 10
	$\chi^2_{\text{flight w.r.t. best PV}}$	> 36
	$\cos \theta_{\text{dir. own PV}}$	> 0.0
	$\text{max}_{\text{daughters}} (\text{DOCA})$	$< 0.5 \text{ mm}$
	$\Sigma_{\text{daughters}} p\text{T}$	$> 1.8 \text{ GeV}/c$
Recombined bachelors	m^{reco}	$< 5.2 \text{ GeV}/c^2$
	$(\chi^2/\text{ndf})_{\text{vertex}}$	< 16
	$\chi^2_{\text{flight w.r.t. best PV}}$	> 16
	$\cos \theta_{\text{dir. own PV}}$	> 0.0
	$\text{max}_{\text{bachelors}} (\text{DOCA})$	$< 0.5 \text{ mm}$
	$\Sigma_{\text{bachelors}} p\text{T}$	$> 1.0 \text{ GeV}/c$
Charged tracks	$p\text{T}$	$> 100 \text{ MeV}/c$
	$p_{D\text{daughter}}$	$> 1.0 \text{ GeV}/c$
	p_{bachelor}	$> 2.0 \text{ GeV}/c$
	$\text{minPVs } \chi^2_{\text{IP}}$	> 4
	$(\chi^2/\text{ndf})_{\text{track}}$	< 3
One D daughter and one bachelor	$p\text{T}$	$> 500 \text{ MeV}/c$
	p	$> 5.0 \text{ GeV}/c$
	$(\chi^2/\text{ndf})_{\text{track}}$	< 2.5
One track	$p\text{T}$	$> 1.7 \text{ GeV}/c$
	p	$> 10.0 \text{ GeV}/c$
	$(\chi^2/\text{ndf})_{\text{track}}$	< 2.5
	$\text{minPVs } \chi^2_{\text{IP}}$	> 16
	minPVs IP	$> 0.1 \text{ mm}$
Global	$N_{\text{long tracks}}$	< 500

It is found that $\sim 0.6\%$ of selected events in the $B^+ \rightarrow D^- K^+ \pi^+$ data sample contain more than one signal decay candidate. A similar proportion of events in the $B^+ \rightarrow D^- \pi^+ \pi^+$ and $B^+ \rightarrow D^+ K^+ \pi^-$ datasets and in simulated samples also contain multiple candidates. These additional decays are retained for further analysis and not treated differently to other candidates.

Table 4.2: Offline selection requirements applied to $B^+ \rightarrow D^- K^+ \pi^+$ and $D^- \pi^+ \pi^+$ datasets prior to NN training. Parameters labelled ‘ \dagger ’ are calculated after a D mass constraint. Requirements marked with a ‘*’ are applied to the $D^- K^+ \pi^+$ data sample only.

Particle	Parameter	Requirement
B	$\dagger m_B^{\text{reco}}$	> 5100 and $< 5800 \text{ MeV}/c^2$
	$\dagger \cos \theta_{\text{dir. own PV}}$	> 0.99997
	$\dagger \chi^2_{\text{flight w.r.t. own PV}}$	> 260
D	m_D^{reco}	> 1770 and $< 1968 \text{ MeV}/c^2$
	$\dagger \chi^2_{\text{flight w.r.t. own PV}}$	> 260
K from D	$(\text{ProbNN}_K \times (1 - \text{ProbNN}_\pi))$	> 0.3
	p	$< 100 \text{ GeV}/c$
$\pi_{\text{high } p_T}$ from D	$(\text{ProbNN}_\pi \times (1 - \text{ProbNN}_K))$	> 0.6
	p	$< 100 \text{ GeV}/c$
$\pi_{\text{low } p_T}$ from D	$(\text{ProbNN}_\pi \times (1 - \text{ProbNN}_K))$	> 0.2
	p	$< 100 \text{ GeV}/c$
*K bachelor	$(\text{ProbNN}_K \times (1 - \text{ProbNN}_\pi))$	> 0.6
	p	> 3 and $< 100 \text{ GeV}/c$
π bachelor	$(\text{ProbNN}_\pi \times (1 - \text{ProbNN}_K))$	> 0.2
	p	$< 100 \text{ GeV}/c$

4.2.4 Neural networks

NEUROBAYES is used twice in each analysis to maximise the discrimination between signal and background events. The first network (NN_D) is designed to select true D mesons, whilst the second (NN_B) suppresses combinatorial background composed of a true D candidate with one or two random tracks. Both NNs are trained using $B^+ \rightarrow D^- \pi^+ \pi^+$ data.¹⁷ Using real data to train a NN is preferable in order to avoid any discrepancies between kinematic variables in data and simulation. Another advantage of this approach is that, since the $B^+ \rightarrow D^- \pi^+ \pi^+$ decay is Cabibbo favoured, a large dataset is available, with an almost identical topology to the other $B \rightarrow Dhh'$ channels.

The **sPlot** technique [100] is used to differentiate signal and background candidates before each NN is trained. For NN_D (NN_B) a fit is performed to the D (B) candidate invariant mass distribution in $B^+ \rightarrow D^- \pi^+ \pi^+$ data in order to calculate signal **sWeights** for each event. More signal-like events are given a larger signal **sWeight** value and a lower background **sWeight**, such that the sum of signal **sWeight** and background **sWeight** for an event is unity.

The result of the fit to $m(K\pi\pi)$, from which the signal **sWeights** used to train NN_D are calculated, is shown in Fig. 4.1 (left). A simple fit model is used: a double bifurcated

¹⁷The full 2011 and 2012 dataset from LHCb is used, as studies show that there is little gain from sub-dividing by year of data taking.

Gaussian PDF to parametrise the signal shape and a linear function to describe the combinatorial background contribution. The produced signal **sWeights** allow NEUROBAYES to learn about kinematic differences between signal-like and background-like events in $D^-\pi^+\pi^+$ data; the parameters used to train NN_D are a subset of those used to train NN_B and are labelled ‘*’ in Tab. 4.3. The output variable produced by applying NN_D to the $B^+ \rightarrow D^-\pi^+\pi^+$ data sample takes values between -1 (background-like events) and 1 (signal-like events), is shown in Fig. 4.1 (right). A loose requirement of $\text{NN}_D > -0.6$ is applied as part of the initial selection process.

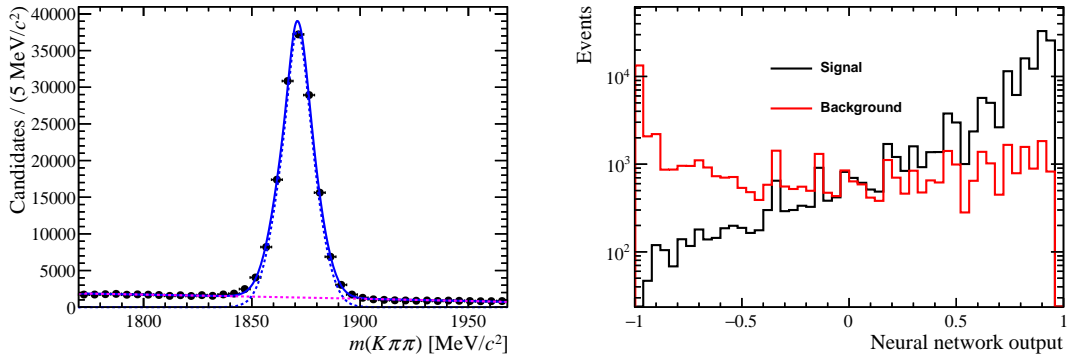


Figure 4.1: (Left) result of the fit to $m(K\pi\pi)$ for the $B^+ \rightarrow D^-\pi^+\pi^+$ data sample, used to obtain **sWeights** as input to NN_D ; (right) NN_D output variable plotted for all $B^+ \rightarrow D^-\pi^+\pi^+$ events.

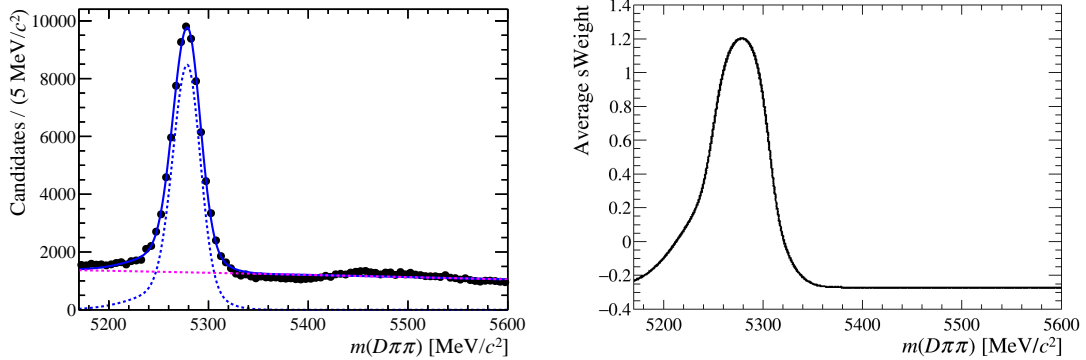


Figure 4.2: (Left) result of the fit to $m(D\pi\pi)$ for the $B^+ \rightarrow D^-\pi^+\pi^+$ data sample, used to obtain **sWeights** as input to NN_B ; (right) distribution of signal **sWeights** as a function of $m(D\pi\pi)$.

A similar mass fit, shown in Fig. 4.2 (left), is performed to the B candidate invariant mass in the range $5170 < m(D\pi\pi) < 5600 \text{ MeV}/c^2$ to calculate the **sWeights** required to train NN_B . Note that the wide structure at $\sim 5450 \text{ MeV}/c^2$ is due to $B^0 \rightarrow D^-\pi^+$ decays reconstructed with a random slow pion; since these events are a form of combinatorial background, the **sWeights** obtained using this simplistic fit model are sufficient for the purpose of training NEUROBAYES to separate signal and background candidates. The signal **sWeight** obtained as a function of B candidate mass is shown in Fig. 4.2 (right).

Table 4.3: Variables used as inputs to train the NEUROBAYES selection. Parameters labelled $*$ used to train NN_D . Parameters labelled \dagger are calculated after a D mass constraint.

Particle	Parameter	NEUROBAYES ranking
B	p_T	10
	p_z	20
	$\dagger \min_{\text{PVs}} \chi_{\text{IP}}^2$	13
	$\dagger \cos \theta_{\text{dir. own PV}}$	22
	$\dagger \chi_{\text{flight w.r.t. own PV}}^2$	21
	$\dagger (\chi^2/\text{ndf})_{\text{end vertex}}$	27
	$\chi_{\text{IP w.r.t. own PV}}^2$	3
	$\chi_{\text{decay time}}^2$	26
	$(\chi^2/\text{ndf})_{\text{vertex}}$	25
	$\chi_{\text{decay time}}^2$ (from vertex fit algorithm)	6
	DOCA (from vertex fit algorithm)	2
	A_{p_T} in 1.5 rad cone	5
	track _{mult} in 1.5 rad cone	19
D	Output from NN_D	24
	$\dagger * \cos \theta_{\text{dir. own PV}}$	9
	$\dagger * \chi_{\text{flight w.r.t. own PV}}^2$	16
	$\dagger * (\chi^2/\text{ndf})_{\text{end vertex}}$	18
	$* \chi_{\text{IP w.r.t. own PV}}^2$	23
	$* \chi_{\text{decay time}}^2$	7
	$* (\chi^2/\text{ndf})_{\text{vertex}}$	14
	$* \cos \theta_{\text{dir. orig. PV}}$	12
	$* \chi_{\text{flight w.r.t. original PV}}^2$	8
	$* (\chi^2/\text{ndf})_{\text{original vertex}}$	4
D daughters, $K\pi$	$\dagger * m^2(K\pi)$	11
D daughters, $\pi\pi$	$\dagger * m^2(\pi\pi)$	17
First bachelor π	$\dagger \min_{\text{PVs}} \chi_{\text{IP}}^2$	1
Second bachelor π	$\dagger \min_{\text{PVs}} \chi_{\text{IP}}^2$	15

Various kinematic variables are included in the NN training, as well as parameters giving information about the fit quality of vertices in the candidate decay. The list of variables also includes the p_T asymmetry, A_{p_T} , and track multiplicity, track_{mult}, in a cone with half-angle of 1.5 units of the plane of pseudorapidity and azimuthal angle (measured in radians) around the B candidate flight direction. These parameters contain information about the isolation of the B candidate from the rest of the event. The neural network input quantities depend only weakly on the kinematics of the B decay. Table 4.3 gives the full list of input variables used to train NN_B and the ranking of each variable according to its importance in the training process. The result of the NN_B training applied to the full $B^+ \rightarrow D^-\pi^+\pi^+$ data sample is shown in Fig. 4.3 (left). A suitable requirement on the NN_B output variable can be determined by considering the approximate yields of

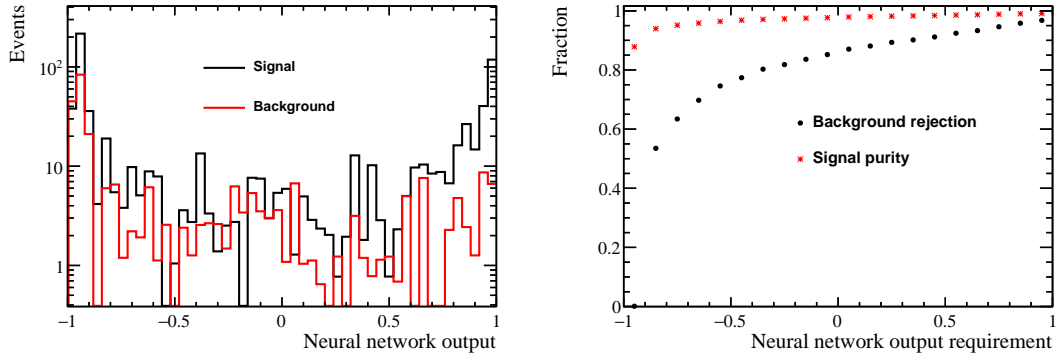


Figure 4.3: (Left) NN_B output variable plotted for all $B^+ \rightarrow D^-\pi^+\pi^+$ events; (right) values of signal purity and background rejection for different requirements on the NN_B output variable, estimated by fitting $m(DK\pi)$.

signal and background events, as a function of NN_B output.

- Approximate yields of signal ($S_{D\pi\pi}$) and background ($B_{D\pi\pi}$) events in the $B^+ \rightarrow D^-\pi^+\pi^+$ data sample are estimated from fits to the $D\pi\pi$ invariant mass distribution. Fits are repeated with different requirements placed on the NN_B output variable.
- Based on the expected Cabibbo suppression of $B^+ \rightarrow D^-K^+\pi^+$, the $D^-K^+\pi^+$ signal yield ($S_{DK\pi}$) is assumed to be about 8 % of $S_{D\pi\pi}$ for all requirements on NN_B . The background yield ($B_{DK\pi}$) surviving a certain NN_B criterion is estimated by fitting the sidebands of $m(DK\pi)$ in $B^+ \rightarrow D^-K^+\pi^+$ data. The values of signal purity and background rejection, as calculated from $S_{DK\pi}$ and $B_{DK\pi}$, are shown as a function of NN_B output in Fig. 4.3 (right).
- The optimal NN_B requirement for each decay mode is found by examining the product of significance ($S_{Dhh'}/\sqrt{S_{Dhh'} + B_{Dhh'}}$) and purity ($S_{Dhh'}/(S_{Dhh'} + B_{Dhh'})$) as a function of NN_B requirement. The results are shown in Fig. 4.4. This figure of merit was found to be effective for studies of D^{**} mesons at LHCb [44], and appears to be appropriate for Dalitz plot analyses. The distributions peak near values of 0.4 and 0.3 for the $DK\pi$ and $D\pi\pi$ samples, respectively, so a requirement of 0.4 is chosen for both decay modes.

The analysis strategy is slightly different for the search for $B^+ \rightarrow D^+K^+\pi^-$ decays, as described in Chap. 7. A loose requirement of $NN_B > -0.7$ is placed on the data samples to remove the most background-like events, and the distribution of the remaining events is used in the mass fit.

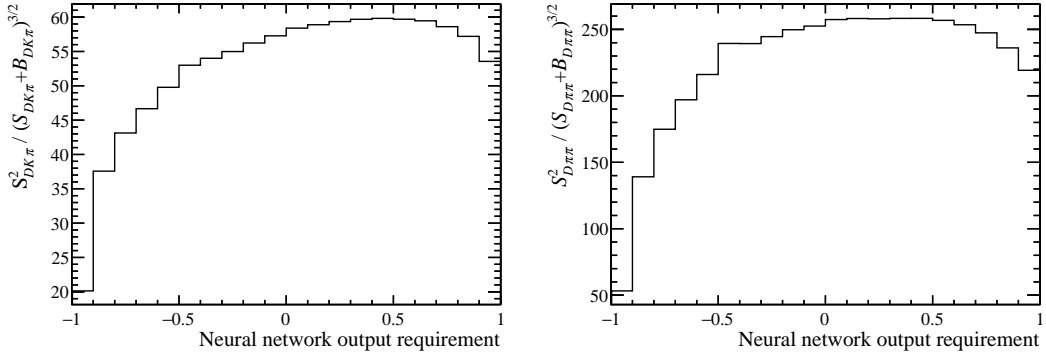


Figure 4.4: Optimisation of the NN_B output requirement for (left) $B^+ \rightarrow D^- K^+ \pi^+$ and (right) $B^+ \rightarrow D^- \pi^+ \pi^+$.

4.2.5 Particle identification requirements

Requirements are placed on the ProbNN_π and ProbNN_K variables (introduced in Sec. 3.4) to reduce backgrounds caused by mis-identified particles in the `thepipihh` data samples. The ProbNN_x parameters take values between 0 and 1, with a higher value corresponding to a higher probability of the particle being of species x . In this thesis the PID selection criteria are of the form $(\text{ProbNN}_x \times (1 - \text{ProbNN}_y)) > X$, which ensures that a particle has a high probability of being species x and is also unlikely to be species y .

The PID requirements for $D^- K^+ \pi^+$ and $D^- \pi^+ \pi^+$ candidates are given in Tab. 4.2. The loosest criterion is $(\text{ProbNN}_\pi \times (1 - \text{ProbNN}_K)) > 0.2$ for pion candidates and $(\text{ProbNN}_K \times (1 - \text{ProbNN}_\pi)) > 0.3$ for kaon candidates.

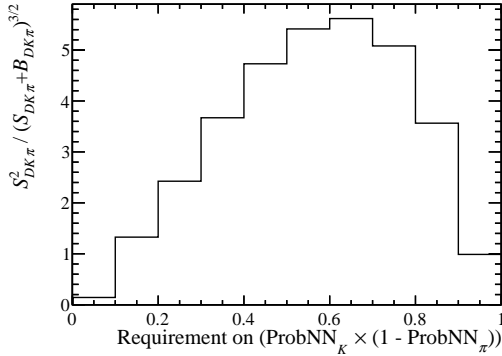


Figure 4.5: Optimisation of the $(\text{ProbNN}_K \times (1 - \text{ProbNN}_\pi))$ requirement made on the bachelor kaon using $B^+ \rightarrow D^- K^+ \pi^+$ data.

A stricter requirement must be applied to the bachelor kaon in the search for $B^+ \rightarrow D^- K^+ \pi^+$ decays, since the main source of background is from the $B^+ \rightarrow D^- \pi^+ \pi^+$ decay with $\pi \rightarrow K$ mis-identification. The value of the requirement is optimised using the same method as the optimisation of the NN_B output requirement described in Sec. 4.2.4, using

$B^+ \rightarrow D^- K^+ \pi^+$ data. The distribution, shown in Fig. 4.5, peaks at a value of 0.6 so bachelor kaon candidates are required to have $(\text{ProbNN}_K \times (1 - \text{ProbNN}_\pi)) > 0.6$.

The decay $B^+ \rightarrow D_s^- K^+ \pi^+$ can also contribute as a background to $B^+ \rightarrow D^- K^+ \pi^+$ if $D_s^- \rightarrow K^+ K^- \pi^-$ is mis-reconstructed as $D^- \rightarrow K^+ \pi^- \pi^-$. Requiring that the pion D daughter with the highest p_T in the lab frame has $(\text{ProbNN}_\pi \times (1 - \text{ProbNN}_K)) > 0.6$ is found to reduce this contribution, but no tight PID requirements are necessary for the other pion D daughter. The hardest p_T pion is more likely to be mis-identified since PID degrades for tracks with high momentum at LHCb, as shown by Fig. 3.24.

4.2.6 Vetoos

Contributions from mis-identified background decays can often be reduced significantly by rejecting events which fail certain PID requirements, as described in Sec. 4.2.5. Some mis-identified backgrounds that are fully reconstructed are visible as narrow peaks in two- or three-body invariant mass distributions, so can be removed completely using vetoes.

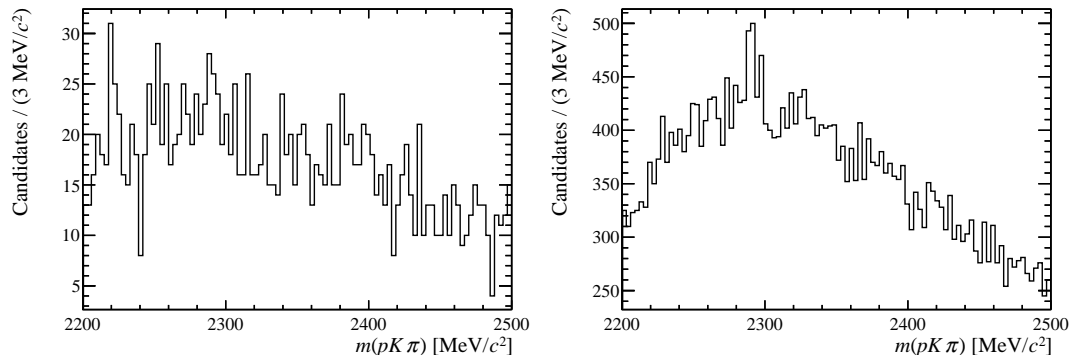


Figure 4.6: Invariant mass distribution of the D daughter candidates with the proton mass assigned to the lower momentum pion for (left) $B^+ \rightarrow D^- K^+ \pi^+$ and (right) $B^+ \rightarrow D^- \pi^+ \pi^+$ data. The initial selection has been applied and events within one standard deviation of the B and D mass are not shown.

One source of potential background is vetoed in all the analyses presented here. The baryonic decay $\Lambda_c^- \rightarrow \bar{p} K^+ \pi^-$ can be mis-reconstructed as $D^- \rightarrow K^+ \pi^- \pi^-$ if there is a $p \rightarrow \pi$ mis-identification. The invariant mass of the three D daughter tracks is plotted in Fig. 4.6, for $B^+ \rightarrow D^- K^+ \pi^+$ and $B^+ \rightarrow D^- \pi^+ \pi^+$ candidates, with the proton mass assigned to the lowest momentum bachelor track. In $B^+ \rightarrow D^- \pi^+ \pi^+$ data, a peak is observed in this $m(pK\pi)$ distribution near the measured value of the Λ_c^- mass. A veto of $2280 < m(pK\pi) < 2300 \text{ MeV}/c^2$ is applied to remove this contribution from all $B \rightarrow Dhh'$ samples. This veto removes 3.5% (4.2%) of candidates after the rest of the selection is applied to $D^- \pi^+ \pi^+$ ($D^- K^+ \pi^+$) data samples. The requirement on $m(pK\pi)$ is more effective than simply applying a tight $(\text{ProbNN}_\pi \times (1 - \text{ProbNN}_p))$ PID requirement on the mis-identified D daughter track.

4.3 Backgrounds

This section contains a brief overview of the methods used to identify any backgrounds surviving all selection requirements applied to the $B^+ \rightarrow D^- K^+ \pi^+$ data sample. Similar studies were performed for the $B^+ \rightarrow D^- \pi^+ \pi^+$ and $B^+ \rightarrow D^+ K^+ \pi^-$ final states. Simulated samples of possible background decay modes are used to estimate the number of events that could be reconstructed as $B^+ \rightarrow D^- K^+ \pi^+$ and survive all selection requirements detailed in Sec. 4.2. The true extent to which a background will contribute in the signal region of the chosen final state depends on the Dalitz plot distribution of the background decay mode, so samples generated with no resonant structure can only be used as an approximation. The performance of PID variables differs in data and simulation, so this introduces an additional source of uncertainty in the results.

In Fig. 4.7 the reconstructed mass distributions of B and D candidates in $DK\pi$ data are compared. There are fewer obvious background events in the D mass distribution, suggesting that the main background sources are candidates containing real D mesons combined with random tracks. It is also clear from Fig. 4.7 (right) that the sidebands of the D candidate mass have no structure, indicating that events from these regions can be used to study *charmless backgrounds*, *i.e.* decays without a real D meson.

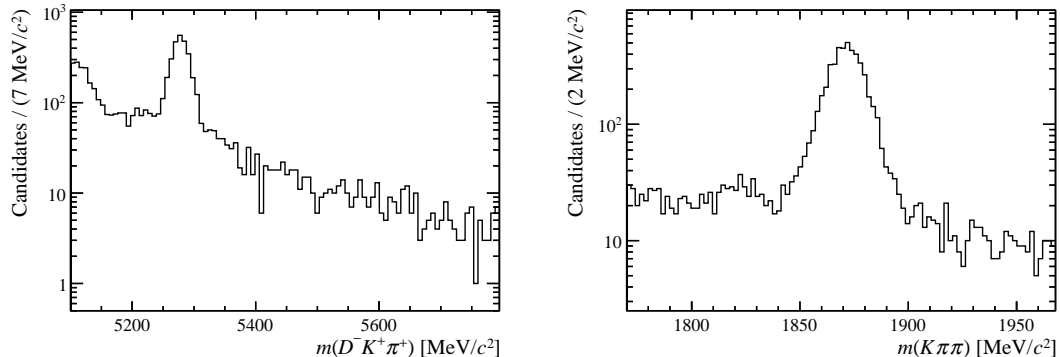


Figure 4.7: Distributions of (left) B and (right) D candidate invariant mass in $B^+ \rightarrow D^- K^+ \pi^+$ data.

Several background categories are considered: *combinatorial background*, which consists of a real or fake D meson reconstructed with two random tracks; *peaking background*, where an alternative decay mode with five final state tracks is incorrectly reconstructed as signal; and *partially reconstructed background* from the decay of a B meson to a real or fake D meson, two charged tracks and additional unreconstructed particles.

4.3.1 Combinatorial background

Combinatorial background events are present over the whole B mass range considered in these studies (5100 – 5800 MeV/ c^2), but the contribution is significantly reduced by the

NN_B requirement described in Sec. 4.2.4. The distribution of all remaining combinatorial background events varies smoothly with B candidate invariant mass, so a first-order polynomial or exponential function is used to parametrise this component for analyses presented in this thesis.

4.3.2 Peaking background

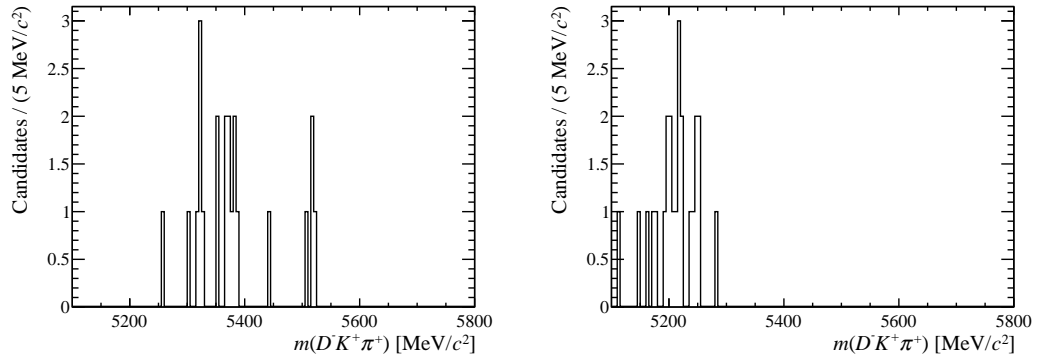


Figure 4.8: Reconstructed $m(D^-K^+\pi^+)$ distributions for simulated decays of potential peaking backgrounds passing the full $B^+ \rightarrow D^-K^+\pi^+$ reconstruction and selection; (left) $B^+ \rightarrow D^-\pi^+\pi^+$ and (right) $B^+ \rightarrow D_s^-K^+\pi^+$.

Several decay modes can be reconstructed as $B^+ \rightarrow D^-K^+\pi^+$ if one or more final state particles are mis-identified. The two main contributions were identified as $B^+ \rightarrow D^-\pi^+\pi^+$ (with the mis-identification of a bachelor pion) and $B^+ \rightarrow D_s^-K^+\pi^+$ (where a D_s^+ daughter kaon is mis-identified as a pion). The reconstructed B candidate invariant mass distributions from simulated samples of each mode are shown in Fig. 4.8. Although the number of events surviving the $D^-K^+\pi^+$ selection is small, both contribute near the signal region, so must be well understood.

To check for additional peaking backgrounds, the invariant mass distributions of various two- and three-body particle combinations are examined in $B^+ \rightarrow D^-K^+\pi^+$ data. The results are shown in Figs. 4.9 and 4.10, with parentheses placed around D daughters to differentiate them from the two bachelor tracks. Peaks are visible in both $m(D(K\pi))$ distributions from the $K^{*0}(892) \rightarrow K^+\pi^-$ decay. An excess at the D^- mass in the $m(D(\pi\pi)K)$ distribution in Fig. 4.10 occurs as the result of multiple candidates. The effect is so small that the events are kept. In a similar study for $B^+ \rightarrow D^-\pi^+\pi^+$ candidates no unexpected resonant contributions are found.

4.3.3 Charmless background

From Fig. 4.7, it appears that charmless backgrounds are not significant for the $B^+ \rightarrow D^-K^+\pi^+$ decay. Data events from the D candidate mass sideband regions ($1770 < m(K\pi\pi) < 1820 \text{ MeV}/c^2$ and $1920 < m(K\pi\pi) < 1970 \text{ MeV}/c^2$) are used to check for the

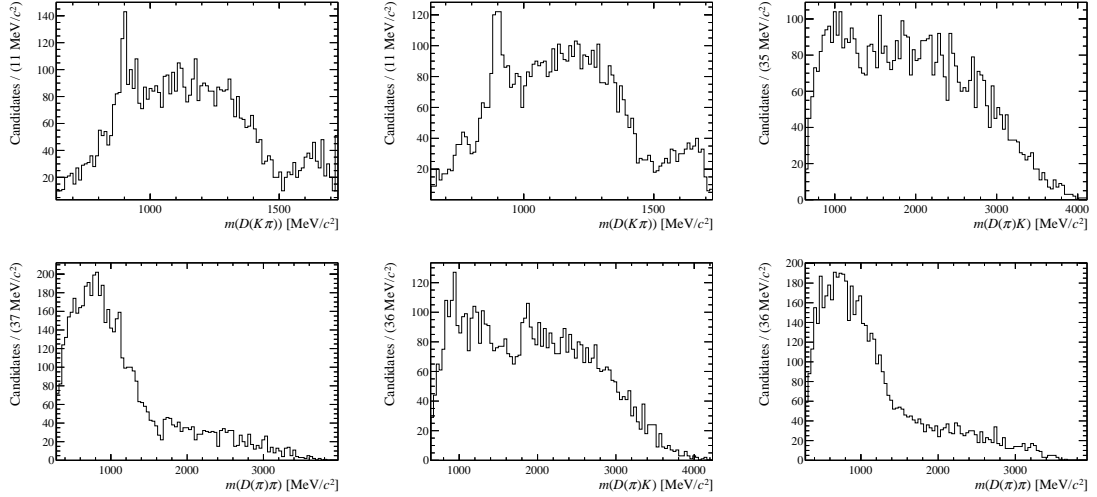


Figure 4.9: Two-body invariant mass distributions for combinations of particles in $B^+ \rightarrow D^- K^+ \pi^+$ data, (top left) K^+ and π^- from D^- , (top middle) K^+ and π^- from D^- , (top right) π^- from D^- with bachelor K^+ , (bottom left) π^- from D^- with bachelor π^+ , (bottom middle) π^- from D^- with bachelor K^+ and (bottom right) π^- from D^- with bachelor π^+ . Note that doubly charged combinations are not considered and the two D daughter pions are randomised.

presence of charmless backgrounds that peak in the reconstructed B candidate mass. Figure 4.11 shows a comparison of the reconstructed B mass distribution for events from the D mass sidebands (red) and full region (black). No peaks are observed in the sidebands for $B^+ \rightarrow D^- K^+ \pi^+$ data¹⁸ suggesting that any residual charmless background can be absorbed into the combinatorial background shape. For $B^+ \rightarrow D^- \pi^+ \pi^+$ data, shown in Fig. 4.11 (right), a peaking charmless background is observed. A requirement that the flight distance (calculated after the D mass constraint) of the D candidate is > 1 mm is found to remove this background. For consistency this requirement is also applied to the $B^+ \rightarrow D^- K^+ \pi^+$ data sample. The effect of this requirement on both $D^- K^+ \pi^+$ and $D^- \pi^+ \pi^+$ data samples is also shown in Fig. 4.11 (blue).

4.3.4 Partially reconstructed background

Partially reconstructed backgrounds contribute in the low mass region (below $5200 \text{ MeV}/c^2$) of the B candidate invariant mass distribution, since one or more of the decay products of the B hadron is missed during the event reconstruction. Such events are not removed by the NN_B requirement due to the similarity of the event topologies. In the case of $B^+ \rightarrow D^- K^+ \pi^+$ the main source of partially reconstructed background is the $B^+ \rightarrow D^{*-} K^+ \pi^+$ mode, where D^{*-} decays to either $D^- \pi^0$ or $D^- \gamma$ and the neutral

¹⁸This is not unexpected as the branching fraction for a final state with net strangeness of 2, such as $K^+ \pi^- \pi^- K^+ \pi^+$, is expected to be negligible in the SM.

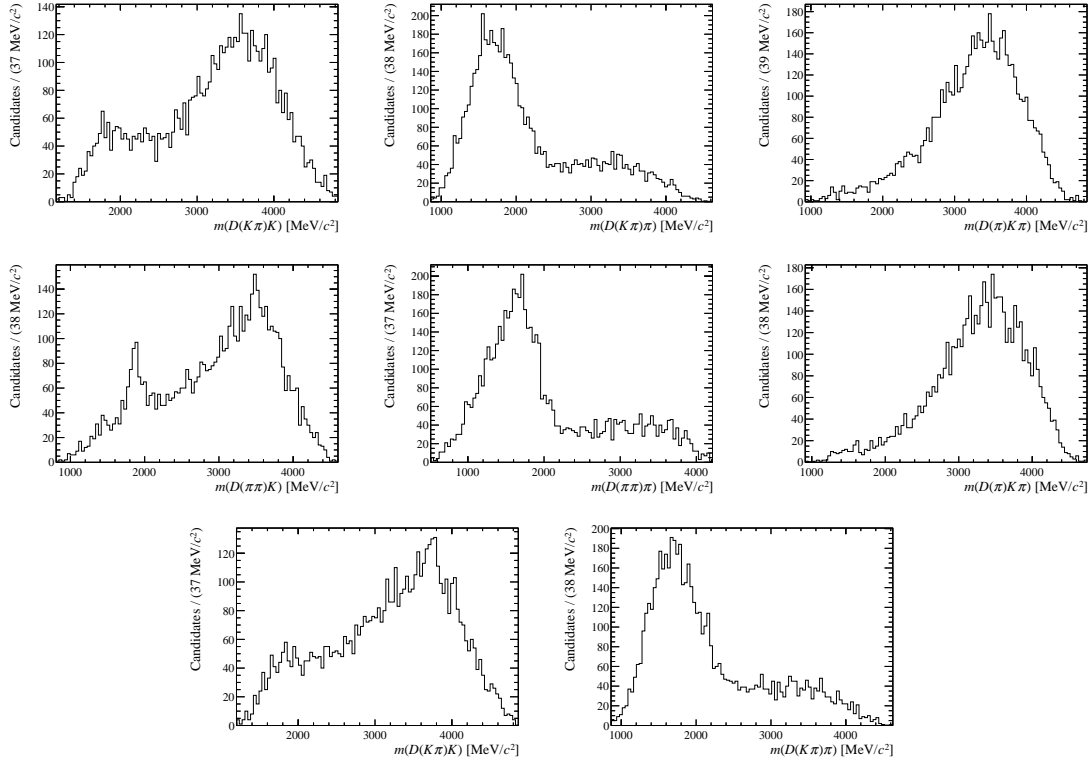


Figure 4.10: Three-body invariant mass distributions for combinations of particles in $B^+ \rightarrow D^- K^+ \pi^+$ data, (top left) K^+ and π^- from D^- with bachelor K^+ , (top middle) K^+ and π^- from D^- with bachelor π^+ and (top right) π^- from D^- with bachelors K^+ and π^+ , (centre left) π^- and π^- from D^- with bachelor K^+ , (centre middle) π^- and π^- from D^- with bachelor π^+ , (centre right) π^- from D^- with bachelors K^+ and π^+ , (bottom left) K^+ and π^- from D^- with bachelor K^+ , (bottom right) K^+ and π^- from D^- with bachelor π^+ . Note that triply charged combinations are not considered and the two D daughter pions are randomised.

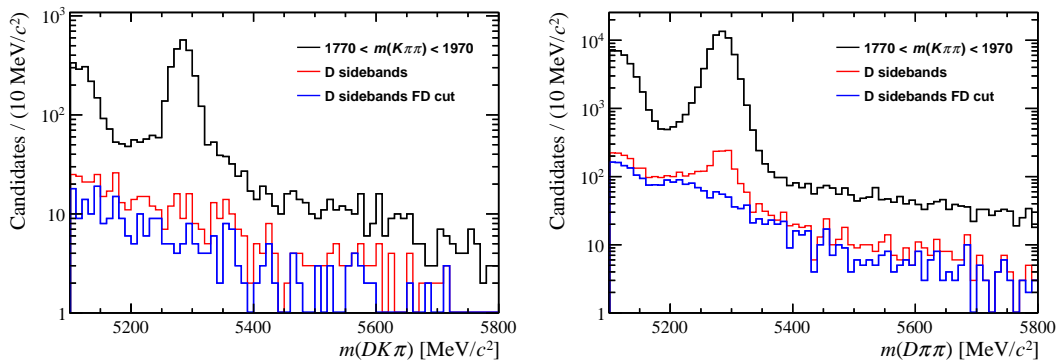


Figure 4.11: Reconstructed B candidate mass distribution for (left) $B^+ \rightarrow D^- K^+ \pi^+$ and (right) $B^+ \rightarrow D^- \pi^+ \pi^+$ data. Events from D candidate mass sideband regions, with (blue) and without (red) a requirement of > 1 mm on the flight distance of the D candidate. The sideband distribution has been scaled to the expected contribution in the full mass window. The B candidate mass distribution for the full sample (black) is overlaid for comparison.

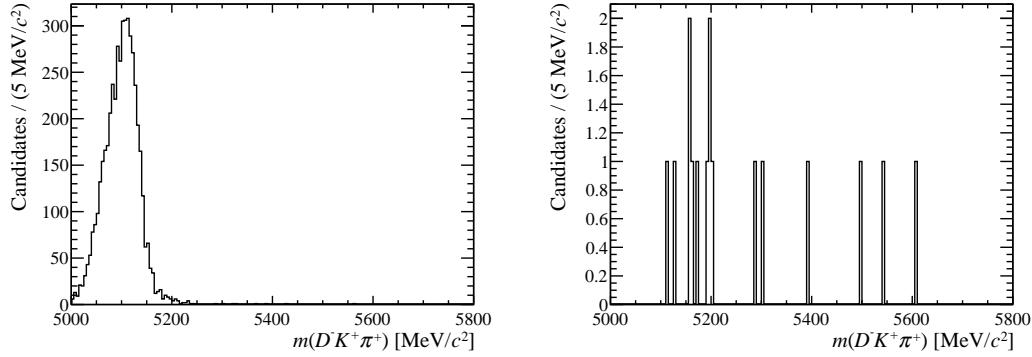


Figure 4.12: Reconstructed $m(D^-K^+\pi^+)$ distributions for simulated decays of potential partially reconstructed backgrounds, passing the full $B^+ \rightarrow D^-K^+\pi^+$ reconstruction and selection; (left) $B^+ \rightarrow D^{*-}K^+\pi^+$ and (right) $B^+ \rightarrow D^{*-}\pi^+\pi^+$.

pion or photon is not included in the reconstructed event. Another contribution is possible from $B^+ \rightarrow D^{*-}\pi^+\pi^+$, which can be reconstructed as $B^+ \rightarrow D^-K^+\pi^+$ if a pion is also mis-identified as a kaon in the same event. The reconstructed $D^-K^+\pi^+$ mass distributions for simulated $B^+ \rightarrow D^{*-}K^+\pi^+$ and $B^+ \rightarrow D^{*-}\pi^+\pi^+$ events are shown in Fig. 4.12.

Other potential backgrounds include $B_{(s)}^0 \rightarrow D_{(s)}^-K^+\pi^+\pi^-$ and $B_{(s)}^0 \rightarrow D_{(s)}^-\pi^+\pi^+\pi^-$. Studies using simulated samples determined the reconstructed $D^-K^+\pi^+$ mass distributions for these modes to be very similar to that of $B^+ \rightarrow D^{*-}K^+\pi^+$.

4.4 Efficiency

The probability of reconstructing and selecting events is not uniform across the phase space of a decay. It is important to understand the variation of efficiency as a function of DP (or SDP¹⁹) position. The total efficiency is calculated from several contributions:

$$\epsilon^{\text{tot}} = \epsilon^{\text{geom}} \times \epsilon^{\text{sel|geom}} \times \epsilon^{\text{PID|sel&geom}} , \quad (4.1)$$

where ϵ^{geom} is the probability that all final state tracks are within the detector acceptance; $\epsilon^{\text{sel|geom}}$ is the probability that a decay survives the selection criteria (including the stripping line and trigger requirements, but excluding PID) and $\epsilon^{\text{PID|sel&geom}}$ is the probability that a decay passes the PID requirements. Additional correction factors are applied to account for known discrepancies between data and simulation, related to the tracking and L0 hadron trigger.

The DP variation of each efficiency source is studied separately using simulated decays. For all contributions except ϵ^{geom} , the efficiency distributions are calculated separately

¹⁹The SDP parameters m' and θ' are defined in Sec. 2.4.3.1.

for events triggered as L0 hadron TOS and candidates passing, at L0, only the global TIS trigger (referred to as ‘!TOS’).

4.4.1 Geometrical efficiency

To determine the geometrical efficiency, ϵ^{geom} , simulated $B \rightarrow Dhh'$ events are generated with the B meson within the LHCb acceptance. The fraction of these simulated events with all five final state tracks in the LHCb acceptance is calculated as a function of SDP position to give ϵ^{geom} . The efficiency distributions obtained for $B^+ \rightarrow D^- K^+ \pi^+$ and $B^+ \rightarrow D^- \pi^+ \pi^+$ are shown in Fig. 4.13.

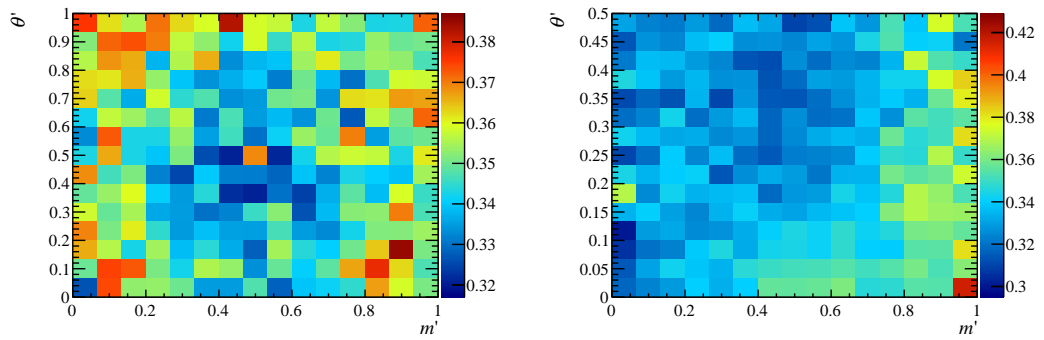


Figure 4.13: Geometrical efficiency, ϵ^{geom} , across the SDP for (left) $B^+ \rightarrow D^- K^+ \pi^+$ and (right) $B^+ \rightarrow D^- \pi^+ \pi^+$ decays.

4.4.2 Selection efficiency

For the selection efficiency, $\epsilon^{\text{sel|geom}}$, events are simulated with all final state tracks within the LHCb detector acceptance. The efficiency in each bin of the SDP is calculated as the fraction of these simulated events that are fully reconstructed and not rejected by the selection requirements. The selection efficiencies obtained for $B^+ \rightarrow D^- K^+ \pi^+$ and $B^+ \rightarrow D^- \pi^+ \pi^+$ are shown in Fig. 4.14.

4.4.2.1 Tracking and L0 hadron trigger corrections

Tracking in simulated events is known to differ slightly from that measured in data, so corrections are applied to the selection efficiency for each track in the final state. First, simulated events are reweighted to match the data distributions of track p , η and the number of tracks in the event. This weighted data sample and the correction factors (known as a function of track p and η) are then used to create an efficiency correction histogram for each final state track. These five histograms multiplied together give the total tracking correction to be applied to the selection efficiency.

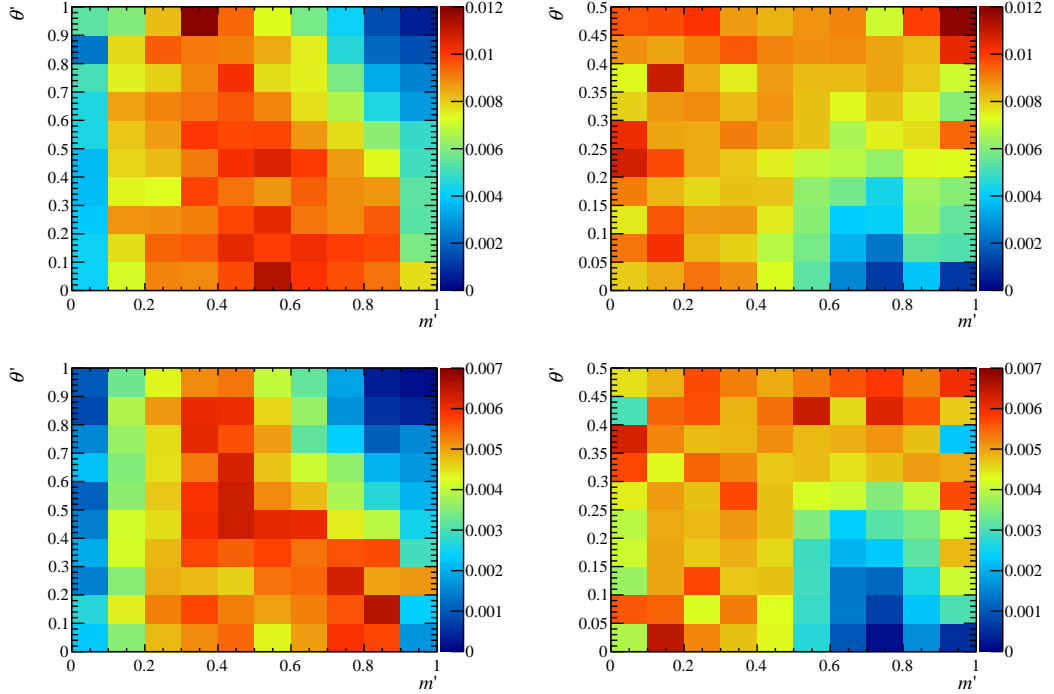


Figure 4.14: Selection efficiency, $\epsilon^{\text{sel|geom}}$, across the SDP for (left) $B^+ \rightarrow D^- K^+ \pi^+$ and (right) $B^+ \rightarrow D^- \pi^+ \pi^+$ decays, determined separately for candidates triggered as (top) L0 hadron TOS and (bottom) L0 global TIS and L0 hadron !TOS.

Further corrections are applied to all candidates to account for the differences between L0 hadron trigger response for real data and simulated events. The probability of the L0 trigger firing (or not) on an event is obtained, for each species of charged particle, from calibration data samples by considering magnet polarity, track E_T and the HCAL region that the track passes through. The equivalent probability for simulated events is taken as the fraction of TIS simulated events triggered (or not) as L0 hadron TOS decays.²⁰ The selection efficiency is corrected by the ratio of data/simulation probabilities in each SDP bin. A small amendment is made to this correction factor in the case of tracks producing overlapping clusters in the calorimeter.

4.4.3 PID efficiency

The PID efficiency, $\epsilon^{\text{PID|sel&geom}}$, cannot be determined directly from simulated samples since PID variables are known to be inaccurately simulated. Instead, calibration data samples from the PIDCALIB package (introduced in Sec. 3.7) are used to model the effect of PID requirements on simulated events. The probability of a particle surviving a specific PID requirement is calculated using the calibration data samples and by considering the track p , p_T and the total number of tracks in the event. The probabilities determined

²⁰A requirement placed on HLT trigger response in the stripping line causes simulated samples to be biased towards TOS events. The trigger correction factor is calculated using simulated decays triggered as TIS to remove any L0 hadron trigger bias.

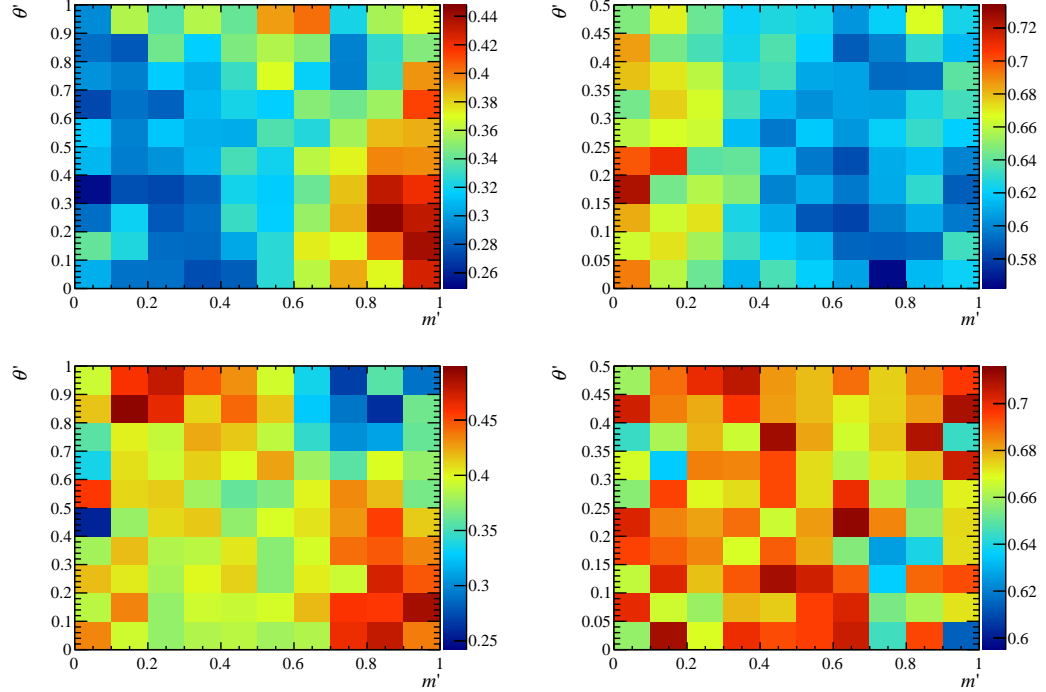


Figure 4.15: PID efficiency, $\epsilon^{\text{PID}|\text{sel\&geom}}$, across the SDP for (left) $B^+ \rightarrow D^- K^+ \pi^+$ and (right) $B^+ \rightarrow D^- \pi^+ \pi^+$ decays, determined separately for candidates triggered as (top) L0 hadron TOS and (bottom) L0 global TIS and L0 hadron !TOS.

for each final state track are multiplied to obtain the probability for the event. The value of $\epsilon^{\text{PID}|\text{sel\&geom}}$ in each SDP bin is the average probability for the events in that bin. The PID efficiencies obtained for $B^+ \rightarrow D^- K^+ \pi^+$ and $B^+ \rightarrow D^- \pi^+ \pi^+$ decays are shown in Fig. 4.15.

4.4.4 Spline interpolation

Limited statistics of the simulated samples introduce artificial fluctuations in the calculated efficiency distributions. To create smooth efficiency profiles a two-dimensional cubic spline is fitted to the histogram for each contribution. The values of the first and second derivatives of the efficiency ($\frac{d\epsilon}{dm'}$, $\frac{d\epsilon}{d\theta'}$ and $\frac{d^2\epsilon}{dm'd\theta'}$) and the absolute efficiency (ϵ) are fixed at the centre of each bin for the purposes of the fit. The fitted spline functions are then used to generate high-resolution efficiency histograms.

4.4.5 Total efficiency

Using Eq. 4.1, the total efficiency is given by multiplying the high-resolution histograms for all contributions. The final efficiency distributions for $B^+ \rightarrow D^- K^+ \pi^+$ and $B^+ \rightarrow D^- \pi^+ \pi^+$ decays are shown in Figs. 4.16 and 4.17, respectively.

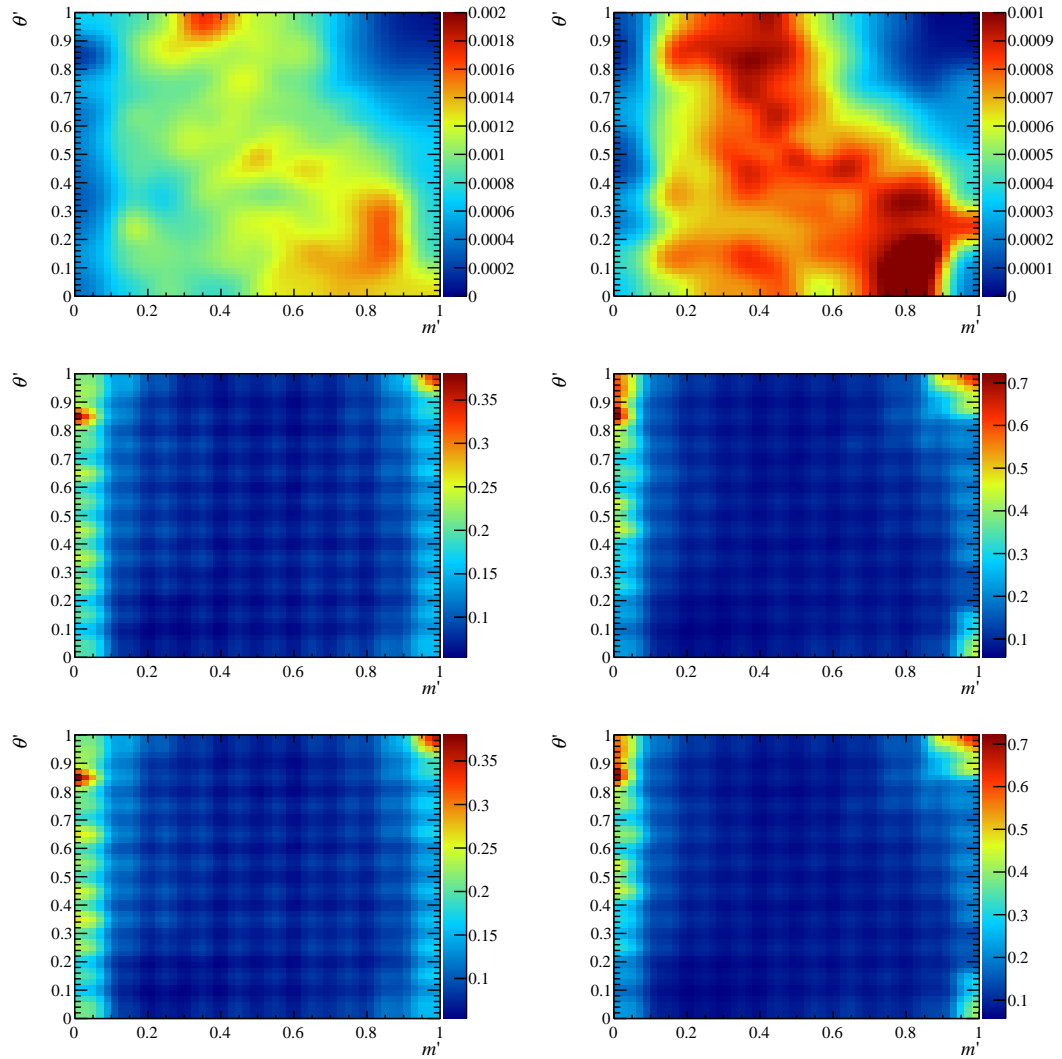


Figure 4.16: (Top) efficiency variation across the SDP for $B^+ \rightarrow D^- K^+ \pi^+$ decays, and the (middle) upper and (bottom) lower relative uncertainties, determined separately for candidates triggered as (left) L0 hadron TOS and (right) L0 global TIS and L0 hadron !TOS.

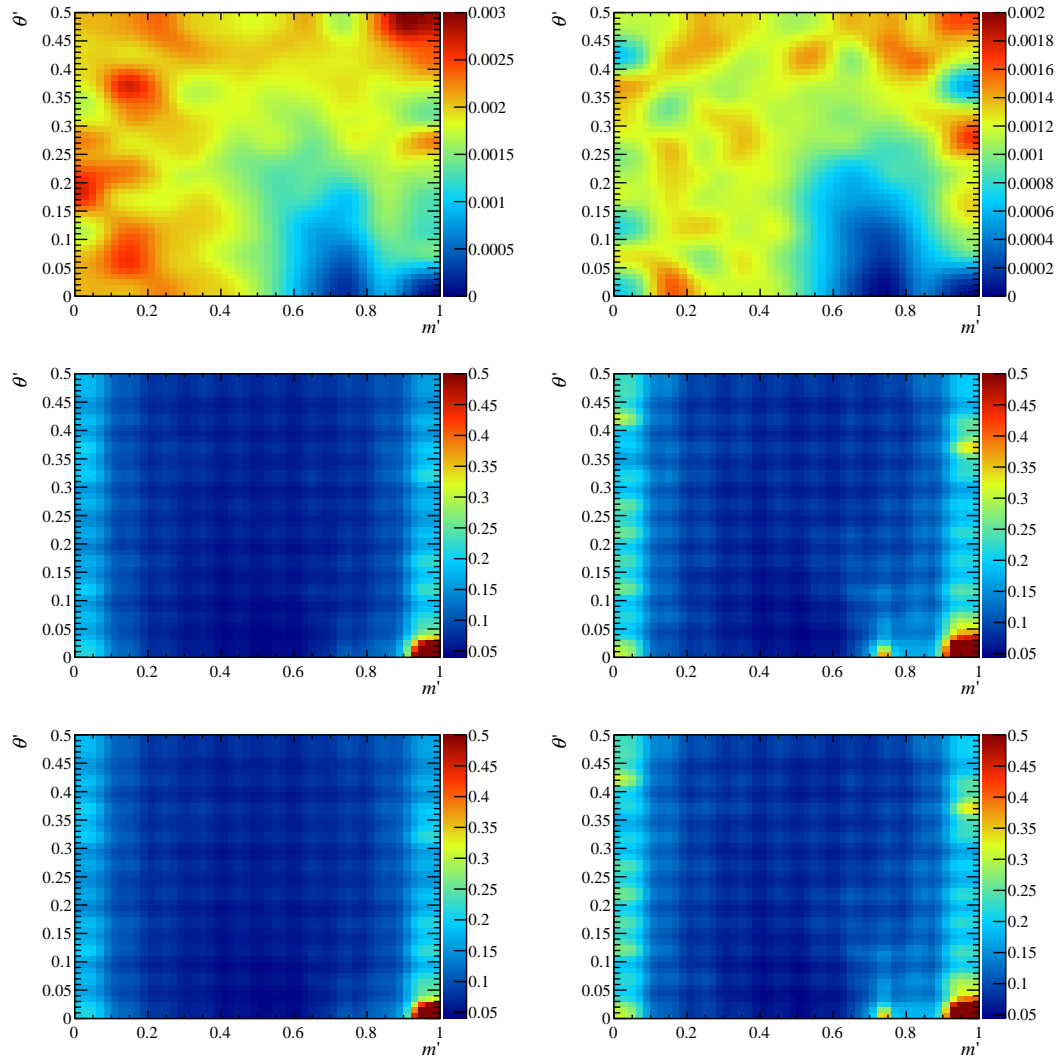


Figure 4.17: (Top) efficiency variation across the SDP for $B^+ \rightarrow D^- \pi^+ \pi^+$ decays, and the (middle) upper and (bottom) lower relative uncertainties, determined separately for candidates triggered as (left) L0 hadron TOS and (right) L0 global TIS and L0 hadron !TOS.

Chapter 5

Branching fraction measurement of the $B^+ \rightarrow D^- K^+ \pi^+$ decay

This chapter describes the first observation and branching fraction measurement of the $B^+ \rightarrow D^- K^+ \pi^+$ decay mode [1]. The $B^+ \rightarrow D^- \pi^+ \pi^+$ decay is used as a normalisation channel. Details of the data selection, background categorisation and efficiency calculations are given in Chap. 4.

5.1 Motivation

Decay diagrams for the $B^+ \rightarrow D^- \pi^+ \pi^+$ and $B^+ \rightarrow D^- K^+ \pi^+$ decay modes are shown in Fig. 5.1. The branching fraction of the $B^+ \rightarrow D^- \pi^+ \pi^+$ decay is large, with a current value of [102]

$$\mathcal{B}(B^+ \rightarrow D^- \pi^+ \pi^+) = (1.07 \pm 0.05) \times 10^{-3}. \quad (5.1)$$

Accounting for Cabibbo suppression due to the ratio of $|V_{us}/V_{ud}|^2$, the branching fraction of the $B^+ \rightarrow D^- K^+ \pi^+$ decay can be expected to be approximately 8 % of this value.

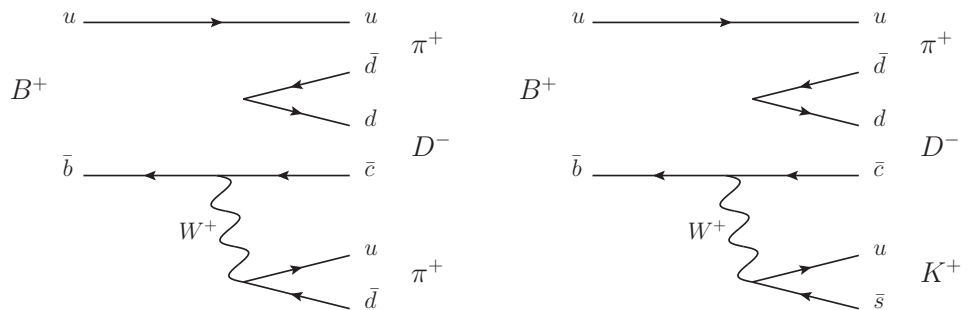


Figure 5.1: Decay diagrams for the (left) $B^+ \rightarrow D^- \pi^+ \pi^+$ and (right) $B^+ \rightarrow D^- K^+ \pi^+$ decay modes.

After all of the selection requirements described in Chap. 4, there remain 74 666 (3 777) $D^- \pi^+ \pi^+$ ($D^- K^+ \pi^+$) candidate decays. The invariant mass distributions for B candidates in both decay modes are shown in Fig. 5.2.

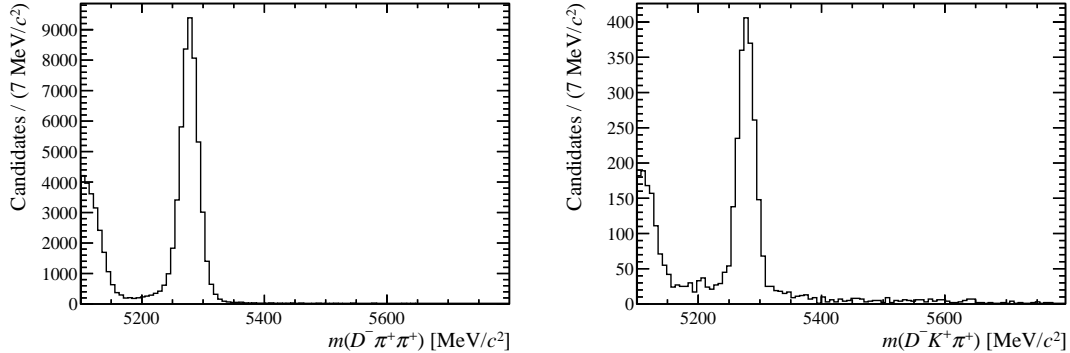


Figure 5.2: B invariant mass distributions for (left) $B^+ \rightarrow D^- \pi^+ \pi^+$ and (right) $B^+ \rightarrow D^- K^+ \pi^+$ candidates surviving the selection requirements described in Chap. 4.

5.2 Fits to B^+ invariant mass distributions

The yields of $B^+ \rightarrow D^- \pi^+ \pi^+$ and $B^+ \rightarrow D^- K^+ \pi^+$ signal decays in the datasets are obtained from unbinned extended maximum likelihood fits performed to candidates in the range $5100 \leq m_B \leq 5800 \text{ MeV}/c^2$.²¹ Both datasets are divided according to the L0 hadron trigger decision, separating events triggered as L0 hadron TOS and candidates passing only the L0 global TIS trigger (referred to as ‘!TOS’). For each decay mode a simultaneous fit is performed to the TOS and !TOS sub-samples.

The following components are included in the fit to $B^+ \rightarrow D^- \pi^+ \pi^+$ candidates:

- $B^+ \rightarrow D^- \pi^+ \pi^+$ signal;
- combinatorial background;
- peaking background from $B^+ \rightarrow D^{(*)-} K^+ \pi^+$ with $K \rightarrow \pi$ mis-identification;
- partially reconstructed background (shape from $B^+ \rightarrow D^{*-} \pi^+ \pi^+$ simulated data samples).

The PDFs in the signal mode fit model are:

- $B^+ \rightarrow D^- K^+ \pi^+$ signal;

²¹Note that no systematic uncertainty is introduced from this choice of B candidate mass range; the distribution of combinatorial background events is smoothly varying in the high mass region and the contributions at low mass are well understood.

- combinatorial background;
- peaking background from $B^+ \rightarrow D^{(*)-} \pi^+ \pi^+$ with $\pi \rightarrow K$ mis-identification;
- peaking background from $B^+ \rightarrow D_s^- K^+ \pi^+$ with $D_s^- \rightarrow K^+ K^- \pi^-$ mis-identification;
- partially reconstructed background (shape from $B^+ \rightarrow D^{*-} K^+ \pi^+$ simulated data samples).

The same fit model is used for TOS and !TOS sub-samples. The signal and background yields in both sub-samples are allowed to vary freely and independently. All remaining fit parameters are shared between the two categories in the simultaneous fit, apart from the slope of the combinatorial background component (as described in Sec. 5.2.1.2).

5.2.1 Fit components

5.2.1.1 Signal

The signal component is parametrised as the sum of two Crystal Ball [103] (CB) functions with a common mean and tails on opposite sides. The form of the CB function, with the tail extending towards low values of x , is

$$\left. \frac{\left(\frac{n}{|\alpha|} \right)^n \exp^{-\frac{1}{2}\alpha^2}}{\left(\frac{n}{|\alpha|} - |\alpha| - x \right)^n} \right|_{x < -|\alpha|}, \left. \exp \left(-\frac{1}{2} \left(\frac{x - \mu}{\sigma} \right)^2 \right) \right|_{x > -|\alpha|}, \quad (5.2)$$

where x is the fitted variable, σ and μ are the width and mean, and α and n are the tail parameters. If $\text{CB}(m; \mu, \sigma, \alpha, n)$ is a normalised CB function in terms of candidate mass, m , the PDF for a double CB function is then given by

$$\mathcal{P}_{\text{sig}}(m) = (f_{\text{CB}}) \text{CB}(m; \mu, \sigma_1, \alpha_1, n_1) + (1 - f_{\text{CB}}) \text{CB}(m; \mu, \sigma_2, \alpha_2, n_2), \quad (5.3)$$

where f_{CB} parametrises the relative normalisation of the two CB functions which is determined from data, as is the ratio of widths, $R_{\text{CB}} = \sigma_2/\sigma_1$.

The B candidate invariant mass distributions from simulated samples of $B^+ \rightarrow D^- \pi^+ \pi^+$ and $B^+ \rightarrow D^- K^+ \pi^+$ decays are fitted to determine the values of the double CB tail parameters for each mode. The results of these fits are shown in Fig. 5.3 and Tab. 5.1.

In the fits to $B^+ \rightarrow D^- \pi^+ \pi^+$ and $B^+ \rightarrow D^- K^+ \pi^+$ data samples the CB tail parameters (α_1 , α_2 , n_1 and n_2) are fixed to the values determined from simulation and constraints are applied to f_{CB} and R_{CB} by including a Gaussian penalty term in the likelihood function. The total signal yield is a free parameter in the fit, as are the CB mean, μ ,

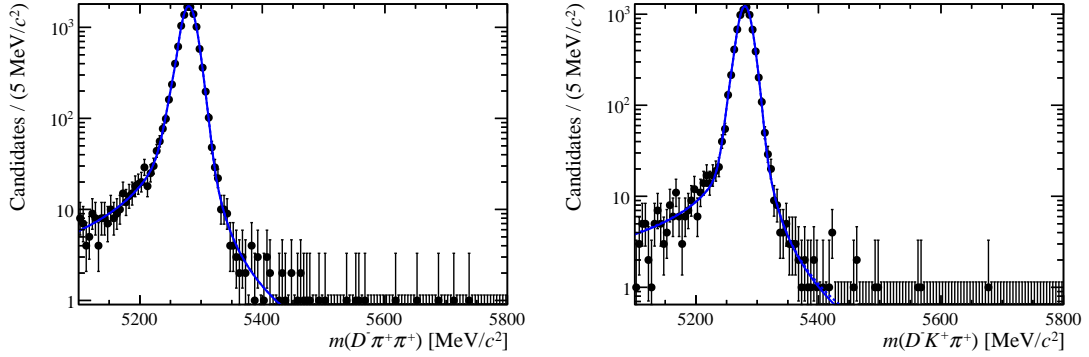


Figure 5.3: Fit to B candidate invariant mass distribution for simulated samples of (left) $B^+ \rightarrow D^- \pi^+ \pi^+$ and (right) $B^+ \rightarrow D^- K^+ \pi^+$ events.

Table 5.1: Parameters of the signal double Crystal Ball shape (Eq. 5.3) obtained from the fits to samples of simulated $D^- \pi^+ \pi^+$ and $D^- K^+ \pi^+$ events.

Parameter	$D^- \pi^+ \pi^+$	$D^- K^+ \pi^+$
μ (MeV/c ²)	5279.93 ± 0.16	5279.97 ± 0.15
σ_1 (MeV/c ²)	17.4 ± 1.1	16.1 ± 0.9
$R_{\text{CB}} = \sigma_2/\sigma_1$	0.62 ± 0.03	0.64 ± 0.02
α_1	-2.21 ± 0.15	-2.09 ± 0.31
α_2	1.73 ± 0.11	2.22 ± 0.10
n_1	1.75 ± 0.44	1.78 ± 0.82
n_2	1.26 ± 0.13	0.77 ± 0.12
f_{CB}	0.37 ± 0.07	0.36 ± 0.09

and one width, σ_1 . The fitted mass of the B^+ meson, μ , differs from the true mass due to reconstruction effects.

5.2.1.2 Combinatorial background

In both mass fits the combinatorial background component is modelled by a first-order polynomial function, where both the background slope and the yield are floated parameters. The combinatorial background slope is allowed to vary between the TOS and !TOS sub-samples.

5.2.1.3 Peaking background

The peaking backgrounds included in the fit to $B^+ \rightarrow D^- K^+ \pi^+$ data are $B^+ \rightarrow D_s^- K^+ \pi^+$, $B^+ \rightarrow D^- \pi^+ \pi^+$ and $B^+ \rightarrow D^{*-} \pi^+ \pi^+$. Contributions from $B^+ \rightarrow D^- \pi^+ \pi^+$ and $B^+ \rightarrow D^{*-} \pi^+ \pi^+$ are combined into a single PDF with the relative fraction of D/D^* modes fixed according to the ratio of their measured branching fractions [3]. The peaking backgrounds contributing to the $B^+ \rightarrow D^- \pi^+ \pi^+$ data sample, $B^+ \rightarrow D^- K^+ \pi^+$ and $B^+ \rightarrow D^{*-} K^+ \pi^+$, are combined in the same manner to create a single PDF.

Each peaking background component is modelled by a smoothed non-parametric PDF obtained from weighted simulated samples. Instead of applying PID requirements directly to the simulated samples, each event is weighted by the probability of it surviving the PID selection, as calculated using calibration data samples from `PiDCALIB`. Rather than including any contributing resonant structures, simulated data samples are generated uniformly in phase space. Simulated events must therefore be reweighted to match the DP distribution in data (or from previous studies) where possible.²²

The PDFs used to describe $B^+ \rightarrow D^{(*)-} \pi^+ \pi^+$ and $B^+ \rightarrow D_s^- K^+ \pi^+$ peaking backgrounds are shown in Fig. 5.4, superimposed on the distributions of simulated events. The PDF for the $B^+ \rightarrow D^{(*)-} K^+ \pi^+$ peaking background, used in the fit to $B^+ \rightarrow D^- \pi^+ \pi^+$, is shown in Fig. 5.5. All peaking background yields are allowed to float in the fits to data.

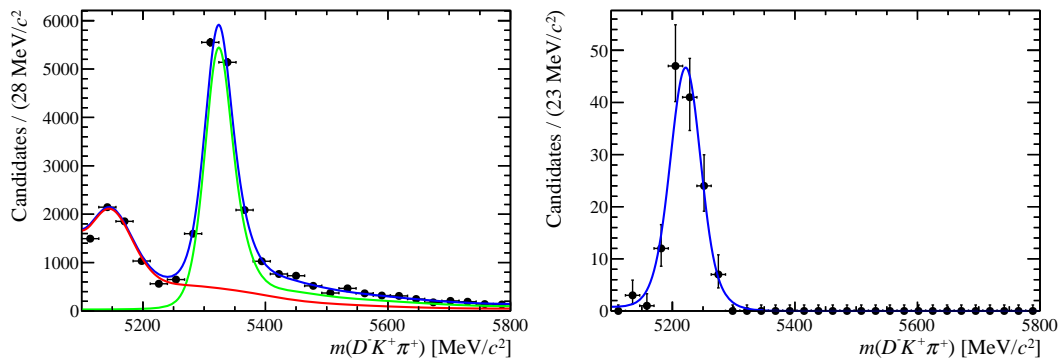


Figure 5.4: Reconstructed B^+ candidate mass distributions of peaking backgrounds to $B^+ \rightarrow D^- K^+ \pi^+$ from simulated samples of (left) $B^+ \rightarrow D^{(*)-} \pi^+ \pi^+$ and (right) $B^+ \rightarrow D_s^- K^+ \pi^+$ decays. For $B^+ \rightarrow D^{(*)-} \pi^+ \pi^+$, the (red) $D^{*-} \pi^+ \pi^+$ and (green) $D^- \pi^+ \pi^+$ contributions are combined with a fixed factor according to the measured branching fractions of the two modes [3].

5.2.1.4 Partially reconstructed background

The main source of partially reconstructed background for the $D^- \pi^+ \pi^+$ mode is $B^+ \rightarrow D^{*-} \pi^+ \pi^+$. The equivalent contribution for the $D^- K^+ \pi^+$ mode is the $B^+ \rightarrow D^{*-} K^+ \pi^+$ decay. Simulated events are used to create smoothed non-parametric PDFs, as shown in Fig. 5.6.

Although the shape of the partially reconstructed component is fixed, an additional floated parameter is included to allow the whole PDF to shift up or down in mass. This parameter corrects for any inaccuracies in the simulated polarisation of the D^{*-} meson which could alter the B candidate invariant mass for these background events. The partially reconstructed background yields are also free parameters in the fits to data.

²²No such weighting can be applied to $B^+ \rightarrow D_s^- K^+ \pi^+$ since the true DP distribution of this decay mode is unknown, except that it peaks at low $m(D_s^- K^+)$ [104, 105].

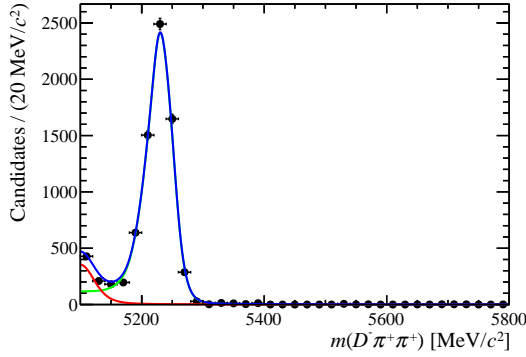


Figure 5.5: Reconstructed B^+ candidate mass distributions of peaking backgrounds to $B^+ \rightarrow D^- \pi^+ \pi^+$ from simulated $B^+ \rightarrow D^{(*)-} K^+ \pi^+$ decays. The ratio of $B^+ \rightarrow D^{*-} K^+ \pi^+$ and $B^+ \rightarrow D^- K^+ \pi^+$ branching fractions is unknown, so the (red) $D^{*-} K^+ \pi^+$ and (green) $D^- K^+ \pi^+$ contributions are combined with a fixed factor according to the measured branching fractions of the $B^+ \rightarrow D^{*-} \pi^+ \pi^+$ and $B^+ \rightarrow D^- \pi^+ \pi^+$ decays [3], following the assumption that the relative fraction of D/D^* modes will be the same for $D^- K^+ \pi^+$ and $D^- \pi^+ \pi^+$.

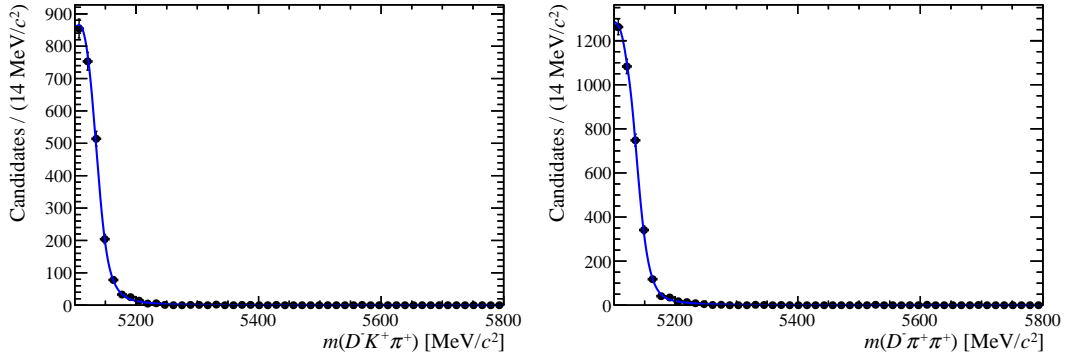


Figure 5.6: Reconstructed B^+ candidate mass distributions of partially reconstructed backgrounds to (left) $B^+ \rightarrow D^- \pi^+ \pi^+$ and (right) $B^+ \rightarrow D^- K^+ \pi^+$, from simulated $B^+ \rightarrow D^{*-} \pi^+ \pi^+$ and $B^+ \rightarrow D^{*-} K^+ \pi^+$ samples, respectively.

5.2.2 Fit validation

The stability of the fit results is tested using simulated data samples. Poisson fluctuations are applied to each component yield from the total fit PDF to generate 1000 unique mass distributions for each decay mode. Independent fits are then performed to each dataset, using the total fit PDF, to obtain a distribution of fitted values for each parameter. The pull distributions²³ of the signal yield parameters are found to be consistent with a Gaussian function of width one and mean zero, indicating that the statistical uncertainties reported by the fit are accurate and that any systematic bias is small.

²³The pull of a fit parameter is the difference between the fitted and generated values, divided by their combined uncertainties.

The pulls for most of the other fit parameters also agree well with the expected Gaussian distribution – the only exception is the pull distribution for the combinatorial background slope parameter. This occurs because the combinatorial background PDF will become negative if the slope parameter exceeds a certain value, and this is not allowed by the fit. From fits performed to simulated samples with 10 times the number of events, the pull distributions obtained for all floated parameters are found to agree with the expected Gaussian distribution. The small bias of the combinatorial background slope parameter is therefore attributed to the comparatively low statistics of the available dataset and is seen not to bias the extracted signal yield results.

5.2.3 Fit results

The results of the simultaneous fit to TOS and !TOS sub-samples of the $B^+ \rightarrow D^- \pi^+ \pi^+$ dataset are shown in Fig. 5.7 and the values of all free parameters are reported in Tab. 5.2.

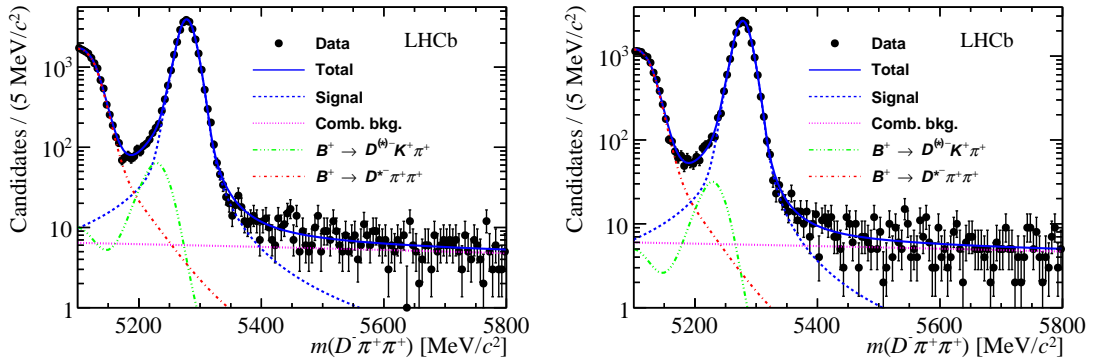


Figure 5.7: Projections of the simultaneous fit to $B^+ \rightarrow D^- \pi^+ \pi^+$ candidates in the L0 (left) TOS and (right) !TOS sub-samples. The data points are shown in black and the fit components are described in the legend.

Table 5.2: Values of the floated parameters obtained from the fit to $D^- \pi^+ \pi^+$ data.

Parameter	TOS	!TOS
$N(B^+ \rightarrow D^{(*)-} K^+ \pi^+)$	807 ± 123	401 ± 84
$N(\text{part. reco. bkg.})$	12120 ± 115	8551 ± 96
$N(\text{comb. bkg.})$	784 ± 54	746 ± 47
$N(\text{signal})$	29190 ± 204	19416 ± 159
Comb. bkg. slope	$(-0.7 \pm 3.4) \times 10^{-4}$	$(-1.0 \pm 3.4) \times 10^{-4}$
f_{CB}		0.548 ± 0.032
R_{CB}		0.655 ± 0.022
μ (MeV/c ²)		5278.10 ± 0.03
σ_1 (MeV/c ²)		17.28 ± 0.13
Part. reco. bkg. shift (MeV/c ²)		-5.3 ± 0.1

The fit to $B^+ \rightarrow D^- K^+ \pi^+$ candidates is shown in Fig. 5.8 and the fitted values of all floated parameters are shown in Tab. 5.3. The total signal yield of 2003 ± 49 $B^+ \rightarrow D^- K^+ \pi^+$ events represents the first observation of this decay mode.

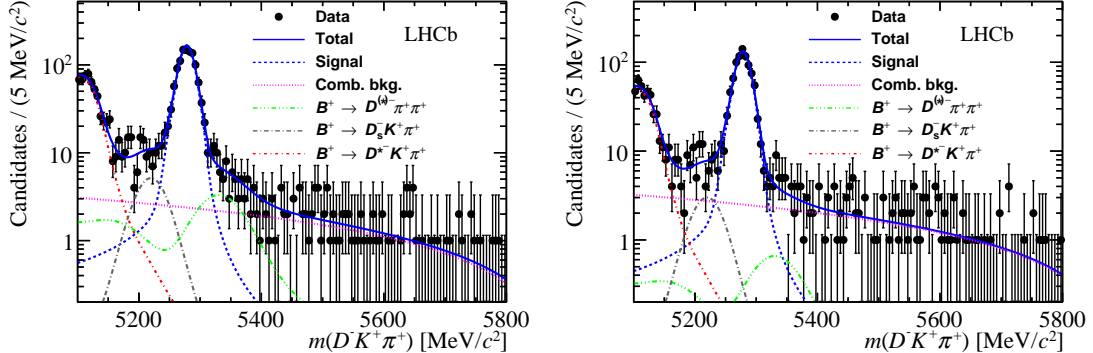


Figure 5.8: Projections of the simultaneous fit to $B^+ \rightarrow D^- K^+ \pi^+$ candidates in the L0 (left) TOS and (right) !TOS sub-samples. The data points are shown in black and the fit components are described in the legend.

Table 5.3: Values of the floated parameters obtained from the fit to $D^- K^+ \pi^+$ data.

Parameter	TOS	!TOS
$N(B^+ \rightarrow D^{(*)-} \pi^+ \pi^+)$	114 ± 34	23 ± 27
$N(B^+ \rightarrow D_s^- K^+ \pi^+)$	69 ± 17	40 ± 15
$N(\text{part. reco. bkg.})$	518 ± 26	361 ± 21
$N(\text{comb. bkg.})$	238 ± 38	253 ± 36
$N(\text{signal})$	1112 ± 37	891 ± 32
Comb. bkg. slope	$(-1.7 \pm 0.3) \times 10^{-4}$	$(-1.7 \pm 0.2) \times 10^{-4}$
f_{CB}		0.604 ± 0.040
R_{CB}		0.654 ± 0.013
μ (MeV/c ²)		5278.27 ± 0.35
σ_1 (MeV/c ²)		15.55 ± 0.47
Part. reco. bkg. shift (MeV/c ²)		-4.5 ± 1.3

5.3 Systematic uncertainties

A summary of the sources of systematic uncertainty affecting the measured ratio of $B^+ \rightarrow D^- K^+ \pi^+ / B^+ \rightarrow D^- \pi^+ \pi^+$ signal yields and the efficiency ratio is given in Tab. 5.4. More detail is given below about each source of uncertainty and the methods used to calculate the relative contributions.

In general, any systematic effect from the selection requirements cancel in the ratio of $B^+ \rightarrow D^- K^+ \pi^+$ and $D^- \pi^+ \pi^+$ yields. An exception is the veto applied to remove $\Lambda_c^- \rightarrow \bar{p} K^+ \pi^-$ events. The invariant mass fits are repeated with the default vetoed mass range (2280–2300 MeV/c²) both widened (to 2270–2310 MeV/c²) and removed. The

Table 5.4: Summary of systematic uncertainties on the measured ratio of $B^+ \rightarrow D^- K^+ \pi^+$ / $B^+ \rightarrow D^- \pi^+ \pi^+$ branching fractions. All values are shown in %. The total is calculated as the sum in quadrature of all contributions.

Source	Uncertainty
A_c^- veto	0.2
Particle identification	2.1
Fit model	2.0
Efficiency modelling	0.8
Total	3.0

observed changes in the fitted signal yields suggest that this veto contributes 0.2 % to the systematic uncertainty on the measured branching fraction ratio.

Any systematic effect from PID requirements applied to the D daughters will cancel in the measured ratio of branching fractions, since the same criteria are used for both decay modes. However, the efficiency of the PID requirements applied to the bachelor particles is a source of uncertainty. Three separate sources of uncertainty are considered to evaluate the remaining uncertainty due to PID: the intrinsic uncertainty of calibration data samples from PIDCALIB is assumed to contribute 1.00 % – 0.5 % for each track which differs in the two final states [106]; small differences between the track kinematics for events in simulated samples, used to reweight the PIDCALIB data samples, and those in data are found to contribute a relative systematic uncertainty of 1.7 %; an uncertainty of 0.7 % is assigned to account for the choice of binning used for kinematic variables in the reweighting procedure. Combining these uncertainties in quadrature gives an overall PID systematic uncertainty of 2.1 %.

The $B^+ \rightarrow D^- \pi^+ \pi^+$ and $B^+ \rightarrow D^- K^+ \pi^+$ fit models described in Sec. 5.2.1 are varied by using alternative PDFs to describe the invariant mass distribution of each component. Parameters fixed in the signal mass PDF are varied within their uncertainties (as determined from fits to simulated data) and the double CB signal PDF is replaced with the sum of two bifurcated Gaussian functions. The amount of smoothing applied to all non-parametric PDFs is varied, and the nominal PDF describing combinatorial background is replaced by an exponential or second-order polynomial function. Where SDP reweighting is applied to simulated samples, the binning of the reweighting histogram is varied. Considering the effects of these model variations on the fitted signal yields and combining the uncertainties in quadrature gives a relative systematic uncertainty of 2.0 % on the measured ratio of branching fractions.

An additional source of potential uncertainty is related to limitations in the knowledge of efficiency variation across the Dalitz plots. For each decay mode, 100 new and unique efficiency distributions are generated by varying the value of every bin within uncertainties. The ratio of efficiency-corrected yields is re-evaluated 100 times using the

alternative efficiency histograms. A Gaussian function is fitted to the distribution of ratio values obtained, the width of which is used to assign a relative systematic uncertainty of 0.8 % on the ratio of branching fractions.

Based on the fit validation studies performed using simulated data, any systematic bias due to the fit model is considered to be negligible. The treatment of multiple candidates is also found to have no significant effect on the final result. All other systematic uncertainties are combined in quadrature to obtain a total relative systematic of 3.0 % on the measured ratio of branching fractions.

5.3.1 Cross checks

The stability of the branching fraction result is checked by performing the $D^- \pi^+ \pi^+$ and $D^- K^+ \pi^+$ mass fits with alternative datasets. The requirements imposed on the NN_B output and PID variables are both tightened and loosened. The data sample is also divided by magnet polarity, year of data taking and L0 hadron trigger decision. The results from all of these cross checks are statistically consistent.

5.4 Results

The branching fraction ratio is calculated using corrected signal yields, $N^{\text{corr}}(Dhh')$:

$$\frac{\mathcal{B}(B^+ \rightarrow D^- K^+ \pi^+)}{\mathcal{B}(B^+ \rightarrow D^- \pi^+ \pi^+)} = \frac{N^{\text{corr}}(D^- K^+ \pi^+)}{N^{\text{corr}}(D^- \pi^+ \pi^+)} , \quad (5.4)$$

where $N^{\text{corr}}(Dhh') = \sum_i (W_i / \epsilon_i^{\text{tot}})$ – the index i runs over all candidates in the mass fit; for each candidate the signal `sWeight`, W_i , is determined from the fit and ϵ_i^{tot} is the event efficiency as a function of Dalitz plot position. The corrected number of candidates and the raw yields are shown for both $B^+ \rightarrow D^- \pi^+ \pi^+$ and $B^+ \rightarrow D^- K^+ \pi^+$ in Tab. 5.5.

Table 5.5: Yields of $B^+ \rightarrow D^- \pi^+ \pi^+$ and $B^+ \rightarrow D^- K^+ \pi^+$ decays obtained from the fits shown in Sec. 5.2.3, and the corrected yields calculated using `sWeights` and event-by-event efficiency corrections.

	TOS	!TOS	All events
$N(D^- \pi^+ \pi^+)$	29190 ± 204	19416 ± 159	48606 ± 259
$N^{\text{corr}}(D^- \pi^+ \pi^+)$	17731649 ± 128308	27397632 ± 230686	45129281 ± 264178
$N(D^- K^+ \pi^+)$	1112 ± 37	891 ± 32	2003 ± 49
$N^{\text{corr}}(D^- K^+ \pi^+)$	1317479 ± 44006	1933198 ± 70985	3250678 ± 83581

Substituting the values from Tab. 5.5 into Eq. 5.4 returns a branching fraction ratio of

$$\frac{\mathcal{B}(B^+ \rightarrow D^- K^+ \pi^+)}{\mathcal{B}(B^+ \rightarrow D^- \pi^+ \pi^+)} = 0.0720 \pm 0.0019 \pm 0.0021 , \quad (5.5)$$

where the first uncertainty is statistical and the second is systematic, from the sources described in Sec. 5.3. This is slightly below, but the same order of magnitude as, the naïve prediction of 8% made in Sec. 5.1.

The world average value of $\mathcal{B}(B^+ \rightarrow D^- \pi^+ \pi^+) = (1.07 \pm 0.05) \times 10^{-3}$ [102] assumes equal production of $B^+ B^-$ and $B^0 \bar{B}^0$ pairs in the decay of the $\Upsilon(4S)$ resonance. This branching fraction is corrected using $\Gamma(\Upsilon(4S) \rightarrow B^+ B^-)/\Gamma(\Upsilon(4S) \rightarrow B^0 \bar{B}^0) = 1.055 \pm 0.025$ [102] to obtain $\mathcal{B}(B^+ \rightarrow D^- \pi^+ \pi^+) = (1.014 \pm 0.054) \times 10^{-3}$. Multiplying Eq. 5.5 by this value gives

$$\mathcal{B}(B^+ \rightarrow D^- K^+ \pi^+) = (7.31 \pm 0.19 \pm 0.22 \pm 0.39) \times 10^{-5}. \quad (5.6)$$

where the first uncertainty is statistical, the second systematic and the third from the uncertainty on the corrected $\mathcal{B}(B^+ \rightarrow D^- \pi^+ \pi^+)$ world average.

Chapter 6

Dalitz plot analysis of $B^+ \rightarrow D^- K^+ \pi^+$ decays

Further to the branching fraction measurement presented in Chap. 5, this chapter details the amplitude analysis of the $B^+ \rightarrow D^- K^+ \pi^+$ decay mode [1] performed to study excited charmed mesons decaying to $D^- \pi^+$. The masses and widths of D^{**} states are presented for those cases where resonance parameters are determined from the fit to data. Product branching fractions of all contributing quasi-two-body decays are also reported.

6.1 Fit strategy

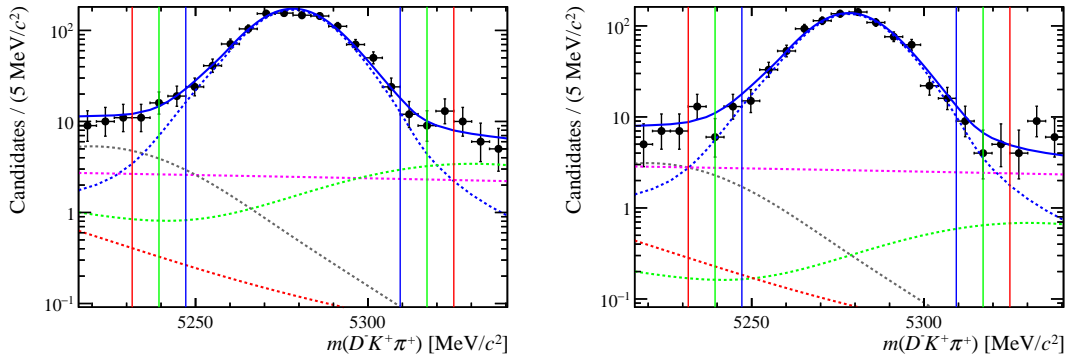


Figure 6.1: Zooms of the signal region of the fit to the B candidate invariant mass distribution of $DK\pi$ (from Fig. 5.8) showing the (blue) $\pm 2\sigma_1$, (green) $\pm 2.5\sigma_1$ and (red) $\pm 3\sigma_1$ regions, with (left) events triggered as L0 hadron TOS and (right) other events.

To increase the purity of the data sample from Chap. 5, a signal region is defined from which events are selected for the Dalitz plot fit; $B^+ \rightarrow D^- K^+ \pi^+$ candidates with $m(DK\pi)$ within $2.5\sigma_1$ of the fitted B candidate mass are retained, corresponding to the range $5239.4 < m(DK\pi) < 5317.1 \text{ MeV}/c^2$. A zoom of the fit to the $DK\pi$ invariant

mass distribution is shown in Fig. 6.1. The fitted values of signal and background yields within the signal region are shown in Tab. 6.1. The yields for two alternative regions, which are used to cross check the Dalitz plot fit results, are also reported. The Dalitz plot distributions of background events are studied with simulated samples, as detailed in Sec. 6.2. The efficiency variation over the $D^- K^+ \pi^+$ phase space must also be understood for the Dalitz plot fit. The high-resolution efficiency histograms shown in Fig. 4.16 are used as input in the fit, as described in Sec. 2.4.3.2.

An unbinned maximum likelihood fit is performed to the selected candidates using the LAURA++ package [99]. As for the fit to the B candidate invariant mass, a simultaneous fit is performed to candidates triggered as L0 hadron TOS and !TOS.²⁴ The same fit model is used for both sub-samples, and resonance parameters are shared between the two fit categories. The efficiency variation and distributions of background events across the Dalitz plot are considered separately for each L0 trigger category.

A study of the angular moments is performed to obtain information about the contributing amplitudes in $B^+ \rightarrow D^- K^+ \pi^+$ data. A preliminary fit model is developed based on the results of previous studies and this moments investigation, shown in Sec. 6.3. The approximate significance of a given component is evaluated as twice the change in the negative log likelihood, NLL, obtained with and without the amplitude. Contributions which are found to be insignificant are removed from the fit model.

Table 6.1: Signal and background yields obtained from the $B^+ \rightarrow D^- K^+ \pi^+$ mass fit, within $\pm 2\sigma_1$, $\pm 2.5\sigma_1$ and $\pm 3\sigma_1$ of the fitted B candidate mass.

Component	Yield (TOS)			Yield (!TOS)		
	$\pm 2\sigma_1$	$\pm 2.5\sigma_1$	$\pm 3\sigma_1$	$\pm 2\sigma_1$	$\pm 2.5\sigma_1$	$\pm 3\sigma_1$
$N(B^+ \rightarrow D^{(*)-} \pi^+ \pi^+)$	20	26	32	4	5	6
$N(B^+ \rightarrow D_s^- K^+ \pi^+)$	10	16	22	6	9	13
$N(\text{part. reco. bkg.})$	2	2	3	1	2	2
$N(\text{comb. bkg.})$	30	37	44	31	39	47
$N(\text{signal})$	1032	1060	1072	826	849	858

6.2 Background Dalitz plot distributions

As shown in Fig. 6.1 and Tab. 6.1, there are three non-negligible background contributions in the signal region: combinatorial background ($\sim 3.5\%$), $B^+ \rightarrow D_s^- K^+ \pi^+$ ($\sim 1.4\%$) and $B^+ \rightarrow D^{(*)-} \pi^+ \pi^+$ ($\sim 1.7\%$). The partially reconstructed background from $B^+ \rightarrow D^{*-} K^+ \pi^+$, which contributes $\sim 0.2\%$, is neglected.

The distribution of combinatorial background over the phase space of the $B^+ \rightarrow D^- K^+ \pi^+$ decay is obtained from data in the high B mass sideband, $5500 < m(DK\pi) <$

²⁴The simultaneous fit is implemented in LAURA++ using the JFIT method [107].

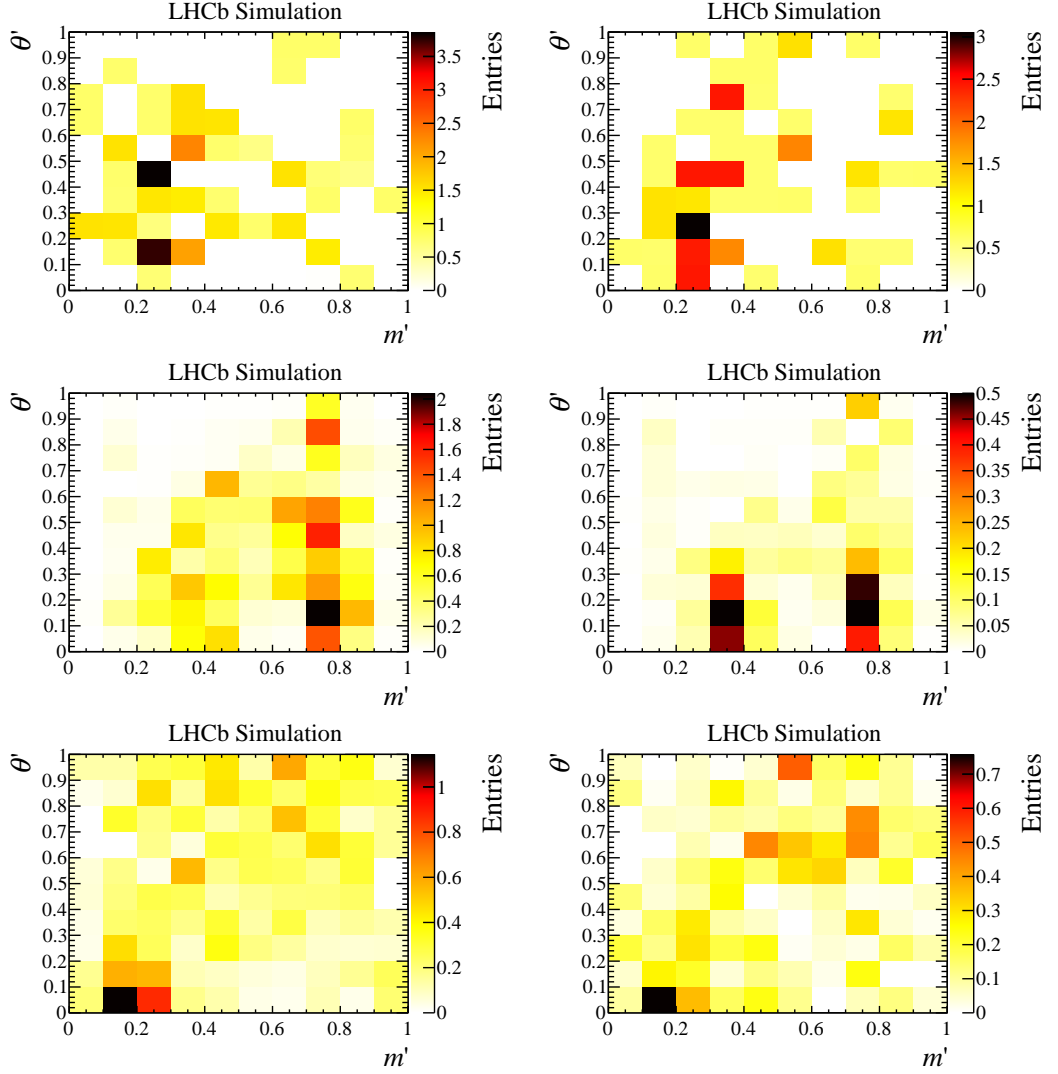


Figure 6.2: Square Dalitz plot distributions used in the Dalitz plot fit for (top) combinatorial background, (middle) $B^+ \rightarrow D^{(*)-} \pi^+ \pi^+$ decays and (bottom) $B^+ \rightarrow D_s^- K^+ \pi^+$ decays. Candidates from the TOS (!TOS) sub-samples are shown in the left (right) column. The SDP parameters m' and θ' are defined in Sec. 2.4.3.1.

5800 MeV/ c^2 . As shown in Fig. 5.8, combinatorial background is the main fit component in this region of the B candidate invariant mass distribution, but there is also a small contribution from $B^+ \rightarrow D^{(*)-} \pi^+ \pi^+$ decays. Using the same methods as described in Sec. 5.2.1.3, the phase space distribution of the peaking background in this region is obtained from weighted samples of simulated $B^+ \rightarrow D^{(*)-} \pi^+ \pi^+$ decays. The distribution of combinatorial background events over the SDP phase space is shown in Fig. 6.2 (top), created by subtracting the distribution of $B^+ \rightarrow D^{(*)-} \pi^+ \pi^+$ events from that of the high sideband data.

The SDP distributions of peaking backgrounds are obtained from simulated samples of $B^+ \rightarrow D^{(*)-} \pi^+ \pi^+$ and $B^+ \rightarrow D_s^- K^+ \pi^+$ decays. The procedures described in Sec. 5.2.1.3 are followed to weight the samples to match the PID response seen in

data. The $B^+ \rightarrow D^{(*)-} \pi^+ \pi^+$ samples are also reweighted to match the DP distribution in $B^+ \rightarrow D^- \pi^+ \pi^+$ data. All weighted simulated events falling within the DP fit signal region are used to obtain the background distributions shown in Fig. 6.2.

6.3 Partial wave analysis using angular moments

A study of the angular moments is performed for $B^+ \rightarrow D^- K^+ \pi^+$ data to investigate which amplitudes should be included in the Dalitz plot fit model. This method is particularly useful for a decay such as $B^+ \rightarrow D^- K^+ \pi^+$, where resonances are only expected to contribute to one pair of daughter particles, since the presence of reflections can make it more difficult to interpret the angular moments.

Moments are calculated from the Legendre polynomials, P_L , up to the order $L = 2J_{\max} = 6$, where J_{\max} is the maximum spin of the potentially observable resonances decaying to $D^- \pi^+$. Each data candidate is weighted according to its value of $P_L(\cos \theta(D^- \pi^+))$. Additionally, event-by-event efficiency corrections are applied and background contributions are subtracted. The average angular moment in each bin of $m(D\pi)$ is calculated as

$$N \langle P_L \rangle = \sum_j^N w_j P_L(\cos(\theta(D^- \pi^+))_j), \quad (6.1)$$

where w_j is the efficiency weight for event j , N is the number of events in a given bin and $P_L(\cos(\theta(D^- \pi^+))_j)$ is the value of the Legendre polynomial of order L for event j .

The moments of the data are shown in Fig. 6.3, for $J_{\max} = 3$. Overlaid for comparison are the moments calculated from an ensemble of pseudoexperiments generated from the default Dalitz plot fit model described in Sec. 6.4. No structure is visible in the distributions of $\langle P_5 \rangle$ and $\langle P_6 \rangle$ from data, which implies that there are no significant spin-3 contributions. Considering, therefore, only contributions up to spin-2, the Legendre moments are related to S-, P- and D-wave amplitudes (denoted $h_J e^{i\delta_J}$ with $J = 0, 1, 2$, respectively) by:

$$\begin{aligned} \langle P_0 \rangle &\propto |h_0|^2 + |h_1|^2 + |h_2|^2, \\ \langle P_1 \rangle &\propto \frac{2}{\sqrt{3}} |h_0| |h_1| \cos(\delta_0 - \delta_1) + \frac{4}{\sqrt{15}} |h_1| |h_2| \cos(\delta_1 - \delta_2), \\ \langle P_2 \rangle &\propto \frac{2}{\sqrt{5}} |h_0| |h_2| \cos(\delta_0 - \delta_2) + \frac{2}{5} |h_1|^2 + \frac{2}{7} |h_2|^2, \\ \langle P_3 \rangle &\propto \frac{6}{7} \sqrt{\frac{3}{5}} |h_1| |h_2| \cos(\delta_1 - \delta_2), \\ \langle P_4 \rangle &\propto \frac{2}{7} |h_2|^2. \end{aligned} \quad (6.2)$$

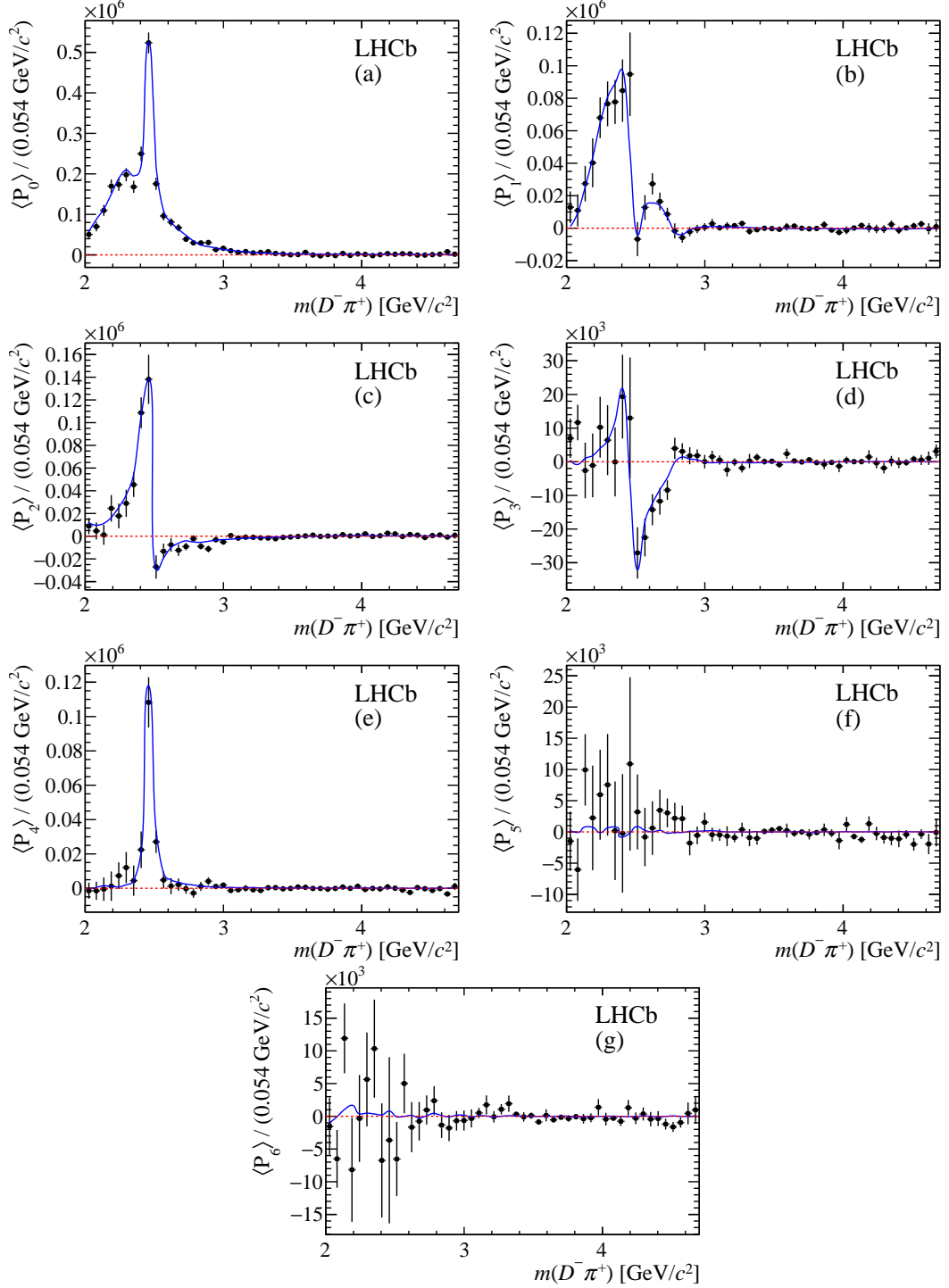


Figure 6.3: The first seven Legendre-polynomial weighted moments for background-subtracted and efficiency-corrected $B^+ \rightarrow D^- K^+ \pi^+$ data (black points) as a function of $m(D^- \pi^+)$. Candidates from both TOS and !TOS sub-samples are included. The blue line shows the result of the DP fit described in Sec. 6.4.

The $\bar{D}_2^*(2460)^0$ resonance is clearly seen in the distribution of $\langle P_4 \rangle$ in Fig. 6.3. The structure observed in $\langle P_3 \rangle$ must arise as a result of interference between P- and D-wave amplitudes, implying that a broad, possibly nonresonant, spin-1 contribution is required at low $m(D^- \pi^+)$. Since the $\langle P_1 \rangle$ and $\langle P_3 \rangle$ distributions differ, there must also be interference between spin-1 and 0 amplitudes, so a broad spin-0 component is needed in the same region of $m(D^- \pi^+)$.

6.4 Dalitz plot fit

The DP and SDP distributions of $B^+ \rightarrow D^- K^+ \pi^+$ candidates in the signal region are shown in Fig. 6.4. This section describes the amplitude model used to fit the dataset and the results obtained.

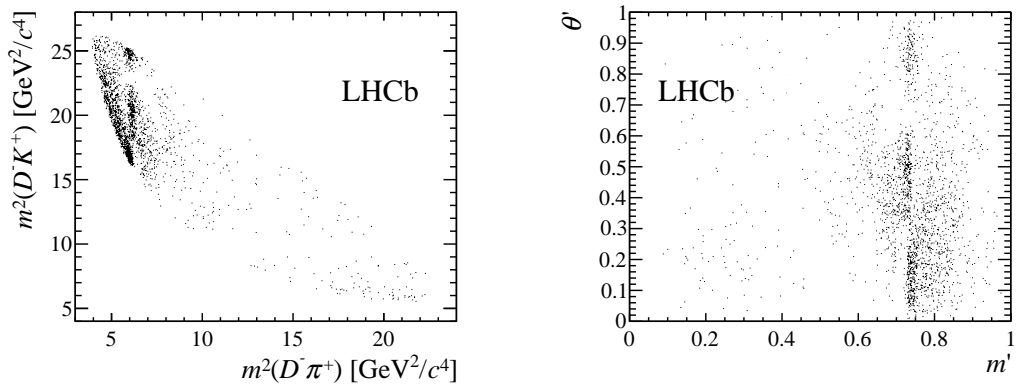


Figure 6.4: Distribution of $B^+ \rightarrow D^- K^+ \pi^+$ candidates in the signal region over (left) the DP and (right) the SDP. Candidates from both TOS and !TOS sub-samples are included.

6.4.1 Fit model

The amplitude model is built from the results of previous spectroscopy studies, summarised in Tab. 2.5, and on the information gained from studies of the angular moments, described above. The Dalitz plot fit is based on the isobar formalism, introduced in Sec. 2.4.2, with the resonant and nonresonant amplitudes shown in Tab. 6.2.

The model includes the well known $\bar{D}_0^*(2400)^0$ and $\bar{D}_2^*(2460)^0$ states, as well as two virtual states – the \bar{D}_v^{*0} state below the $m(D\pi)$ threshold and \bar{B}_v^{*0} above the upper kinematic limit on the $m^2(DK)$ axis. An additional high mass state ' $\bar{D}_J^*(2760)^0$ ' is also found to improve the fit. More information about the study of the spin of this resonance is given later. The mass and width parameters of the $\bar{D}_2^*(2460)^0$ and $\bar{D}_J^*(2760)^0$ states are floated in the fit. There is less sensitivity to the parameters of other resonances, so these are fixed to the PDG average values [102] with appropriate model uncertainties assigned to account for this choice. The final two components are S-wave and P-wave

Table 6.2: Amplitudes included in the $B^+ \rightarrow D^- K^+ \pi^+$ Dalitz plot fit. Resonances labelled with subscript v are virtual. Parameters (and uncertainties) are taken from the PDG [102] unless stated otherwise. More detail about the RBW and EFF models is given in Sec. 2.4.2.3.

Contribution	Spin	DP axis	Model	Parameters
$\bar{D}_0^*(2400)^0$	0	$m^2(D\pi)$	RBW	$m = 2318 \pm 29 \text{ MeV}/c^2, \Gamma = 267 \pm 40 \text{ MeV}$
$\bar{D}_2^*(2460)^0$	2	$m^2(D\pi)$	RBW	Determined from data (see Tab. 6.4)
$\bar{D}_J^*(2760)^0$?	$m^2(D\pi)$	RBW	
Nonresonant	0	$m^2(D\pi)$	EFF	Determined from data (see Tab. 6.4)
Nonresonant	1	$m^2(D\pi)$	EFF	
$\bar{D}_v^*(2007)^0$	1	$m^2(D\pi)$	RBW	$m = 2006.98 \pm 0.15 \text{ MeV}/c^2, \Gamma = 2.1 \text{ MeV}$
\bar{B}_v^{*0}	1	$m^2(DK)$	RBW	$m = 5325.2 \pm 0.4 \text{ MeV}/c^2, \Gamma = 0.0 \text{ MeV}$

nonresonant shapes, each described by an exponential term with one floated parameter in the fit. The decision to include both spin-0 and spin-1 nonresonant contributions is motivated by the angular moments study in Sec. 6.3.

The spin of the $\bar{D}_J^*(2760)^0$ has not been determined in previous studies, but the nature of the Dalitz plot analysis technique allows the spin of individual resonances to be tested. Alternative fits are performed to test all spin values up to and including 3, and the spin-1 hypothesis is found to have the smallest NLL. Fits with a $\bar{D}_J^*(2760)^0$ resonance of spin-0, 2 or 3 have $2\Delta\text{NLL} = 37.3, 49.5$ and 48.2 units, respectively. The value of $2\Delta\text{NLL}$ obtained from a fit without the $\bar{D}_J^*(2760)^0$ state is 75.0 units. The significance of the $\bar{D}_J^*(2760)^0$ resonance is not formally evaluated, but based on the square root of this $2\Delta\text{NLL}$ value the component clearly has a statistical significance of more than 5σ .

6.4.2 Fit results

The real and imaginary parts of the c_j terms introduced in Sec. 2.4.2 are floated in the Dalitz plot fit. The amplitude of each resonance is determined relative to the reference amplitude, $\bar{D}_2^*(2460)^0$, which has real and imaginary parts of c_j fixed to 1 and 0, respectively. The results for the floated real and imaginary parts of each amplitude are reported in Tab. 6.3, as are the derived values of magnitudes, phases and fit fractions. The total fit fraction exceeds 100 %, mostly due to constructive interference between the $\bar{D}_0^*(2400)^0$ and S-wave nonresonant contributions. The values of other floated parameters are shown in Tab. 6.4: the masses and widths of the $\bar{D}_2^*(2460)^0$ and $\bar{D}_1^*(2760)^0$ states (to be compared to previously measured values in Tab. 2.5) and the exponential shape parameters for the S-wave and P-wave nonresonant components.

The statistical uncertainties quoted for all floated parameters are just the (parabolic) uncertainties returned by the fit. In order to account for correlations between parameters,

Table 6.3: Results of the default fit to data. Note that the sum of the fit fractions need not be 100% due to interference effects.

Contribution	Fit fraction (%)	Real part	Imaginary part	Magnitude	Phase (rad)
$\bar{D}_0^*(2400)^0$	8.3 ± 2.6	-0.04 ± 0.07	-0.51 ± 0.07	0.51 ± 0.09	-1.65 ± 0.16
$\bar{D}_2^*(2460)^0$	31.8 ± 1.5	1.00	0.00	1.00	0.00
$\bar{D}_1^*(2760)^0$	4.9 ± 1.2	-0.32 ± 0.06	-0.23 ± 0.07	0.39 ± 0.05	-2.53 ± 0.24
Nonresonant (S-wave)	38.0 ± 7.4	0.93 ± 0.09	-0.58 ± 0.08	1.09 ± 0.09	-0.56 ± 0.09
Nonresonant (P-wave)	23.8 ± 5.6	-0.43 ± 0.09	0.75 ± 0.09	0.87 ± 0.09	2.09 ± 0.15
$\bar{D}_v^*(2007)^0$	7.6 ± 2.3	0.16 ± 0.08	0.46 ± 0.09	0.49 ± 0.07	1.24 ± 0.17
\bar{B}_v^{*0}	3.6 ± 1.9	-0.07 ± 0.08	0.33 ± 0.07	0.34 ± 0.06	1.78 ± 0.23
Total fit fraction	118.1				

Table 6.4: Floated parameters for the fit to data, with statistical uncertainties only.

Contribution	Floated parameters	
$\bar{D}_2^*(2460)^0$	$m = 2464.0 \pm 1.4 \text{ MeV}/c^2$	$\Gamma = 43.8 \pm 2.9 \text{ MeV}$
$\bar{D}_1^*(2760)^0$	$m = 2781 \pm 18 \text{ MeV}/c^2$	$\Gamma = 177 \pm 32 \text{ MeV}$
Nonresonant (S-wave)	$\alpha_S = 0.36 \pm 0.03 \text{ (GeV}/c^2)^{-2}$	
Nonresonant (P-wave)	$\alpha_P = 0.36 \pm 0.04 \text{ (GeV}/c^2)^{-2}$	

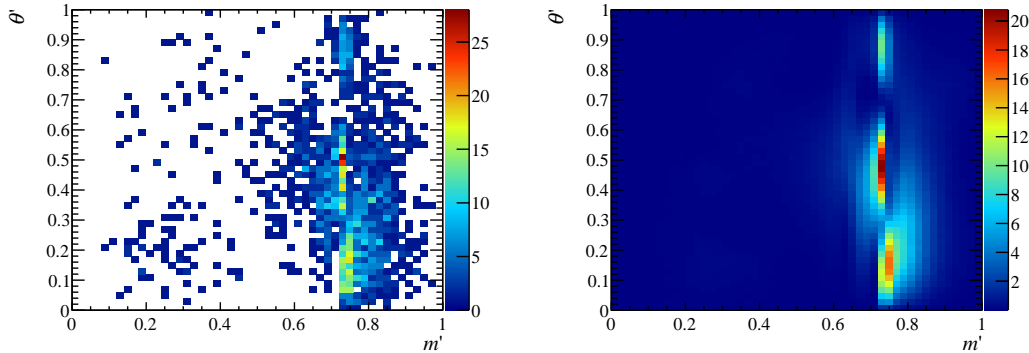


Figure 6.5: The distribution across the SDP of (left) data and (right) the fit model.

the statistical uncertainties for all derived parameters – magnitudes and phases of c_j and (interference) fit fractions – are calculated using large samples of pseudoexperiments.

The SDP distributions of data and the fit model are compared in Fig. 6.5. To evaluate the consistency of the two samples, the two-dimensional χ^2 value is calculated by comparing the data and the fit model in 100 equally populated bins across the SDP. This corresponds to a minimum bin content of 19 events. The 2D pull, *i.e.* the difference between the bin occupancy for data and the fit model divided by the combined uncertainty of both values, in each bin is plotted in Fig. 6.6 (left). The distribution of pulls is found to be roughly Gaussian, as shown in Fig. 6.6 (right).

The distribution of χ^2 values obtained from this procedure is, itself, expected to follow a χ^2 distribution with number of degrees of freedom, ndf , bounded by $n_{\text{bins}} - 1$ and $n_{\text{bins}} - n_{\text{pars}} - 1$, where the number of model parameters floated in the fit to data, n_{pars} , is

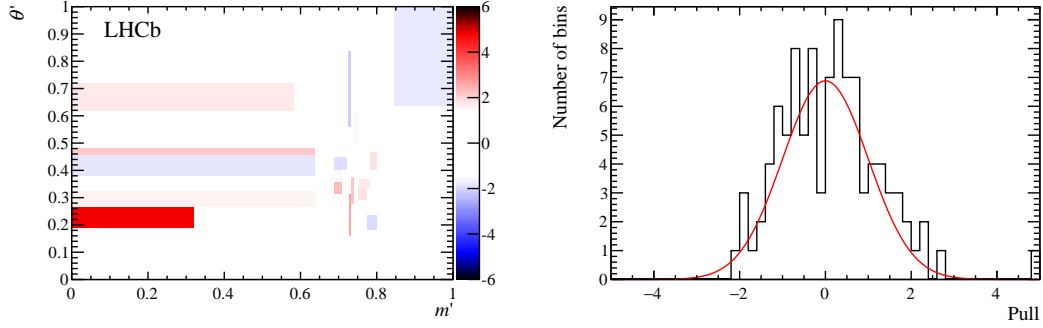


Figure 6.6: The pulls between data and the fit model for 100 equally populated bins across the SDP. (Left) the pull in each bin and (right) the distribution of pulls with a Gaussian of mean zero and width one superimposed.

18. The χ^2/ndf obtained using this binning is calculated to be between $136.4/81 = 1.68$ and $136.4/99 = 1.35$. Although these χ^2/ndf values correspond to a small p -value, other goodness of fit tests motivated by Ref. [108] suggest that the fit model gives a good, but imperfect, description of the data.

One-dimensional projections of the nominal fit model and the data onto $m(D\pi)$, $m(DK)$ and $m(K\pi)$ are shown in Fig. 6.7. In Fig. 6.8 (left), zoomed views of the $m(D\pi)$ invariant mass projection are provided for the threshold region and around the $\bar{D}_2^*(2460)^0$ and $\bar{D}_1^*(2760)^0$ resonances. The fit model in the threshold and $\bar{D}_2^*(2460)^0$ areas demonstrates a good description of the data. Projections of the cosine of the $D\pi$ helicity angle in the same regions of $m(D\pi)$ are shown in Fig. 6.8 (right). Strong interference effects are visible between the P-wave contributions in the region of the $\bar{D}_1^*(2760)^0$ state. Again, good agreement is seen, suggesting that the spin content of the resonant contributions is correct.

6.4.2.1 Secondary minima

In a Dalitz plot fit it is common to find multiple solutions corresponding to local minima in the parameter likelihood space. To ensure that the global minimum is found for a fit model, each fit is repeated 500 times with randomised initial values of the c_j parameters. The solution with the smallest NLL is taken as the default result, but six secondary minima are found with $2\Delta\text{NLL}$ values of 0.80, 2.84, 3.30, 9.25, 12.63 and 13.81 units from the global minimum, respectively. The number of fits finding each minimum is shown in Fig. 6.9, from which it is clear that the global minimum is the most populated.

The fit results corresponding to the five lowest likelihood values are presented in Fig. 6.10, in terms of the complex coefficients of each resonance component in the fit model. Although these secondary minima are not all well separated from the global minimum, their presence is not a concern for the results of this analysis. The solution with $2\Delta\text{NLL} = 0.80$ is found by only one of the 500 experiments and appears to be essentially identical to the

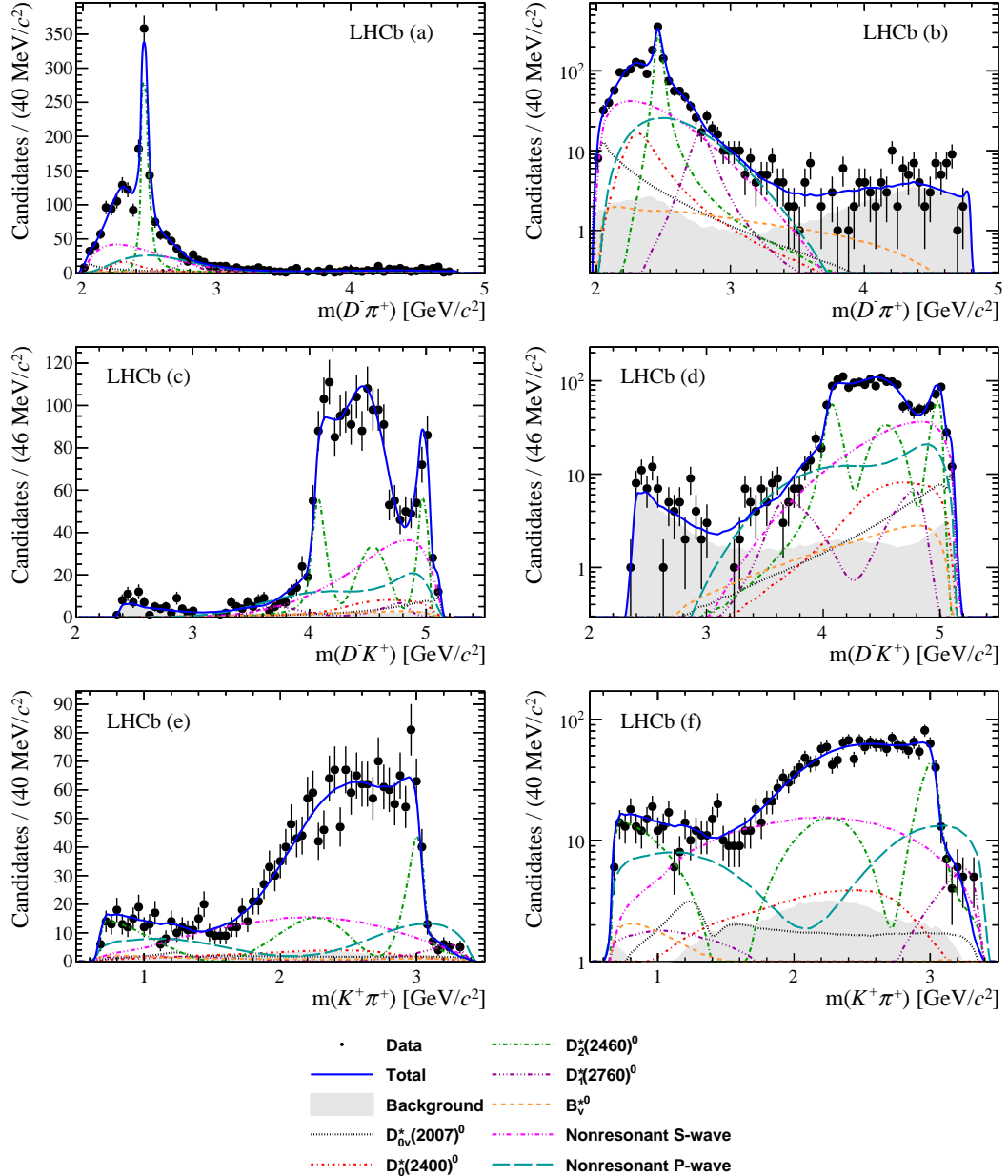


Figure 6.7: Projections of the data and amplitude fit onto (a) $m(D\pi)$, (c) $m(DK)$ and (e) $m(K\pi)$, with the same projections shown in (b), (d) and (f) with a logarithmic y -axis scale. Components are described in the legend. Destructive interference between the contributions is visible where individual components appear above the total fit line.

global minimum. The main difference between the best and the second solution (with $2\Delta\text{NLL} = 2.84$) is in the phases of the $\bar{D}^*(2007)^0$ and P-wave nonresonant components – the effects on the fit fractions (and interference fit fractions) are rather small. The third minimum (with $2\Delta\text{NLL} = 3.30$) has a large sum of fit fractions of almost 200 %, therefore it is unlikely to be a correct physical description of the Dalitz plot. Both of these minima differ from the best solution due to interference effects between broad structures that contribute to the same partial wave. Such effects are not surprising. The

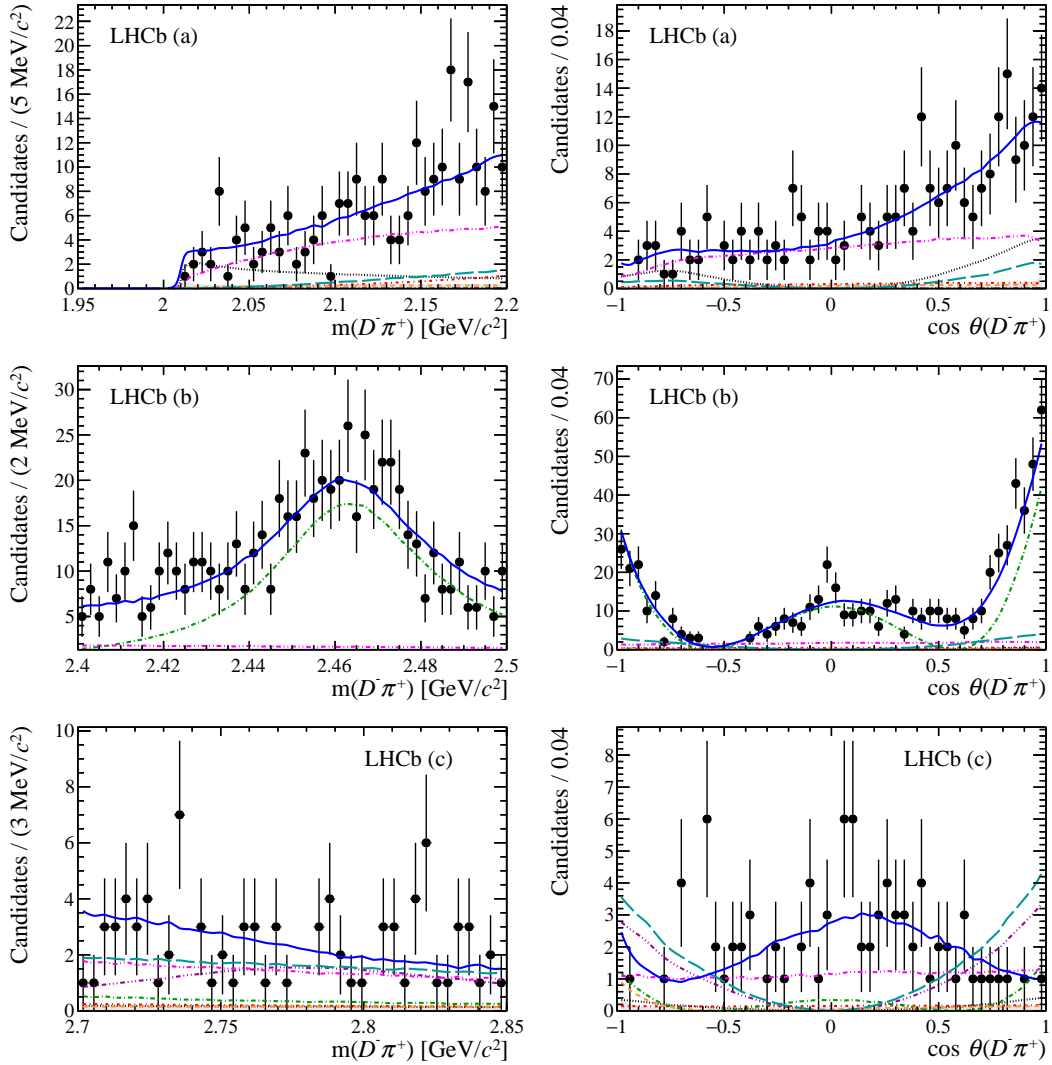


Figure 6.8: Projections of the data and amplitude fit onto (left) $m(D\pi)$ and (right) the cosine of the helicity angle for the $D\pi$ system in (top) the threshold region, (middle) the $\bar{D}_2^*(2460)^0$ region and (bottom) the $\bar{D}_1^*(2760)^0$ region. Components are as shown in Fig. 6.7. Destructive interference between the contributions is visible where individual components appear above the total fit line.

floated mass and width parameters for the $\bar{D}_2^*(2460)^0$ and $\bar{D}_1^*(2760)^0$ states are found to be roughly stable in these alternative minima.

6.4.3 Testing the baseline model

To determine whether any resonances are missing from the nominal fit model, the fit is repeated many times with an additional arbitrary state included. A range of possible mass and width values are tested, with the parameters fixed in each fit. Resonances decaying to $K^+\pi^+$, D^-K^+ or $D^-\pi^+$ are all included in the study, with spin-0, 1, 2 or 3 considered. The results in terms of the change in $2\Delta\text{NLL}$ are shown in Fig. 6.11.

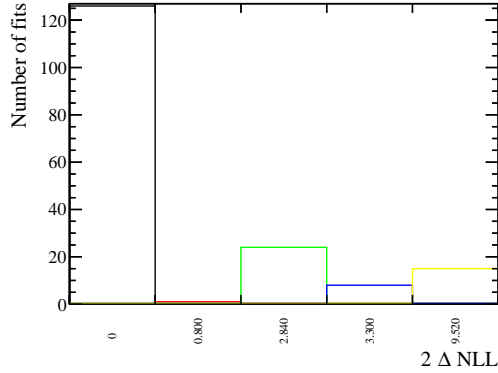


Figure 6.9: The number of experiments finding each minimum. From 500 fits the global minimum is found by 126 experiments, 71 fits failed to converge and the remainder reported a worse likelihood.

The largest improvement to the likelihood (~ 16 units) is found for a fit model with a spin-2 resonance decaying to $K^+ \pi^+$ with a mass of $\sim 2100 \text{ MeV}/c^2$. The second largest is from the inclusion of a resonance at $m(DK) \sim 3000 \text{ MeV}/c^2$ with a width of 50 MeV. It is highly unlikely that any physical resonance could exist in either the $D^- K^+$ or $K^+ \pi^+$ combinations, so the improved likelihood is an indication that the model has uncertainties due to fluctuations or systematic mismodelling of the Dalitz plot distribution. The quoted results in Sec. 6.6 account for effects like these in the statistical and systematic uncertainties.

For the $m(D^- \pi^+)$ combination, the largest changes in $2\Delta\text{NLL}$ are observed with a narrow spin-0 resonance at approximately $2500 \text{ MeV}/c^2$ and for a spin-1 resonance at the kinematic threshold. The former suggests that there are inaccuracies with the $D\pi$ S-wave model, whilst the latter is likely to be due to difficulty modelling the efficiency variation at the edge of the Dalitz plot.

To summarise, there is no evidence of any additional resonances contributing significantly to the Dalitz plot. There may be inaccuracies in some models, but these are accounted for by the systematic uncertainties discussed in Sec. 6.5.

6.5 Systematic uncertainties

Sources of systematic uncertainty are categorised as either experimental or model uncertainties. Experimental systematic uncertainties arise from imperfect knowledge of: the signal and background yields in the signal region; the SDP distributions of the background components; the efficiency variation across the SDP, and as a result of fit bias. Model uncertainties are from: parameters which are fixed in the Dalitz plot fit model; the inclusion or exclusion of marginal contributing amplitudes; the choice of models for the S- and P-wave nonresonant contributions. The total systematic uncertainty for each

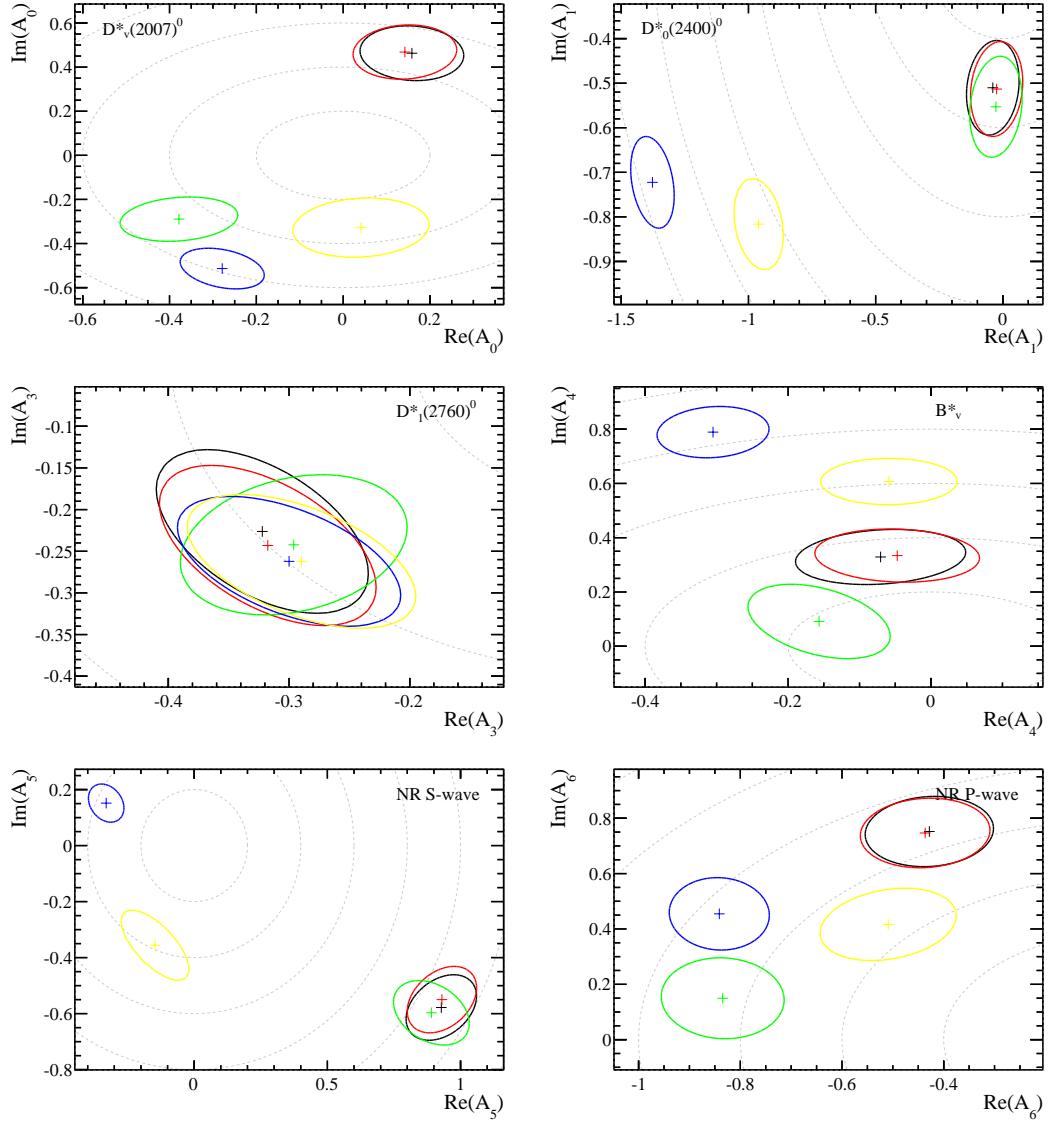


Figure 6.10: Plots of the real and imaginary parts of the fit amplitudes, comparing (black) the best fit against secondary minima with $2\Delta\text{NLL}$ values that are (red) 0.80, (green) 2.84, (blue) 3.30 and (yellow) 9.25 units worse than the best fit. The coloured contour around each point marks the 1σ uncertainty ellipse. Grey dashed contours mark the $(0,0)$ position to aid comparison of magnitudes. The corresponding resonance component is labelled on each plot.

measured parameter is calculated by combining the contributions from all sources in quadrature.

6.5.1 Experimental uncertainties

The signal and background yields in the signal region are fixed to values determined from the fit to the B candidate invariant mass distribution, as described in Sec. 6.1. The total uncertainty on each yield (including systematic uncertainties evaluated as in Sec. 5.3) is

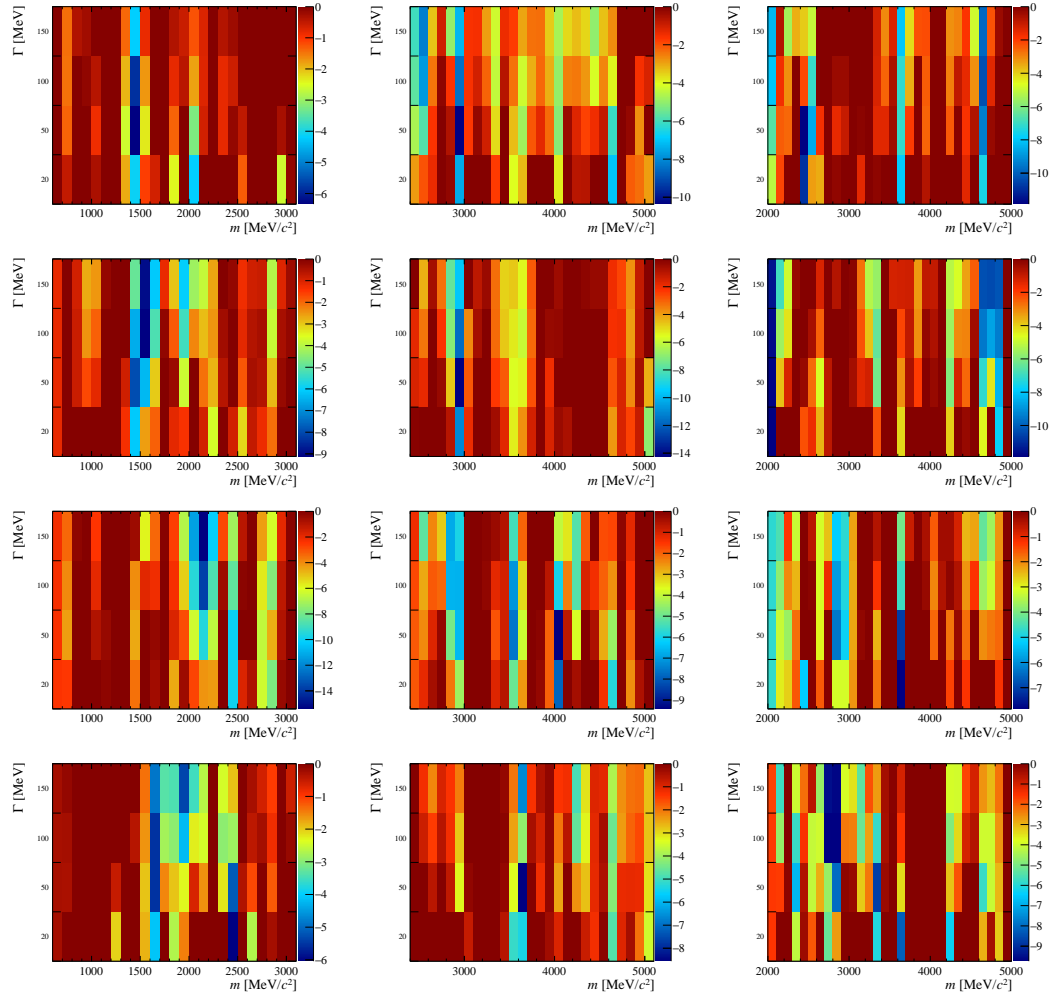


Figure 6.11: $2\Delta\text{NLL}$ profiles for fits including an additional (left) $K\pi$, (centre) DK and (right) $D\pi$ resonance of spin (top – bottom) 0, 1, 2 or 3. Note that the z -axis scale is different for each plot.

calculated, and the fixed yields varied by the appropriate amount in the Dalitz plot fit. The deviations from the default fit result are assigned as systematic uncertainties.

To evaluate the effect of imperfect knowledge of the background distributions over the SDP, the Dalitz plot fit is repeated many times replacing the default histograms in Fig. 6.2 with alternative distributions obtained by varying each bin within its uncertainties. The systematic uncertainty on a fitted parameter is taken as the RMS of the distribution of the change from the default fitted value. Additional sources of uncertainty are considered for the $B^+ \rightarrow D^{(*)-} \pi^+ \pi^+$ background – the ratio of $D^{*-} \pi^+ \pi^+$ and $D^- \pi^+ \pi^+$ contributions is varied and the reweighting applied to the SDP distribution of simulated samples is removed.

To quantify the uncertainty related to the knowledge of the variation of efficiency across the SDP, the efficiency distributions in Fig. 4.16 are varied within their errors. Varying each bin of the map independently does not account for correlations between adjacent

bins. Instead, the efficiency histograms are divided into regions of 3×3 bins; only the value of the central bin is varied directly and linear interpolation is used to find the variation of surrounding bins. The process is repeated many times to create a large set of alternative efficiency distributions and the effects on the fit results are assigned as systematic uncertainties. An additional systematic uncertainty is evaluated by varying the binning scheme of the calibration data sample from PIDCALIB used to determine the PID efficiencies.

An ensemble of pseudoexperiments is generated to investigate systematic uncertainties related to possible intrinsic fit bias. It is unrealistic to expect to be able to eradicate all biases from a complicated fit such as this, but by studying pseudoexperiments it is possible to check the size of any bias and ensure that the effects are reasonably well understood. The values of fit parameters obtained from the ensemble are found to be close to the input values, and Gaussian functions are fitted to each distribution. The systematic uncertainty on each parameter is assigned as the sum in quadrature of the difference between the generated and mean output values and the uncertainty on the mean of the output value determined from the Gaussian fit.

The experimental systematic uncertainties on the fit fractions and complex coefficients are summarised in Tab. 6.5. A breakdown of the sources contributing to the total experimental uncertainty is given in Tab. 6.6. The largest source of experimental systematic uncertainty on the fit fractions is due to the efficiency variation.

Table 6.5: Experimental systematic uncertainties on the fit fractions and complex amplitudes.

Contribution	Fit fraction (%)	Isobar model coefficients			
		Real part	Imaginary part	Magnitude	Phase (rad)
$\bar{D}_0^*(2400)^0$	0.6	0.03	0.02	0.02	0.06
$\bar{D}_2^*(2460)^0$	0.9	—	—	—	—
$\bar{D}_1^*(2760)^0$	0.4	0.03	0.03	0.01	0.08
S-wave nonresonant	1.5	0.03	0.03	0.02	0.04
P-wave nonresonant	2.1	0.03	0.05	0.03	0.05
$\bar{D}_v^*(2007)^0$	1.3	0.03	0.04	0.04	0.07
\bar{B}_v^0	0.9	0.22	0.02	0.03	0.11

6.5.2 Model uncertainties

Systematic uncertainties due to parameters which are fixed in the default fit model are determined by varying the parameters within their uncertainties and repeating the fit. The mass and width parameters of the $\bar{D}_0^*(2400)^0$ resonance are varied by the uncertainties shown in Tab. 6.2. The Blatt–Weisskopf barrier radius, r_{BW} , is varied from the nominal value of 4 GeV^{-1} to 3 and 5 GeV^{-1} . The systematic uncertainty on each fit parameter is assigned as the maximum deviation from the value obtained from the default fit model.

Table 6.6: Breakdown of experimental systematic uncertainties on the fit fractions (%) and masses (MeV/c^2) and widths (MeV).

	Nominal	S/B frac.	Eff.	Bkg.	Fit bias	Total
$\bar{D}_0^*(2400)^0$	8.3 ± 2.6	0.2	0.5	0.1	0.3	0.6
$\bar{D}_2^*(2460)^0$	31.8 ± 1.5	0.2	0.8	0.0	0.2	0.9
$\bar{D}_1^*(2760)^0$	4.9 ± 1.2	0.2	0.2	0.1	0.2	0.4
S-wave nonresonant	38.0 ± 7.4	0.7	0.5	0.4	1.2	1.5
P-wave nonresonant	23.8 ± 5.6	1.0	1.6	0.7	0.5	2.1
$\bar{D}_v^*(2007)^0$	7.6 ± 2.3	0.7	1.0	0.3	0.3	1.3
\bar{B}_v^{*0}	3.6 ± 1.9	0.3	0.3	0.2	0.8	0.9
$m(\bar{D}_2^*(2460)^0)$	2464.0 ± 1.4	0.1	0.1	0.0	0.2	0.2
$\Gamma(\bar{D}_2^*(2460)^0)$	43.8 ± 2.9	0.3	0.3	0.0	0.4	0.6
$m(\bar{D}_1^*(2760)^0)$	2781 ± 18	1	4	0	2	6
$\Gamma(\bar{D}_1^*(2760)^0)$	177 ± 32	3	1	2	5	7

The components which contribute least in the fit model are the \bar{B}_v^{*0} and $\bar{D}_1^*(2760)^0$ states (see Tab. 6.3). The effect of removing the \bar{B}_v^{*0} component from the model is tested. Since the $\bar{D}_1^*(2760)^0$ resonance is found to be a significant amplitude in the fit, this state is not removed, but a spin-3 state is added to the model instead. This model alteration is motivated by the results of the Dalitz plot analysis of $\bar{B}_s^0 \rightarrow D^0 K^+ \pi^-$ decays [55, 109], in which a structure at $m(D^0 K^+) \sim 2.86 \text{ GeV}/c^2$ is found to have contributions from both spin-1 and spin-3. Although there is no evidence here for a spin-3 resonance in $B^+ \rightarrow D^- K^+ \pi^+$ decays, the excess at $m(D^- \pi^+) \sim 2.76 \text{ GeV}/c^2$ could have a similar composition. Therefore an additional spin-3 state, $\bar{D}_3^*(2760)^0$, with mass and width fixed to the values reported in Ref. [110] is added to the model as a test. For both of these model variations, the change in each fit parameter is assigned as the systematic uncertainty.

The nonresonant S- and P-wave contributions are each described by a power-law model rather than the default EFF lineshape *i.e.* $R(m) = e^{-\alpha m^2} \rightarrow R(m) = (m^2)^{-\alpha}$. The ad-hoc choice of using an effective pole mass (defined in Eq. 2.37) for virtual resonance contributions is investigated by using a fixed width in Eq. 2.35 to remove the dependence on m_0^{eff} . The systematic uncertainty on each fit parameter is assigned as the change in the fitted value.

The model systematic uncertainties on the fit fractions and complex coefficients are summarised in Tab. 6.7. The contributions for the fit fractions, masses and widths are shown separately in Tab. 6.8. The largest contributing source of model uncertainty on the fit fractions is the addition and removal of marginal components from the model and the variation of fixed parameters. In general, the model uncertainties are larger than the experimental systematic uncertainties for the fit fractions and the masses and widths.

Table 6.7: Model uncertainties on the fit fractions and complex amplitudes.

Contribution	Fit fraction (%)	Isobar model coefficients			
		Real part	Imaginary part	Magnitude	Phase (rad)
$\bar{D}_0^*(2400)^0$	2.0	0.28	0.13	0.15	0.51
$\bar{D}_2^*(2460)^0$	1.4	–	–	–	–
$\bar{D}_1^*(2760)^0$	0.9	0.03	0.03	0.03	0.08
S-wave nonresonant	10.8	0.17	0.15	0.20	0.11
P-wave nonresonant	3.7	0.34	0.68	0.12	0.95
$\bar{D}_v^*(2007)^0$	1.5	0.56	0.77	0.05	0.60
\bar{B}_v^{*0}	1.6	0.09	0.08	0.07	0.27

Table 6.8: Breakdown of model uncertainties on the fit fractions (%) and masses (MeV/ c^2) and widths (MeV).

	Nominal	Add/rem	Alt. models	Fixed params	Total
$\bar{D}_0^*(2400)^0$	8.3 ± 2.6	2.0	0.1	0.2	2.0
$\bar{D}_2^*(2460)^0$	31.8 ± 1.5	1.3	0.2	0.4	1.4
$\bar{D}_1^*(2760)^0$	4.9 ± 1.2	0.8	0.1	0.3	0.9
S-wave nonresonant	38.0 ± 7.4	4.8	4.5	5.4	10.8
P-wave nonresonant	23.8 ± 5.6	2.6	2.1	3.0	3.7
$\bar{D}_v^*(2007)^0$	7.6 ± 2.3	0.6	0.1	1.4	1.5
\bar{B}_v^{*0}	3.6 ± 1.9	0.7	1.0	1.1	1.6
$m(\bar{D}_2^*(2460)^0)$	2464.0 ± 1.4	0.5	0.1	0.1	0.5
$\Gamma(\bar{D}_2^*(2460)^0)$	43.8 ± 2.9	0.8	1.4	0.6	1.7
$m(\bar{D}_1^*(2760)^0)$	2781 ± 18	6	6	1	11
$\Gamma(\bar{D}_1^*(2760)^0)$	177 ± 32	16	9	1	20

6.5.3 Cross checks

The Dalitz plot fit is performed with a number of alternative datasets to confirm the stability of the results. The data sample is divided according to: the charge of the B candidate; the polarity of the magnet and the year of data taking. The requirements imposed on the NN $_B$ output and PID variables are both tightened and loosened, and alternative signal regions are tested by selecting candidates within $\pm 2\sigma_1$ and $\pm 3\sigma_1$ of the fitted B candidate mass. The default amplitude model is used to perform a fit to each sub-sample individually. The results of the cross check fits are found to be consistent with the default results, although in some cases one of the secondary minima described in Sec. 6.4.2.1 becomes the preferred solution.

6.6 Results

The masses and widths of the $\bar{D}_2^*(2460)^0$ and $\bar{D}_1^*(2760)^0$ states are determined to be

$$m(\bar{D}_2^*(2460)^0) = (2464.0 \pm 1.4 \pm 0.2 \pm 0.5) \text{ MeV}/c^2, \quad (6.3)$$

$$\Gamma(\bar{D}_2^*(2460)^0) = (43.8 \pm 2.9 \pm 0.6 \pm 1.7) \text{ MeV}, \quad (6.4)$$

$$m(\bar{D}_1^*(2760)^0) = (2781 \pm 18 \pm 6 \pm 11) \text{ MeV}/c^2, \quad (6.5)$$

$$\Gamma(\bar{D}_1^*(2760)^0) = (177 \pm 32 \pm 7 \pm 20) \text{ MeV}, \quad (6.6)$$

where the three quoted errors are statistical, experimental systematic uncertainties and from model variations, respectively. The measured mass and width parameters of the $\bar{D}_2^*(2460)^0$ are within 2σ of the world average values [3]. The mass of the $\bar{D}_1^*(2760)^0$ resonance is similarly consistent with previous measurements, but the width is larger than previous measurements by 2 to 3 times the uncertainties. This is the first measurement of the spin of the $\bar{D}_1^*(2760)^0$ resonance and the first observation of the $B^+ \rightarrow \bar{D}_1^*(2760)^0 K^+$ and $B^+ \rightarrow \bar{D}_2^*(2460)^0 K^+$ decays.

The results for the real and imaginary parts of the resonance amplitudes are reported in Tab. 6.9. The derived magnitudes and phases for each resonance are shown in Tab. 6.10.

Table 6.9: Results for the complex amplitudes and their uncertainties. The three quoted errors are statistical, experimental systematic and model uncertainties, respectively.

Contribution	Isobar model coefficients	
	Real part	Imaginary part
$\bar{D}_0^*(2400)^0$	$-0.04 \pm 0.07 \pm 0.03 \pm 0.28$	$-0.51 \pm 0.07 \pm 0.02 \pm 0.13$
$\bar{D}_2^*(2460)^0$	1.00	0.00
$\bar{D}_1^*(2760)^0$	$-0.32 \pm 0.06 \pm 0.03 \pm 0.03$	$-0.23 \pm 0.07 \pm 0.03 \pm 0.03$
S-wave nonresonant	$0.93 \pm 0.09 \pm 0.03 \pm 0.17$	$-0.58 \pm 0.08 \pm 0.03 \pm 0.15$
P-wave nonresonant	$-0.43 \pm 0.09 \pm 0.03 \pm 0.34$	$0.75 \pm 0.09 \pm 0.05 \pm 0.68$
$\bar{D}_v^*(2007)^0$	$0.16 \pm 0.08 \pm 0.03 \pm 0.56$	$0.46 \pm 0.09 \pm 0.04 \pm 0.77$
\bar{B}_v^{*0}	$-0.07 \pm 0.08 \pm 0.22 \pm 0.09$	$0.33 \pm 0.07 \pm 0.02 \pm 0.08$

The results for the fit fractions are given in Tab. 6.11. Since the measurement of $\mathcal{B}(B^+ \rightarrow D^- K^+ \pi^+)$ corresponds to the first observation of this decay mode, the resonant contributions to the decay are also previously unobserved. The fit fraction for each resonance is converted into a quasi-two-body product branching fractions by multiplying by $\mathcal{B}(B^+ \rightarrow D^- K^+ \pi^+) = (7.31 \pm 0.19 \pm 0.22 \pm 0.39) \times 10^{-5}$, as determined in Sec. 5.4. The calculated product branching fractions are also shown in Tab. 6.11.²⁵

²⁵The branching fractions for the resonance decays to $D^- \pi^+$ are unknown, so absolute branching fractions cannot be obtained from these values.

Table 6.10: Results for the complex amplitudes and their uncertainties. The three quoted errors are statistical, experimental systematic and model uncertainties, respectively.

Contribution	Isobar model coefficients		
	Magnitude	Phase (rad)	
$\bar{D}_0^*(2400)^0$	$0.51 \pm 0.09 \pm 0.02 \pm 0.15$	$-1.65 \pm 0.16 \pm 0.06 \pm 0.50$	
$\bar{D}_2^*(2460)^0$	1.00		0.00
$\bar{D}_1^*(2760)^0$	$0.39 \pm 0.05 \pm 0.01 \pm 0.03$	$-2.53 \pm 0.24 \pm 0.08 \pm 0.08$	
S-wave nonresonant	$1.09 \pm 0.09 \pm 0.02 \pm 0.20$	$-0.56 \pm 0.09 \pm 0.04 \pm 0.11$	
P-wave nonresonant	$0.87 \pm 0.09 \pm 0.03 \pm 0.11$	$2.09 \pm 0.15 \pm 0.05 \pm 0.95$	
$\bar{D}_v^*(2007)^0$	$0.49 \pm 0.07 \pm 0.04 \pm 0.05$	$1.24 \pm 0.17 \pm 0.07 \pm 0.60$	
\bar{B}_v^{*0}	$0.34 \pm 0.06 \pm 0.03 \pm 0.07$	$1.78 \pm 0.23 \pm 0.11 \pm 0.27$	

Table 6.11: Results for the fit fractions (%) and product branching fractions $\mathcal{B}(B^+ \rightarrow RK^+) \times \mathcal{B}(R \rightarrow D^- \pi^+)$ (10^{-6}). The three quoted errors for the fit fractions are statistical, experimental systematic and model uncertainties, respectively. The additional source of uncertainty on the branching fractions is from $B(B^+ \rightarrow D^- K^+ \pi^+)$ [2].

Contribution	Fit fraction (%)	Product branching fraction (10^{-6})
$\bar{D}_0^*(2400)^0$	$8.3 \pm 2.6 \pm 0.6 \pm 2.0$	$6.1 \pm 1.9 \pm 0.5 \pm 1.5 \pm 0.4$
$\bar{D}_2^*(2460)^0$	$31.8 \pm 1.5 \pm 0.9 \pm 1.4$	$23.2 \pm 1.1 \pm 0.6 \pm 1.0 \pm 1.6$
$\bar{D}_1^*(2760)^0$	$4.9 \pm 1.2 \pm 0.4 \pm 0.9$	$3.6 \pm 0.9 \pm 0.3 \pm 0.7 \pm 0.2$
S-wave nonresonant	$38.0 \pm 7.4 \pm 1.5 \pm 10.8$	$27.8 \pm 5.4 \pm 1.1 \pm 7.9 \pm 1.9$
P-wave nonresonant	$23.8 \pm 5.6 \pm 2.1 \pm 3.7$	$17.4 \pm 4.1 \pm 1.5 \pm 2.7 \pm 1.2$
$\bar{D}_v^*(2007)^0$	$7.6 \pm 2.3 \pm 1.3 \pm 1.5$	$5.6 \pm 1.7 \pm 1.0 \pm 1.1 \pm 0.4$
\bar{B}_v^{*0}	$3.6 \pm 1.9 \pm 0.9 \pm 1.6$	$2.6 \pm 1.4 \pm 0.6 \pm 1.2 \pm 0.2$

Chapter 7

Search for $B^+ \rightarrow D^+ K^+ \pi^-$ decays

This chapter describes the search for the rare $B^+ \rightarrow D^+ K^+ \pi^-$ decay, and the subsequent measurement of its branching fraction using the $B^+ \rightarrow D^- K^+ \pi^+$ decay as a control mode. The quasi-two-body contributions from $B^+ \rightarrow D_2^*(2460)^0 K^+$ and $B^+ \rightarrow D^+ K^*(892)^0$ are also studied; the results of the searches for these decay modes are presented in Sec. 7.6.

7.1 Motivation

The GLW method, detailed in Sec. 2.2.5.1, allows a measurement of the CKM angle γ using $B^+ \rightarrow D K^+$ decays with the neutral D meson decaying to CP eigenstates. The sensitivity to γ comes from the interference of $\bar{b} \rightarrow \bar{c}$ and $\bar{b} \rightarrow \bar{u}$ amplitudes, which both contribute to the B^+ decay and are indistinguishable given the identical final state. A challenge with this method is that the ratio of magnitudes of the suppressed and favoured B^+ decay amplitudes, r_B , is not known independently and must be determined simultaneously with γ to enable the CKM angle to be extracted precisely. This shortcoming can be addressed by also considering alternative final states of the D meson (*e.g.* the ADS method described in Sec. 2.2.5.1) that provide complementary information on r_B and γ [111, 112].

In the case of $B^+ \rightarrow D^{**} K^+$ decays, where D^{**} represents an excited D or \bar{D} meson such as the $D_2^*(2460)$ state which can decay to both $D^\pm \pi^\mp$ and $D\pi^0$, it is possible to obtain a clean determination of the corresponding value of r_B [31]. The relative branching fractions of the $\bar{b} \rightarrow \bar{u}$ mediated $B^+ \rightarrow D^{**0} K^+ \rightarrow D^+ \pi^- K^+$ and the $\bar{b} \rightarrow \bar{c}$ mediated $B^+ \rightarrow \bar{D}^{**0} K^+ \rightarrow D^- \pi^+ K^+$ processes give the value of r_B^2 , whilst the $B^+ \rightarrow D^{**} K^+ \rightarrow D\pi^0 K^+$ final state, where the D meson is reconstructed using CP eigenstate decay modes, provides sensitivity to γ . Although study of the $B^+ \rightarrow D\pi^0 K^+$

decay would be experimentally challenging due to the π^0 meson in the final state,²⁶ knowledge of r_B in these decays will indicate whether or not a competitive measurement of γ could be made using this approach. Decay diagrams for $B^+ \rightarrow \bar{D}_2^*(2460)^0 K^+$ and $B^+ \rightarrow D_2^*(2460)^0 K^+$ final decays are shown in Fig. 7.1.

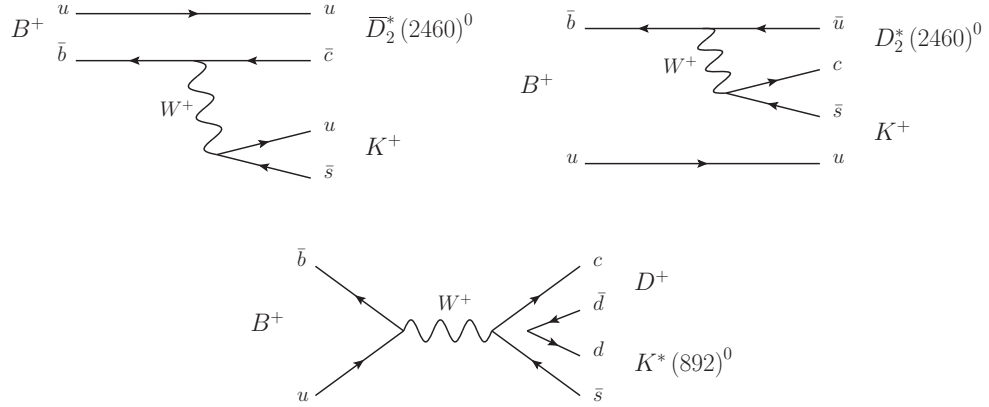


Figure 7.1: Decay diagrams for (top left) $B^+ \rightarrow \bar{D}_2^*(2460)^0 K^+$, (top right) $B^+ \rightarrow D_2^*(2460)^0 K^+$ and (bottom) $B^+ \rightarrow D^+ K^*(892)^0$ channels.

The resonant structure of the $B^+ \rightarrow D^- K^+ \pi^+$ decay has been studied in the Dalitz plot analysis documented in Chap. 6, but knowledge of the amplitudes contributing to $B^+ \rightarrow D^+ K^+ \pi^-$ is required. The expected low signal yield of $B^+ \rightarrow D^+ K^+ \pi^-$ decays in the available data sample makes a full amplitude analysis unrealistic. An alternative approach is taken, exploiting the angular decay information to separate different spin states in the region of the narrow $D_2^*(2460)^0$ resonance. The same method can also be used to search for $B^+ \rightarrow D^+ K^*(892)^0$ decays, which contribute to the $D^+ K^+ \pi^-$ final state and are of interest since they are mediated by annihilation amplitudes, as shown in Fig. 7.1 (bottom). A previous LHCb analysis of this mode saw a small but not statistically significant excess of signal candidates and set an upper limit $\mathcal{B}(B^+ \rightarrow D^+ K^*(892)^0) < 1.8 \times 10^{-6}$ at the 90 % credibility level [113].

7.2 Event selection and analysis strategy

The yields of $B^+ \rightarrow D^+ K^+ \pi^-$ and $B^+ \rightarrow D^- K^+ \pi^+$ decay contributions in the datasets are obtained from unbinned extended maximum likelihood fits performed to candidates in the range $5100 \leq m(DK\pi) \leq 5800 \text{ MeV}/c^2$. To avoid biasing the results of this search, the signal region of the $D^+ K^+ \pi^-$ sample is not examined until the selection strategy and fit model are finalised. This is referred to as a ‘blind’ analysis. Prior to unblinding, the quality of the fit to the $B^+ \rightarrow D^+ K^+ \pi^-$ candidate invariant mass distribution can only be judged by considering the pull distributions in the signal region and applying

²⁶Design differences between the Belle II and LHCb experiments make the former better suited to study processes with neutral particles in the final state.

the fit model to an ensemble of pseudoexperiments generated with a variety of $D^+ K^+ \pi^-$ signal yields.

The final states of the signal ($D^+ K^+ \pi^-$) and control ($D^- K^+ \pi^+$) modes differ only by the relative charges of two particles, so the selection requirements are very similar to those described in Chap. 4 for $B^+ \rightarrow D^- K^+ \pi^+$ candidates. Since many effects cancel in the final ratio of branching fractions, identical requirements are applied to both data samples. The stripping lines used to select $B^+ \rightarrow D^+ K^+ \pi^-$ and $D^- K^+ \pi^+$ candidates also differ only by the charges of selected final state tracks. The requirements imposed by these lines are shown in Tab. 4.1. Both $DK\pi$ final states are reconstructed with $D^+ \rightarrow K^- \pi^+ \pi^+$.

The selection requirements are based on those described in Chap. 4; the same loose preselection is applied to both data samples and two NNs are used to separate background events from signal decays. A loose requirement is placed on the discriminating variable from the first network (NN_D) and the same parameter is used as an input to the second network (NN_B), which is designed to identify signal $B \rightarrow Dhh'$ decays. As described in Sec. 7.2.2, another loose requirement is placed on NN_B output. No attempt is made to optimise the value of either criterion since the precise value of the discriminant requirement does not strongly affect the sensitivity to the decay.

7.2.1 Selection differences

The suppressed $B^+ \rightarrow D^+ K^+ \pi^-$ mode has fewer dangerous peaking backgrounds than the control channel, so the PID requirements are loosened to retain more candidates. A looser PID requirement of $(\text{ProbNN}_K \times (1 - \text{ProbNN}_\pi)) > 0.5$ is placed on the bachelor kaon to reduce the contribution of $B^+ \rightarrow D^- \pi^+ \pi^+$ decays to the $B^+ \rightarrow D^- K^+ \pi^+$ data sample. The other kaon track in the final state must satisfy $(\text{ProbNN}_K \times (1 - \text{ProbNN}_\pi)) > 0.3$, and only events where all pions have $(\text{ProbNN}_\pi \times (1 - \text{ProbNN}_K)) > 0.2$ are retained.

These PID requirements reduce the background levels, but additional constraints must be imposed to reject contributions from specific decay modes. Only candidates with $m(DK) < 5140 \text{ MeV}/c^2$ are kept, in order to remove backgrounds from $B^0 \rightarrow D^- K^+$ decays combined with a random pion candidate. Similarly, potential $B^0 \rightarrow D^- \pi^+$ background is eliminated by requiring $m(D\pi) < 4790 \text{ MeV}/c^2$. Contributions from $B^+ \rightarrow D^+ \bar{D}^0$ decays, with $\bar{D}^0 \rightarrow K^+ \pi^-$, are removed by rejecting candidates within $\sim 3\sigma$ of the D^0 mass, corresponding to $1830 < m(K\pi) < 1890 \text{ MeV}/c^2$. Although each of these backgrounds affects only one of the $DK\pi$ final states, the vetoes are applied to both data samples to avoid biasing the relative efficiency.

7.2.2 Fit strategy

To maximise the chance of a first observation the maximum number of signal candidates must be retained by the selection procedure. For the analyses described in Chaps. 5, 6 and 8, a non-negligible number of signal decays are removed by placing a requirement on the NN_B discriminator, designed to separate the signal decays from the combinatorial background, as described in Chap. 4. An alternative approach is to bin the data in this output variable, rather than simply removing events which fail a certain criterion. A simultaneous fit can then be performed to the B^+ candidate invariant mass in bins of the NN_B output. This gives the largest possible number of signal (S) candidates, and good separation from the background (B) candidates when the S/B ratio is allowed to differ between the NN_B bins.

For this study, a loose preselection of $NN_B > -0.7$ is applied to both $D^- K^+ \pi^+$ and $D^+ K^+ \pi^-$ data samples; the remaining region is then divided into six bins with boundaries at $-0.7, 0.40, 0.73, 0.89, 0.95, 0.969, 1.0$. Since the signal region is blinded until after the fit model is finalised, various binning schemes are tested by generating and fitting simulated data samples with 30 $D^+ K^+ \pi^-$ signal events.²⁷ The scheme with six NN_B bins is found to give the greatest sensitivity to the $B^+ \rightarrow D^+ K^+ \pi^-$ signal (the fit is found to be unstable with more bins due to the increased number of free parameters). The bin boundaries are chosen such that all NN_B bins contain approximately the same number of $B^+ \rightarrow D^- K^+ \pi^+$ candidates.

After all of the selection requirements described, 7724 $B^+ \rightarrow D^- K^+ \pi^+$ candidate events remain. There are 4278 $B^+ \rightarrow D^+ K^+ \pi^-$ candidates surviving the same selection (excluding candidates in the blinded signal region of $5250 \leq m(D^+ K^+ \pi^-) \leq 5320 \text{ MeV}/c^2$). The B candidate invariant mass distributions are shown in Fig. 7.2.

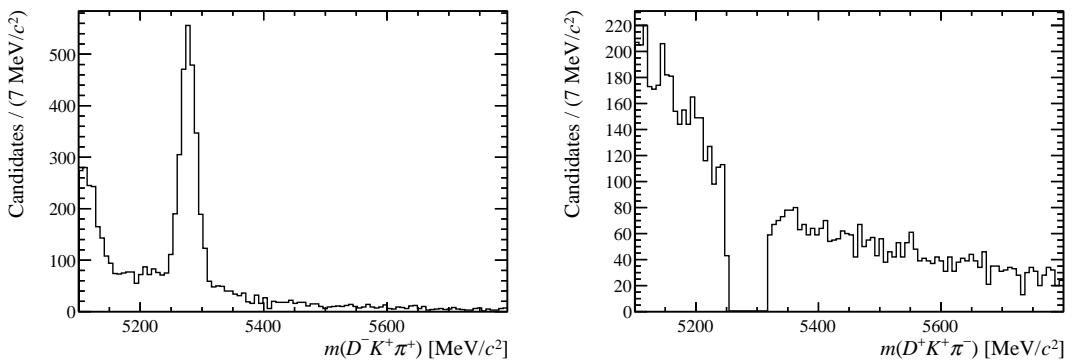


Figure 7.2: B invariant mass distributions for (left) $D^- K^+ \pi^+$ and (right) $D^+ K^+ \pi^-$ candidates after the initial selection and loose requirement on NN_B output. Note that candidates with $5250 \leq m(D^+ K^+ \pi^-) \leq 5320 \text{ MeV}/c^2$ are not plotted for the $B^+ \rightarrow D^+ K^+ \pi^-$ mode.

²⁷A $B^+ \rightarrow D^+ K^+ \pi^-$ signal yield of 30 events is based on the naïve expectation of the signal decay being ~ 100 times suppressed relative to the favoured $B^+ \rightarrow D^- K^+ \pi^+$ decay mode.

7.3 Fits to B^+ invariant mass distributions

The components in the fit to the control mode are the same as those for the fits documented in Chap. 5, with some modifications to the fit PDFs to account for the selection differences described in Sec. 7.2. For the signal mode fewer PDFs are required in the fit model:

- B signal;
- combinatorial background;
- partially reconstructed background from $\bar{B}_s^0 \rightarrow D^+ K^+ \pi^- \pi^-$.

The decay $B^+ \rightarrow D^+ \pi^+ \pi^-$ (equivalent to the background of $B^+ \rightarrow D^- \pi^+ \pi^+$ for the control mode) is expected to be suppressed with respect to $D^+ K^+ \pi^-$ in the SM, and no significant contribution from $B^+ \rightarrow D_s^+ K^+ \pi^-$ is expected. The main source of partially reconstructed background for $B^+ \rightarrow D^+ K^+ \pi^-$ is expected to be $\bar{B}_s^0 \rightarrow D^+ K^+ \pi^- \pi^-$. This decay mode is not yet observed, but since other related decays have been observed the branching fraction is expected to be sizeable. Another potential source of partially reconstructed background is the decay $B^+ \rightarrow D^{*+} K^+ \pi^-$. This contribution is expected to have a branching fraction ~ 3 times less than that of the $D^+ K^+ \pi^-$ signal, which is rare. No component is included for this background in the fit to $B^+ \rightarrow D^+ K^+ \pi^-$ candidates; any events from this source are instead absorbed into the $\bar{B}_s^0 \rightarrow D^+ K^+ \pi^- \pi^-$ component.

First the control mode data sample, $B^+ \rightarrow D^- K^+ \pi^+$, is fitted simultaneously in the six bins of NN_B output variable. Each contribution has a total yield which is floated, along with five fraction parameters that describe the relative yield of a component in each NN_B bin of the simultaneous fit.²⁸ Combinatorial and partially reconstructed backgrounds each have a dedicated set of fraction parameters ($f_{\text{comb}}^1 - f_{\text{comb}}^6$ and $f_{\text{part}}^1 - f_{\text{part}}^6$, respectively). The remaining contributions from signal and peaking backgrounds all share a common set of fractions ($f_{\text{sig}}^1 - f_{\text{sig}}^6$) as this helps to stabilise the fit in the low background bins. The larger signal yield for $D^- K^+ \pi^+$ allows the values of the signal fractions to be accurately determined. In the subsequent fit to the $D^+ K^+ \pi^-$ sample these parameters are then fixed to the values from the control mode mass fit.

²⁸Note that the fraction of a yield contained in the purest NN_B bin, f_x^6 , is given by $1 - f_x^1 - f_x^2 - f_x^3 - f_x^4 - f_x^5$.

Table 7.1: Parameters of the signal double Crystal Ball shape (Eq. 5.3) obtained from the fits to samples of simulated $D^- K^+ \pi^+$ and $D^+ K^+ \pi^-$ events.

Parameter	$D^- K^+ \pi^+$	$D^+ K^+ \pi^-$
μ (MeV/c ²)	5279.80 ± 0.15	5279.95 ± 0.21
σ_1 (MeV/c ²)	14.2 ± 1.6	15.2 ± 1.2
$R_{CB} = \sigma_2/\sigma_1$	0.78 ± 0.10	0.64 ± 0.05
α_1	-1.29 ± 0.45	-2.06 ± 0.32
α_2	1.90 ± 0.15	1.69 ± 0.23
n_1	3.89 ± 2.01	2.40 ± 1.77
n_2	1.07 ± 0.31	1.63 ± 0.52
f_{CB}	0.31 ± 0.16	0.42 ± 0.11

7.3.1 Fit components

7.3.1.1 Signal

As in Chap. 5, the signal component is parametrised as the sum of two CB functions with a common mean and tails on opposite sides. The same signal shape is used for all NN_B bins in the simultaneous fit. The $DK\pi$ invariant mass distributions from simulated samples of $B^+ \rightarrow D^- K^+ \pi^+$ and $B^+ \rightarrow D^+ K^+ \pi^-$ events are fitted with a double CB function to determine the tail parameters for each decay mode. The results of these fits to simulated samples are shown in Fig. 7.3 and Tab. 7.1. For the fits to $B^+ \rightarrow D^- K^+ \pi^+$ and $B^+ \rightarrow D^+ K^+ \pi^-$ candidates in data, the signal shape parameters are free, constrained or fixed, in the way described in Sec. 5.2.1. The fit parameters for the $B^+ \rightarrow D^- K^+ \pi^+$ mode are less precise than those reported in Tab. 5.1 due to the requirements on PID variables and NN_B output being loosened.

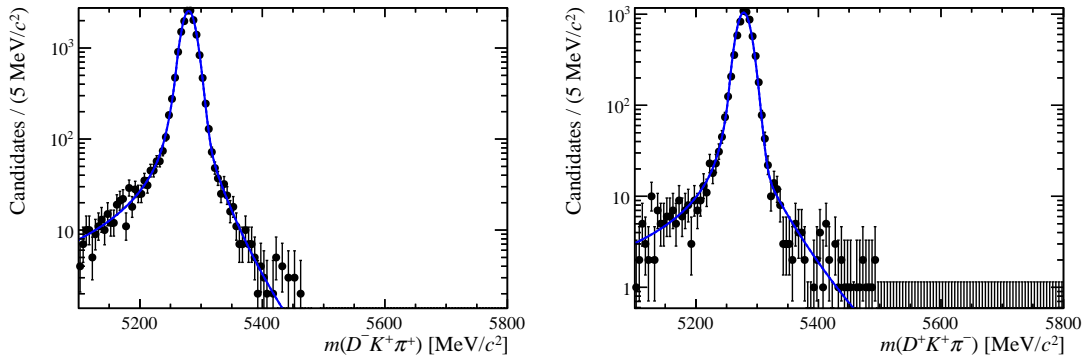


Figure 7.3: Fit to the B^+ candidate invariant mass distribution for simulated samples of (left) $B^+ \rightarrow D^- K^+ \pi^+$ and (right) $B^+ \rightarrow D^+ K^+ \pi^-$ events. Note that since the same signal shape is used for all NN_B bins in the simultaneous fit, only the loose requirement of $NN_B > -0.7$ is applied to these samples.

For the fit to the signal mode the fractional yields in each NN_B bin are fixed to be the same as those obtained from the $B^+ \rightarrow D^- K^+ \pi^+$ fit. The NN_B response for the two

decay modes is tested by comparing the distribution of the NN_B discriminator for simulated $D^- K^+ \pi^+$ and $D^+ K^+ \pi^-$ samples. The result, in Fig. 7.4, shows that the behaviour of the two modes appears to be similar. The Kolmogorov–Smirnov test suggests that these two distributions are statistically compatible at $\mathcal{O}(10^{-8})$. The visible differences are found to be due to correlations between the NN_B and Dalitz plot variables. The fit to $B^+ \rightarrow D^+ K^+ \pi^-$ candidates does not converge if these fractional yield parameters are allowed to vary. The systematic effect introduced by fixing the parameters to the values obtained for the control channel is investigated in Sec. 7.4.1.

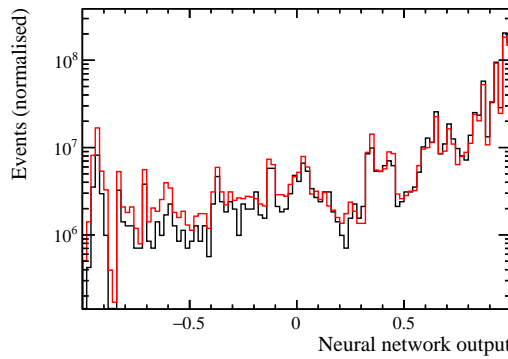


Figure 7.4: Comparison of the NN_B output variable for simulated data samples of signal modes $D^- K^+ \pi^+$ (red) and $D^+ K^+ \pi^-$ (black).

7.3.1.2 Combinatorial background

The combinatorial background component in both mass fits is modelled by an exponential function. The exponential slope is treated as a free parameter, allowed to take different values for fits to $B^+ \rightarrow D^- K^+ \pi^+$ and $B^+ \rightarrow D^+ K^+ \pi^-$ candidates, but the same value is used for all six NN_B bins in each simultaneous fit. The total combinatorial background yield in each fit, and the fractions in each NN_B bin (f_{comb}^i) are all floated in both data fits.

7.3.1.3 Peaking background

The peaking backgrounds included in the fit to $B^+ \rightarrow D^- K^+ \pi^+$ data are $B^+ \rightarrow D_s^- K^+ \pi^+$, $B^+ \rightarrow D^- \pi^+ \pi^+$ and $B^+ \rightarrow D^{*-} \pi^+ \pi^+$ (where the latter two are combined into a single PDF). No peaking background components are included in the $D^+ K^+ \pi^-$ fit.

Each peaking background is modelled by a smoothed non-parametric PDF obtained from simulated events. The samples of simulated $B^+ \rightarrow D^{(*)-} \pi^+ \pi^+$ events are reweighted to match the Dalitz plot distribution observed in data. No such weighting can be applied to $B^+ \rightarrow D_s^- K^+ \pi^+$ since the true DP distribution of this decay mode is not known, except

that it peaks at low $m(D_s^- K^+)$ [104, 105]. The PDFs used to describe $B^+ \rightarrow D^{(*)-} \pi^+ \pi^+$ and $B^+ \rightarrow D_s^- K^+ \pi^+$ contributions are shown in Fig. 7.5. The total yield of each peaking background is allowed to float in the fit to data, though the relative fractions of these backgrounds in each NN_B bin are fixed to be the same as those for the signal component (f_{sig}^i).

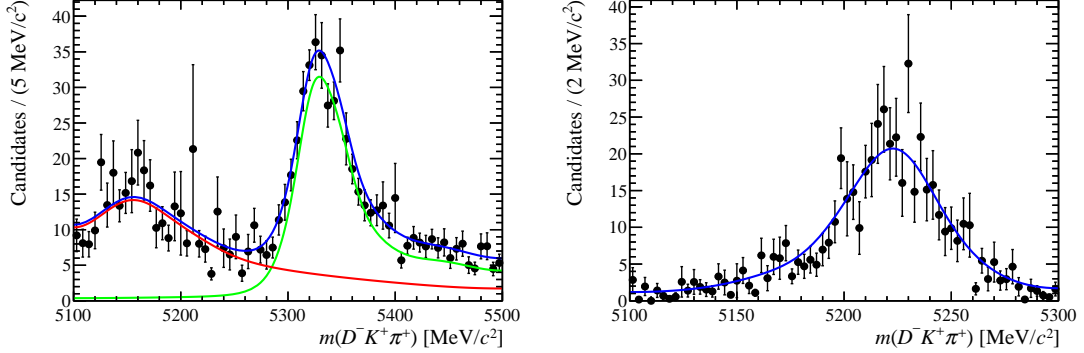


Figure 7.5: Reconstructed B^+ candidate mass distributions of peaking backgrounds to $B^+ \rightarrow D^- K^+ \pi^+$ from simulated samples of (left) $B^+ \rightarrow D^{(*)-} \pi^+ \pi^+$ and (right) $B^+ \rightarrow D_s^- K^+ \pi^+$ decays. For the $B^+ \rightarrow D^{(*)-} \pi^+ \pi^+$ shape, the (red) $D^{*-} \pi^+ \pi^+$ and (green) $D^- \pi^+ \pi^+$ contributions are combined with a fixed factor according to the measured branching fractions of the two modes [3].

7.3.1.4 Partially reconstructed background

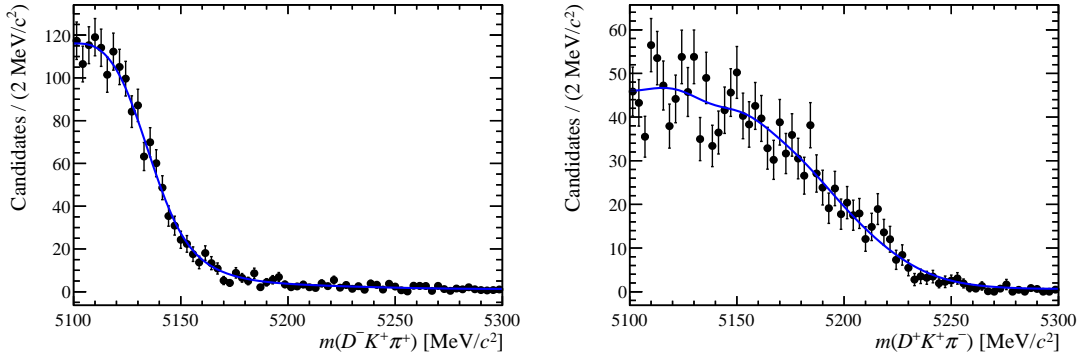


Figure 7.6: Reconstructed B^+ candidate mass distributions of partially reconstructed backgrounds to (left) $B^+ \rightarrow D^- K^+ \pi^+$ and (right) $B^+ \rightarrow D^+ K^+ \pi^-$, from simulated $B^+ \rightarrow D^{*-} K^+ \pi^+$ and $\bar{B}_s^0 \rightarrow D^+ K^+ \pi^- \pi^-$ samples, respectively.

The main source of partially reconstructed background for $D^- K^+ \pi^+$ is $B^+ \rightarrow D^{*-} K^+ \pi^+$, whilst $\bar{B}_s^0 \rightarrow D^+ K^+ \pi^- \pi^-$ is the dominant contribution for $D^+ K^+ \pi^-$. Simulated events are generated to produce smoothed non-parametric PDFs to describe these components in the fits to data. The true phase space distribution of $\bar{B}_s^0 \rightarrow D^+ K^+ \pi^- \pi^-$ decays is unknown, so five separate $\bar{B}_s^0 \rightarrow D^+ K^+ \pi^- \pi^-$ samples are generated and combined: four with resonances ($\bar{B}_s^0 \rightarrow D_0^*(2420)^0 K^*(892)^0$, $D_2^*(2460)^0 K^*(892)^0$, $D_{s1}^*(2860)^+ \pi^-$, $D_{s3}^*(2860)^+ \pi^-$) and one flat in phase space. The

DP distribution of $B^+ \rightarrow D^{*-} K^+ \pi^+$ decays is also not known, so the simulated events are not reweighted. The resultant PDFs are shown in Fig. 7.6.

The total yields of these partially reconstructed backgrounds are free parameters in the simultaneous fits to data. In the $D^- K^+ \pi^+$ fit the fractions of $B^+ \rightarrow D^{*-} K^+ \pi^+$ background in each NN_B bin (f_{part}^i) are allowed to float. For the subsequent fit to $D^+ K^+ \pi^-$ data the corresponding fractions for the partially reconstructed $\bar{B}_s^0 \rightarrow D^+ K^+ \pi^- \pi^-$ background are fixed to values obtained in the control mode fit.

7.3.2 Fit validation

Simulated data samples are generated and fitted with these models to check the stability of the fit and ensure that the extracted signal yields are unbiased. For each decay mode the total fit PDF is used to generate 1000 unique mass distributions, where each component yield is varied from the true value with the application of Poisson fluctuations. In the case of the $D^+ K^+ \pi^-$ fit, ensembles are generated with the B^+ signal yield set to values of 30 and 0 since the signal region and fitted yield are blinded. The data samples are then all fitted independently with the fit model described above to obtain the distributions of each fit parameter and their pulls. The obtained pull distributions for all fit parameters are found to be consistent with a Gaussian of width one and mean zero, indicating that the statistical uncertainties reported by the fit are accurate and any systematic bias is small.

7.3.3 Fit results

The fit to the $B^+ \rightarrow D^- K^+ \pi^+$ data sample is shown in Fig. 7.7 and the values of all free parameters are reported in Tab. 7.2. In the signal $D^+ K^+ \pi^-$ mode fit, the fraction of events in the core CB function (f_{CB}) and the ratio of CB widths (R_{CB}) are floated with Gaussian constraints formed from the fit to simulated $B^+ \rightarrow D^+ K^+ \pi^-$ events. The mean and width of the signal shape are fixed to the values obtained from the control mode fit and presented in Tab. 7.2. This strategy stabilises the signal peak position in cases of low signal yield. All fractional yields (f_x^i) are fixed to the values obtained in the control mode fit, with the exception of those for the combinatorial background, which are floated.

The unblinded fit to $B^+ \rightarrow D^+ K^+ \pi^-$ candidates is shown in Fig. 7.8 and Tab. 7.2. A signal yield of 164 ± 21 events is observed. The statistical significance of the $B^+ \rightarrow D^+ K^+ \pi^-$ signal peak is evaluated to be 11.2σ , based on the square root of twice the change in negative log likelihood from the value obtained in a fit with zero signal yield. Figure 7.9 shows weighted mass distributions of all $B^+ \rightarrow D^- K^+ \pi^+$ and

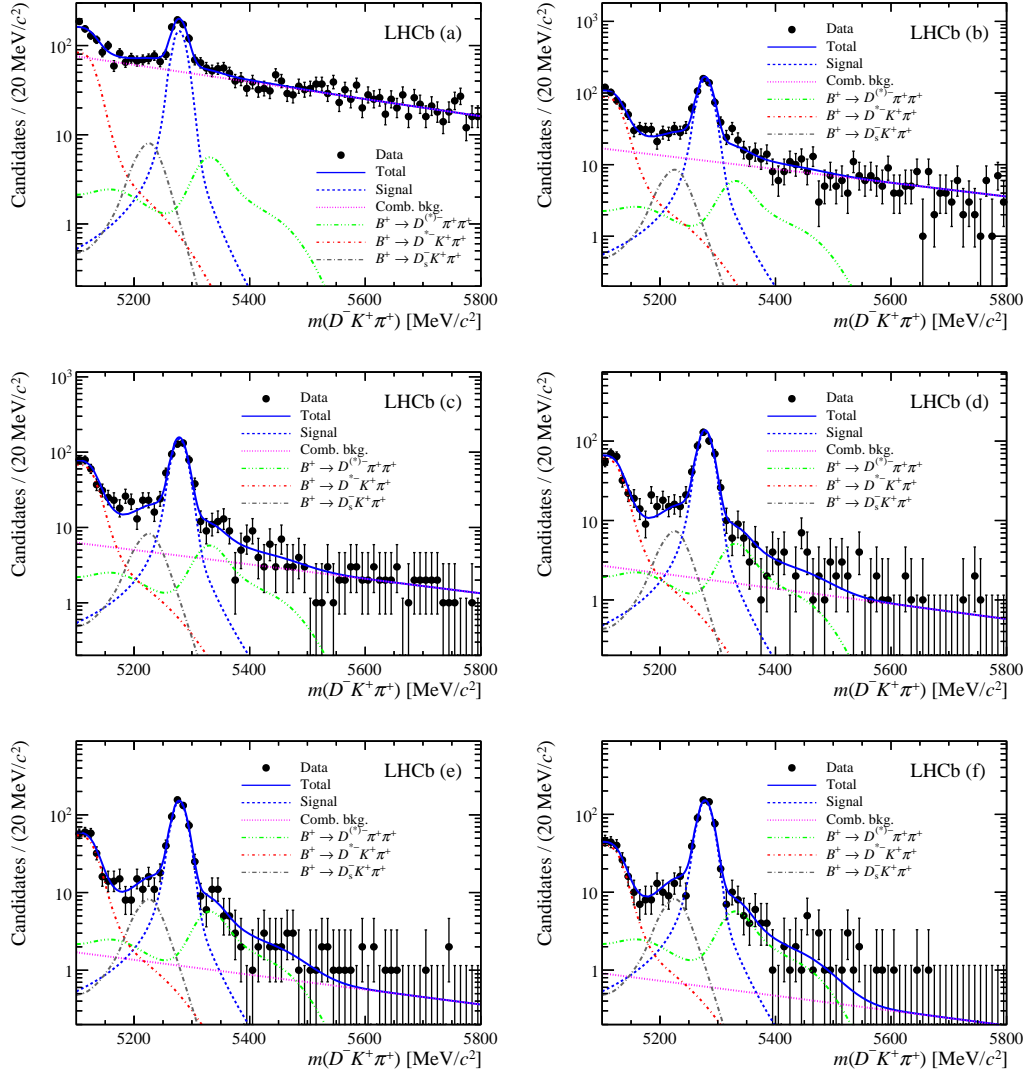


Figure 7.7: Projections of the simultaneous fit to $B^+ \rightarrow D^- K^+ \pi^+$ candidates in each of the six bins of the NN_B output. From top to bottom, left to right, they are $[-0.70, 0.40]$, $[0.40, 0.73]$, $[0.73, 0.89]$, $[0.89, 0.95]$, $[0.95, 0.969]$, $[0.969, 1.00]$. The data points are shown in black and the fit components are described in the legend.

$B^+ \rightarrow D^+ K^+ \pi^-$ events. Candidates from each bin of NN_B output are weighted according to the value of $S/(S + B)$, where S is the fitted number of signal events and B is the number of background events within $\mu \pm 2.5\sigma_1$.

7.3.4 Efficiency

The method described in Sec. 4.4 is used to study the efficiency variation for $B^+ \rightarrow D^+ K^+ \pi^-$ candidates over the Dalitz plot. High-resolution histograms are generated for each contribution and multiplied together to create the final distributions shown in Fig. 7.10.

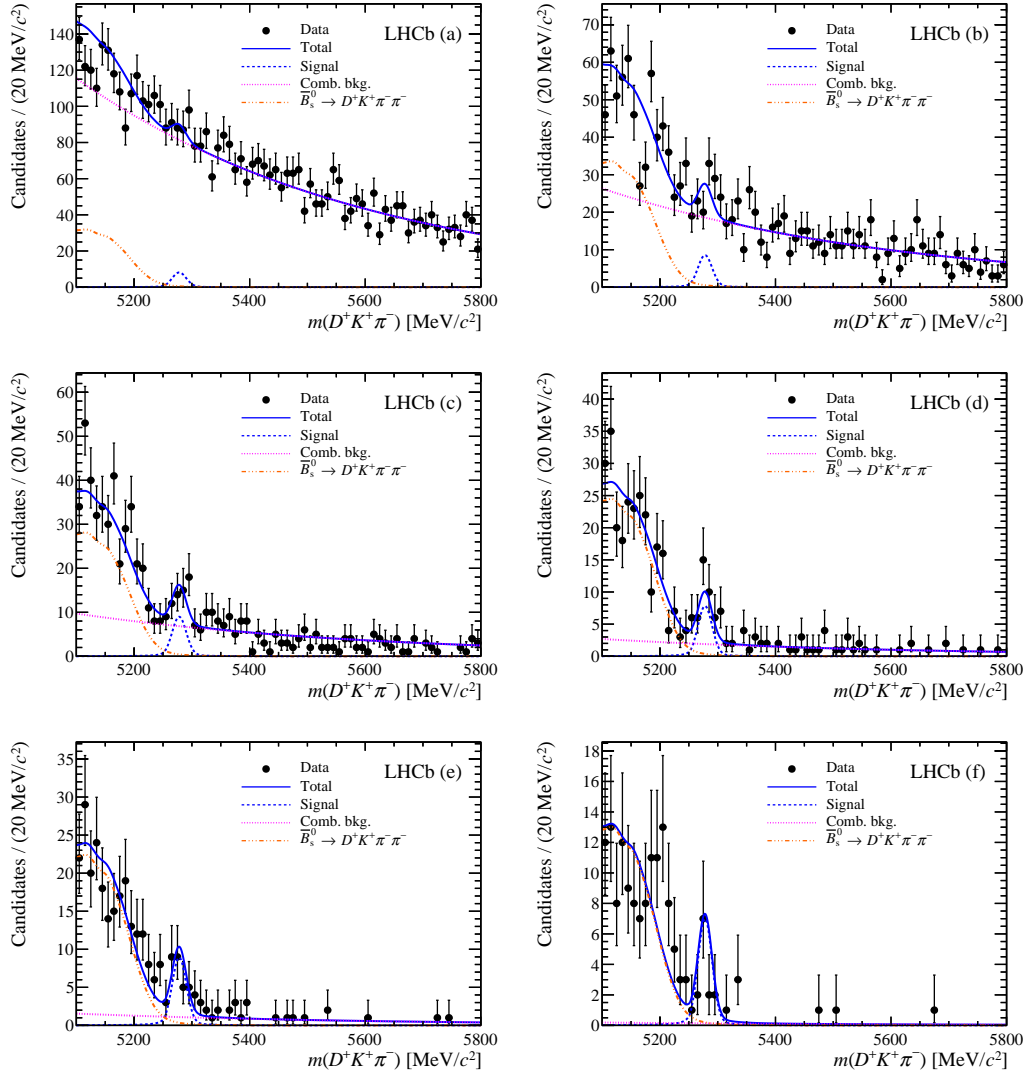


Figure 7.8: Projections of the unblinded simultaneous fit to $B^+ \rightarrow D^+ K^+ \pi^-$ candidates in each of the six bins of the NN_B output. From top to bottom, left to right, they are $[-0.70, 0.40]$, $[0.40, 0.73]$, $[0.73, 0.89]$, $[0.89, 0.95]$, $[0.95, 0.969]$, $[0.969, 1.00]$. The data points are shown in black and the fit components are described in the legend.

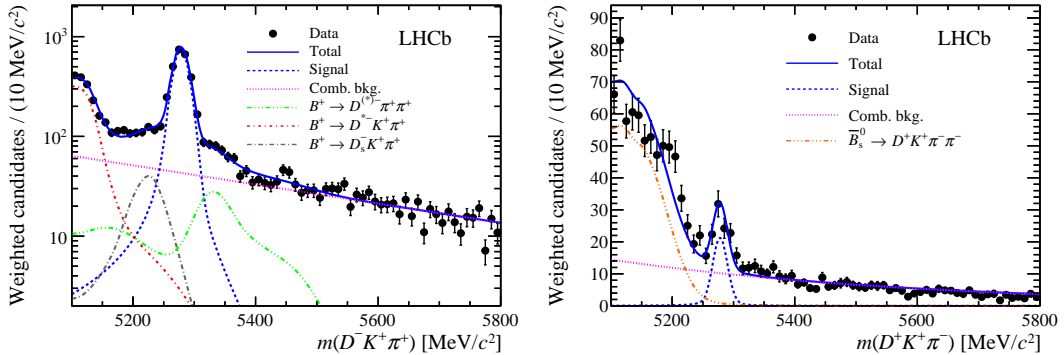


Figure 7.9: Weighted distribution of (left) $B^+ \rightarrow D^- K^+ \pi^+$ and (right) $B^+ \rightarrow D^+ K^+ \pi^-$ candidates for all six NN_B bins. Each NN_B bin is weighted by the value of $S/(S + B)$, as described in the text. The data points are shown in black and the fit components are described in the legend.

Table 7.2: Values of the floated parameters from independent fits to $B^+ \rightarrow D^- K^+ \pi^+$ and $B^+ \rightarrow D^+ K^+ \pi^-$ decay modes.

Parameter	$D^- K^+ \pi^+$	$D^+ K^+ \pi^-$
f_{comb}^1	0.727 ± 0.0055	0.7436 ± 0.008
f_{sig}^1	0.1661 ± 0.009	fixed
$f_{\text{part.}}^1$	0.214 ± 0.018	fixed
f_{comb}^2	0.1611 ± 0.0076	0.171 ± 0.0062
f_{sig}^2	0.1755 ± 0.0061	fixed
$f_{\text{part.}}^2$	0.225 ± 0.012	fixed
f_{comb}^3	0.06 ± 0.0031	0.0583 ± 0.0039
f_{sig}^3	0.1709 ± 0.0052	fixed
$f_{\text{part.}}^3$	0.1727 ± 0.0084	fixed
f_{comb}^4	0.0261 ± 0.0023	0.0164 ± 0.0022
f_{sig}^4	0.1509 ± 0.0049	fixed
$f_{\text{part.}}^4$	0.1525 ± 0.0079	fixed
f_{comb}^5	0.0166 ± 0.0022	0.0093 ± 0.0018
f_{sig}^5	0.1686 ± 0.0053	fixed
$f_{\text{part.}}^5$	0.136 ± 0.0075	fixed
$N(D^{(*)}\pi\pi)$	548 ± 67	—
$N(D_s K\pi)$	342 ± 42	—
$N(\text{part. reco. bkg.})$	1676 ± 57	1425 ± 54
$N(\text{comb. bkg.})$	3710 ± 110	5945 ± 89
$N(\text{signal})$	3101 ± 66	164 ± 21
Exponential slope	-0.00218 ± 0.00013	-0.00196 ± 0.00008
R_{CB}	0.82 ± 0.018	0.795 ± 0.014
f_{CB}	0.15 ± 0.029	0.095 ± 0.027
Mean	5277.95 ± 0.29	fixed
Width	15.41 ± 0.29	fixed

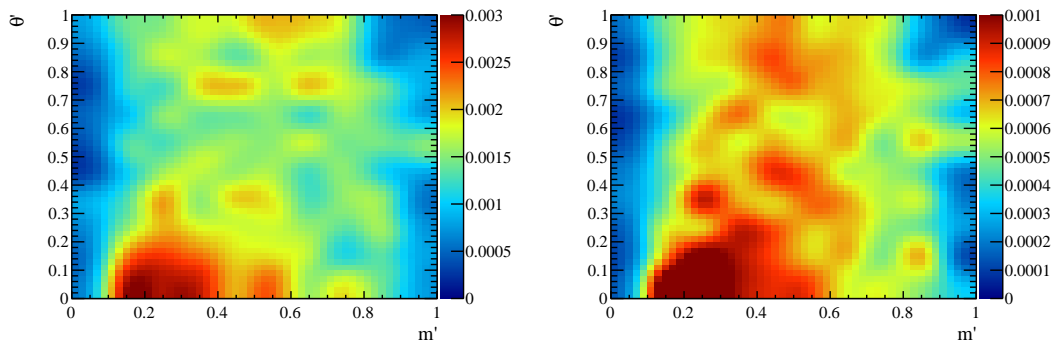


Figure 7.10: Efficiency variation across the SDP for $B^+ \rightarrow D^+ K^+ \pi^-$, determined separately for candidates triggered as (left) L0 hadron TOS and (right) L0 global TIS and L0 hadron !TOS.

7.4 Systematic uncertainties

Several sources of systematic uncertainty are considered for the $B^+ \rightarrow D^+ K^+ \pi^-$ branching fraction measurement. The relative contribution of each source is summarised in Tab. 7.3 and the determination of each value is described below. Systematic effects on the signal yield are required to determine the significance of the branching fraction measurement. Due to correlations between uncertainties, for the uncertainty of the branching fraction result itself the relevant quantity is the systematic effect on the branching fraction ratio.

Table 7.3: Summary of systematic uncertainties from the search for the decay $B^+ \rightarrow D^+ K^+ \pi^-$. All values are shown in %. In cases where an uncertainty affects both $D^- K^+ \pi^+$ and $D^+ K^+ \pi^-$ yields, correlations are taken into account by applying the same check to both modes together to calculate the effect on the branching fraction ratio.

Source	$N(D^- K^+ \pi^+)$	$N(D^+ K^+ \pi^-)$	BF ratio
Fit model			
Signal PDF	0.95	1.60	1.96
Combinatorial background PDF	0.53	4.59	4.41
$\bar{B}_s^0 \rightarrow D^+ K^+ \pi^- \pi^-$ background PDF	–	0.97	0.97
PDFs for backgrounds in $B^+ \rightarrow D^- K^+ \pi^+$ fit	0.84	0.86	1.07
PDF smoothing	0.52	0.81	1.34
Signal NN_B bin fractions	–	0.32	0.32
Partially reconstructed background NN_B bin fractions	–	4.16	4.16
Peaking background NN_B bin fractions	0.13	0.47	0.60
Fit bias	0.18	0.75	0.93
Multiple candidates	0.19	0.61	0.41
Subtotal	1.50	6.67	6.78
Efficiency ratio			
Map variation	–	–	5.87
PidCALIB binning	–	–	0.76
Total			
Total	1.50	6.67	9.00

7.4.1 Fit model

The $B^+ \rightarrow D^- K^+ \pi^+$ and $B^+ \rightarrow D^+ K^+ \pi^-$ fit models described in Sec. 7.3.1 are varied by using alternative PDFs to describe the invariant mass distribution of each component. In both fits, parameters fixed in the signal mass PDF are varied within their uncertainties (determined from simulation) and the exponential combinatorial background PDF is replaced by a second-order polynomial. To account for possible correlations between the B^+ candidate mass and variables used to train NN_B , the mass and width of the signal PDF are allowed to take different values in the least pure NN_B bin. The slope parameter of the exponential shape is also allowed to vary in this NN_B bin.²⁹ The

²⁹The statistics in the two purest NN_B bins are too low to allow these parameters to vary individually in all six bins.

$\bar{B}_s^0 \rightarrow D^+ K^+ \pi^- \pi^-$ PDF is replaced by a shape made with a $\bar{B}_s^0 \rightarrow D_{s1}^*(2536)^+ \pi^-$ contribution instead of the two $D_{sJ}^*(2860)^+ \pi^-$ samples described in Sec. 7.3.1.4.³⁰ The DP reweighting is removed from the $B^+ \rightarrow D^{(*)-} \pi^+ \pi^+$ background PDF, and $B^+ \rightarrow D_s^- K^+ \pi^+$, which is unweighted in the nominal fit, is weighted so as to enhance the contribution at low $m(D_s K)$. The amount of smoothing applied to all non-parametric PDFs is reduced.

One source of uncertainty is the method of fixing fractional yields ($f_x^1 - f_x^6$) in each NN_B bin for the fit to $B^+ \rightarrow D^+ K^+ \pi^-$ candidates. In the case of $f_{\text{sig}}^1 - f_{\text{sig}}^6$ this assumes that the NN_B response is identical for $B^+ \rightarrow D^+ K^+ \pi^-$ and $B^+ \rightarrow D^- K^+ \pi^+$ decays. The systematic uncertainty is evaluated by correcting the fractional yields found in the $B^+ \rightarrow D^- K^+ \pi^+$ fit by the ratio of fractional yields from simulation. The uncertainty due to $f_{\text{part}}^1 - f_{\text{part}}^6$ is estimated in the same way, using samples of simulated $\bar{B}_s^0 \rightarrow D^+ K^+ \pi^- \pi^-$ and $B^+ \rightarrow D^{*-} K^+ \pi^+$ events. For peaking backgrounds in the $D^- K^+ \pi^+$ fit, the associated systematic uncertainty is calculated by fixing the fractional yields in each NN_B bin to the values found in simulation rather than using the same fractional yields as the signal decay.

The magnitude of any systematic bias in the fitting procedure is evaluated by fitting simulated data samples similar to those described in Sec. 7.3.2, but generated with the observed signal yields. The systematic uncertainty of each $DK\pi$ yield is taken as the difference between the nominal fit result and the mean of a Gaussian fitted to the signal yield obtained from fits to simulated samples.

Rather than retaining all multiple candidates in the dataset, a $DK\pi$ candidate is selected at random from events with more than one. This procedure is repeated 100 times to obtain a set of different data samples, and the mass fit is performed on each. The spread in the measured signal yield is assigned as the systematic uncertainty.

7.4.2 Efficiency ratio

The effect of geometrical acceptance can be determined precisely from simulation, but efficiency variations across phase space may not be modelled correctly in simulated data samples and the limited statistics are a source of systematic uncertainty. To quantify the systematic effect, the two $DK\pi$ efficiency distributions are varied within their errors, as described in Sec. 6.5.1. For PID efficiency, there is an additional effect from the choice of PIDCALIB binning scheme (described in Sec. 4.4.3). Other possible sources of uncertainty on the ratio of efficiencies are found to be negligible.

³⁰A dedicated study of the $\bar{B}_s^0 \rightarrow D^+ K^+ \pi^- \pi^-$ decay mode in the future could reduce this source of uncertainty, but it is not a limiting factor for this measurement of $B^+ \rightarrow D^+ K^+ \pi^-$.

7.4.3 Cross checks

The stability of the branching fraction result is checked by performing the $D^- K^+ \pi^+$ and $D^+ K^+ \pi^-$ mass fits with alternative datasets. The requirements imposed on the NN_B output and PID variables relating to the bachelor kaon are varied, and the number of NN_B bins used in the simultaneous mass fits is altered. The nominal datasets are also divided by L0 trigger category, magnet polarity and year of data taking. For all checks, the ratio of the two fitted signal yields is found to be consistent with that obtained from the nominal fit results.

7.5 Results

The ratio of $DK\pi$ branching fractions is calculated as

$$\frac{\mathcal{B}(B^+ \rightarrow D^+ K^+ \pi^-)}{\mathcal{B}(B^+ \rightarrow D^- K^+ \pi^+)} = \frac{N^{\text{corr}}(D^+ K^+ \pi^-)}{N^{\text{corr}}(D^- K^+ \pi^+)} , \quad (7.1)$$

where $N^{\text{corr}}(DK\pi) = \sum_i (W_i/\epsilon_i^{\text{tot}})$ are calculated as described in Sec. 5.4. The corrected number of candidates and the raw yields are shown for both $D^+ K^+ \pi^-$ and $D^- K^+ \pi^+$ final states in Tab. 7.4.

Table 7.4: Raw yields and event-by-event efficiency-corrected numbers of events for the $D^+ K^+ \pi^-$ and $D^- K^+ \pi^+$ datasets.

	$D^- K^+ \pi^+$	$D^+ K^+ \pi^-$
N	3101 ± 66	164 ± 21
N_{corr}	3925314 ± 91404	284977 ± 47713

From Eq. 7.1, the ratio of branching fractions is determined to be

$$\frac{\mathcal{B}(B^+ \rightarrow D^+ K^+ \pi^-)}{\mathcal{B}(B^+ \rightarrow D^- K^+ \pi^+)} = 0.0726 \pm 0.0123(\text{stat}) \pm 0.0065(\text{syst}) . \quad (7.2)$$

Using $\mathcal{B}(B^+ \rightarrow D^- K^+ \pi^+) = (7.31 \pm 0.19 \pm 0.22 \pm 0.39) \times 10^{-5}$ [1] from Chap. 5 gives

$$\mathcal{B}(B^+ \rightarrow D^+ K^+ \pi^-) = (5.31 \pm 0.90 \pm 0.48 \pm 0.35) \times 10^{-6} , \quad (7.3)$$

where the first uncertainty is statistical, the second systematic and the third from the uncertainty on the measured value of $\mathcal{B}(B^+ \rightarrow D^- K^+ \pi^+)$.

The statistical significance of the $B^+ \rightarrow D^+ K^+ \pi^-$ signal is evaluated by examining the likelihood, \mathcal{L} , of the mass fit for different values of $D^+ K^+ \pi^-$ signal yield. The signal significance is calculated as $\sqrt{2\Delta(-\ln\mathcal{L})}$, where $\Delta(-\ln\mathcal{L})$ is the difference in negative log likelihood between the best fit and for a fit with a signal yield of zero. Without systematic effects, the statistical significance is 11.2σ , as shown by the red likelihood

profile in Fig. 7.11. Considering the effect of systematic uncertainties which affect the signal yield, the signal significance is 8.0σ .

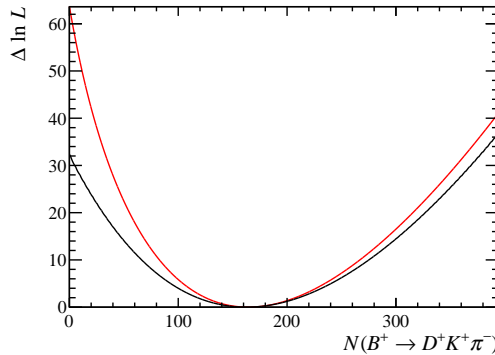


Figure 7.11: Change in negative log likelihood for the fit to $B^+ \rightarrow D^+ K^+ \pi^-$ candidates, as a function of the $D^+ K^+ \pi^-$ signal yield. Curves are shown both with (black) and without (red) systematic uncertainties considered.

The Dalitz plot distribution of $B^+ \rightarrow D^+ K^+ \pi^-$ candidates is shown in Fig. 7.12 with sideband subtraction used to remove backgrounds. The invariant mass distributions are also shown. There is little clear structure in the Dalitz plot. An excess at high $m(D\pi)$ and low $m(DK)$ is likely to be due to residual partially reconstructed background events. Some excess is seen at low $m(D\pi)$, but it is rather broad and seems more likely to be due to S-wave rather than the $D_2^*(2460)$ resonance. There is also a possible excess at low $m(K\pi)$, but again there is no obvious narrow peak.

7.6 Quasi-two-body decays

The $D^+ K^+ \pi^-$ data sample described in Sec. 7.2 is also studied to measure the contributions from the quasi-two-body $B^+ \rightarrow D_2^*(2460)^0 K^+$ and $B^+ \rightarrow D^+ K^*(892)^0$ decays. Unfortunately the observed yield of the $B^+ \rightarrow D^+ K^+ \pi^-$ decay is insufficient to perform a full Dalitz plot analysis. In addition, contributions from other intermediate states cannot be reduced to a negligible level simply by placing requirements on the two-body invariant masses. Instead angular decay distributions are used to isolate particular resonances; the quasi-two-body yields are obtained from fits to the B^+ invariant mass distribution of candidates in the appropriate two-body invariant mass range, with weights applied for angular moments and efficiency correction. The $B^+ \rightarrow D^- K^+ \pi^+$ mode is again used for normalisation to reduce potential sources of systematic bias.

Specific partial waves can be separated by weighting the data according to the value of the Legendre polynomial of order L , P_L , evaluated as a function of the cosine of the helicity angle of the $K^+ \pi^-$ or $D^+ \pi^-$ system.³¹ If only resonances up to spin J_{\max} are

³¹The helicity angle is defined as the angle between the momentum vectors of the pion and the B^+ candidate in the $K^+ \pi^-$ or $D^+ \pi^-$ rest frame.

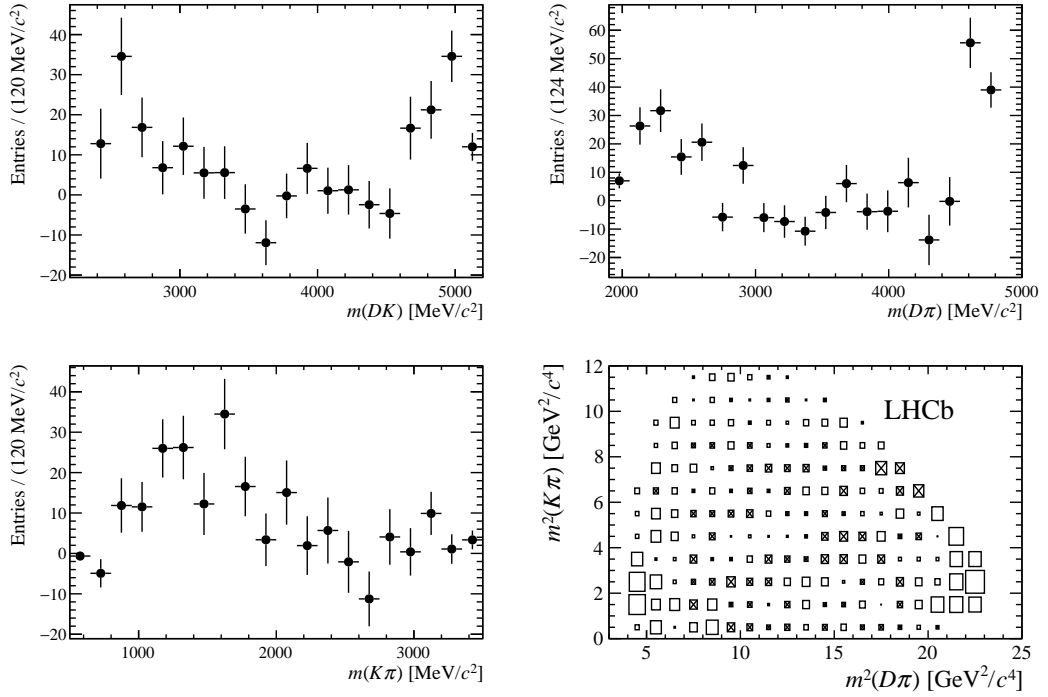


Figure 7.12: $B^+ \rightarrow D^+ K^+ \pi^-$ Dalitz plot (bottom right) and invariant mass distributions with sideband subtraction applied. The signal region is defined as $5260 \leq m(D^+ K^+ \pi^-) \leq 5310 \text{ MeV}/c^2$ and the sideband region as $m(D^+ K^+ \pi^-) > 5400 \text{ MeV}/c^2$. Areas of boxes are proportional to signal yields, with negative yields indicated by crosses.

present in a certain mass region then the $P_{2J_{\max}}$ moment will isolate the highest spin state. In the absence of high partial waves, the second and fourth Legendre moments are given by

$$P_2 = \frac{2|h_0||h_2|\cos(\delta_0 - \delta_2)}{\sqrt{5}} + \frac{2|h_1|^2}{5} + \frac{2|h_2|^2}{7}, \quad (7.4)$$

$$P_4 = \frac{2|h_2|^2}{7}, \quad (7.5)$$

where the amplitudes of spin J are denoted $h_J e^{i\delta_J}$. Thus weighting by the fourth Legendre moment isolates spin 2 contributions, and in the low $m(K^+ \pi^-)$ region P_2 weights can be used to study the $K^*(892)^0$ resonance contribution.

7.6.1 Fit strategy

In the limit that only $D^+ \pi^-$ resonances up to spin-2 contribute, weighting data by P_4 in the relevant region of $m(D^+ \pi^-)$ will isolate the $B^+ \rightarrow D_2^*(2460)^0 K^+$ component. Similarly, applying P_2 weights to data at low $m(K^+ \pi^-)$ can separate the $K^*(892)^0$ resonant contribution. To isolate resonant structures in $m(D\pi)$ the angular weights are calculated from the $D\pi$ helicity angle, while the $K\pi$ weights are used for resonances in

$m(K\pi)$. The helicity angles and two-body invariant masses are calculated with a constraint imposed on the B meson mass. Event-by-event efficiency corrections, determined as a function of Dalitz plot position, are also applied. Higher partial waves occur due to the tails of higher spin resonances or reflections from resonances decaying to a different pair of final state particles; such contributions also cause an excess of events in regions away from the resonance peak, therefore sideband subtraction can be used to account for the effect.

The branching fraction of $B^+ \rightarrow D_2^*(2460)^0 K^+$ is measured relative to the previously observed $B^+ \rightarrow \bar{D}_2^*(2460)^0 K^+$ in $B^+ \rightarrow D^- K^+ \pi^+$ decays (detailed in Chap. 6). Candidates are selected within a region of approximately $\pm 2\Gamma$, where Γ is the natural width [3], around the peaks of the $\bar{D}_2^*(2460)^0$ resonance in $m(D^\pm \pi^\mp)$. This corresponds to 2364.6–2560.6 MeV/ c^2 . Applying an event-by-event efficiency correction and P_4 angular weights to both $D^+ K^+ \pi^-$ and $D^- K^+ \pi^+$ samples ensures that the relative normalisations cancel in the ratio – the branching fraction ratio is then obtained directly from the ratio of fitted yields. For the signal mode there may be higher moments present, as any K^{**} resonances in $m(K\pi)$ would contribute as reflections. In the narrow two-body invariant mass range considered, higher moments will give a shape which is approximately linear with $m(D\pi)$. Thus the effect of any bias from reflections can be estimated by subtracting the yields obtained from similar fits to events from the sidebands of the $\bar{D}_2^*(2460)^0$ mass region. Sideband subtraction is applied to both signal and normalisation modes, with the sidebands defined as the ranges $3\Gamma < |m(D\pi) - m(D_2^*(2460)^0)| < 5\Gamma$, corresponding to 2217.6–2315.6 MeV/ c^2 and 2609.6–2707.6 MeV/ c^2 .

Since there is no contribution from K^{**} resonances in $B^+ \rightarrow D^- K^+ \pi^+$, the measurement of $B^+ \rightarrow K^*(892)^0 D^+$ is normalised using the full $B^+ \rightarrow D^- K^+ \pi^+$ sample. Event-by-event efficiency corrections and angular weights are applied to $D^+ K^+ \pi^-$ candidates within $\pm 2\Gamma$ of the $K^*(892)^0$ resonance ($801.0 < m(K^+ \pi^-) < 990.6$ MeV/ c^2). Candidates for the $D^- K^+ \pi^+$ decay are also efficiency-corrected, but no requirement is placed on $m(K^+ \pi^+)$ and P_0 angular weights are applied (equivalent to 1.0 for all events). The relative efficiency normalisation therefore cancels in the ratio of extracted yields, but a correction factor of $1/\left(\frac{2}{5}\right)$ must be applied to the weighted yield obtained for $B^+ \rightarrow K^*(892)^0 D^+$ (from Eq. 7.4). In addition, a correction is applied to account for the efficiency of the $K^*(892)^0$ signal region requirement on $D^+ K^+ \pi^-$ data ($\epsilon(K^*(892)^0)$), which is determined to be 0.857 ± 0.006 using simulated decays. Any effect from the reflections of D^{**} resonances is estimated using sideband regions of 658.8–753.6 MeV/ c^2 and 1038.0–1132.8 MeV/ c^2 around the $K^*(892)^0$ resonance in $m(K^+ \pi^-)$.

Measured signal yields are obtained from binned minimum χ^2 fits to the B^+ candidate mass distribution. These are used to measure the branching fraction ratios

$$\frac{\mathcal{B}(B^+ \rightarrow D_2^*(2460)^0 K^+)}{\mathcal{B}(B^+ \rightarrow \bar{D}_2^*(2460)^0 K^+)} \equiv (r_B(D_2^*(2460)K^+))^2 = \frac{\tilde{N}^{\text{corr}}(B^+ \rightarrow D_2^*(2460)^0 K^+)}{\tilde{N}^{\text{corr}}(B^+ \rightarrow \bar{D}_2^*(2460)^0 K^+)} , \quad (7.6)$$

$$\frac{\mathcal{B}(B^+ \rightarrow D^+ K^*(892)^0 \rightarrow D^+ K^+ \pi^-)}{\mathcal{B}(B^+ \rightarrow D^- K^+ \pi^+)} = \frac{\tilde{N}^{\text{corr}}(B^+ \rightarrow D^+ K^*(892)^0) \cdot (\frac{5}{2})}{\tilde{N}^{\text{corr}}(B^+ \rightarrow D^- K^+ \pi^+) \epsilon(K^*(892)^0)} , \quad (7.7)$$

where \tilde{N}^{corr} are the yields obtained from the fit after accounting for subtraction of higher moments as estimated from the sideband regions.

7.6.2 Fit model

The fit models employed are based on those detailed in Sec. 7.3.1, though some alterations are made. The events from all six NN_B bins are combined for the fit; it is no longer necessary to bin the data in the NN_B output and perform a simultaneous fit because the combinatorial background is substantially reduced by the weighting procedure. The remaining combinatorial background events are modelled by a linear PDF rather than an exponential, to allow the weighted background yield to become negative. Angular moment weighting and two-body invariant mass requirements are applied to simulated samples of $B^+ \rightarrow D^{(*)-} \pi^+ \pi^+$ and $\bar{B}_s^0 \rightarrow D^+ K^+ \pi^- \pi^-$ decays to create alternative non-parametric functions to model these backgrounds. No background is expected from mis-identified $B^+ \rightarrow D_s^- K^+ \pi^+$ decays after angular weights have been applied, so no component is included in the fits to $D^- K^+ \pi^+$ events. Legendre moment weights are found to have little effect on the signal MC shape for $D^+ K^+ \pi^-$ and $D^- K^+ \pi^+$ candidates, so the signal PDFs are not modified from those introduced in Sec. 7.3.1. For partially reconstructed background from $B^+ \rightarrow D^{*-} K^+ \pi^+$ decays, the shape is also unchanged.

Simulated pseudoexperiments and $B^+ \rightarrow D^- K^+ \pi^+$ candidates are used to validate the analysis strategy and fit model. The fit fraction for $B^+ \rightarrow \bar{D}_2^*(2460)^0 K^+$ decays measured with this method is found to agree with the result obtained from the Dalitz plot analysis presented in Chap. 6.

7.6.3 Fit results

Fits to the efficiency-corrected and angular-weighted data samples are shown in Figs. 7.13 and 7.14. Note that the coarse and variable binning in these fits is tuned to obtain stable fits with the default configuration (*i.e.* no empty bins in either signal or sideband regions, since the χ^2 fit does not handle these well). Table 7.5 shows the signal yields obtained from these fits.

Figure 7.13 (centre right) shows that, as expected, the weighting procedure isolates the $B^+ \rightarrow \bar{D}_2^*(2460)^0 K^+$ decay, but no evidence is seen for the suppressed $B^+ \rightarrow D_2^*(2460)^0 K^+$ channel or for $B^+ \rightarrow D^+ K^*(892)^0$ decays in the remaining fits.

Table 7.5: Results of the binned minimum χ^2 fits to efficiency-corrected B^+ candidate invariant mass distributions in each resonance region and with weighting according to angular distributions as described in the text.

	Lower sideband	Signal region	Upper sideband	\tilde{N}^{corr}
$\tilde{N}(B^+ \rightarrow D_2^*(2460)^0 K^+)$	-200 ± 2500	500 ± 3000	200 ± 2200	500 ± 4500
$\tilde{N}(B^+ \rightarrow \bar{D}_2^*(2460)^0 K^+)$	28000 ± 14000	293000 ± 24000	-600 ± 4200	266000 ± 28000
$\tilde{N}(B^+ \rightarrow D^+ K^*(892)^0)$	1700 ± 1900	-3000 ± 5000	9500 ± 4000	-14000 ± 7000
$\tilde{N}(B^+ \rightarrow D^- K^+ \pi^+)$	—	4670000 ± 110000	—	—

7.6.4 Systematics

Systematic uncertainties due to fit model choices are evaluated by considering the effect on the signal yields of the following model variations: the linear combinatorial background shape is replaced by a flat PDF; the $\bar{B}_s^0 \rightarrow D^+ K^+ \pi^- \pi^-$ background component is removed from all fits to the $D^+ K^+ \pi^-$ mode; all other PDFs in the fit models are varied in the same way as described in Sec. 7.4.1.

The efficiency distributions used for the efficiency correction are varied in the same way described in Sec. 7.4.2 to determine the associated systematic uncertainty. The uncertainty in $\epsilon(K^*(892)^0)$ of Eq. 7.7 is also accounted for. An additional uncertainty is assigned due to the effect of changing the sideband regions from the default of $3\Gamma \leftrightarrow 5\Gamma$ to $4\Gamma \leftrightarrow 6\Gamma$.

The total systematic uncertainty is obtained by combining all sources in quadrature. No cross checks are performed for these quasi-two-body mode results as they are on the limit of statistical sensitivity and subdividing the data sample makes the fits unstable.

7.6.5 Results

After sideband subtraction using the yields presented in Tab. 7.5, the ratio of branching fractions is measured to be

$$\frac{\mathcal{B}(B^+ \rightarrow D_2^*(2460)^0 K^+)}{\mathcal{B}(B^+ \rightarrow \bar{D}_2^*(2460)^0 K^+)} = (r_B(D_2^*(2460)K^+))^2 = 0.002 \pm 0.015(\text{stat}) \pm 0.005(\text{syst}) \quad (7.8)$$

which gives

$$r_B(D_2^*(2460)K^+) = 0.04 \pm 0.18(\text{stat}) \pm 0.06(\text{syst}) . \quad (7.9)$$

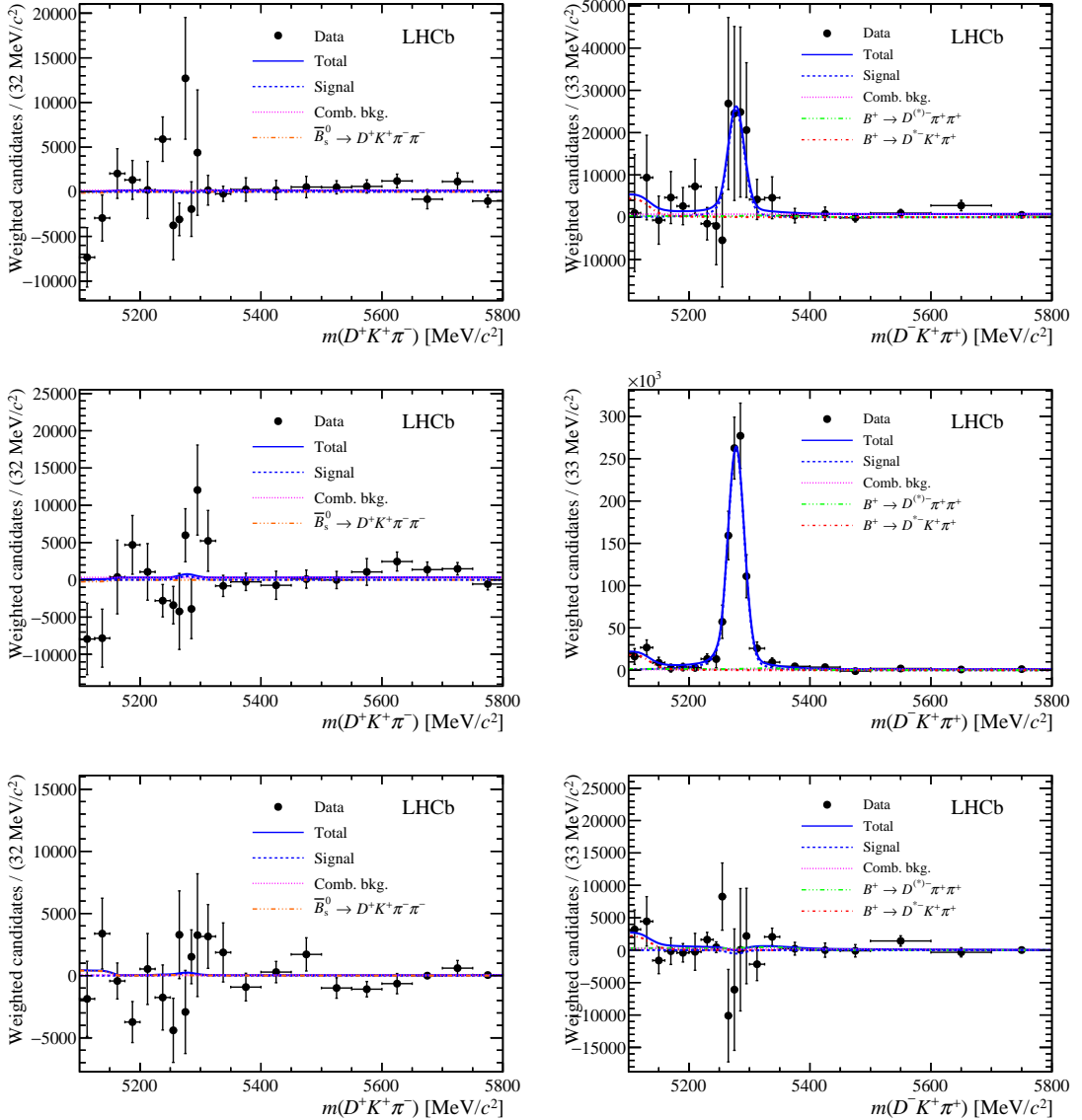


Figure 7.13: Results of binned minimum χ^2 fits to the B^+ candidate invariant mass distributions of (left) $B^+ \rightarrow D^+ K^+ \pi^-$ and (right) $B^+ \rightarrow D^- K^+ \pi^+$ candidates with efficiency corrections and P_4 weights applied. Candidates in the ranges (top) $2217.6 < m(D^+ \pi^-) < 2315.6 \text{ MeV}/c^2$, (middle) $2364.6 < m(D^+ \pi^-) < 2560.6 \text{ MeV}/c^2$ and (bottom) $2609.6 < m(D^+ \pi^-) < 2707.6 \text{ MeV}/c^2$ are shown. The components are as described in the legend.

Assuming Gaussian uncertainties, upper limits at 90 (95) % confidence level (CL) are obtained by integrating the likelihood in the region of positive branching fraction:

$$(r_B(D_2^*(2460)K^+))^2 < 0.027 \text{ (0.033)} \quad \text{and} \quad r_B(D_2^*(2460)K^+) < 0.30 \text{ (0.36)}. \quad (7.10)$$

Similarly for $B^+ \rightarrow D^+ K^*(892)^0 \rightarrow D^+ K^+ \pi^-$ the sideband subtracted yields give

$$\frac{\mathcal{B}(B^+ \rightarrow D^+ K^*(892)^0 \rightarrow D^+ K^+ \pi^-)}{\mathcal{B}(B^+ \rightarrow D^- K^+ \pi^+)} = -0.008 \pm 0.004(\text{stat}) \pm 0.003(\text{syst}). \quad (7.11)$$

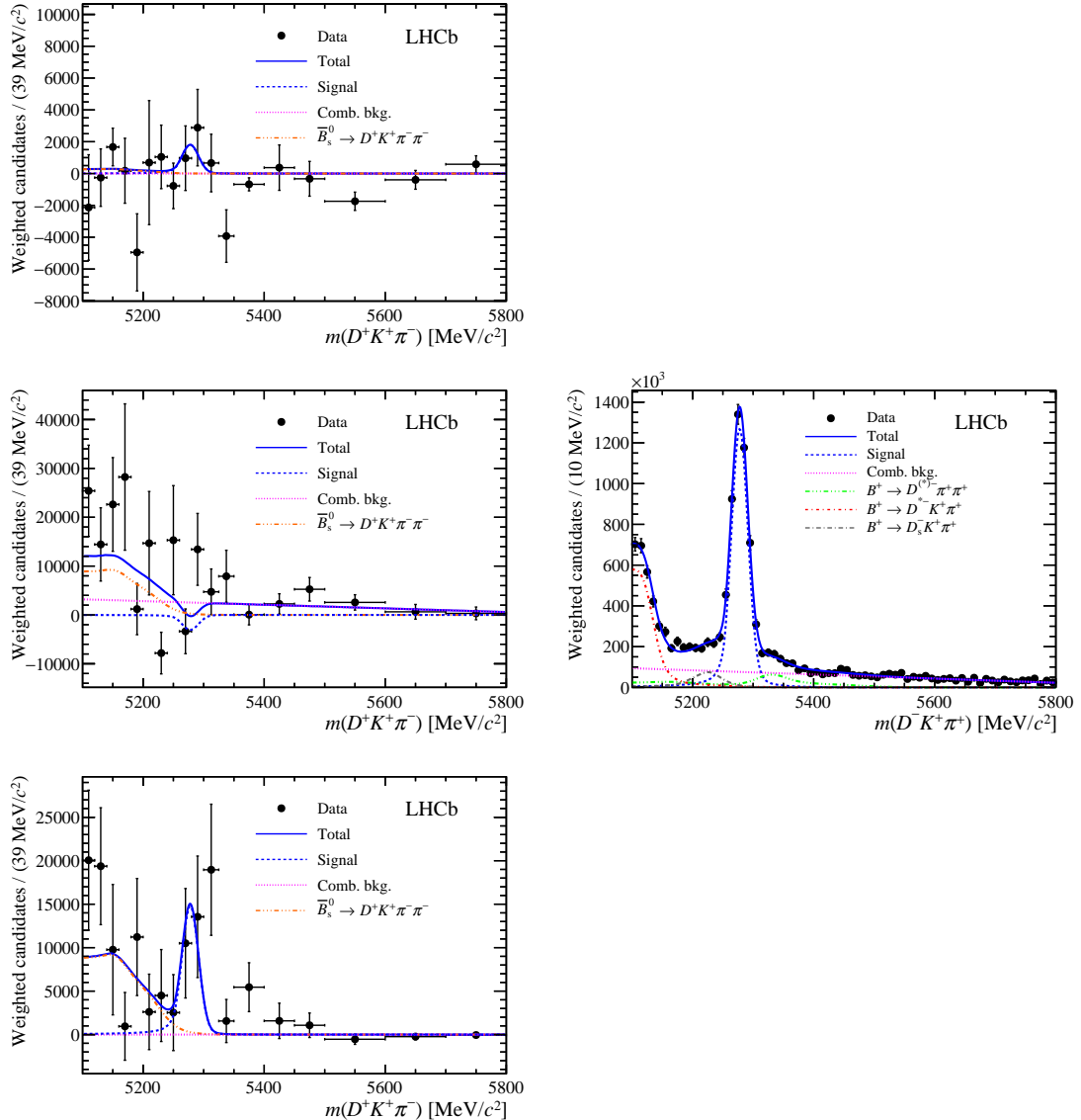


Figure 7.14: Results of binned minimum χ^2 fits to the B^+ candidate invariant mass distributions of (left) $B^+ \rightarrow D^+ K^+ \pi^-$ candidates with efficiency corrections and P_2 weights applied and (right) efficiency-corrected $B^+ \rightarrow D^- K^+ \pi^+$ candidates without any angular weight applied. In the left column, candidates in the ranges (top) $658.8 < m(K^+ \pi^-) < 753.6 \text{ MeV}/c^2$, (middle) $801.0 < m(K^+ \pi^-) < 990.6 \text{ MeV}/c^2$ and (bottom) $1038.0 < m(K^+ \pi^-) < 1132.8 \text{ MeV}/c^2$ are shown, while in the right column the whole $m(K^+ \pi^-)$ range is included. The components are as described in the legend.

Given the lack of significance, limits are set on the quasi-two-body branching fractions. Assuming Gaussian uncertainties, a Gaussian is constructed for each measured ratio, centred at the calculated value and with width equal to the total uncertainty. Each Gaussian PDF is then integrated from 0 to infinity and the limits at 90 % (95 %) CL are reported as the value U for which the integral from 0 to U is 90 % (95 %) of the integral from 0 to infinity.

Following this procedure and using the product branching fraction value from Chap. 6 of

$\mathcal{B}(B^+ \rightarrow \bar{D}_2^*(2460)^0 K^+) \times \mathcal{B}(\bar{D}_2^*(2460)^0 \rightarrow D^- \pi^+) = (23.2 \pm 1.1 \pm 0.6 \pm 1.0 \pm 1.6) \times 10^{-6}$
the result is

$$\begin{aligned} \mathcal{B}(B^+ \rightarrow D_2^*(2460)^0 K^+) \times \mathcal{B}(D_2^*(2460)^0 \rightarrow D^+ \pi^-) &= (0.4 \pm 3.5 \pm 1.1 \pm 0.1) \times 10^{-7}, \\ &< 6.3 (7.5) \times 10^{-7} \text{ at 90 (95) \% CL,} \end{aligned} \quad (7.12)$$

where the three quoted uncertainties are statistical, systematic and due to the measured product branching fraction of the normalisation mode. This is the first limit on this decay mode.

The measured value $\mathcal{B}(B^+ \rightarrow D^- K^+ \pi^+) = (7.31 \pm 0.19 \pm 0.22 \pm 0.39) \times 10^{-5}$ [1] gives

$$\begin{aligned} \mathcal{B}(B^+ \rightarrow D^+ K^*(892)^0) &= (-8.7 \pm 4.3 \pm 3.1 \pm 0.4) \times 10^{-7}, \\ &< 4.9 (6.1) \times 10^{-7} \text{ at 90 (95) \% CL,} \end{aligned} \quad (7.13)$$

where the third uncertainty is due to the normalisation channel branching fraction, which is dominated by the uncertainty on $\mathcal{B}(B^+ \rightarrow D^- \pi^+ \pi^+)$ [3]. This supersedes the previous limit which was obtained with a subset of the data [113].

Chapter 8

Dalitz plot analysis of $B^+ \rightarrow D^- \pi^+ \pi^+$ decays

In this chapter the Dalitz plot analysis of the $B^+ \rightarrow D^- \pi^+ \pi^+$ decay mode is described and the results of the fit are presented. The formalism of the DP fit is presented in Sec. 2.4. The masses and widths of contributing D^{**} states are reported as well as the product branching fractions of the contributing quasi-two-body amplitudes.

8.1 Fit strategy

This Dalitz plot analysis of the $B^+ \rightarrow D^- \pi^+ \pi^+$ decay is based on the data sample used as normalisation for the measurement of the $B^+ \rightarrow D^- K^+ \pi^+$ branching fraction (described in Chap. 5). The purity of the dataset used for the DP fit is increased by selecting $B^+ \rightarrow D^- \pi^+ \pi^+$ candidates with $m(D^- \pi^+ \pi^+)$ within $2.5\sigma_1$ of the fitted B candidate mass (where σ_1 is the fitted width of the B^+ peak in Sec. 5.2.3). This corresponds to the range $5235.3 < m(D^- \pi^+ \pi^+) < 5320.8 \text{ MeV}/c^2$. The full mass fit to $B^+ \rightarrow D^- \pi^+ \pi^+$ candidates is shown in Fig. 5.7 and Fig. 8.1 shows the region near to the fitted B mass, with the signal region of $\pm 2.5\sigma_1$ indicated by the vertical green lines. The signal and background yields in this signal region, obtained from the full mass fit, are given in Tab. 8.1. The component yields for two alternative regions of $\pm 2\sigma_1$ and $\pm 3\sigma_1$ are also reported.

Since the $B^+ \rightarrow D^- \pi^+ \pi^+$ decay channel has such large statistics it is necessary to have the best possible understanding of the efficiency variation across the Dalitz plot. As a result, only $B^+ \rightarrow D^- \pi^+ \pi^+$ events categorised as L0 hadron TOS are retained for the Dalitz plot fit – unlike the analysis of $B^+ \rightarrow D^- K^+ \pi^+$ data (documented in Chap. 6), for which a simultaneous fit is performed to TOS and !TOS candidates. The high-resolution histogram of L0 hadron TOS efficiency variation, shown in Fig. 4.16, is used

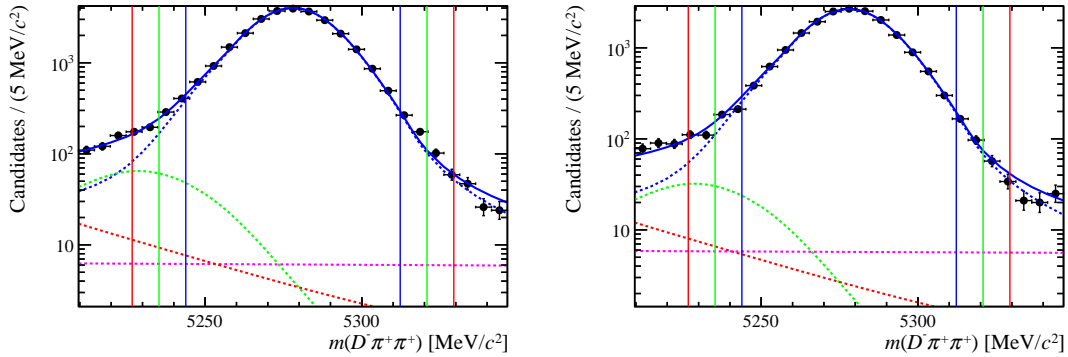


Figure 8.1: Zooms of the signal region of the fit to the B candidate invariant mass distribution of $D^- \pi^+ \pi^+$ showing the (blue) $\pm 2 \sigma_1$, (green) $\pm 2.5 \sigma_1$ and (red) $\pm 3 \sigma_1$ regions, with (left) events triggered as L0 hadron TOS and (right) other events.

Table 8.1: Signal and background yields obtained from the $B^+ \rightarrow D^- \pi^+ \pi^+$ mass fit, within $\pm 2 \sigma_1$, $\pm 2.5 \sigma_1$ and $\pm 3 \sigma_1$ of the fitted B candidate mass.

Component	Yield (TOS)			Yield (!TOS)		
	$\pm 2 \sigma_1$	$\pm 2.5 \sigma_1$	$\pm 3 \sigma_1$	$\pm 2 \sigma_1$	$\pm 2.5 \sigma_1$	$\pm 3 \sigma_1$
$N(B^+ \rightarrow D^{(*)-} K^+ \pi^+)$	149	243	350	74	120	174
$N(\text{part. reco. bkg.})$	53	70	90	37	50	64
$N(\text{comb. bkg.})$	82	103	123	77	97	116
$N(\text{signal})$	27220	27956	28277	18105	18595	18808

as an input in the fit and Sec. 8.2 describes the study of the distributions of background contributions over the SDP. Information about the contributing amplitudes is obtained from a study of the angular moments for $B^+ \rightarrow D^- \pi^+ \pi^+$ data. The results of this investigation are shown in Sec. 8.3.

8.2 Background Dalitz plot distributions

Two non-negligible background contributions in the signal region are visible in Fig. 8.1 and Tab. 8.1: combinatorial background ($\sim 0.4\%$), and $B^+ \rightarrow D^{(*)-} K^+ \pi^+$ ($\sim 0.8\%$). The $\sim 0.2\%$ contribution from partially reconstructed background is neglected.

The distribution of combinatorial background events over the $B^+ \rightarrow D^- \pi^+ \pi^+$ Dalitz plot is obtained from data in the high B^+ mass sideband, $5500 < m(D^- \pi^+ \pi^+) < 5800 \text{ MeV}/c^2$. The main component in this region is combinatorial background, as shown in Fig. 5.7. Given the small contribution of combinatorial background in the signal region, the effect of other components in the high mass sideband is neglected. The SDP distribution of combinatorial background events is therefore taken as that of candidates in the high mass sideband region of $m(D\pi\pi)$, which is shown in Fig. 8.2 (left).

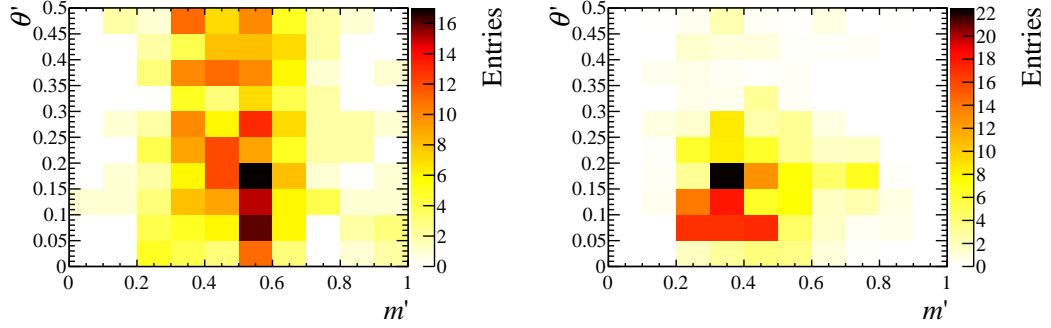


Figure 8.2: Square Dalitz plot distributions used in the Dalitz plot fit for (left) combinatorial background and (right) $B^+ \rightarrow D^{(*)-} K^+ \pi^+$ decays.

The SDP distribution of mis-identified (and partially reconstructed) background contributions from $B^+ \rightarrow D^{(*)-} K^+ \pi^+$ decays is obtained from samples of simulated events. As described in Sec. 5.2.1.3, the simulated samples are weighted to account for the differences observed in PID variables for data and simulation and to match the DP distribution observed in $B^+ \rightarrow D^- K^+ \pi^+$ data. The SDP distribution of all weighted simulated events falling within the DP fit signal region is shown Fig. 8.2 (right).

8.3 Partial wave analysis using angular moments

A study of the angular moments for $B^+ \rightarrow D^- \pi^+ \pi^+$ data is performed, following the strategy outlined in Sec. 6.3. Note that due to the identical particles in the final state of the $B^+ \rightarrow D^- \pi^+ \pi^+$ decay, only the moments calculated below $m(D^- \pi^+) \approx 3.1 \text{ GeV}/c^2$ can be interpreted in the same way as those in Sec. 6.3.³² The full range of the $D^- \pi^+$ helicity angle distribution is not available at higher values of $m(D^- \pi^+)$, so the formalism of the moments analysis is then broken as the orthogonality of the Legendre polynomials does not hold if the angular range is restricted.

The moments are calculated for each bin of $m(D\pi)$ using Eq. 6.1, as in Sec. 6.3, and the results are shown in Fig. 8.3. Structures are visible in the distributions of $\langle P_5 \rangle$ and $\langle P_6 \rangle$, suggesting that there are spin-3 contributions in this decay mode. Resonances with a spin of more than 3 are not expected as the distributions of the seventh and eighth moments (shown in Fig. 8.4) are approximately flat. Extending the expressions

³²The exact value is easily calculated from Eq. 2.29, noting that the folding starts where $m_{\pi^+ \pi^+}$ is maximal, *i.e.* $m_{\pi^+ \pi^+} = m_{B^+} - m_{D^-}$. Then

$$m_{D^- \pi^+ \max}^2 = m_{D^- \pi^+ \min}^2 = m_{B^+} m_{D^-} + m_{\pi^+}^2,$$

giving a value of $m_{D^- \pi^+} \approx 3.145 \text{ GeV}/c^2$ (taking masses from Ref. [3]). Similarly, the value where the folding ends is determined taking the minimal value $m_{\pi^+ \pi^+} = 2m_{\pi^+}$ to obtain

$$m_{D^- \pi^+ \max}^2 = m_{D^- \pi^+ \min}^2 = \frac{1}{2} (m_{B^+}^2 + m_{D^-}^2 - 2m_{\pi^+}^2),$$

giving $m_{D^- \pi^+} \approx 3.958 \text{ GeV}/c^2$.

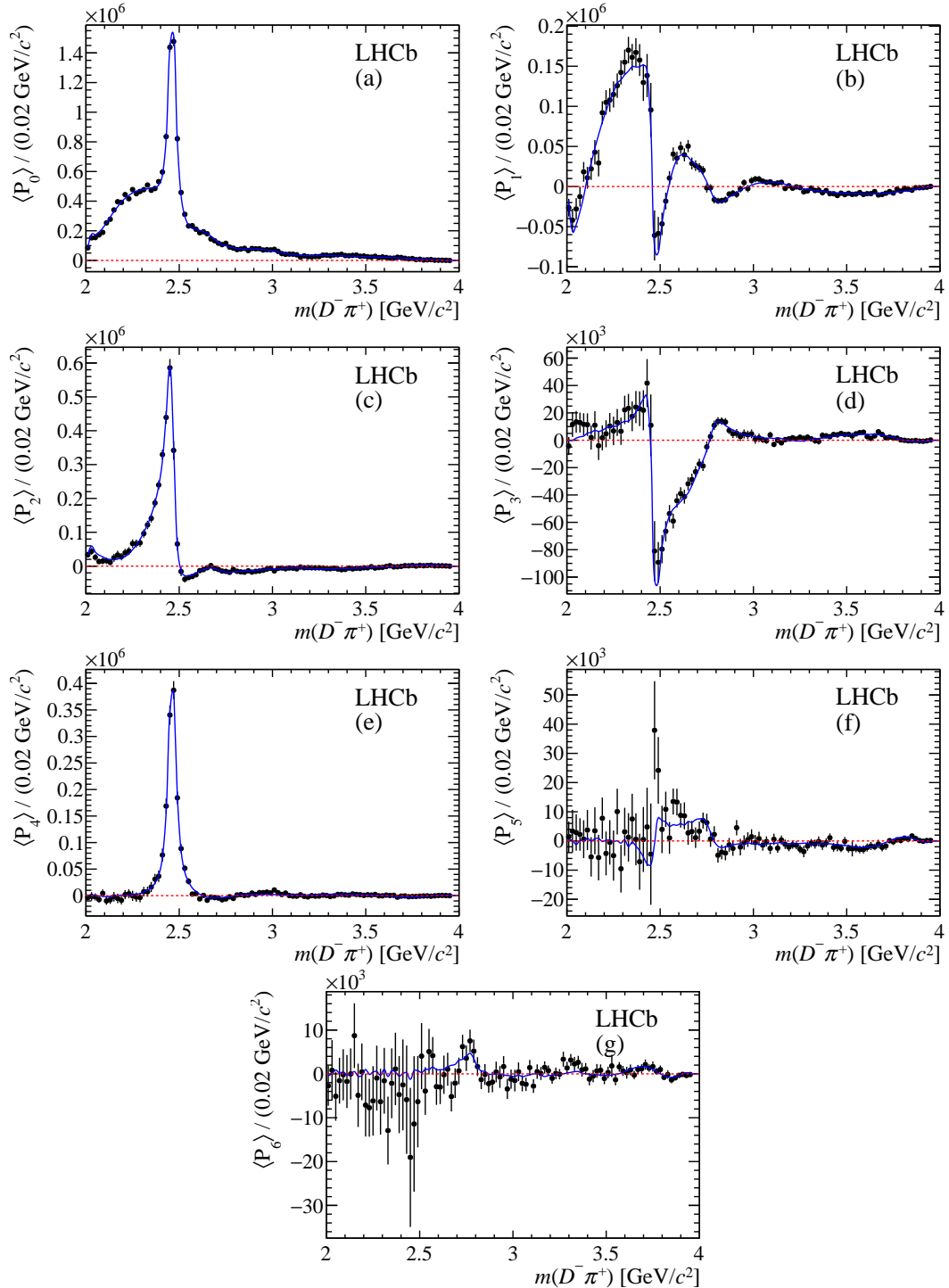


Figure 8.3: The first seven Legendre-polynomial weighted moments for background-subtracted and efficiency-corrected $B^+ \rightarrow D^- \pi^+ \pi^+$ data (black points) as a function of $m(D^- \pi^+)$. Only candidates categorised as L0 hadron TOS are considered. The blue line shows the result of the DP fit described in Sec. 8.4.

in Eq. 6.2 to include contributions up to spin-3, the Legendre moments can be related to S-, P-, D- and F-wave amplitudes (denoted $h_J e^{i\delta_J}$ with $J = 0, 1, 2, 3$, respectively) by:

$$\begin{aligned}
\langle P_0 \rangle &= |h_0|^2 + |h_1|^2 + |h_2|^2 + |h_3|^2, \\
\langle P_1 \rangle &= \frac{2}{\sqrt{3}} |h_0| |h_1| \cos(\delta_0 - \delta_1) + \frac{4}{\sqrt{15}} |h_1| |h_2| \cos(\delta_1 - \delta_2) + \\
&\quad \frac{6}{\sqrt{35}} |h_2| |h_3| \cos(\delta_2 - \delta_3), \\
\langle P_2 \rangle &= \frac{6}{5} \sqrt{\frac{3}{7}} |h_3| |h_1| \cos(\delta_1 - \delta_3) + \frac{2 |h_0| |h_2| \cos(\delta_0 - \delta_2)}{\sqrt{5}} + \\
&\quad \frac{2 |h_1|^2}{5} + \frac{2 |h_2|^2}{7} + \frac{4 |h_3|^2}{15}, \\
\langle P_3 \rangle &= \frac{6}{7} \sqrt{\frac{3}{5}} |h_1| |h_2| \cos(\delta_1 - \delta_2) + \frac{2 |h_0| |h_3| \cos(\delta_0 - \delta_3)}{\sqrt{7}} + \\
&\quad \frac{8 |h_2| |h_3| \cos(\delta_2 - \delta_3)}{3\sqrt{35}}, \\
\langle P_4 \rangle &= \frac{8 |h_1| |h_3| \cos(\delta_1 - \delta_3)}{3\sqrt{21}} + \frac{2 |h_2|^2}{7} + \frac{2 |h_3|^2}{11}, \\
\langle P_5 \rangle &= \frac{20}{33} \sqrt{\frac{5}{7}} |h_2| |h_3| \cos(\delta_2 - \delta_3), \\
\langle P_6 \rangle &= \frac{100 |h_3|^2}{429}.
\end{aligned} \tag{8.1}$$

The $\bar{D}_2^*(2460)^0$ resonance is clearly seen as a peak in the distribution of $\langle P_4 \rangle$ in Fig. 8.3. The distributions of $\langle P_1 \rangle$ and $\langle P_3 \rangle$ also have visible structures which are similar to those observed in $B^+ \rightarrow D^- K^+ \pi^+$ data in Sec. 6.3. These features suggest that there is interference between S- and P-wave amplitudes and between P- and D-wave amplitudes, so broad spin-0 and spin-1 components are also required at low $m(D^- \pi^+)$ in this decay mode.

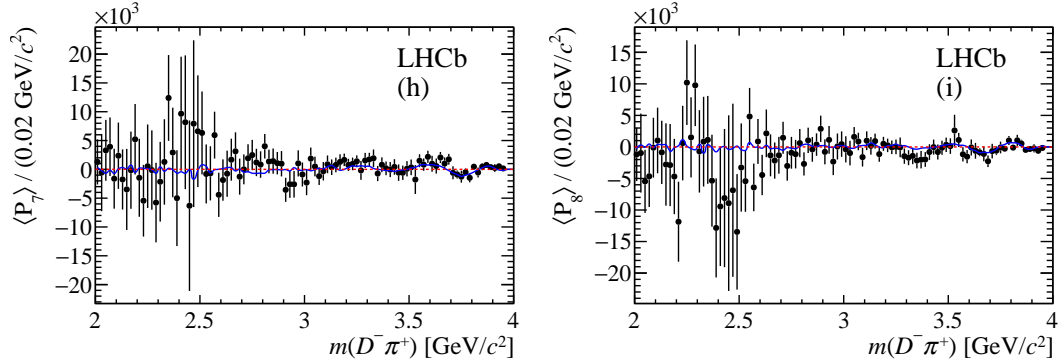


Figure 8.4: Seventh and eighth Legendre-polynomial weighted moments for background-subtracted and efficiency-corrected $B^+ \rightarrow D^- \pi^+ \pi^+$ data (black points) as a function of $m(D^- \pi^+)$. Only candidates categorised as L0 hadron TOS are considered. The blue line shows the result of the DP fit described in Sec. 8.4.

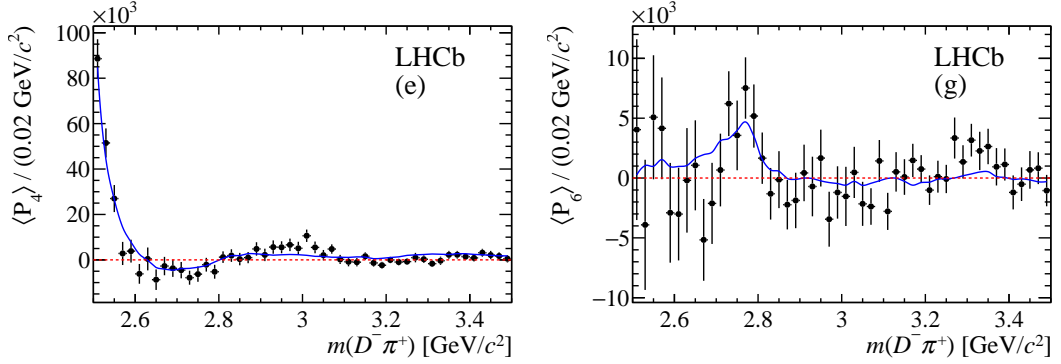


Figure 8.5: Zoomed views of the distributions of fourth and sixth Legendre-polynomial weighted moments for background-subtracted and efficiency-corrected $B^+ \rightarrow D^- \pi^+ \pi^+$ data (black points) as a function of $m(D^- \pi^+)$. Only candidates categorised as L0 hadron TOS are considered. The blue line shows the result of the DP fit described in Sec. 8.4.

No evidence of structures with spin greater than 3 are seen as shown by the seventh and eighth moments in Fig. 8.4. Structures in these higher moments would suggest spin 4 contributions. Zoomed views of the fourth and sixth moments in the region around $m(D\pi) = 3 \text{ GeV}/c^2$ are shown in Fig. 8.5. A wide bump is visible in the fourth moment at $m(D\pi) \approx 3 \text{ GeV}/c^2$. Although this is close to the point where the Dalitz plot folding affects the interpretation of the moments, this enhancement suggests that an additional spin-2 resonance could be contributing in this region of the DP. From other recent Dalitz plot studies of three-body B meson decays [55, 109, 110], a spin-3 resonance could be expected in the region around $m(D\pi) = 2.76 \text{ GeV}/c^2$. A peak is seen at this value of $m(D^- \pi^+)$ in the sixth moment, so a spin-3 state is included in the Dalitz plot fit model.

8.4 Dalitz plot fit

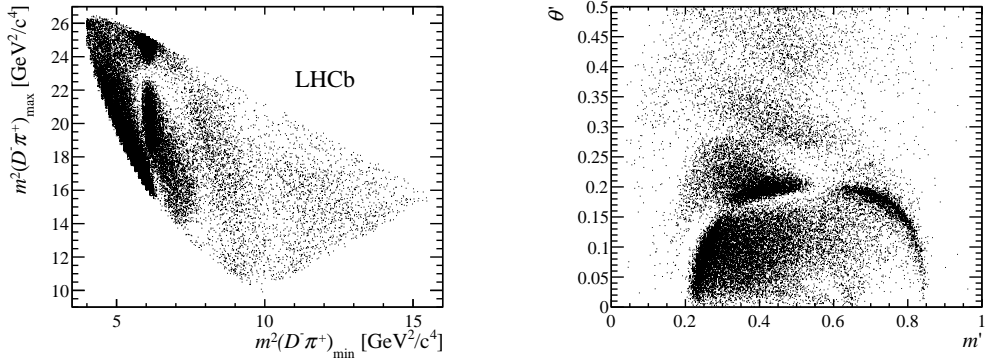


Figure 8.6: The distribution of data in (left) normal Dalitz plot representation and (right) SDP.

Figure 8.6 shows the distribution of $B^+ \rightarrow D^- \pi^+ \pi^+$ candidates in the signal region. The amplitude model used to fit the dataset is described below, followed by the results obtained.

8.4.1 Fit model

The LAURA++ package [99] is used to perform an unbinned maximum likelihood fit to the selected $B^+ \rightarrow D^- \pi^+ \pi^+$ candidates, with amplitudes combined according to the isobar model (introduced in Sec. 2.4.2). All resonant and nonresonant amplitudes included in the baseline fit model are summarised in Tab. 8.2. The decays of both $B^+ \rightarrow D^- K^+ \pi^+$ and $B^+ \rightarrow D^- \pi^+ \pi^+$ are expected only to have contributions from resonances decaying to $D^- \pi^+$, so this model is an extension of the one developed for the fit to $B^+ \rightarrow D^- K^+ \pi^+$ decays (see Chap. 6). Additional spin-2 and spin-3 states are required in the DP model for $B^+ \rightarrow D^- \pi^+ \pi^+$ in order to obtain a good description of the high statistic data sample and a stable fit result. Alternative models are also employed to describe the S-wave and P-wave amplitudes. More information about the contributions to each partial wave is given below.

Table 8.2: Resonances that are included in the fit to the data sample. Resonances labelled with subscript v are virtual. Parameters (and uncertainties) are taken from the PDG [3] unless stated otherwise.

Resonance	Spin	DP axis	Model	Parameters
$\bar{D}_2^*(2460)^0$	2	$m^2(D\pi)$	RBW	Determined from data (see Tab. 8.4)
$\bar{D}_1^*(2760)^0$	1	$m^2(D\pi)$		
$\bar{D}_3^*(2760)^0$	3	$m^2(D\pi)$		
$\bar{D}_2^*(3000)^0$	2	$m^2(D\pi)$		
$\bar{D}_v^*(2007)^0$	1	$m^2(D\pi)$	RBW	$m = 2006.98 \pm 0.15 \text{ MeV}/c^2$, $\Gamma = 2.1 \text{ MeV}$
\bar{B}_v^{*0}	1	$m^2(D\pi)$	RBW	$m = 5325.2 \pm 0.4 \text{ MeV}/c^2$, $\Gamma = 0.0 \text{ MeV}$
Total S-wave	0	$m^2(D\pi)$	Splines	See text

S-wave

Results of the moments study presented in Sec. 8.3 suggest that a spin-0 resonance is present in the region of the well-known $\bar{D}_0^*(2400)^0$ state and, as in many similar analyses, an additional spin-0 nonresonant component is required. Fit models with both of these two spin-0 contributions were found to be destabilised by strong S-wave interference, so a model-independent approach is employed to describe the entire spin-0 partial wave. This approach was first applied to the $K\pi$ S-wave [114]. Subsequent uses include further studies of the $K\pi$ S-wave [115, 116, 117, 118] as well as the K^+K^- [119] and $\pi^+\pi^-$ [120] S-waves, in various processes. This analysis represents the first use of the method for the $D\pi$ S-wave description.

The total $D\pi$ S-wave is fitted using splines to describe the magnitude and phase of the spin-0 amplitude. Knots are defined at fixed values of $m(D\pi)$ and splines give a smooth interpolation of the magnitude and phase of the S-wave between these points. The knot positions used in the nominal model are shown as vertical red lines in Fig. 8.7, overlaid on the $m(D\pi)$ invariant mass projection of data. The S-wave magnitude and phase are both fixed to zero at the highest mass knot in order to ensure sensible behaviour at the kinematic limit, and for the knot at $m(D\pi) = 2.4 \text{ GeV}/c^2$, close to the $\bar{D}_2^*(2460)^0$ resonance, the magnitude and phase values are fixed to 0.5 and 0, respectively, as a reference. The magnitude and phase values are floated at every other knot position.

For this final state, with two same-sign pions, the implementation of this spline model gives the fit a great deal of freedom and the S-wave splines are found to absorb contributions from the reflections of other partial waves. To protect against this unwanted behaviour, no knots are used in the region of $m^2(D^- \pi^+)$ where both $m^2(D^- \pi^+)_\text{min}$ and $m^2(D^- \pi^+)_\text{max}$ are possible, *i.e.* between the two values given in footnote 32. The fit stability was found to improve with this alteration. The absence of knots between $m(D\pi) \sim 4.1 \text{ GeV}/c^2$ and the kinematic limit also aids the fit stability by allowing the $D\pi$ S-wave magnitude to decrease smoothly and monotonically, as expected.

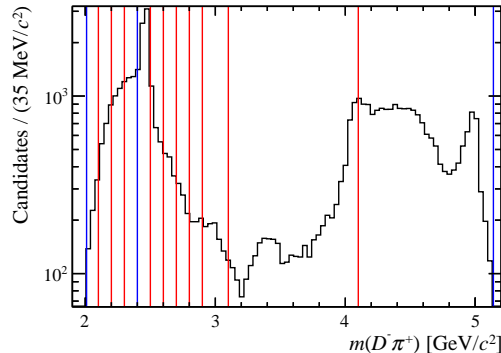


Figure 8.7: Projection of $D\pi\pi$ data onto $m(D\pi)$, with the knot positions of the S-wave splines indicated by vertical red lines. The first and last knots are indicated by blue lines, as is the knot at $m(D\pi) = 2.4 \text{ GeV}/c^2$ for which the magnitude and phase values are fixed.

P-wave

Unlike the $D^- K^+ \pi^+$ DP fit model, no P-wave nonresonant component is included. Two spin-1 virtual states are used in the model: $\bar{D}^*(2007)^0$ (below threshold in $m^2(D\pi)$) gives a reasonably good description of the low mass P-wave contribution and the fit is improved with the inclusion of the \bar{B}^{*0} state (above the upper kinematic limit in $m^2(D\pi)$).

Following the observation of the $\bar{D}_1^*(2760)^0$ meson in the $B^+ \rightarrow D^- K^+ \pi^+$ final state [1], at least one spin-1 resonance is expected at a similar mass. The baseline fit model

contains a spin-1 resonance, modelled with the RBW function with floated mass and width parameters.

D-wave

The $\bar{D}_2^*(2460)^0$ state is well-known, and is clearly visible in both the $m(D\pi)$ invariant mass distribution and the distribution of $\langle P_4 \rangle$ (shown in Figs. 8.7 and 8.3, respectively). The resonance is included in the fit model, described by a RBW function. The mass and width of the $\bar{D}_2^*(2460)^0$ resonance are free parameters in the fit; there is some disagreement between previous measurements (see Figs. 2.9 and 2.10) and floating the mass and width parameters was found to improve the stability of the fit.

Motivated by the structure observed at $m(D\pi) \sim 3.0 \text{ GeV}/c^2$ in the $\langle P_4 \rangle$ distribution, a second spin-2 resonance is included. The mass and width parameters of this state are also floated in the fit.

F-wave

A spin-3 state, modelled using the RBW function with floated mass and width parameters, is included in the DP fit model. The moments study described in Sec. 8.3 shows the necessity for a spin-3 resonance at $m(D^- \pi^+) \sim 2.75 \text{ GeV}/c^2$. An additional motivation for including this state is the observation of the $\bar{D}_3^*(2760)^-$ meson in a study of $B^0 \rightarrow \bar{D}^0 \pi^+ \pi^-$ decays [110] – a decay mode related to the $B^+ \rightarrow D^- \pi^+ \pi^+$ final state by isospin symmetry.

8.4.2 Fit results

The free parameters of the Dalitz plot fit are the real and imaginary parts of the c_j terms introduced in Sec. 2.4.2, the mass and width parameters of some resonances and the magnitude and phase of the $D\pi$ S-wave at each knot. For the $\bar{D}_2^*(2460)^0$ resonance, the real and imaginary parts of c_j are fixed to 1 and 0, respectively, and the amplitudes of all other contributions are determined relative to this reference amplitude. The results for the floated real and imaginary parts of each amplitude are reported in Tab. 8.3, as are the derived values of magnitudes, phases and fit fractions. The values of the masses and widths of the $\bar{D}_2^*(2460)^0$, $\bar{D}_1^*(2760)^0$, $\bar{D}_3^*(2760)^0$ and $\bar{D}_2^*(3000)^0$ states are given in Tab. 8.4. Note that the statistical uncertainties quoted for all floated parameters are just the (parabolic) uncertainties returned by the fit.

The floated mass and width parameters in Tab. 8.4 can be compared to previously measured values, presented in Tab. 2.5 and Sec. 6.6. The fitted width of the $\bar{D}_2^*(2460)^0$ state is found to be slightly narrower than, but statistically consistent with, that reported

Table 8.3: Results of the default fit to data. Note that the sum of the fit fractions need not be 100% due to interference effects.

Contribution	Fit fraction (%)	Isobar model coefficients			
		Real part	Imaginary part	Magnitude	Phase (rad)
$\bar{D}_2^*(2460)^0$	35.7 ± 0.6	1.00	0.00	1.00	0.00
$\bar{D}_1^*(2760)^0$	8.3 ± 0.6	-0.38 ± 0.02	0.30 ± 0.02	0.48 ± 0.02	2.47 ± 0.09
$\bar{D}_3^*(2760)^0$	1.0 ± 0.1	0.17 ± 0.01	0.00 ± 0.01	0.17 ± 0.01	0.01 ± 0.20
$\bar{D}_2^*(3000)^0$	0.2 ± 0.1	0.05 ± 0.02	-0.06 ± 0.02	0.08 ± 0.01	-0.84 ± 0.28
$\bar{D}^*(2007)_v^0$	10.8 ± 0.7	0.51 ± 0.03	-0.20 ± 0.05	0.55 ± 0.02	-0.38 ± 0.19
\bar{B}_v^0	2.7 ± 1.0	0.27 ± 0.03	0.04 ± 0.04	0.27 ± 0.05	0.14 ± 0.38
Total S-wave	57.0 ± 0.8	1.21 ± 0.02	-0.35 ± 0.04	1.26 ± 0.01	-0.28 ± 0.05
Total fit fraction	115.7				

from the analysis of the $B^+ \rightarrow D^- K^+ \pi^+$ decay mode in Chap. 6, and is in agreement with the world average (see Fig. 2.10). The value of $m(\bar{D}_2^*(2460)^0)$ is also consistent with the result from Chap. 6, but is in some tension with the world average (see Fig. 2.9). The mass of the spin-1 state referred to as ‘ $\bar{D}_1^*(2760)^0$ ’ in Tab. 8.4 is measured to be $2681.1 \text{ MeV}/c^2$, which is $\sim 100 \text{ MeV}/c^2$ lower than that of the similar P-wave resonance included in the DP fit model for $B^+ \rightarrow D^- K^+ \pi^+$ decays. Previous studies of D^{**} states have found evidence for several states in the range $2600 < m(D^- \pi^+) < 2780 \text{ MeV}/c^2$ [43, 44] which could correspond to two spin-1 resonances in this region.

Table 8.4: Floated parameters for the fit to data, with statistical uncertainties only.

Contribution	Floated parameters
$\bar{D}_2^*(2460)^0$	$m = 2463.7 \pm 0.4 \text{ MeV}/c^2$ $\Gamma = 47.0 \pm 0.8 \text{ MeV}$
$\bar{D}_1^*(2760)^0$	$m = 2681.1 \pm 5.6 \text{ MeV}/c^2$ $\Gamma = 186.7 \pm 8.5 \text{ MeV}$
$\bar{D}_3^*(2760)^0$	$m = 2775.5 \pm 4.5 \text{ MeV}/c^2$ $\Gamma = 95.3 \pm 9.6 \text{ MeV}$
$\bar{D}_2^*(3000)^0$	$m = 3213.8 \pm 28.7 \text{ MeV}/c^2$ $\Gamma = 186.0 \pm 37.6 \text{ MeV}$

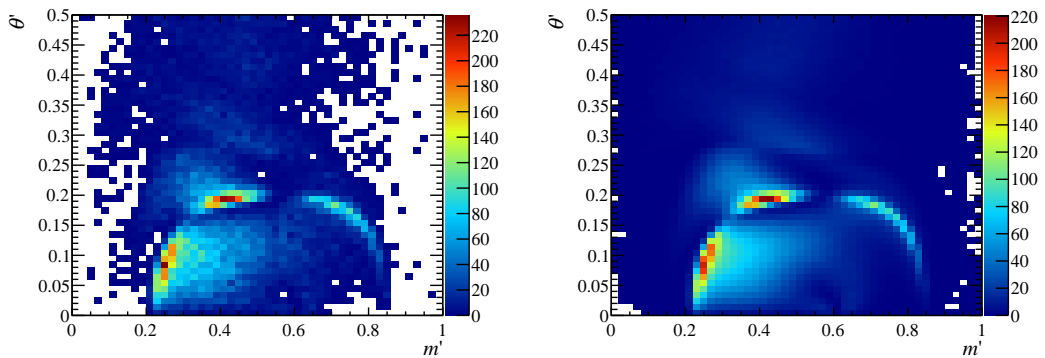


Figure 8.8: The distribution across the SDP of (left) data and (right) the fit model.

Figure 8.8 compares the SDP distribution of events simulated according to the fit model to that observed in the $B^+ \rightarrow D^- \pi^+ \pi^+$ data sample. Dividing each of these distributions into 484 equally populated bins (with a minimum bin content of 57 entries) gives a 2D

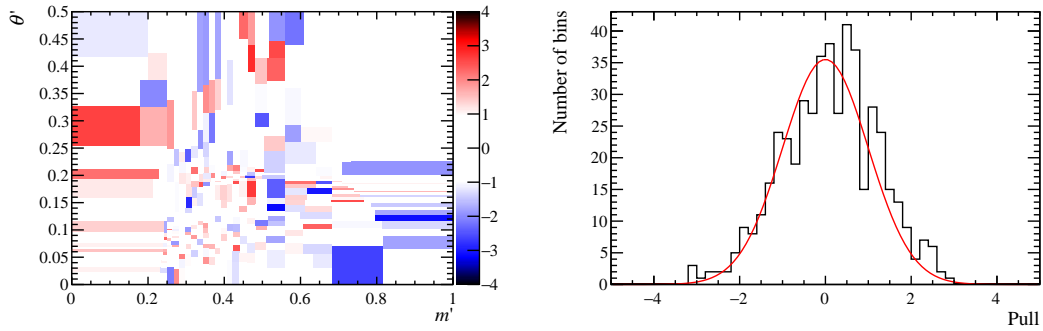


Figure 8.9: The pulls between data and the fit model for 484 equally populated bins across the SDP. (Left) the pull in each bin and (right) the distribution of pulls with a Gaussian of mean zero and width one superimposed.

χ^2/ndf between $607.38/449 = 1.35$ and $607.38/483 = 1.26$. The 2D pulls for this binning scheme are plotted in Fig. 8.9 (left), where the distribution of pulls is found to be roughly Gaussian, as shown in Fig. 8.9 (right). These relatively high χ^2/ndf values, which correspond to very low p -values, are no larger than the values obtained for other amplitude analyses of similar complexity. Note also that systematic uncertainties are not considered in this calculation; if uncorrelated systematic uncertainties on each bin are of the same magnitude as the statistical uncertainties then a value of $\chi^2/\text{ndf} \approx \sqrt{2}$ is to be expected.

One-dimensional projections of the nominal fit model and the data onto $m(D\pi)_{\min}$, $m(D\pi)_{\max}$ and $m(\pi\pi)$ are shown in Fig. 8.10. The fit model is seen to give a good description of the data sample. In Fig. 8.11 (left), zoomed views of the $m(D\pi)_{\min}$ invariant mass projection are provided for regions at threshold and around the $\bar{D}_2^*(2460)^0$, $\bar{D}_1^*(2760)^0$ and $\bar{D}_2^*(3000)^0$ resonances. Projections of the cosine of the $D\pi$ helicity angle in the same regions of $m(D\pi)_{\min}$ are shown in Fig. 8.11 (right). Good agreement is seen in all these projections, suggesting that the model gives an acceptable description of the data and the spin assignments of the $\bar{D}_1^*(2760)^0$, $\bar{D}_3^*(2760)^0$ and $\bar{D}_2^*(3000)^0$ states are correct.

The floated knot values and splines describing the total $D\pi$ S-wave partial wave are shown in Fig. 8.12. The real and imaginary values at each point are calculated from the magnitude and phase and shown in the Argand plane in Fig. 8.13.

All of the $\bar{D}_1^*(2760)^0$, $\bar{D}_3^*(2760)^0$ and $\bar{D}_2^*(3000)^0$ states are found to be significant, based on the large change observed in the NLL if any of these resonances is removed from the baseline fit model. The significance of each contribution is not evaluated formally, but the effect of the systematic uncertainties is considered by performing a similar likelihood ratio test with the alternative models that are found to give the largest uncertainties on the parameters of these resonances (see Sec. 8.5). The significances of the $\bar{D}_1^*(2760)^0$ and $\bar{D}_3^*(2760)^0$ states are found to be above 10σ and that for the $\bar{D}_2^*(3000)^0$ state is 5.8σ .

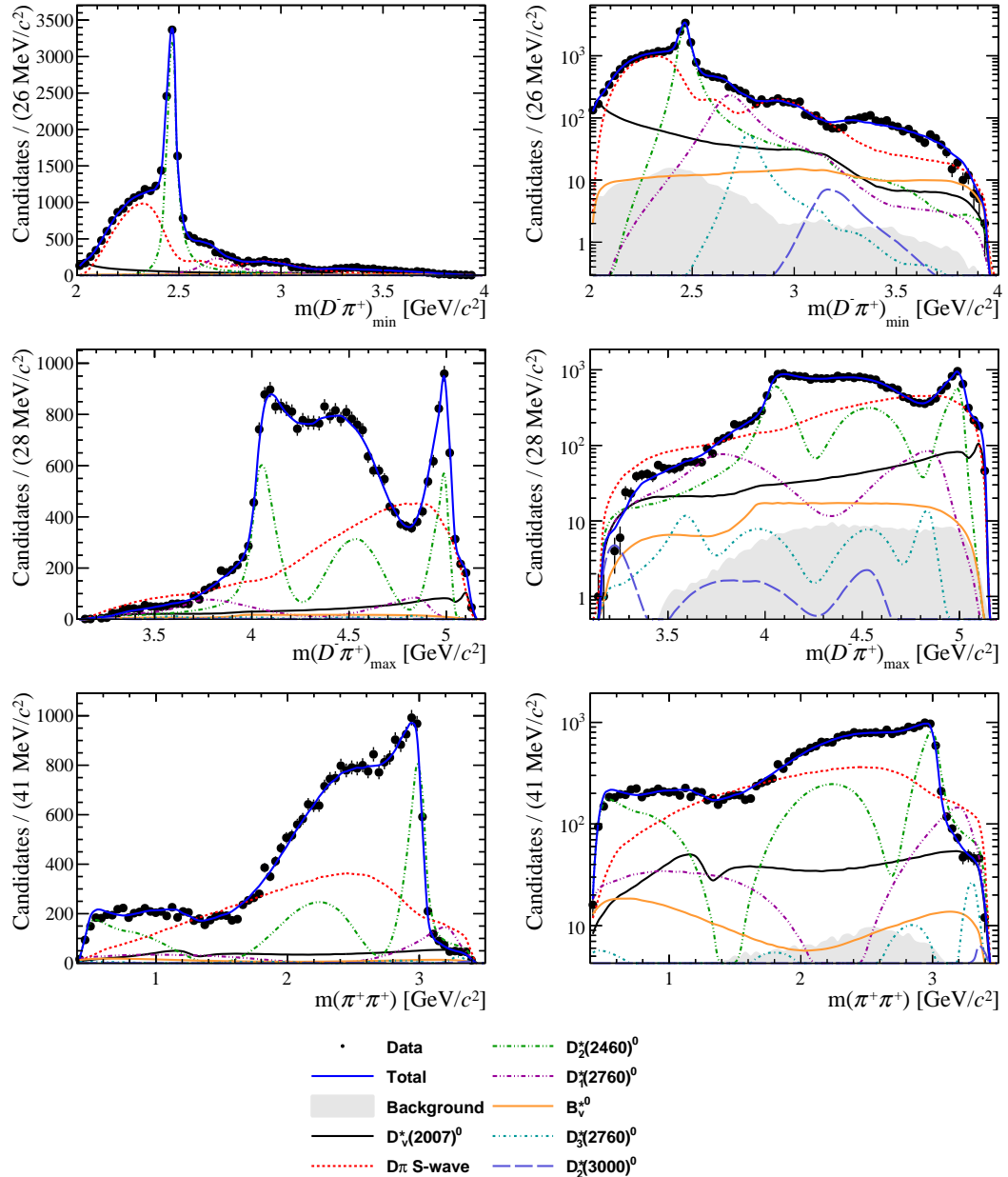


Figure 8.10: Projections of the data and amplitude fit onto (top) $m(D\pi)_{\min}$, (middle) $m(D\pi)_{\max}$ and (bottom) $m(\pi\pi)$, with the same projections shown (right) with a logarithmic y -axis scale. Components are described in the legend. Destructive interference between the contributions is visible where individual components appear above the total fit line.

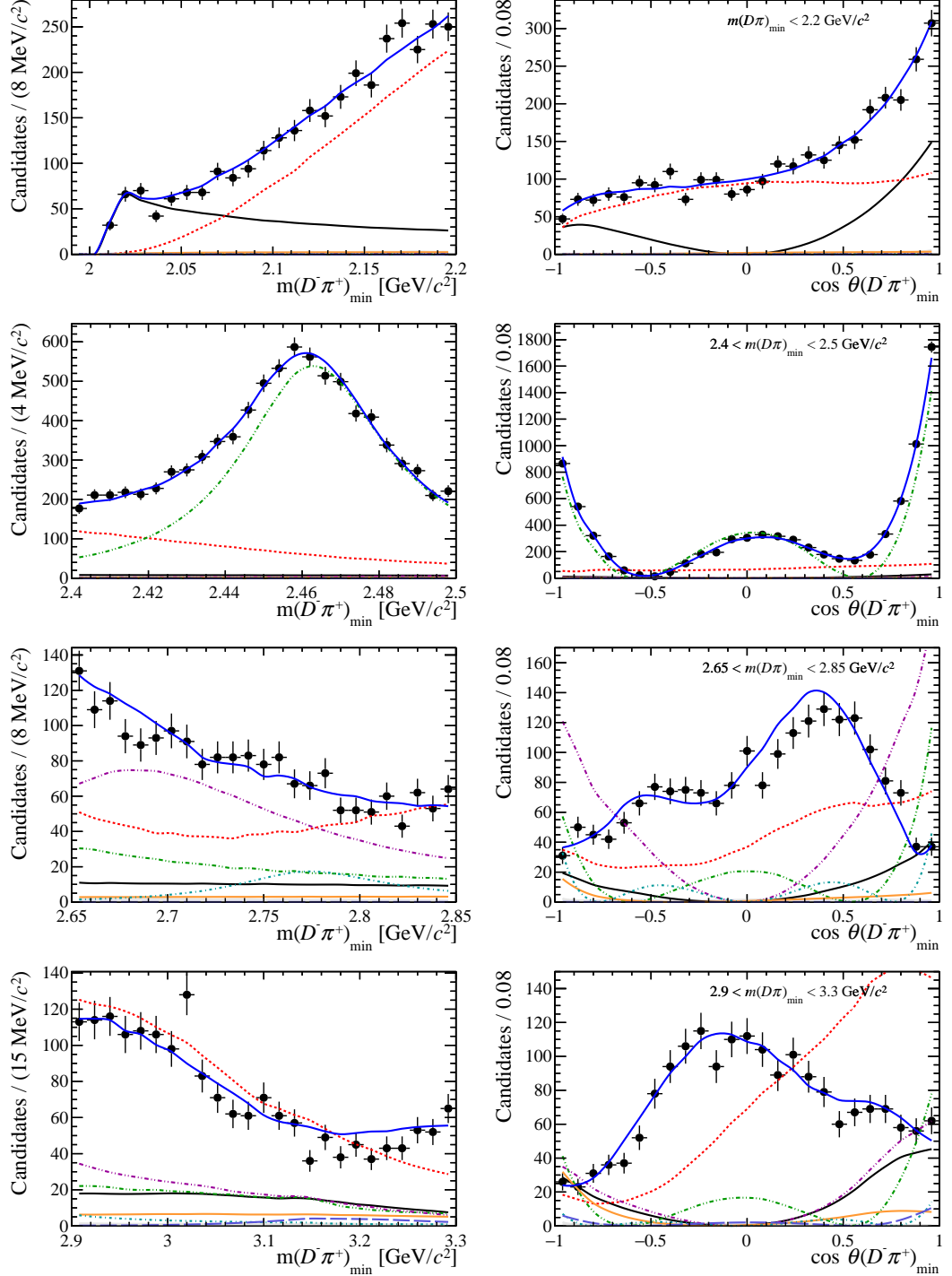


Figure 8.11: Projections of the data and amplitude fit onto (left) $m(D\pi)$ and (right) the cosine of the helicity angle for the $D\pi$ system in (from top to bottom) the threshold region, the $\bar{D}_2^*(2460)^0$ region, the $\bar{D}_1^*(2760)^0$ region and the $\bar{D}_2^*(3000)^0$ region. Components are as shown in Fig. 8.10. Destructive interference between the contributions is visible where individual components appear above the total fit line.

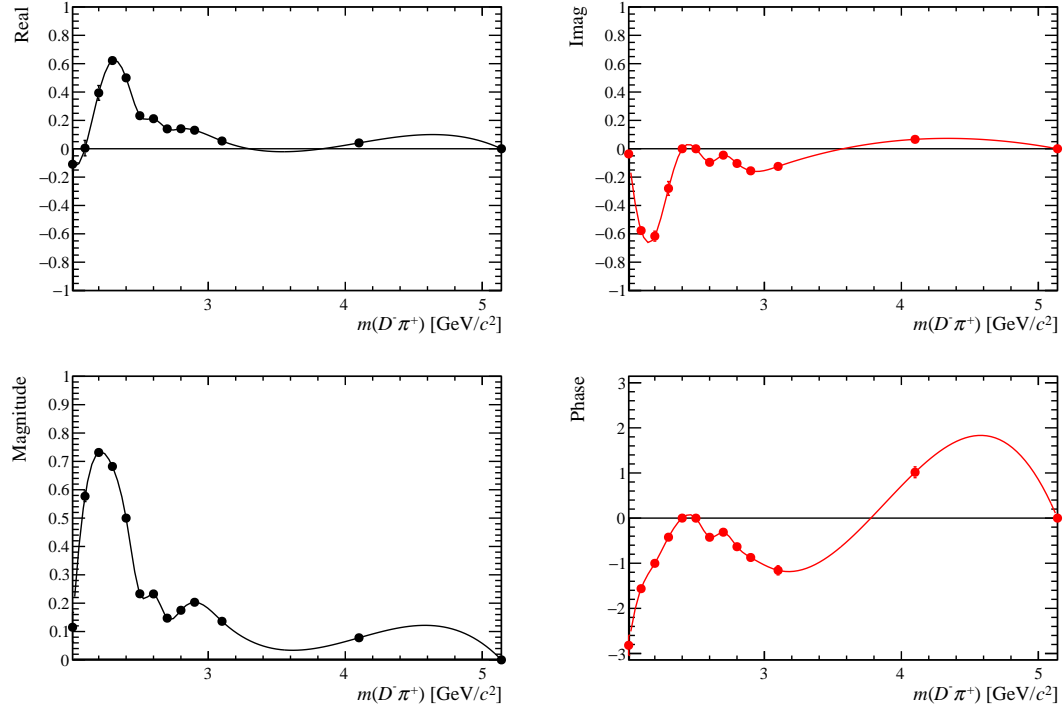


Figure 8.12: Total $D\pi$ S-wave partial wave splines (smooth lines) and knots (points), shown in terms of (top) real and imaginary parts and (bottom) magnitude and phase.

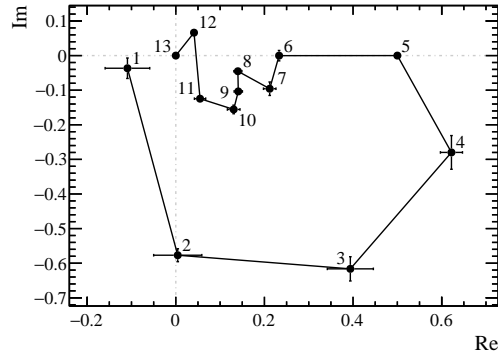


Figure 8.13: Real and imaginary values of the S-wave partial wave, shown in an Argand diagram. The left most point is that at the lowest value of $m(D\pi)$, with mass increasing along the connected points. Each point, labelled 1–13, corresponds to the position of a knot in the spline, at values of $m(D\pi) = \{2.01, 2.10, 2.20, 2.30, 2.40, 2.50, 2.60, 2.70, 2.80, 2.90, 3.10, 4.10, 5.14\}$ GeV/c^2 . The points at $(0.5, 0.0)$ and $(0.0, 0.0)$ are fixed. The anticlockwise rotation of the phase is as expected for a resonance.

8.4.2.1 Secondary minima

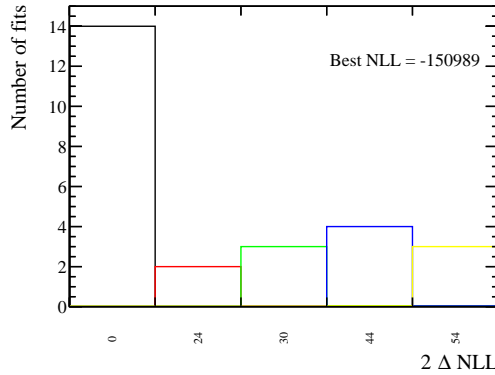


Figure 8.14: The number of experiments finding each minimum. From 100 fits the global minimum is found by 14 experiments, 30 fits failed to converge and the remainder reported a worse likelihood.

The fit is repeated 100 times with randomised initial values of the c_j parameters. The results presented above correspond to the solution with the smallest NLL, but several secondary minima are found, as shown in Fig. 8.14. The global minimum is clearly the most populated solution and all secondary minima have $2\Delta\text{NLL}$ values at least 24 units worse than that of this result. These alternative solutions are not a concern for the results of this analysis, but the results corresponding to each of the minima, in terms of the complex coefficients, are presented in Fig. 8.15.

8.4.3 Testing the baseline model

8.4.3.1 Adding fixed resonances

The completeness of the baseline model is tested by repeating the fit with many different arbitrary fixed resonances added to the fit model. A range of mass and width values are tested for resonances decaying to either $D^- \pi^+$ or $\pi^+ \pi^+$. Since the spline describes the full $D^- \pi^+$ S-wave, states with spin-1, 2, 3 or 4 are considered in the study. The change in $2\Delta\text{NLL}$ for each additional resonance is shown in Fig. 8.16.

Some significant improvements are seen from the addition of a resonance with a width of 20 MeV decaying to $D^- \pi^+$. The inclusion of such a narrow state in the model is not well motivated. Since a large improvement in NLL is observed for a variety of resonance mass and spin values it seems likely that the fit is using the extra freedom from these narrow states to fit fluctuations in the dataset.

Some large values of $2\Delta\text{NLL}$ are also observed from the addition of a doubly charged resonance decaying to $\pi^+ \pi^+$. These states are clearly unphysical, particularly as the improvement occurs only for a few isolated mass and width values. The solutions seem

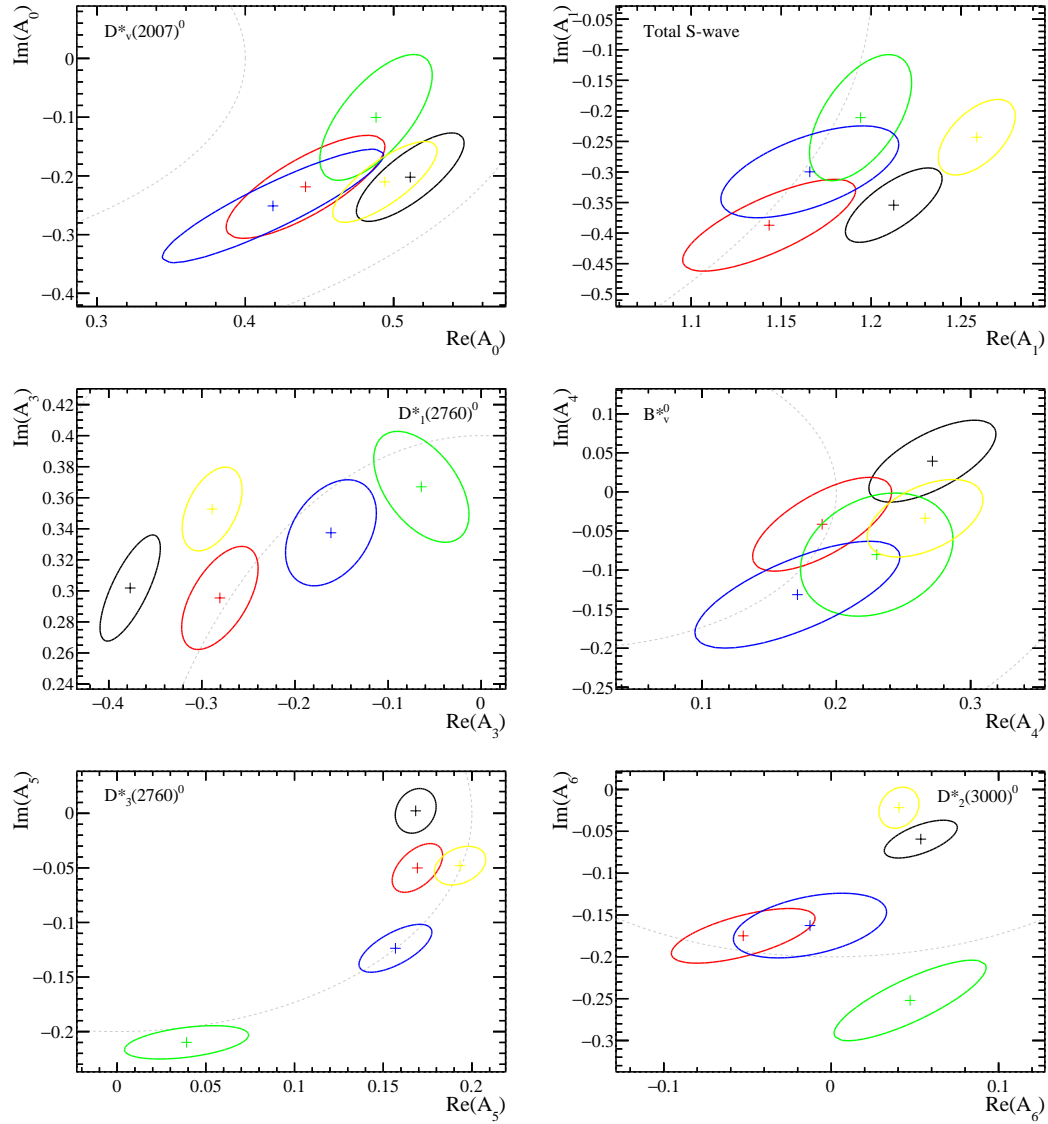


Figure 8.15: Plots of the real and imaginary parts of the fit amplitudes, comparing (black) the best fit against secondary minima with $2\Delta\text{NLL}$ values that are (red) 24, (green) 30, (blue) 44 and (yellow) 54 units worse than the best fit. The coloured contour around each point marks the 1σ uncertainty ellipse. Grey dashed contours mark the $(0,0)$ position to aid comparison of magnitudes. The corresponding resonance component is labelled on each plot.

to occur in the event that some alternative solution is found where a floated parameter is at the boundary of its allowed values in the minimisation software.

The NLL is also found to improve significantly with the inclusion of an extra spin-2 state, with a mass of either ~ 2900 or ~ 3200 MeV/ c^2 and a width of 100–150 MeV. This result is in agreement with the findings from the moments investigation and the nominal Dalitz plot fit results, documented in Secs. 8.3 and 8.4.2, respectively. The spin-2 state in the default model has a mass of (3213.8 ± 28.7) MeV/ c^2 , though Fig. 8.5 from the moments study suggests that a D-wave contribution is required at $m(D\pi) \sim 2900$ MeV/ c^2 .

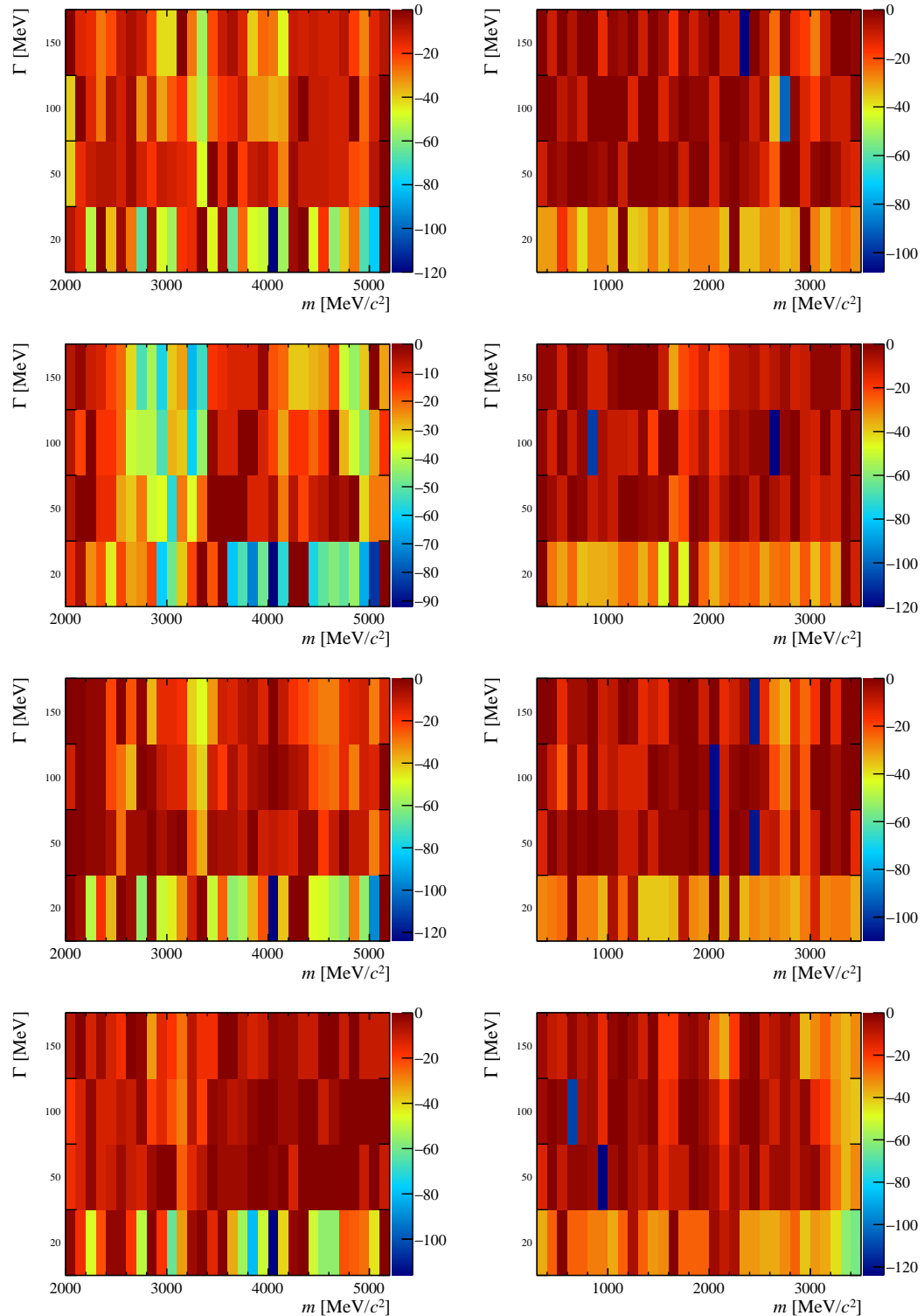


Figure 8.16: $-2\Delta\text{NLL}$ profiles for fits including an additional (left) $D\pi$, and (right) $\pi\pi$ resonance of spin (top – bottom) 1, 2, 3 or 4. Note that the z -axis scale is different for each plot.

8.4.3.2 Alternative models

Discrepancies between the data and fit model are seen in the regions of low $m(D\pi)_{\text{max}}$ and high $m(\pi\pi)$. In case the fit result is biased by a mis-modelling effect in this region of phase space, the fit is repeated with the regions $m(D\pi)_{\text{max}} < 3.3 \text{ GeV}/c^2$ and $m(\pi\pi) > 3.05 \text{ GeV}/c^2$ vetoed separately. With these alterations to the dataset most fit parameters are found to be roughly stable, but no significant improvement is observed in the 2D χ^2 .

The high mass regions of the S-wave splines are investigated by including additional knots in the range $4.1 < m(D\pi) < 5 \text{ GeV}/c^2$. A model-independent description for the P-wave is also tested – similar to that used for the S-wave but with fewer knots. Both of these model alterations were found to make the fit unstable.

The addition of nonresonant P-wave components is also considered; the exponential form factor parametrisation from Eq. 2.38 is used and an additional test is made by including a varying phase in this nonresonant description. Including either of these components does not significantly improve the fit quality.

Finally, potential contributions from an isospin 2 S-wave component in $m(\pi^+\pi^+)$ are investigated, based on a study of the $D^+ \rightarrow K^-\pi^+\pi^+$ decay performed by the CLEO collaboration [115]. The isospin 2 component has a large fit fraction in the final fit and there is significant destructive interference between this amplitude and the $D\pi$ S-wave, suggesting that the solution is not physical.

8.5 Systematic uncertainties

As described in Sec. 6.5, the sources of systematic uncertainty for the results of a Dalitz plot fit can be classified as either experimental systematic uncertainties or model uncertainties. Each source is described below.

8.5.1 Experimental uncertainties

Sources of experimental systematic uncertainty include imperfect knowledge of: the relative numbers of signal and background events in the signal region; the efficiency variation and background distributions as a function of SDP position, and as a result of possible fit bias. The experimental systematic uncertainties for this analysis are evaluated using exactly the same methods described in Sec. 6.5.1.

To quantify the systematic uncertainty due to the signal and background yields, the Dalitz plot fit is repeated with the fixed yields varied within their uncertainties. A set of alternative histograms is produced for each background distribution and for the efficiency variation across the SDP. The fit is repeated with these varied histograms and

the systematic uncertainty is evaluated by considering the change in each floated fit parameter. Systematic uncertainties related to possible intrinsic fit biases are investigated with an ensemble of pseudoexperiments.

The experimental systematic uncertainties on the complex coefficients and fit fractions are summarised in Tab. 8.5. A breakdown of the contribution from each source to the total experimental uncertainty is given in Tab. 8.6. The efficiency variation is the largest source of experimental systematic uncertainty on the fit fractions and floated resonance parameters.

Table 8.5: Experimental systematic uncertainties on the fit fractions and complex amplitudes.

Contribution	Fit fraction (%)	Isobar model coefficients			
		Real part	Imaginary part	Magnitude	Phase (rad)
$\bar{D}_2^*(2460)^0$	1.37	–	–	–	–
$\bar{D}_1^*(2760)^0$	0.69	0.055	0.077	0.010	0.184
$\bar{D}_3^*(2760)^0$	0.13	0.012	0.047	0.014	0.112
$\bar{D}_2^*(3000)^0$	0.07	0.024	0.050	0.013	0.517
$\bar{D}_v^*(2007)^0$	0.74	0.018	0.107	0.014	0.150
\bar{B}_v^*	1.43	0.115	0.118	0.131	0.188
Total S-wave	0.62	0.015	0.072	0.017	0.051

Table 8.6: Breakdown of experimental systematic uncertainties on the fit fractions (%) and masses (MeV/c^2) and widths (MeV).

	Nominal	S/B frac.	Eff.	Bkgd.	Fit bias	Total
$\bar{D}_2^*(2460)^0$	35.7 ± 0.6	0.1	1.3	0.0	0.2	1.4
$\bar{D}_1^*(2760)^0$	8.3 ± 0.6	0.0	0.7	0.1	0.1	0.7
$\bar{D}_3^*(2760)^0$	1.0 ± 0.1	0.0	0.1	0.0	0.0	0.1
$\bar{D}_2^*(3000)^0$	0.2 ± 0.1	0.0	0.1	0.0	0.0	0.1
$\bar{D}_v^*(2007)^0$	10.8 ± 0.7	0.0	0.7	0.1	0.1	0.7
\bar{B}_v^*	2.7 ± 1.0	0.0	1.4	0.1	0.2	1.4
Total S-wave	57.0 ± 0.8	0.1	0.6	0.1	0.1	0.6
$m(\bar{D}_2^*(2460)^0)$	2463.7 ± 0.4	0.0	0.3	0.1	0.1	0.3
$\Gamma(\bar{D}_2^*(2460)^0)$	47.0 ± 0.8	0.1	0.9	0.1	0.0	0.9
$m(\bar{D}_1^*(2760)^0)$	2681.1 ± 5.6	0.1	4.8	0.9	0.2	4.9
$\Gamma(\bar{D}_1^*(2760)^0)$	186.7 ± 8.5	0.5	8.4	1.0	1.2	8.6
$m(\bar{D}_3^*(2760)^0)$	2775.5 ± 4.5	0.4	4.4	0.6	0.4	4.5
$\Gamma(\bar{D}_3^*(2760)^0)$	95.3 ± 9.6	0.9	5.9	1.5	4.9	7.9
$m(\bar{D}_2^*(3000)^0)$	3213.8 ± 28.7	2.6	28.6	13.0	8.9	32.7
$\Gamma(\bar{D}_2^*(3000)^0)$	186.0 ± 37.6	2.1	31.3	7.6	11.9	34.4

8.5.2 Model uncertainties

Systematic uncertainties due to the model choices include fixed parameters in the Dalitz plot fit model, the addition or removal of marginal components to the fit model and

alternative models for the contributing amplitudes in each partial wave. Details of the evaluation techniques are given in Sec. 6.5.2.

The Blatt–Weisskopf radius parameter is varied from its default value of 4 GeV^{-1} to 3 and 5 GeV^{-1} . The larger of the differences on each fitted parameter is taken as the associated uncertainty. The systematic uncertainty introduced by the fixed spline knot positions is evaluated by including additional knots at low values of $m(D\pi)$ and considering the change in the fit results. These two effects are combined in quadrature.

As discussed in Sec. 2.3.3, it is possible that there is more than one spin-1 resonance in the range $2.6 < m(D\pi) < 2.8 \text{ GeV}/c^2$. The measured parameters of the $\bar{D}_1^*(2760)^0$ resonance are most consistent with those given for the $\bar{D}^*(2650)$ state in Tab. 2.5, therefore the effect of including an additional $\bar{D}_1^*(2760)$ contribution is considered as a source of systematic uncertainty. Separate fits are performed with the parameters of the $\bar{D}_1^*(2760)^0$ state fixed to the values determined by BaBar [43] and LHCb [44] and the larger of the deviations from the baseline results is taken as the associated uncertainty. Any effect of the mass dependence of the virtual resonances is evaluated by using a constant width for all virtual resonances to remove the dependence on m_0^{eff} in Eq. 2.35.

A discrepancy between the model and the data is seen in the low $m(D\pi)_{\text{max}}$ region, as discussed in Sec. 8.4. Since this may not be accounted for by the other sources of systematic uncertainty, the effect on the results is determined by performing a fit where this region of the DP is vetoed. Systematic uncertainties are assigned as the difference in the fitted parameters compared to the baseline fit.

The model systematic uncertainties on the complex coefficients and fit fractions are summarised in Tab. 8.7. A breakdown of the contribution from each source to the total model uncertainty is given in Tab. 8.8. The various parameters are affected differently by the sources of model uncertainty, with some being affected by the variation of fixed parameters in the model, others (notably the parameters associated with the $\bar{D}_1^*(2760)^0$ amplitude) by the introduction of an additional $\bar{D}_1^*(2760)^0$ resonance, and some changing when the poorly-modelled region of phase space is vetoed.

Table 8.7: Model uncertainties on the fit fractions and complex amplitudes.

Contribution	Fit fraction (%)	Isobar model coefficients			
		Real part	Imaginary part	Magnitude	Phase (rad)
$\bar{D}_2^*(2460)^0$	0.89	–	–	–	–
$\bar{D}_1^*(2760)^0$	1.79	0.075	0.028	0.055	0.123
$\bar{D}_3^*(2760)^0$	0.25	0.019	0.016	0.019	0.094
$\bar{D}_2^*(3000)^0$	0.08	0.042	0.035	0.013	0.633
$\bar{D}_v^*(2007)^0$	2.34	0.052	0.050	0.059	0.079
\bar{B}_v^*	1.61	0.098	0.049	0.091	0.248
Total S-wave	0.87	0.024	0.027	0.017	0.025

Table 8.8: Breakdown of model uncertainties on the fit fractions (%) and masses (MeV/c^2) and widths (MeV).

	Nominal	Fixed params.	Add $\bar{D}_1^*(2760)^0$	Alt. models	DP veto	Total
$\bar{D}_2^*(2460)^0$	35.7 ± 0.6	0.9	0.0	0.0	0.1	0.9
$\bar{D}_1^*(2760)^0$	8.3 ± 0.6	0.2	0.9	0.0	1.5	1.8
$\bar{D}_3^*(2760)^0$	1.0 ± 0.1	0.0	0.0	0.0	0.2	0.2
$\bar{D}_2^*(3000)^0$	0.2 ± 0.1	0.0	0.0	0.0	0.1	0.1
$\bar{D}_v^*(2007)^0$	10.8 ± 0.7	2.3	0.1	0.0	0.2	2.3
\bar{B}_v^*	2.7 ± 1.0	1.2	0.2	0.0	1.0	1.6
Total S-wave	57.0 ± 0.8	0.8	0.4	0.0	0.1	0.9
$m(\bar{D}_2^*(2460)^0)$	2463.7 ± 0.4	0.4	0.1	0.0	0.4	0.6
$\Gamma(\bar{D}_2^*(2460)^0)$	47.0 ± 0.8	0.2	0.0	0.0	0.1	0.3
$m(\bar{D}_1^*(2760)^0)$	2681.1 ± 5.6	4.7	11.8	0.1	3.0	13.1
$\Gamma(\bar{D}_1^*(2760)^0)$	186.7 ± 8.5	3.2	4.5	0.3	6.0	8.2
$m(\bar{D}_3^*(2760)^0)$	2775.5 ± 4.5	3.4	0.4	0.0	3.3	4.7
$\Gamma(\bar{D}_3^*(2760)^0)$	95.3 ± 9.6	2.8	3.2	0.0	32.9	33.1
$m(\bar{D}_2^*(3000)^0)$	3213.8 ± 28.7	25.3	0.9	0.5	25.8	36.2
$\Gamma(\bar{D}_2^*(3000)^0)$	186.0 ± 37.6	7.1	18.7	0.2	59.5	62.8

8.5.3 Cross checks

A number of cross checks are performed to test the stability of the results. The data sample is divided according to: the year of data taking, the magnet polarity and the charge of the B candidate. Alternative data samples are created by varying the signal region to be within $\pm 2\sigma_1$ or $\pm 3\sigma_1$ of the fitted B candidate mass, and the requirements on the NN_B discriminator and PID variables are tightened and loosened. Fits are performed to each sub-sample individually and the results of these cross check fits are found to be consistent with the default results.

8.6 Results

The masses and widths of the $\bar{D}_2^*(2460)^0$, $\bar{D}_1^*(2760)^0$, $\bar{D}_3^*(2760)^0$ and $\bar{D}_2^*(3000)^0$ resonances are determined to be

$$m(\bar{D}_2^*(2460)^0) = (2463.7 \pm 0.4 \pm 0.4 \pm 0.6) \text{ MeV}/c^2, \quad (8.2)$$

$$\Gamma(\bar{D}_2^*(2460)^0) = (47.0 \pm 0.8 \pm 0.9 \pm 0.3) \text{ MeV}, \quad (8.3)$$

$$m(\bar{D}_1^*(2760)^0) = (2681.1 \pm 5.6 \pm 4.9 \pm 13.1) \text{ MeV}/c^2, \quad (8.4)$$

$$\Gamma(\bar{D}_1^*(2760)^0) = (186.7 \pm 8.5 \pm 8.6 \pm 8.2) \text{ MeV}, \quad (8.5)$$

$$m(\bar{D}_3^*(2760)^0) = (2775.5 \pm 4.5 \pm 4.5 \pm 4.7) \text{ MeV}/c^2, \quad (8.6)$$

$$\Gamma(\bar{D}_3^*(2760)^0) = (95.3 \pm 9.6 \pm 7.9 \pm 33.1) \text{ MeV}, \quad (8.7)$$

$$m(\bar{D}_2^*(3000)^0) = (3213.8 \pm 28.7 \pm 32.7 \pm 36.2) \text{ MeV}/c^2, \quad (8.8)$$

$$\Gamma(\bar{D}_2^*(3000)^0) = (186.0 \pm 37.6 \pm 34.4 \pm 62.8) \text{ MeV}. \quad (8.9)$$

where the three quoted errors are statistical, experimental systematic and model uncertainties, respectively. The results for the $\bar{D}_2^*(2460)^0$ are consistent with the PDG averages [3] shown in Figs. 2.9 and 2.10. The $\bar{D}_1^*(2760)^0$ state has parameters close to those measured for the “ $D^*(2650)$ ” observed by LHCb in prompt production in pp collisions [44]. As discussed in Sec. 2.3.3, two states with spin-parity $J^P = 1^-$ are expected in this region. Similarly, the $\bar{D}_3^*(2760)^0$ state has parameters close to those for the $\bar{D}^*(2760)$ states reported in Refs. [43, 44] and for the charged $\bar{D}_3^*(2760)^-$ state [110]. The $\bar{D}_2^*(3000)^0$ state has parameters that are not consistent with any previously observed resonance, although due to the large uncertainties it cannot be ruled out that it has a common origin with the $D^*(3000)$ state that was reported, without evaluation of systematic uncertainties, in Ref. [44].

Results for the complex coefficients multiplying each amplitude are reported in Tab. 8.9 and those that describe the $D\pi$ S-wave amplitude are shown in Tab. 8.10. These complex numbers are reported in terms of real and imaginary parts and also in terms of magnitude

Table 8.9: Results for the complex amplitudes. The three quoted errors are statistical, experimental systematic and model uncertainties, respectively.

Contribution	Isobar model coefficients	
	Real part	Imaginary part
$\bar{D}_2^*(2460)^0$	1.00	0.00
$\bar{D}_1^*(2760)^0$	$-0.38 \pm 0.02 \pm 0.05 \pm 0.08$	$0.30 \pm 0.02 \pm 0.08 \pm 0.03$
$\bar{D}_3^*(2760)^0$	$0.17 \pm 0.01 \pm 0.01 \pm 0.02$	$0.00 \pm 0.01 \pm 0.05 \pm 0.02$
$\bar{D}_2^*(3000)^0$	$0.05 \pm 0.02 \pm 0.02 \pm 0.04$	$-0.06 \pm 0.02 \pm 0.05 \pm 0.03$
$\bar{D}_v^*(2007)^0$	$0.51 \pm 0.03 \pm 0.02 \pm 0.05$	$-0.20 \pm 0.05 \pm 0.11 \pm 0.05$
\bar{B}_v^*	$0.27 \pm 0.03 \pm 0.11 \pm 0.10$	$0.04 \pm 0.04 \pm 0.12 \pm 0.05$
Total S-wave	$1.21 \pm 0.02 \pm 0.01 \pm 0.02$	$-0.35 \pm 0.04 \pm 0.07 \pm 0.03$
	Magnitude	
	Phase (rad)	
$\bar{D}_2^*(2460)^0$	1.00	0.00
$\bar{D}_1^*(2760)^0$	$0.48 \pm 0.02 \pm 0.01 \pm 0.06$	$2.47 \pm 0.09 \pm 0.18 \pm 0.12$
$\bar{D}_3^*(2760)^0$	$0.17 \pm 0.01 \pm 0.01 \pm 0.02$	$0.01 \pm 0.20 \pm 0.11 \pm 0.09$
$\bar{D}_2^*(3000)^0$	$0.08 \pm 0.01 \pm 0.01 \pm 0.01$	$-0.84 \pm 0.28 \pm 0.52 \pm 0.63$
$\bar{D}_v^*(2007)^0$	$0.55 \pm 0.02 \pm 0.01 \pm 0.06$	$-0.38 \pm 0.19 \pm 0.15 \pm 0.08$
B_v^*	$0.27 \pm 0.05 \pm 0.13 \pm 0.09$	$0.14 \pm 0.38 \pm 0.19 \pm 0.25$
Total S-wave	$1.26 \pm 0.01 \pm 0.02 \pm 0.02$	$-0.28 \pm 0.05 \pm 0.05 \pm 0.03$

and phase as, due to correlations, the propagation of uncertainties from one form to the other may not be trivial.

The fit fractions for resonant contributions (shown in Tab. 8.11) are converted into quasi-two-body product branching fractions by multiplying by the $B^+ \rightarrow D^- \pi^+ \pi^+$ branching fraction. This value is taken from the world average after a correction for the relative branching fractions of $B^+ B^-$ and $B^0 \bar{B}^0$ pairs at the $\Upsilon(4S)$ resonance [3], giving $\mathcal{B}(B^+ \rightarrow D^- \pi^+ \pi^+) = (1.014 \pm 0.054) \times 10^{-3}$. The product branching fractions are also shown in Tab. 8.11; they cannot be converted into absolute branching fractions because the branching fractions for the resonance decays to $D\pi$ are unknown.

Table 8.10: Results for the $D\pi$ S-wave amplitude at the spline knots. The three quoted errors are statistical, experimental systematic and model uncertainties, respectively.

Knot mass (GeV/c ²)	$D\pi$ S-wave amplitude	
	Real part	Imaginary part
2.0	$-0.11 \pm 0.05 \pm 0.07 \pm 0.09$	$-0.04 \pm 0.03 \pm 0.05 \pm 0.11$
2.1	$0.00 \pm 0.05 \pm 0.11 \pm 0.05$	$-0.58 \pm 0.02 \pm 0.03 \pm 0.03$
2.2	$0.39 \pm 0.05 \pm 0.08 \pm 0.05$	$-0.62 \pm 0.04 \pm 0.07 \pm 0.04$
2.3	$0.62 \pm 0.02 \pm 0.03 \pm 0.01$	$-0.28 \pm 0.05 \pm 0.10 \pm 0.03$
2.4	0.50	0.00
2.5	$0.23 \pm 0.01 \pm 0.01 \pm 0.01$	$-0.00 \pm 0.02 \pm 0.04 \pm 0.01$
2.6	$0.21 \pm 0.01 \pm 0.01 \pm 0.01$	$-0.10 \pm 0.02 \pm 0.03 \pm 0.06$
2.7	$0.14 \pm 0.01 \pm 0.01 \pm 0.01$	$-0.05 \pm 0.01 \pm 0.02 \pm 0.02$
2.8	$0.14 \pm 0.01 \pm 0.01 \pm 0.01$	$-0.10 \pm 0.01 \pm 0.02 \pm 0.04$
2.9	$0.13 \pm 0.01 \pm 0.02 \pm 0.01$	$-0.16 \pm 0.01 \pm 0.02 \pm 0.02$
3.1	$0.05 \pm 0.01 \pm 0.02 \pm 0.02$	$-0.12 \pm 0.01 \pm 0.01 \pm 0.01$
4.1	$0.04 \pm 0.01 \pm 0.01 \pm 0.01$	$0.07 \pm 0.01 \pm 0.01 \pm 0.01$
5.1	0.00	0.00

	Magnitude	Phase (rad)
2.0	$0.12 \pm 0.05 \pm 0.07 \pm 0.06$	$-2.82 \pm 0.22 \pm 0.28 \pm 1.47$
2.1	$0.58 \pm 0.02 \pm 0.03 \pm 0.03$	$-1.56 \pm 0.09 \pm 0.17 \pm 0.08$
2.2	$0.73 \pm 0.01 \pm 0.03 \pm 0.02$	$-1.00 \pm 0.08 \pm 0.15 \pm 0.08$
2.3	$0.68 \pm 0.01 \pm 0.03 \pm 0.01$	$-0.42 \pm 0.08 \pm 0.14 \pm 0.05$
2.4	0.50	0.00
2.5	$0.23 \pm 0.01 \pm 0.01 \pm 0.01$	$-0.00 \pm 0.06 \pm 0.07 \pm 0.05$
2.6	$0.23 \pm 0.01 \pm 0.01 \pm 0.03$	$-0.42 \pm 0.09 \pm 0.13 \pm 0.24$
2.7	$0.15 \pm 0.01 \pm 0.01 \pm 0.01$	$-0.31 \pm 0.07 \pm 0.11 \pm 0.15$
2.8	$0.17 \pm 0.01 \pm 0.01 \pm 0.01$	$-0.63 \pm 0.08 \pm 0.10 \pm 0.19$
2.9	$0.20 \pm 0.01 \pm 0.01 \pm 0.01$	$-0.87 \pm 0.09 \pm 0.12 \pm 0.10$
3.1	$0.14 \pm 0.00 \pm 0.01 \pm 0.01$	$-1.16 \pm 0.10 \pm 0.13 \pm 0.13$
4.1	$0.08 \pm 0.00 \pm 0.01 \pm 0.01$	$1.02 \pm 0.12 \pm 0.20 \pm 0.16$
5.1	0.00	0.00

Table 8.11: Results for the fit fractions (%) and product branching fractions $\mathcal{B}(B^+ \rightarrow R\pi^+) \times \mathcal{B}(R \rightarrow D^-\pi^+)$ (10^{-4}). The three quoted errors for the fit fractions are statistical, experimental systematic and model uncertainties, respectively. The additional source of uncertainty on the branching fractions is from $\mathcal{B}(B^+ \rightarrow D^-\pi^+\pi^+)$ [3].

Contribution	Fit fraction (%)	Product branching fraction (10^{-4})
$\bar{D}_2^*(2460)^0$	$35.69 \pm 0.62 \pm 1.37 \pm 0.89$	$3.62 \pm 0.06 \pm 0.14 \pm 0.09 \pm 0.19$
$\bar{D}_1^*(2760)^0$	$8.32 \pm 0.62 \pm 0.69 \pm 1.79$	$0.84 \pm 0.06 \pm 0.07 \pm 0.18 \pm 0.04$
$\bar{D}_3^*(2760)^0$	$1.01 \pm 0.13 \pm 0.13 \pm 0.25$	$0.10 \pm 0.01 \pm 0.01 \pm 0.02 \pm 0.01$
$\bar{D}_2^*(3000)^0$	$0.23 \pm 0.07 \pm 0.07 \pm 0.08$	$0.02 \pm 0.01 \pm 0.01 \pm 0.01 \pm 0.00$
$\bar{D}_v^*(2007)^0$	$10.79 \pm 0.68 \pm 0.74 \pm 2.34$	$1.09 \pm 0.07 \pm 0.07 \pm 0.24 \pm 0.06$
\bar{B}_v^*	$2.69 \pm 1.01 \pm 1.43 \pm 1.61$	$0.27 \pm 0.10 \pm 0.14 \pm 0.16 \pm 0.01$
Total S-wave	$56.96 \pm 0.78 \pm 0.62 \pm 0.87$	$5.78 \pm 0.08 \pm 0.06 \pm 0.09 \pm 0.31$

Chapter 9

Summary

This thesis documents the study of $B \rightarrow Dhh'$ decays using a data sample corresponding to 3.0 fb^{-1} of pp collision data recorded in 2011 and 2012 by the LHCb experiment. Results include the calculation of branching fractions for two three-body decay modes and numerous quasi-two-body decays, as well as the measurement of resonance parameters using amplitude analysis techniques.

First observations are reported for $B^+ \rightarrow D^- K^+ \pi^+$ and $B^+ \rightarrow D^+ K^+ \pi^-$ decays. The branching fraction of the $B^+ \rightarrow D^- K^+ \pi^+$ mode is measured relative to that of the favoured $B^+ \rightarrow D^- \pi^+ \pi^+$ decay as

$$\frac{\mathcal{B}(B^+ \rightarrow D^- K^+ \pi^+)}{\mathcal{B}(B^+ \rightarrow D^- \pi^+ \pi^+)} = 0.0720 \pm 0.0019(\text{stat}) \pm 0.0021(\text{syst}), \quad (9.1)$$

which gives

$$\mathcal{B}(B^+ \rightarrow D^- K^+ \pi^+) = (7.31 \pm 0.19 \pm 0.22 \pm 0.39) \times 10^{-5}, \quad (9.2)$$

where the quoted uncertainties are statistical, systematic and from the branching fraction of the normalisation channel, respectively. A search is performed for the suppressed $B^+ \rightarrow D^+ K^+ \pi^-$ decay. Using the $B^+ \rightarrow D^- K^+ \pi^+$ final state as a control mode, the ratio of branching fractions is measured to be

$$\frac{\mathcal{B}(B^+ \rightarrow D^+ K^+ \pi^-)}{\mathcal{B}(B^+ \rightarrow D^- K^+ \pi^+)} = 0.0726 \pm 0.0123(\text{stat}) \pm 0.0065(\text{syst}). \quad (9.3)$$

Multiplying by the measured value of $\mathcal{B}(B^+ \rightarrow D^- K^+ \pi^+)$ gives

$$\mathcal{B}(B^+ \rightarrow D^+ K^+ \pi^-) = (5.31 \pm 0.90 \pm 0.48 \pm 0.35) \times 10^{-6}, \quad (9.4)$$

where here the third uncertainty is from $\mathcal{B}(B^+ \rightarrow D^- K^+ \pi^+)$. Both of these three-body decays are observed with large significance.

A Dalitz plot fit was performed to $B^+ \rightarrow D^- K^+ \pi^+$ candidates in order to study excited charmed mesons decaying to $D^- \pi^+$. The choice of amplitudes in the fit model was influenced by the angular moments of the decay. The default amplitude model contains resonant contributions from the $\bar{D}_0^*(2400)^0$, $\bar{D}_2^*(2460)^0$ and $\bar{D}_1^*(2760)^0$ states, in addition to both S-wave and P-wave nonresonant amplitudes and virtual $\bar{D}_v^*(2007)^0$ and \bar{B}_v^{*0} resonances. This model was found to give a good description of the data. The results represent the first observation of the $B^+ \rightarrow \bar{D}_1^*(2760)^0 K^+$ decay and the first conclusive evidence that the $\bar{D}_1^*(2760)^0$ state has spin 1. The masses and widths of the $\bar{D}_2^*(2460)^0$ and $\bar{D}_1^*(2760)^0$ states are also reported,

$$m(\bar{D}_2^*(2460)^0) = (2464.0 \pm 1.4 \pm 0.5 \pm 0.2) \text{ MeV}/c^2, \quad (9.5)$$

$$\Gamma(\bar{D}_2^*(2460)^0) = (43.8 \pm 2.9 \pm 1.7 \pm 0.6) \text{ MeV}, \quad (9.6)$$

$$m(\bar{D}_1^*(2760)^0) = (2781 \pm 18 \pm 11 \pm 6) \text{ MeV}/c^2, \quad (9.7)$$

$$\Gamma(\bar{D}_1^*(2760)^0) = (177 \pm 32 \pm 20 \pm 7) \text{ MeV}, \quad (9.8)$$

where the second and third uncertainties on each value are experimental systematic uncertainties and from model variations, respectively.

The fit fractions are derived for all contributing amplitudes in the $B^+ \rightarrow D^- K^+ \pi^+$ Dalitz plot. Multiplication by the measured value of $\mathcal{B}(B^+ \rightarrow D^- K^+ \pi^+)$ provides the product branching fractions shown in Tab. 9.1.

Table 9.1: Results for the product branching fractions $\mathcal{B}(B^+ \rightarrow R K^+) \times \mathcal{B}(R \rightarrow D^- \pi^+)$ (10^{-6}). The four quoted errors are statistical, experimental systematic, model systematic and inclusive branching fraction uncertainties, respectively. Note that this table is identical to Tab. 6.11.

Contribution	Product branching fraction (10^{-6})
$\bar{D}_0^*(2400)^0$	$6.1 \pm 1.9 \pm 0.5 \pm 1.5 \pm 0.4$
$\bar{D}_2^*(2460)^0$	$23.2 \pm 1.1 \pm 0.6 \pm 1.0 \pm 1.6$
$\bar{D}_1^*(2760)^0$	$3.6 \pm 0.9 \pm 0.3 \pm 0.7 \pm 0.2$
S-wave nonresonant	$27.8 \pm 5.4 \pm 1.1 \pm 7.9 \pm 1.9$
P-wave nonresonant	$17.4 \pm 4.1 \pm 1.5 \pm 2.7 \pm 1.2$
$\bar{D}_v^*(2007)^0$	$5.6 \pm 1.7 \pm 1.0 \pm 1.1 \pm 0.4$
\bar{B}_v^{*0}	$2.6 \pm 1.4 \pm 0.6 \pm 1.2 \pm 0.2$

The Dalitz plot of $B^+ \rightarrow D^+ K^+ \pi^-$ decays appears to be dominated by broad structures rather than narrow resonant contributions. Fits are performed to candidates weighted by the $K\pi$ or $D\pi$ angular distributions to search for the quasi-two-body decays $B^+ \rightarrow D^+ K^*(892)^0$ and $B^+ \rightarrow D_2^*(2460)^0 K^+$, respectively. No significant signal is observed for either decay mode and upper limits are set on the branching fractions. For the $B^+ \rightarrow D^+ K^*(892)^0$ decay, the result is

$$\begin{aligned} \mathcal{B}(B^+ \rightarrow D^+ K^*(892)^0) &= (-8.7 \pm 4.3 \pm 3.1 \pm 0.4) \times 10^{-7}, \\ &< 4.9 (6.1) \times 10^{-7} \text{ at 90 (95) \% CL,} \end{aligned} \quad (9.9)$$

where the uncertainties are statistical, systematic and due to the uncertainty on the value of $\mathcal{B}(B^+ \rightarrow D^- K^+ \pi^+)$. This supersedes the previous limit, which was calculated with a different method and using a subset of this dataset [113]. For the $B^+ \rightarrow D_2^*(2460)^0 K^+$ decay the measured product branching fraction is

$$\begin{aligned} \mathcal{B}(B^+ \rightarrow D_2^*(2460)^0 K^+) \times \mathcal{B}(D_2^*(2460)^0 \rightarrow D^+ \pi^-) &= (0.4 \pm 3.5 \pm 1.1 \pm 0.1) \times 10^{-5}, \\ &< 6.3 (7.5) \times 10^{-5} \text{ at 90 (95) \% CL,} \end{aligned} \quad (9.10)$$

where here the third uncertainty is from the value of $\mathcal{B}(B^+ \rightarrow \bar{D}_2^*(2460)^0 K^+) \times \mathcal{B}(\bar{D}_2^*(2460)^0 \rightarrow D^- \pi^+)$. There are no previous experimental results on this decay mode.

The ratio of magnitudes of the suppressed and favoured $DK\pi$ modes gives

$$\begin{aligned} r_B(D_2^*(2460)K^+) &= 0.04 \pm 0.18 \pm 0.06, \\ &< 0.30 (0.36), \end{aligned} \quad (9.11)$$

where the quoted uncertainties are statistical and systematic, respectively. There are insufficient statistics to perform a full Dalitz plot analysis of the $B^+ \rightarrow D^+ K^+ \pi^-$ decay mode with the current dataset. The results in this thesis indicate that, with a larger sample of candidates, it will be interesting to study the resonant contributions in the $B^+ \rightarrow D^+ K^+ \pi^-$ decay to understand the potential for a measurement of the CKM angle γ using $B^+ \rightarrow DK^+ \pi^0$ decays.

Further studies of excited charmed mesons were made by performing a Dalitz plot fit to $B^+ \rightarrow D^- \pi^+ \pi^+$ decay candidates. Again, the angular moments of the decay were first investigated to gain information about the potential contributions of individual partial waves. The nominal amplitude model contains resonant contributions from the $\bar{D}_2^*(2460)^0$, $\bar{D}_1^*(2760)^0$, $\bar{D}_3^*(2760)^0$ and $\bar{D}_2^*(3000)^0$ states and the virtual $\bar{D}_v^*(2007)^0$ and \bar{B}_v^{*0} resonances. A model-independent approach was used to model the full $D\pi$ S-wave. The masses and widths of the $\bar{D}_2^*(2460)^0$, $\bar{D}_1^*(2760)^0$, $\bar{D}_3^*(2760)^0$ and $\bar{D}_2^*(3000)^0$ states are measured,

$$m(\bar{D}_2^*(2460)^0) = (2463.7 \pm 0.4 \pm 0.4 \pm 0.6) \text{ MeV}/c^2, \quad (9.12)$$

$$\Gamma(\bar{D}_2^*(2460)^0) = (47.0 \pm 0.8 \pm 0.9 \pm 0.3) \text{ MeV}, \quad (9.13)$$

$$m(\bar{D}_1^*(2760)^0) = (2681.1 \pm 5.6 \pm 4.9 \pm 13.1) \text{ MeV}/c^2, \quad (9.14)$$

$$\Gamma(\bar{D}_1^*(2760)^0) = (186.7 \pm 8.5 \pm 8.6 \pm 8.2) \text{ MeV}, \quad (9.15)$$

$$m(\bar{D}_3^*(2760)^0) = (2775.5 \pm 4.5 \pm 4.5 \pm 4.7) \text{ MeV}/c^2, \quad (9.16)$$

$$\Gamma(\bar{D}_3^*(2760)^0) = (95.3 \pm 9.6 \pm 7.9 \pm 33.1) \text{ MeV}, \quad (9.17)$$

$$m(\bar{D}_2^*(3000)^0) = (3213.8 \pm 28.7 \pm 32.7 \pm 36.2) \text{ MeV}/c^2, \quad (9.18)$$

$$\Gamma(\bar{D}_2^*(3000)^0) = (186.0 \pm 37.6 \pm 34.4 \pm 62.8) \text{ MeV}. \quad (9.19)$$

Table 9.2: Results for the product branching fractions $\mathcal{B}(B^+ \rightarrow R\pi^+) \times \mathcal{B}(R \rightarrow D^-\pi^+)$ (10^{-4}). The four quoted errors are due to the statistical, experimental systematic, model systematic and inclusive branching fraction uncertainties, respectively. Note that this table is identical to Tab. 8.11.

Contribution	Product branching fraction (10^{-4})
$\bar{D}_2^*(2460)^0$	$3.62 \pm 0.06 \pm 0.14 \pm 0.09 \pm 0.19$
$\bar{D}_1^*(2760)^0$	$0.84 \pm 0.06 \pm 0.07 \pm 0.18 \pm 0.04$
$\bar{D}_3^*(2760)^0$	$0.10 \pm 0.01 \pm 0.01 \pm 0.02 \pm 0.01$
$\bar{D}_2^*(3000)^0$	$0.02 \pm 0.01 \pm 0.01 \pm 0.01 \pm 0.00$
$\bar{D}_v^*(2007)^0$	$1.09 \pm 0.07 \pm 0.07 \pm 0.24 \pm 0.06$
\bar{B}_v^*	$0.27 \pm 0.10 \pm 0.14 \pm 0.16 \pm 0.01$
Total S-wave	$5.78 \pm 0.08 \pm 0.06 \pm 0.09 \pm 0.31$

where the second and third uncertainties on each value are experimental systematic uncertainties and from model variations, respectively.

The fit fractions of all amplitudes in the $B^+ \rightarrow D^-\pi^+\pi^+$ Dalitz plot are also reported. The product branching fractions shown in Tab. 9.2 are obtained by multiplying each fit fraction by the world average value of the branching fraction for the $B^+ \rightarrow D^-\pi^+\pi^+$ decay.

Appendix A

VELO material description

This appendix documents my work on the material description of the VELO sub-detector at the LHCb experiment. The study presented is an extension of work by other members of the collaboration, which is described in more detail in Refs. [73] and [121].

Minimising the material budget was an important consideration during the design phase of the LHCb detector. In order to optimise the performance of the experiment it is necessary to reduce both the amount of multiple scattering and the number of particle interactions that occur in the detector material. Now an accurate description of the VELO material is required for event simulation models and to estimate the amount of multiple scattering undergone by interacting particles when reconstructing tracks.

A.1 Method

Interaction data is used to study the material description of the VELO. A particle interacting with the detector material can produce other particles, and it is possible to reconstruct their production vertex if some of these tracks are charged and pass through the VELO acceptance. The distribution of detector material can then be investigated by considering the density of these reconstructed vertices.

This study uses data taken during pp collisions in 2011 and 2012, but only interactions of the proton beam with gas in the beam pipe are considered. Beam gas events have been found to produce a uniform flux of interactions in the VELO region and have low backgrounds, so these data are well suited for studying the material distribution in the VELO.

The software trigger is used to select events which are consistent with a beam gas interaction from the Run I data sample. Interaction vertices are reconstructed using at least three tracks, where each track is required to have hits in three or more R- and

ϕ -sensors of the VELO. A requirement is placed on the vertex radius to remove vertices along the beam line and any remaining non-material interactions are effectively removed by requiring that each event has only one vertex. After these selection requirements, approximately 10 million (4 million) events remain from the 2011 (2012) data samples.

A.2 Results

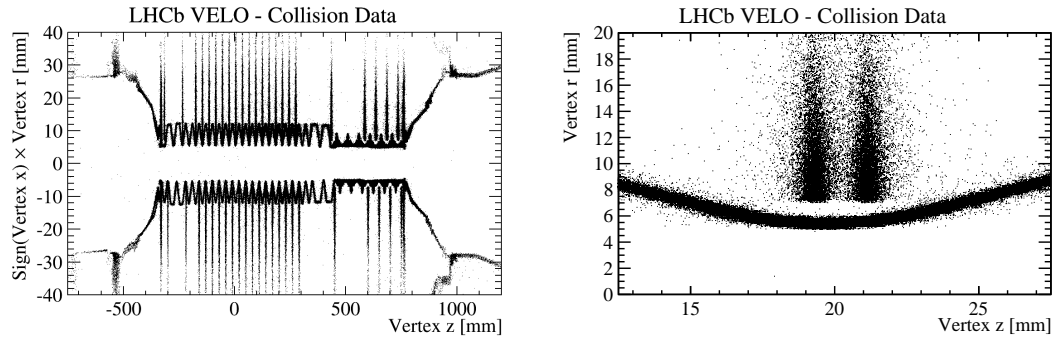


Figure A.1: Reconstructed vertices of hadronic interactions in the LHCb VELO material from 2011 and 2012 data. (left) The whole VELO system. (right) Zoom of a pair of R- and ϕ -sensors to check the distance between the sensors and foil.

Figure A.1 shows cross-sections of the VELO obtained from reconstructed vertices of hadronic interactions in LHCb data. Vertices between $-5 < y < 5$ mm in data are plotted in the $r'z$ plane, where r' is the transverse radius of the vertex multiplied by +1 or -1 depending on the sign of the x coordinate to separate the left and right halves of the detector. The full RF foil and the sensors in each VELO module can be seen. These vertex distributions offer a method to check the relative positions of the various VELO components. The individual R- and ϕ -sensors in a single module are shown in Fig. A.1 (right). It is important to check the clearance of all VELO sensors from the RF foil, since if these were to touch it could damage the RF foil or cause an electrical short. All the sensors are found to be close to, but not touching, the RF foil.

The method described above can be applied to simulated data to examine the detector model used in the simulation process. Structures in the simulated detector must be described reasonably accurately, but complex shapes such as the RF foil are simplified in order to reduce CPU time. Figure A.2 shows a few of the downstream VELO modules, reconstructed from vertices in both data and simulated events. Good agreement is seen between the distributions from the two samples, though the shape of the RF foil used in simulation is clearly more angular than the true material distribution. The mass of the RF foil, which is the dominant component of the VELO material, is reproduced correctly in simulation to within $\sim 2\%$ [73].

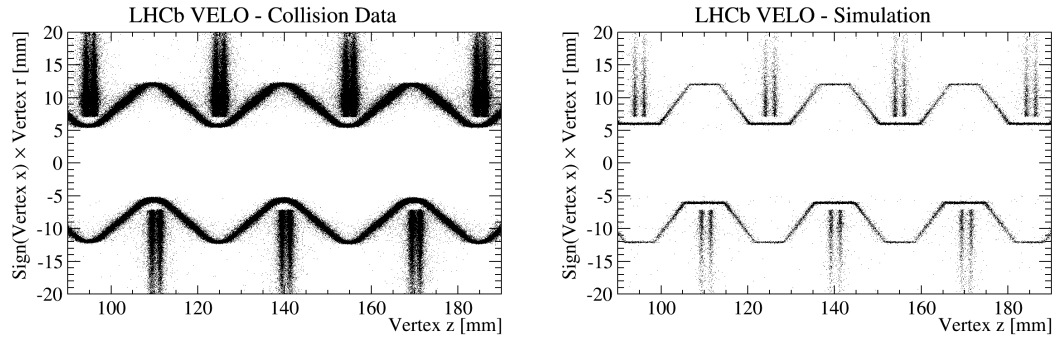


Figure A.2: Reconstructed vertices of hadronic interactions in the LHCb VELO material from (left) data and (right) simulated events.

The reconstructed vertices can also be used to determine the size of the aperture available to the beam. As a result of unquantified effects from the construction and positioning of the RF foil, the true aperture value is otherwise not known precisely. It is useful to know how accurately the true aperture value compares to the design value; knowledge of the true aperture radius is particularly important for the design of the VELO upgrade since the aim is to place sensors closer to the beam line in the upgraded detector.

The aperture presented to the beam by the RF foil is at its smallest radius in the regions around sensor slots. Vertices within ± 1 mm of the nominal z position of the centre of each slot are considered for the measurement of the aperture. Figure A.3 shows the distribution of vertices in four such regions. Requirements (indicated by the lines in Fig. A.3) are placed on the vertex positions in order to select only those in the region where the RF foil is closest to the beam. The selected vertices for each slot position are fitted using a circle with floated radius and centre. The fitted circles are all shown in Fig. A.4, with the conservative assumption that the RF foil has a thickness of 0.3 mm. By combining all the fitted circles, the true aperture is found to be 4.9 mm. This value is to be compared to the nominal aperture of 5.5 mm specified in the VELO design. Considering also the welding of the foil to the RF box, the measured aperture is 4.5 mm which is well within the tolerance of 2.4 mm reserved for mechanical imperfections of the foil when the design radius was originally set.

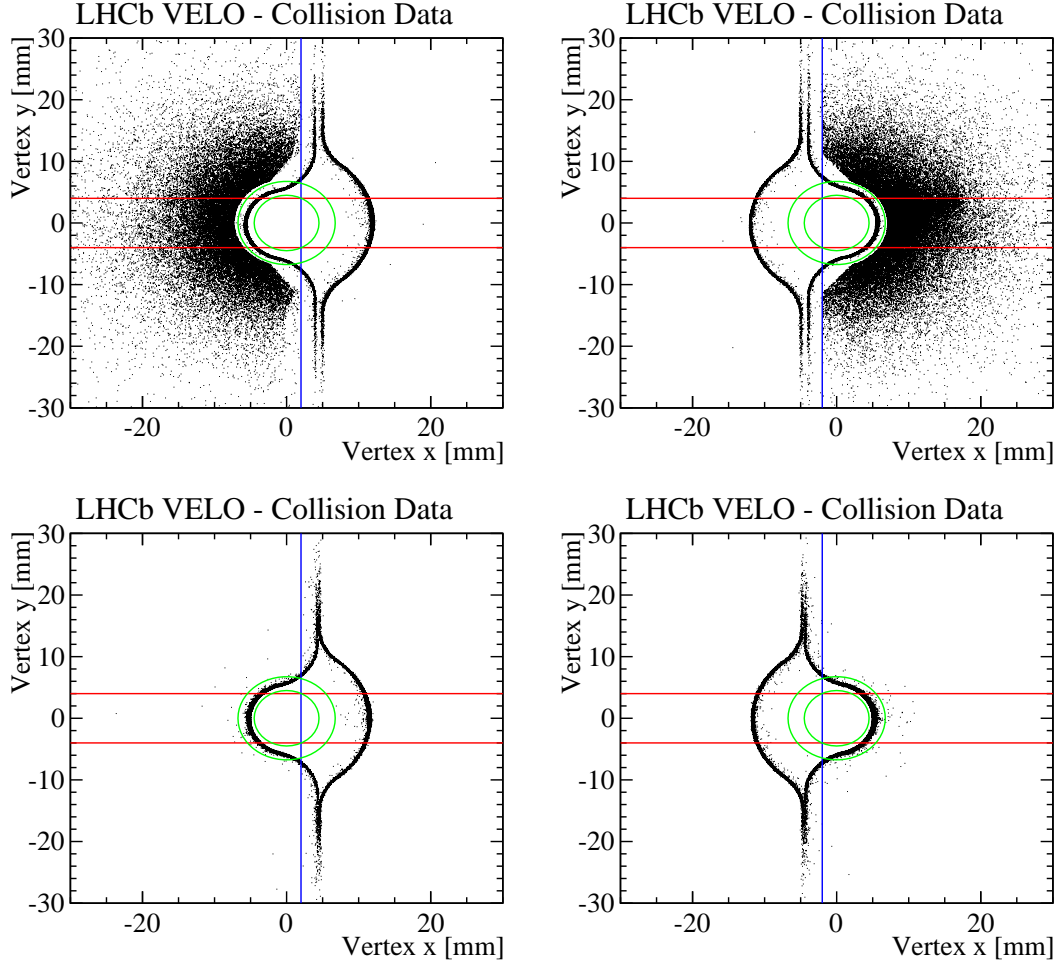


Figure A.3: Reconstructed vertices of hadronic interactions in the LHCb VELO material from 2011 and 2012 data. (top) Slots in the RF foil with a sensor: (left) $79 < z < 81$ mm and (right) $64 < z < 66$ mm. (bottom) Slots in the RF foil without a sensor: (left) $399 < z < 401$ mm and (right) $384 < z < 386$ mm. Vertices selected for further analysis must satisfy the conditions: $4.50 < r < 6.57$ mm (*i.e.* within the two green circles), $|y| < 4$ mm (*i.e.* between the two red lines) and $x > -2$ mm or $x < 2$ mm, depending on the side of the detector and indicated by the vertical blue line.

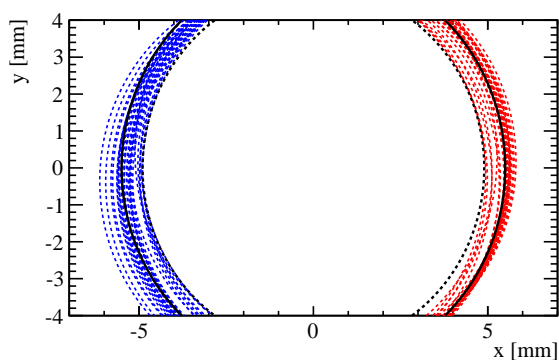


Figure A.4: A visualisation of the true aperture presented to the beam by the RF foil. The fitted circles from each slot position are shown as red and blue dashed semi-circles, where the fitted radius has been reduced by 0.15 mm to account for the thickness of the RF foil. The combination of the fitted circles corresponds to a true aperture of 4.9 mm (dashed black circle). The nominal aperture, corresponding to a circle of radius 5.5 mm, is overlaid (solid black line).

Bibliography

- [1] **LHCb** Collaboration, R. Aaij *et al.*, “First observation and amplitude analysis of the $B^- \rightarrow D^+ K^- \pi^-$ decay,” *Phys. Rev.* **D91** (2015) 092002, [arXiv:1503.02995 \[hep-ex\]](https://arxiv.org/abs/1503.02995). Cited on pages 2, 21, 22, 57, 77, 88, 121, 129, and 137.
- [2] **LHCb** Collaboration, R. Aaij *et al.*, “First observation of the rare $B^+ \rightarrow D^+ K^+ \pi^-$ decay,” *Phys. Rev.* **D93** (2015) 051101(R), [arXiv:1512.02494 \[hep-ex\]](https://arxiv.org/abs/1512.02494). Cited on pages 2, 57, and 106.
- [3] **Particle Data Group** Collaboration, K. Olive *et al.*, “Review of particle physics,” *Chin. Phys.* **C38** (2014) 090001. Cited on pages 4, 5, 11, 21, 59, 80, 81, 82, 105, 114, 124, 129, 132, 136, 151, 152, and 153.
- [4] **CMS** Collaboration, S. Chatrchyan *et al.*, “Observation of a new boson at a mass of 125 GeV with the CMS experiment at the LHC,” *Phys. Lett.* **B716** (2012) 30–61, [arXiv:1207.7235 \[hep-ex\]](https://arxiv.org/abs/1207.7235). Cited on pages 4 and 32.
- [5] **ATLAS** Collaboration, G. Aad *et al.*, “Observation of a new particle in the search for the Standard Model Higgs boson with the ATLAS detector at the LHC,” *Phys. Lett.* **B716** (2012) 1 – 29, [arXiv:1207.7214 \[hep-ex\]](https://arxiv.org/abs/1207.7214). Cited on pages 4 and 32.
- [6] F. Englert and R. Brout, “Broken symmetry and the mass of gauge vector mesons,” *Phys. Rev. Lett.* **13** (1964) 321–323. Cited on page 4.
- [7] P. W. Higgs, “Broken symmetries and the masses of gauge bosons,” *Phys. Rev. Lett.* **13** (1964) 508–509. Cited on page 4.
- [8] G. S. Guralnik, C. R. Hagen, and T. W. B. Kibble, “Global conservation laws and massless particles,” *Phys. Rev. Lett.* **13** (1964) 585–587. Cited on page 4.
- [9] **Belle** Collaboration, S. K. Choi *et al.*, “Observation of a resonance-like structure in the $\pi^\pm \psi'$ mass distribution in exclusive $B \rightarrow K \pi^\pm \psi'$ decays,” *Phys. Rev. Lett.* **100** (2008) 142001, [arXiv:0708.1790 \[hep-ex\]](https://arxiv.org/abs/0708.1790). Cited on page 5.
- [10] **Belle** Collaboration, K. Chilikin *et al.*, “Experimental constraints on the spin and parity of the $Z(4430)^+$,” *Phys. Rev.* **D88** (2013) 074026, [arXiv:1306.4894 \[hep-ex\]](https://arxiv.org/abs/1306.4894). Cited on page 5.

- [11] **LHCb** Collaboration, R. Aaij *et al.*, “Observation of the resonant character of the $Z(4430)^-$ state,” *Phys. Rev. Lett.* **112** (2014) 222002, [arXiv:1404.1903](https://arxiv.org/abs/1404.1903) [hep-ex]. Cited on page 5.
- [12] **LHCb** Collaboration, R. Aaij *et al.*, “Observation of $J/\psi p$ resonances consistent with pentaquark states in $\Lambda_b^0 \rightarrow J/\psi p K^-$ decays,” *Phys. Rev. Lett.* **115** (2015) 072001, [arXiv:1507.03414](https://arxiv.org/abs/1507.03414) [hep-ex]. Cited on page 5.
- [13] E. Noether, “Invariant variation problems,” *Transport Theory and Statistical Physics* **1** (1971) 186–207, <http://dx.doi.org/10.1080/00411457108231446>. Cited on page 5.
- [14] L. D. Landau, “On the conservation laws for weak interactions,” *Nucl. Phys.* **3** (1957) 127–131. Cited on page 6.
- [15] S. Okubo, “Decay of the Sigma+ hyperon and its antiparticle,” *Phys. Rev.* **109** (1958) 984–985. Cited on page 6.
- [16] R. D. Peccei and H. R. Quinn, “Constraints imposed by CP conservation in the presence of instantons,” *Phys. Rev.* **D16** (1977) 1791–1797. Cited on page 6.
- [17] A. D. Sakharov, “Violation of CP invariance, C asymmetry, and baryon asymmetry of the universe,” *Soviet Physics Uspekhi* **34** (1991) 392. Cited on page 7.
- [18] M. E. Peskin, “Particle physics: Song of the electroweak penguin,” *Nature* **452** (2008) 293–294. Cited on page 7.
- [19] J. H. Christenson, J. W. Cronin, V. L. Fitch, and R. Turlay, “Evidence for the 2π decay of the K_2^0 meson,” *Phys. Rev. Lett.* **13** (1964) 138–140. Cited on pages 8 and 9.
- [20] **LHCb** Collaboration, R. Aaij *et al.*, “Observation of CP violation in $B^\pm \rightarrow DK^\pm$ decays,” *Phys. Lett.* **B712** (2012) 203, [arXiv:1203.3662](https://arxiv.org/abs/1203.3662) [hep-ex]. Cited on page 8.
- [21] **LHCb** Collaboration, R. Aaij *et al.*, “Measurement of the CP -violating phase β in $\bar{B}^0 \rightarrow J/\psi \pi^+ \pi^-$ decays and limits on penguin effects,” *Phys. Lett.* **B742** (2015) 38, [arXiv:1411.1634](https://arxiv.org/abs/1411.1634) [hep-ex]. Cited on page 9.
- [22] N. Cabibbo, “Unitary symmetry and leptonic decays,” *Phys. Rev. Lett.* **10** (1963) 531–533. Cited on page 10.
- [23] M. Kobayashi and T. Maskawa, “ CP -violation in the renormalizable theory of weak interaction,” *Progress of Theoretical Physics* **49** (1973) 652–657. Cited on page 10.

[24] L. Wolfenstein, “Violation of CP invariance and the possibility of very weak interactions,” *Phys. Rev. Lett.* **13** (1964) 562–564. Cited on page 10.

[25] **CKMfitter** Collaboration, J. Charles *et al.*, “ CP violation and the CKM matrix: Assessing the impact of the asymmetric B factories,” *Eur. Phys. J.* **C41** (2005) 1–131, [arXiv:hep-ph/0406184](https://arxiv.org/abs/hep-ph/0406184) [hep-ph]. Cited on pages 11, 12, and 13.

[26] C. Jarlskog, “Commutator of the quark mass matrices in the standard electroweak model and a measure of maximal CP violation,” *Phys. Rev. Lett.* **55** (1985) 1039. Cited on page 12.

[27] **UTfit** Collaboration, M. Bona *et al.*, “The 2004 UTfit collaboration report on the status of the unitarity triangle in the standard model,” *JHEP* **07** (2005) 028, [arXiv:hep-ph/0501199](https://arxiv.org/abs/hep-ph/0501199) [hep-ph]. Cited on page 12.

[28] **LHCb** Collaboration, “Improved constraints on γ : CKM2014 update,” Sep, 2014. LHCb-CONF-2014-004. Cited on page 12.

[29] M. Gronau and D. London, “How to determine all the angles of the unitarity triangle from $B^0 \rightarrow DK_s^0$ and $B_s^0 \rightarrow D\phi$,” *Phys. Lett.* **B253** (1991) 483–488. Cited on page 14.

[30] M. Gronau and D. Wyler, “On determining a weak phase from charged B decay asymmetries,” *Phys. Lett.* **B265** (1991) 172–176. Cited on page 14.

[31] N. Sinha, “Determining γ using $B \rightarrow D^{**}K$,” *Phys. Rev.* **D70** (2004) 097501, [arXiv:hep-ph/0405061](https://arxiv.org/abs/hep-ph/0405061) [hep-ph]. Cited on pages 15, 57, and 107.

[32] D. Atwood and A. Soni, “Role of a charm factory in extracting CKM-phase information via $B \rightarrow DK$,” *Phys. Rev.* **D68** (2003) 033003. Cited on page 15.

[33] **BaBar** Collaboration, P. del Amo Sanchez *et al.*, “Measurement of D^0 – \bar{D}^0 mixing parameters using $D^0 \rightarrow K_s^0\pi^+\pi^-$ and $D^0 \rightarrow K_s^0K^+K^-$ decays,” *Phys. Rev. Lett.* **105** (2010) 081803, [arXiv:1004.5053](https://arxiv.org/abs/1004.5053) [hep-ex]. Cited on page 17.

[34] **LHCb** Collaboration, R. Aaij *et al.*, “Measurement of CP violation and constraints on the CKM angle γ in $B^\pm \rightarrow DK^\pm$ with $D \rightarrow K_S^0\pi^+\pi^-$ decays,” *Nucl. Phys.* **B888** (2014) 169, [arXiv:1407.6211](https://arxiv.org/abs/1407.6211) [hep-ex]. Cited on page 17.

[35] **LHCb** Collaboration, R. Aaij *et al.*, “A model-independent Dalitz plot analysis of $B^\pm \rightarrow DK^\pm$ with $D \rightarrow K_S^0h^+h^-$ ($h = \pi, K$) decays and constraints on the CKM angle γ ,” *Phys. Lett.* **B718** (2012) 43–55, [arXiv:1209.5869](https://arxiv.org/abs/1209.5869) [hep-ex]. Cited on page 17.

[36] A. Giri, Y. Grossman, A. Soffer, and J. Zupan, “Determining γ using $B^\pm \rightarrow DK^\pm$ with multibody D decays,” *Phys. Rev.* **D68** (2003) 054018. Cited on page 17.

[37] **CLEO** Collaboration, J. Libby *et al.*, “Model-independent determination of the strong-phase difference between D^0 and $\bar{D}^0 \rightarrow K_{S,L}^0 h^+ h^-$ ($h = \pi, K$) and its impact on the measurement of the CKM angle γ/ϕ_3 ,” *Phys. Rev.* **D82** (2010) 112006, [arXiv:1010.2817 \[hep-ex\]](https://arxiv.org/abs/1010.2817). Cited on page 17.

[38] **Belle** and **BaBar** Collaborations. A. J. Bevan *et al.*, “The physics of the B Factories,” *Eur. Phys. J.* **C74** (2014) 3026, [arXiv:1406.6311 \[hep-ex\]](https://arxiv.org/abs/1406.6311). Cited on pages 19 and 23.

[39] S. Godfrey and N. Isgur, “Mesons in a relativized quark model with chromodynamics,” *Phys. Rev.* **D32** (1985) 189–231. Cited on page 19.

[40] S. Godfrey and K. Moats, “Properties of excited charm and charm-strange mesons,” [arXiv:1510.08305 \[hep-ph\]](https://arxiv.org/abs/1510.08305). Cited on page 19.

[41] **BaBar** Collaboration, B. Aubert *et al.*, “Dalitz plot analysis of $B^- \rightarrow D^+ \pi^- \pi^-$,” *Phys. Rev.* **D79** (2009) 112004, [arXiv:0901.1291 \[hep-ex\]](https://arxiv.org/abs/0901.1291). Cited on page 20.

[42] **Belle** Collaboration, K. Abe *et al.*, “Study of $B^- \rightarrow D^{**0} \pi^-$ ($D^{**0} \rightarrow D^{(*)+} \pi^-$) decays,” *Phys. Rev.* **D69** (2004) 112002, [arXiv:hep-ex/0307021 \[hep-ex\]](https://arxiv.org/abs/hep-ex/0307021). Cited on page 21.

[43] **BaBar** Collaboration, P. del Amo Sanchez *et al.*, “Observation of new resonances decaying to $D\pi$ and $D^*\pi$ in inclusive e^+e^- collisions near $\sqrt{s} = 10.58$ GeV,” *Phys. Rev.* **D82** (2010) 111101, [arXiv:1009.2076 \[hep-ex\]](https://arxiv.org/abs/1009.2076). Cited on pages 21, 139, 149, and 151.

[44] **LHCb** Collaboration, R. Aaij *et al.*, “Study of D_J meson decays to $D^+ \pi^-$, $D^0 \pi^+$ and $D^{*+} \pi^-$ final states in pp collisions,” *JHEP* **09** (2013) 145, [arXiv:1307.4556 \[hep-ex\]](https://arxiv.org/abs/1307.4556). Cited on pages 21, 22, 64, 139, 149, and 151.

[45] **Particle Data Group** Collaboration, K. A. Olive *et al.*, “Review of particle physics,” *Chin. Phys.* **C38** (2014) 090001. and 2015 update. Cited on pages 21 and 22.

[46] R. H. Dalitz, “On the analysis of tau-meson data and the nature of the tau-meson,” *Phil. Mag.* **44** (1953) 1068–1080. Cited on page 23.

[47] **LHCb** Collaboration, R. Aaij *et al.*, “Amplitude analysis of $B^0 \rightarrow \bar{D}^0 K^+ \pi^-$ decays,” *Phys. Rev.* **D92** (2015) 012012, [arXiv:1505.01505 \[hep-ex\]](https://arxiv.org/abs/1505.01505). Cited on page 24.

[48] G. N. Fleming, “Recoupling effects in the isobar model. 1. General formalism for three-pion scattering,” *Phys. Rev.* **135** (1964) B551–B560. Cited on page 25.

- [49] D. Morgan, “Phenomenological analysis of $I = \frac{1}{2}$ single-pion production processes in the energy range 500 to 700 MeV,” *Phys. Rev.* **166** (1968) 1731–1759. Cited on page 25.
- [50] D. Herndon, P. Soding, and R. J. Cashmore, “Generalised isobar model formalism,” *Phys. Rev.* **D11** (1975) 3165. Cited on page 25.
- [51] C. Zemach, “Three-pion decays of unstable particles,” *Phys. Rev.* **133** (1964) B1201. Cited on page 26.
- [52] C. Zemach, “Use of angular-momentum tensors,” *Phys. Rev.* **140** (1965) B97–B108. Cited on page 26.
- [53] J. Blatt and V. E. Weisskopf, *Theoretical nuclear physics*. J. Wiley (New York), 1952. Cited on page 26.
- [54] **BaBar** Collaboration, B. Aubert *et al.*, “Dalitz-plot analysis of the decays $B^\pm \rightarrow K^\pm \pi^\mp \pi^\pm$,” *Phys. Rev.* **D72** (2005) 072003, [hep-ex/0507004](#). Cited on page 26.
- [55] **LHCb** Collaboration, R. Aaij *et al.*, “Dalitz plot analysis of $B_s^0 \rightarrow \bar{D}^0 K^- \pi^+$ decays,” *Phys. Rev.* **D90** (2014) 072003, [arXiv:1407.7712 \[hep-ex\]](#). Cited on pages 26, 103, and 135.
- [56] **Belle** Collaboration, A. Garmash *et al.*, “Dalitz analysis of the three-body charmless decays $B^+ \rightarrow K^+ \pi^+ \pi^-$ and $B^+ \rightarrow K^+ K^+ K^-$,” *Phys. Rev.* **D71** (2005) 092003, [arXiv:hep-ex/0412066 \[hep-ex\]](#). Cited on page 27.
- [57] **BaBar** Collaboration, J. Lees *et al.*, “Measurement of CP -violating asymmetries in $B^0 \rightarrow (\rho\pi)^0$ decays using a time-dependent Dalitz plot analysis,” *Phys. Rev.* **D88** (2013) 012003, [arXiv:1304.3503 \[hep-ex\]](#). Cited on page 28.
- [58] **LHCb** Collaboration, A. A. Alves *et al.*, “The LHCb Detector at the LHC,” *JINST* **3** (2008) S08005. Cited on pages 31, 36, 39, 41, 42, 43, 45, 46, and 47.
- [59] L. Evans and P. Bryant, “LHC Machine,” *JINST* **3** S08001 (2008) . Cited on page 31.
- [60] “CERN accelerator complex,” accessed August 2015.
<http://cds.cern.ch/record/841493>. Cited on page 32.
- [61] **ATLAS** Collaboration, G. Aad *et al.*, “The ATLAS Experiment at the CERN Large Hadron Collider,” *JINST* **3** (2008) S08003. Cited on page 32.
- [62] **CMS** Collaboration, S. Chatrchyan *et al.*, “The CMS experiment at the CERN LHC,” *JINST* **3** (2008) S08004. Cited on page 32.
- [63] **ALICE** Collaboration, K. Aamodt *et al.*, “The ALICE experiment at the CERN LHC,” *JINST* **3** (2008) S08002. Cited on page 32.

[64] **BaBar** Collaboration, B. Aubert *et al.*, “The BaBar detector,” *Nucl. Instrum. Meth.* **A479** (2002) 1–116, [arXiv:hep-ex/0105044](https://arxiv.org/abs/hep-ex/0105044) [hep-ex]. Cited on page 33.

[65] **Belle** Collaboration, A. Abashian *et al.*, “The Belle Detector,” *Nucl. Instrum. Meth.* **A479** (2002) 117–232. Cited on page 33.

[66] **LHCb** Collaboration, R. Aaij *et al.*, “Measurement of $\sigma(pp \rightarrow b\bar{b}X)$ at $\sqrt{s} = 7$ TeV in the forward region,” *Phys. Lett.* **B694** (2010) 209–216, [arXiv:1009.2731](https://arxiv.org/abs/1009.2731) [hep-ex]. Cited on page 33.

[67] **LHCb** Collaboration, R. Aaij *et al.*, “Prompt charm production in pp collisions at $\sqrt{s} = 7$ TeV,” *Nucl. Phys.* **B871** (2013) 1, [arXiv:1302.2864](https://arxiv.org/abs/1302.2864) [hep-ex]. Cited on page 33.

[68] **LHCb** Collaboration, “Prompt charm production in pp collisions at $\sqrt{s} = 7$ TeV,” Dec, 2010. Cited on page 33.

[69] T. Sjostrand, S. Mrenna, and P. Z. Skands, “PYTHIA 6.4 Physics and Manual,” *JHEP* **0605** (2006) 026, [arXiv:hep-ph/0603175](https://arxiv.org/abs/hep-ph/0603175) [hep-ph]. Cited on page 33.

[70] “LHCb material for presentations,” accessed August 2015. https://lhcb.web.cern.ch/lhcb/speakersbureau/html/bb_ProductionAngles.html. Cited on page 33.

[71] **LHCb** Collaboration, *LHCb reoptimized detector design and performance: Technical Design Report*. Geneva, 2003. LHCb-TDR-009. Cited on page 35.

[72] **LHCb** Collaboration, “LHCb VELO (VErtex LOcator): Technical Design Report,” 2001. LHCb-TDR-005. Cited on page 35.

[73] R. Aaij *et al.*, “Performance of the LHCb Vertex Locator,” *JINST* **9** (2014) P09007, [arXiv:1405.7808](https://arxiv.org/abs/1405.7808) [physics.ins-det]. Cited on pages 35, 53, 158, and 159.

[74] **LHCb** Collaboration, “LHCb magnet: Technical Design Report,” 2000. LHCb-TDR-001. Cited on page 37.

[75] **LHCb** Collaboration, R. Aaij *et al.*, “LHCb detector performance,” *Int. J. Mod. Phys.* **A30** (2015) 1530022, [arXiv:1412.6352](https://arxiv.org/abs/1412.6352) [hep-ex]. Cited on pages 37, 53, 54, and 55.

[76] **LHCb** Collaboration, “LHCb inner tracker: Technical Design Report,” 2002. LHCb-TDR-008. Cited on page 38.

[77] **LHCb** Collaboration, “LHCb outer tracker: Technical Design Report,” 2001. LHCb-TDR-006. Cited on page 38.

- [78] R. Arink *et al.*, “Performance of the LHCb Outer Tracker,” *JINST* **9** (2014) P01002, [arXiv:1311.3893 \[physics.ins-det\]](https://arxiv.org/abs/1311.3893). Cited on pages 38 and 39.
- [79] “LHCb Silicon Tracker material for publications,” accessed August 2015. <http://www.physik.unizh.ch/groups/lhcb/public/material/>. Cited on page 38.
- [80] **LHCb** Collaboration, “LHCb RICH: Technical Design Report,” 2000. LHCb-TDR-003. Cited on page 40.
- [81] M. Adinolfi *et al.*, “Performance of the LHCb RICH detector at the LHC,” *Eur. Phys. J.* **C73** (2013) 2431, [arXiv:1211.6759 \[physics.ins-det\]](https://arxiv.org/abs/1211.6759). Cited on pages 40, 53, 55, and 56.
- [82] **LHCb** Collaboration, “LHCb calorimeters: Technical Design Report,” 2000. LHCb-TDR-002. Cited on page 43.
- [83] R. Aaij *et al.*, “Performance of the LHCb calorimeters,” LHCb-DP-2013-004. in preparation. Cited on page 43.
- [84] O. Deschamps, “LHCb Calorimeters - Commissioning & performance,” accessed August 2015. <http://cds.cern.ch/record/1271718/>. Cited on page 44.
- [85] **LHCb** Collaboration, “LHCb muon system: Technical Design Report,” 2001. LHCb-TDR-004. Cited on page 45.
- [86] F. Archilli *et al.*, “Performance of the muon identification at LHCb,” *JINST* **8** (2013) P10020, [arXiv:1306.0249 \[physics.ins-det\]](https://arxiv.org/abs/1306.0249). Cited on page 45.
- [87] A. A. Alves Jr. *et al.*, “Performance of the LHCb muon system,” *JINST* **8** (2013) P02022, [arXiv:1211.1346 \[physics.ins-det\]](https://arxiv.org/abs/1211.1346). Cited on page 47.
- [88] **LHCb** Collaboration, “LHCb trigger system: Technical Design Report,” 2003. LHCb-TDR-010. Cited on page 48.
- [89] R. Aaij *et al.*, “The LHCb trigger and its performance in 2011,” *JINST* **8** (2013) P04022, [arXiv:1211.3055 \[hep-ex\]](https://arxiv.org/abs/1211.3055). Cited on page 48.
- [90] V. V. Gligorov and M. Williams, “Efficient, reliable and fast high-level triggering using a bonsai boosted decision tree,” *JINST* **8** (2013) P02013, [arXiv:1210.6861 \[physics.ins-det\]](https://arxiv.org/abs/1210.6861). Cited on pages 49 and 59.
- [91] **LHCb** Collaboration, “LHCb online system, data acquisition and experiment control: Technical Design Report,” 2001. LHCb-TDR-007. Cited on page 50.
- [92] **LHCb** Collaboration, “LHCb computing: Technical Design Report,” 2005. LHCb-TDR-011. Cited on page 50.

[93] G. Barrand *et al.*, “GAUDI - A software architecture and framework for building HEP data processing applications,” *Comput. Phys. Commun.* **140** (2001) 45–55. Cited on page 50.

[94] T. Sjöstrand, S. Ask, J. R. Christiansen, R. Corke, N. Desai, *et al.*, “An Introduction to PYTHIA 8.2,” [arXiv:1410.3012 \[hep-ph\]](https://arxiv.org/abs/1410.3012). Cited on page 50.

[95] D. Lange, “The EvtGen particle decay simulation package,” *Nucl. Instrum. Meth.* **A462** (2001) 152–155. Cited on page 50.

[96] Warwick EvtGen group, “<http://evtgen.warwick.ac.uk/>,” October 2014. Cited on page 50.

[97] **GEANT4** Collaboration, S. Agostinelli *et al.*, “GEANT4: A Simulation toolkit,” *Nucl. Instrum. Meth.* **A506** (2003) 250–303. Cited on page 50.

[98] R. Brun and F. Rademakers, “ROOT: An object oriented data analysis framework,” *Nucl. Instrum. Meth.* **A389** (1997) 81–86. Cited on page 51.

[99] T. Latham *et al.*, October 2014. **Laura++** Dalitz plot fitting package, <http://laura.hepforge.org/>. Cited on pages 51, 89, and 136.

[100] M. Pivk and F. R. Le Diberder, “sPlot: a statistical tool to unfold data distributions,” *Nucl. Instrum. Meth.* **A555** (2005) 356–369, [arXiv:physics/0402083 \[physics.data-an\]](https://arxiv.org/abs/physics/0402083). Cited on pages 51 and 61.

[101] M. Feindt and U. Kerzel, “The NeuroBayes neural network package,” *Nucl. Instrum. Meth.* **A559** (2006) 190. <http://www.sciencedirect.com/science/article/pii/S0168900205022679>. Cited on page 52.

[102] **Particle Data Group** Collaboration, J. Beringer *et al.*, “Review of particle physics,” *Phys. Rev.* **D86** (2012) 010001. Cited on pages 77, 87, 93, and 94.

[103] T. Skwarnicki, *A study of the radiative cascade transitions between the Upsilon-prime and Upsilon resonances*. PhD thesis, Institute of Nuclear Physics, Krakow, 1986. DESY-F31-86-02. Cited on page 79.

[104] **BaBar** Collaboration, B. Aubert *et al.*, “Observation of tree-level B decays with $s\bar{s}$ production from gluon radiation,” *Phys. Rev. Lett.* **100** (2008) 171803, [arXiv:0707.1043 \[hep-ex\]](https://arxiv.org/abs/0707.1043). Cited on pages 81 and 114.

[105] **Belle** Collaboration, J. Wiechczynski *et al.*, “Measurement of $B \rightarrow D_s^{(*)} K\pi$ branching fractions,” *Phys. Rev.* **D80** (2009) 052005, [arXiv:0903.4956 \[hep-ex\]](https://arxiv.org/abs/0903.4956). Cited on pages 81 and 114.

[106] **LHCb** Collaboration, R. Aaij *et al.*, “Measurements of the branching fractions of the decays $B_s^0 \rightarrow D_s^\mp K^\pm$ and $B_s^0 \rightarrow D_s^- \pi^+$,” *JHEP* **06** (2012) 115 CERN-PH-EP-2012-091, LHCb-PAPER-2011-022, [arXiv:1204.1237 \[hep-ex\]](https://arxiv.org/abs/1204.1237). Cited on page 85.

[107] E. Ben-Haim, R. Brun, B. Echenard, and T. E. Latham, “JFIT: a framework to obtain combined experimental results through joint fits,” [arXiv:1409.5080 \[physics.data-an\]](https://arxiv.org/abs/1409.5080). Cited on page 89.

[108] M. Williams, “How good are your fits? Unbinned multivariate goodness-of-fit tests in high energy physics,” *JINST* **5** (2010) P09004, [arXiv:1006.3019 \[hep-ex\]](https://arxiv.org/abs/1006.3019). Cited on page 96.

[109] **LHCb** Collaboration, R. Aaij *et al.*, “Observation of overlapping spin-1 and spin-3 $\bar{D}^0 K^-$ resonances at mass 2.86 GeV/ c^2 ,” *Phys. Rev. Lett.* **113** (2014) 162001, [arXiv:1407.7574 \[hep-ex\]](https://arxiv.org/abs/1407.7574). Cited on pages 103 and 135.

[110] **LHCb** Collaboration, R. Aaij *et al.*, “Dalitz plot analysis of $B^0 \rightarrow \bar{D}^0 \pi^+ \pi^-$ decays,” *Phys. Rev.* **D92** (2015) 032002, [arXiv:1505.01710 \[hep-ex\]](https://arxiv.org/abs/1505.01710). Cited on pages 103, 135, 138, and 151.

[111] D. Atwood, I. Dunietz, and A. Soni, “Enhanced CP violation with $B \rightarrow K D^0 (\bar{D}^0)$ modes and extraction of the CKM angle γ ,” *Phys. Rev. Lett.* **78** (1997) 3257–3260, [arXiv:hep-ph/9612433 \[hep-ph\]](https://arxiv.org/abs/hep-ph/9612433). Cited on page 107.

[112] D. Atwood, I. Dunietz, and A. Soni, “Improved methods for observing CP violation in $B^\pm \rightarrow K^\pm D$ and measuring the CKM phase γ ,” *Phys. Rev.* **D63** (2001) 036005, [arXiv:hep-ph/0008090 \[hep-ph\]](https://arxiv.org/abs/hep-ph/0008090). Cited on page 107.

[113] **LHCb** Collaboration, R. Aaij *et al.*, “First evidence for the annihilation decay mode $B^+ \rightarrow D_s^+ \phi$,” *JHEP* **02** (2013) 043, [arXiv:1210.1089 \[hep-ex\]](https://arxiv.org/abs/1210.1089). Cited on pages 108, 129, and 156.

[114] **E791** Collaboration, E. M. Aitala *et al.*, “Model independent measurement of S-wave $K^- \pi^+$ systems using $D^+ \rightarrow K \pi \pi$ decays from Fermilab E791,” *Phys. Rev.* **D73** (2006) 032004, [arXiv:hep-ex/0507099 \[hep-ex\]](https://arxiv.org/abs/hep-ex/0507099). Cited on page 136.

[115] **CLEO** Collaboration, G. Bonvicini *et al.*, “Dalitz plot analysis of the $D^+ \rightarrow K^- \pi^+ \pi^+$ decay,” *Phys. Rev.* **D78** (2008) 052001, [arXiv:0802.4214 \[hep-ex\]](https://arxiv.org/abs/0802.4214). Cited on pages 136 and 147.

[116] **FOCUS** Collaboration, J. M. Link *et al.*, “The $K^- \pi^+$ S-wave from the $D^+ \rightarrow K^- \pi^+ \pi^+$ decay,” *Phys. Lett.* **B681** (2009) 14–21, [arXiv:0905.4846 \[hep-ex\]](https://arxiv.org/abs/0905.4846). Cited on page 136.

[117] **BaBar** Collaboration, P. del Amo Sanchez *et al.*, “Analysis of the $D^+ \rightarrow K^- \pi^+ e^+ \nu_e$ decay channel,” *Phys. Rev.* **D83** (2011) 072001, [arXiv:1012.1810 \[hep-ex\]](https://arxiv.org/abs/1012.1810). Cited on page 136.

[118] **BaBar** Collaboration, J. P. Lees *et al.*, “Measurement of the $I=1/2$ $K\pi$ \mathcal{S} -wave amplitude from Dalitz plot analyses of $\eta_c \rightarrow K\bar{K}\pi$ in two-photon interactions,” [arXiv:1511.02310 \[hep-ex\]](https://arxiv.org/abs/1511.02310). Cited on page 136.

[119] **BaBar** Collaboration, B. Aubert *et al.*, “Amplitude analysis of the decay $D^0 \rightarrow K^- K^+ \pi^0$,” *Phys. Rev.* **D76** (2007) 011102, [arXiv:0704.3593 \[hep-ex\]](https://arxiv.org/abs/0704.3593). Cited on page 136.

[120] **BaBar** Collaboration, B. Aubert *et al.*, “Dalitz plot analysis of $D_s^+ \rightarrow \pi^+ \pi^- \pi^+$,” *Phys. Rev.* **D79** (2009) 032003, [arXiv:0808.0971 \[hep-ex\]](https://arxiv.org/abs/0808.0971). Cited on page 136.

[121] **LHCb** Collaboration, M. Ferro-Luzzi, T. Latham, and C. Wallace, “Determination of the aperture of the LHCb VELO RF foil,” LHCb-PUB-2014-012. Cited on page 158.